Neutron spectroscopy in the layered quantum magnet SrCu$_2$(BO$_3$)$_2$ and in transition metal phosphorus trisulfides (MPS$_3$)

PAR

Diane Virginie Marie LANÇON

EPFL

ÉCOLE POLYTECHNIQUE
FÉDÉRALE DE LAUSANNE

Suisse
2017

Abstract

Collective magnetic excitations are a fascinating aspect of condensed matter physics, where neutron scattering can provide valuable insight into the magnetic properties of physical realisations of model systems. This thesis focuses on the excitation spectra of layered quantum magnets in the case of the frustrated quantum magnet $SrCu_2(BO_3)_2$ and the family of quasi-2D antiferromagnets MPS_3, with M a transition metal.

- $SrCu_2(BO_3)_2$ is a physical realisation of the two-dimensional Shastry-Sutherland theoretical model, constructed as orthogonal dimers with the product of singlets on the strong antiferromagnetic J bond as an exact ground state. The spin interactions for such a particular geometry induces strong frustration which leads to unconventional magnetism and exotic phases of matter. This work is concerned with a series of aspects of the magnetic excitations in this compound. The excitation spectra as a function of field, temperature and pressure are measured using neutron time-of-flight spectroscopy. The experimental results show that correlations, bound magnons and finite temperature properties are highly unconventional and these results are compared with existing theories on frustrated model systems. In addition, predicted topological properties of $SrCu_2(BO_3)_2$ in an applied field are confirmed experimentally.

- The transition metal phosphorus trisulfides (MPS_3) are a family of quasi two-dimensional materials on a honeycomb lattice with weakly bound magnetic planes. This work focuses mainly on the exchange interactions and critical properties of $FePS_3$, which is largely anisotropic with the S=2 Fe^{2+} moments pointing normal to the (a, b) plane. Inelastic neutron scattering on single crystals is used to measure the spin wave dispersion, providing new insight on the strength of the coupling interactions and anisotropies and showing that $FePS_3$ is a good two-dimensional model antiferromagnet. Similar experiments on powdered samples of $NiPS_3$ show low-Q dispersive spin waves with a small spin-gap. Critical properties of $FePS_3$ close to the Néel temperature are further discussed, as the magnetic nature of the measured quasi-elastic scattering is confirmed. Based on magnetization measurements in high pulsed fields, a possible tricritical point in the 40-50T range is proposed.

The work presented in this thesis has been carried out in a collaboration between the Institut Laue Langevin in Grenoble and the Laboratory for Quantum Magnetism of the EPFL.

Key words: Quantum magnetism, frustrated magnetism, Shastry-Sutherland model, strongly correlated system, topological magnon insulator, spin wave theory, quasi-2D antiferromagnets, phase transitions, neutron scattering, triple axis spectroscopy, time of flight spectroscopy

Résumé

L'étude des excitations magnétiques est un domaine de la physique du solide au sein de laquelle la diffusion des neutrons permet de confronter les modèles théoriques aux propriétés magnétiques des matériaux. Cette thèse se concentre sur les spectres d'excitations magnétiques d'aimants quantiques, et en particulier, sur l'aimant frustré $SrCu_2(BO_3)_2$ et sur la famille des MPS_3 aux des propriétés antiferromagnétiques quasi-2D.

- $SrCu_2(BO_3)_2$ est une réalisation du réseau de Shastry-Sutherland, un modèle en deux dimensions de dimers orthogonaux construit tel que le produit des singletons sur le lien antiferromagnétique fort J est un état fondamental. Dans cette géométrie, les interactions de spins sont fortement frustrées, ce qui implique un magnétisme non conventionnel. L'évolution des spectres d'excitations magnétiques en fonction de la température, d'un champ magnétique et de la pression appliquée est mesurée par spectroscopie dite "temps-de-vol". L'analyse des résultats expérimentaux montre que les correlations entre les magnons et les propriétées à températures finies sont hautement non conventionnelles. Ces résultats sont comparés à des modèles théoriques existants. De plus, une confirmation de prédiction théorique portant sur propriétés topologiques de $SrCu_2(BO_3)_2$ soumis à un champ magnétique est obtenue expérimentalement.

- La famille des MPS_3 (avec M un métal de transition) aux propriétés antiferromagnétiques quasi-2D a une structure en nid d'abeilles dont les plans magnétiques ne sont que faiblement liés. Ce travail s'intéresse principalement aux interactions d'échange et aux propriétés critiques du composé anisotropique $FePS_3$ dont les moments Fe^{2+} sont perpendiculaires au plan (a, b). La dispersion des ondes de spin est mesurée par diffusion inélastique des neutrons avec des monocristaux, permettant d'étudier les interactions d'échange et l'anisotropie de $FePS_3$. Ce composé apparaît ainsi comme un bon modèle d'antiferromagnétisme en deux dimensions. Des expériences similaires sur poudre permettent d'étudier les ondes de spin de $NiPS_3$. Les propriétés critiques de $FePS_3$ à la température de Néel sont présentées, à la lumière de la nature magnétique de la diffusion quasi-élastique mesurée. Un point tricritique autour de 40-50T est envisagé d'après des mesures de susceptibilité magnétique pour des hauts champs pulsés.

Le travail présenté dans cette thèse a été préparé dans le cadre d'une collaboration entre l'Institut Laue Langevin à Grenoble et le Laboratoire de Magnétisme Quantique de l'EPFL.

Mots clefs : Magnétisme quantique, magnétisme frustré, modèle de Shastry-Sutherland, systèmes fortement corrélés, isolants topologiques magnoniques, ondes de spin, transitions de phase, diffusion des neutrons, spectroscopie trois-axes, spectroscopie par temps de vol

Acknowledgements

Acknowledgements

Contents

Contents

Introduction

Collective magnetism is a complex and diverse research subject in condensed matter physics. Deceptively simple materials, well characterized microscopically, can display exotic magnetic behaviour due to large quantum effects. Quantum fluctuations in systems with reduced dimensionality may have enhanced spin correlations, leading to strongly correlated systems.

In this context, layered quantum magnets are of particular interest as quasi-2D materials, as the weak coupling between the magnetic planes makes these compounds test-beds for fundamental magnetism . By measuring time-dependent and space-dependant correlations, and in particular spin correlations, neutron scattering is an excellent probe of quantum magnetism. Hence, neutron scattering experiments on physical realisations of fundamental theoretical models of magnetism bring new insight.

In particular, the research field of frustrated magnetism aims to understand unconventional behaviour, defined in contrast to conventional magnets that show long-ranged order and non-degenerate ground states. In the absence of such characteristics, the systems show strong quantum effects and exotic phases of matter. Particular lattice geometries (like Kagomé or Shastry-Sutherland lattices) or local constraints (like spin ice for a anisotropic ferromagnet on a pyrochlore lattice) lead to frustration as not all the interactions can be satisfied, and hence lead to degenerate states. As opposed to a conventional magnet, with a phase transition between a paramagnetic state to a long-ranged ordered phase, there is no particular ordering transition in a frustrated magnet due to the degeneracy of states and the system is instead strongly correlated.

Starting from the magnetic atoms with unpaired localized electrons, organised on a lattice with a specific geometry, the quantum-mechanical object of interest is the electronic spin $\mathbf{S}$. It is defined as a quantized angular momentum (in units of $\hbar$) and the eigenvalue of the operator $\mathbf{S}^2$ is $S(S+1)\,\hbar^2$. The spin degree of freedom of neighbouring magnetic atoms interact either when they have a direct orbital overlap, through double exchange, or by a pathway through non-magnetic atoms. It is thus the overlap and geometric arrangement of the atomic orbitals which define the spin interactions.

Contents

Heisenberg Hamiltonian. The isotropic Heisenberg Hamiltonian can be considered as a starting effective model to describe localised spins on a lattice, with pairs of spins coupled through a bilinear energy J. This is usually the starting point for any study of a real material [1], where particularities of the interactions, geometry, dimensionality, or crystal field are then described as deviations from the model in the form of anisotropies. The most general form of this model is defined by the following Hamiltonian :

$$H = - \sum_{(i,j), \alpha = x, y, z} J_{ij}^{\alpha} S_i^{\alpha} S_j^{\alpha} \tag{1}$$

where (i, j) indicates a sum over the pairs ij and the spin operators S are quantum mechanical operators obeying the commutation relations of angular momentum $[S^x, S^y] = iS^z$.
J corresponds to the exchange parameter. In the chosen convention, $J < 0$ corresponds to an antiferromagnetic coupling while $J > 0$ is ferromagnetic.

When $J^x = J^y = J^z$, the coupling is fully isotropic, corresponding to an ideal Heisenberg Hamiltonian. Other combinations are anisotropic, such as the Ising model with $J^x = J^y = 0$ or the XY model corresponding to a planar anisotropy with $J^z = 0$.

Such ideal Hamiltonians rarely describe fully the magnetic properties of real materials as there are further perturbation terms, and the identification of these deviations and their effect is often the object of study in quantum magnetism. Among possible perturbation terms are single-ion anisotropies or a particular crystal environment introducing anisotropies such as the Dzyaloshinskii-Moriya interaction. In addition, this ideal model can be restricted to nearest neighbours, but further couplings must often be included, for example to reproduce frustration effects which depend on competing interactions particular to the lattice geometry. Similarly, this model is lattice-dependent and thus can be used for one or two-dimensional models, which can display radically different properties compared to three-dimensional models.

Forms of collective magnetism. Collective magnetism can take diverse forms depending on parameters such as the competing interactions, the lattice geometries, the effective dimensionality and the spin value. A first situation is the appearance of magnetic long-ranged order below a critical temperature, which is an extremely common scenario in real magnetic materials. Far below the ordering transition temperature, quantum fluctuations become more important. Low-energy fluctuations, called spin waves, are considered semi-classical, with quantum fluctuations only weakly appearing as a renormalisation of quantities in spin wave theory such as spin wave velocity and staggered magnetisation. A chapter will be dedicated to the transition metal phosphorus trisulfides family (MPS_3), which are antiferromagnets on a honeycomb lattice below the Néel temperature [2]. Linear spin wave theory is thus relevant to describe their magnetic excitations.

Radically different are materials in which there is no magnetic long-ranged order even at zero temperature, with an exponentially decreasing correlation function at large distances. This

absence of long-ranged order was predicted by Haldane in 1983 to occur in an S=1 Heisenberg chain [3], and confirmed in both organic [4] and inorganic [5] quasi one-dimensional compounds. A consequence of the finite correlation length is the presence of a spin gap, where there are no low-energy excitations. The ground state is a spin singlet and the spin gap corresponds to the energy difference between the ground state energy and the energy of the singlet to triplet excitation. These magnetic systems are classified as gapped spin liquids [6]. The frustrated quantum magnet $SrCu_2(BO_3)_2$ with a spin gap of 34 K [7] will be discussed in this context.

Finally, non-gapped spin liquids, with low lying excitations in the singlet-triplet gap, are also widely studied in quantum magnetism such, for example in Kagomé lattice geometries with possible resonating valence bond states[8], but are beyond the scope of this work.

0.1 Thesis outline

This thesis is concerned with layered quantum magnets with reduced dimensionality probed by inelastic neutron scattering. Neutron scattering as a probe of magnetism is discussed in chapter 1. The work is then divided in two main chapters discussing aspects of collective magnetism relevant in either the frustrated quantum magnet $SrCu_2(BO_3)_2$ which displays no long-ranged magnetic order due to its competing interactions on a particular 2D geometry, or in the MPS_3 family of quasi-two dimensional antiferromagnets on a honeycomb lattice. They are largely independent from each other and can be read separately. Finally, two appendices will discuss selected aspects of magnetism in compounds relevant either to spintronics (Mn-doped ZnO in appendix A) or to superconductivity (incommensurate magnetic order in FeTeSe, CrAs and MnP in appendix B).

The detailed layout is as follows :

- $SrCu_2(BO_3)_2$ in chapter 2 : The Shastry-Sutherland geometry of orthogonal dimers with exact ground state is realised in $SrCu_2(BO_3)_2$ (SCBO), making it a good model system with unconventional magnetism and exotic phases of matter. Frustration in this compound leads to fully localised singlet-triplet excitations observed as a flat band in the excitation spectra. Its coupling exchange constants place $SrCu_2(BO_3)_2$ in the dimer-singlet phase with no long-ranged order, very close to a possible quantum phase transition to a proposed plaquette phase. This phase can be reached and studied by tuning the strength of the exchange, for example using hydrostatic pressure.

  This work focuses on the impact of strong frustration and correlations in this model system by measuring the neutron excitation spectrum for a broad range of energies, and its evolution with temperature, applied magnetic field and applied pressure. The results confirm the strength of the interaction couplings, and show that bound state formation and possible correlated hopping have dramatic effects on the dynamical response of the system. By measuring and analysing the unusual finite temperature properties of the singlet-triplet mode of $SrCu_2(BO_3)_2$, a Q-dependent correlated decay of the singlet-

triplet modes is shown to be strongly sensitive to thermal population of the triplet states. Due to a buckling of the $CuBO_3$ planes, the Dzyaloshinskii-Moriya interaction creates strong anisotropies in this compound, weakly splitting the degenerate singlet-triplet mode. Coupled with the strongly frustrated geometry, the Dzyaloshinskii-Moriya interaction makes SCBO a potential topological magnon insulator, which we discuss using neutron experimental evidence.

- The MPS_3 family in chapter 3: Transition metal phosphorus trisulfides (MPS_3) are a family of quasi two-dimensional antiferromagnets on a honeycomb lattice (M=Fe,Ni,Co,Mn). The magnetic planes are only weakly bound by Van der Waals forces, thus reducing the strength of the interlayer couplings and allowing rotational twinning. Although their crystallographic structure are very similar, members of the MPS_3 family have different magnetic properties. In particular, $FePS_3$ is largely anisotropic with properties of an Ising antiferromagnet below $T_N = 123$ K with $S = 2$ moments normal to the (a, b) plane. Each moment is ferromagnetically coupled to two of its nearest neighbours and antiferromagnetically coupled to its third.

  Using neutron diffraction to study the presence of magnetic domains, this work explains discrepancies observed in literature and confirms $\mathbf{k} = [01\frac{1}{2}]$ as the magnetic propagation vector. By measuring the gapped dispersion of the doubly degenerate spin waves in $FePS_3$ using inelastic neutron scattering, the anisotropy and exchange coupling constants were extracted and shown to explain the dynamical properties of $FePS_3$ as a 2D-antiferromagnet model system. The phase transition at the Néel temperature shows both first order characteristics and critical scattering in $FePS_3$, while the measured quasi-elastic scattering is found to be magnetic. Finally, $FePS_3$ has an honeycomb lattice and a large single ion anisotropy, which makes it a potential candidate compound for the presence of tri-critical point. The magnetization measurements at high pulsed fields carried out on single crystals provide some evidence for such a tri-critical point in the 40-50 T range.

  In addition, the excitation spectra of $NiPS_3$ has also been measured for a powdered sample using time-of-flight spectroscopy, showing highly dispersive low-Q spin waves with a small spin-gap.

Two additional topics will be briefly explored in the appendices :

- Mn-doped ZnO in appendix A : Spin correlations in dilute magnetic semiconductors can be explored using polarised neutron scattering in order to assess claims of ferromagnetism in lightly Mn-doped ZnO. Ferromagnetism in dilute magnetic semi conductors would make them potential candidates for technological application of magnetic properties. By studying the structural and magnetic properties of powdered samples using polarized neutron scattering, the observed ferromagnetic behaviour of Mn-doped ZnO is shown to coincides with the presence of MnO nanoparticles, whereas cluster-free Mn-doped ZnO behaves paramagnetically.

- Unconventional superconductivity in appendix B: incommensurate correlations in new superconductors are discussed for three compounds : the iron chalcogenide $Fe_{1+y}Te_{0.7}Se_{0.3}$; and the binary pnictides CrAs and MnP. The interplay of magnetism and superconductivity is at the heart of research on unconventional superconductors, which focuses on the evolution of magnetic order close to the superconducting phase, for example by doping the parent compound or by applying hydrostatic pressure. In particular, a new narrow magnetic phase is discovered in MnP at 15 kbar applied pressure, and the magnetic phase observed from neutron diffraction for 25 kbar is shown to be incommensurate along c and to extend at least to 55 kbar applied pressure.

1 | Materials and Methods

1.1 Neutron Scattering

Neutron scattering is a powerful and versatile probe of condensed matter physics as it allows the direct measurement of correlations functions, both in time and space. The wavelength of thermal neutrons ($\sim$ 2 Å) is similar to inter-atomic distances, and their energy ($\sim$ 25 meV) is comparable to lattice vibrations and elementary excitations. Neutrons are uncharged, thus only interacting weakly and non-destructively with matter, penetrating deeply into materials and thus allowing bulk studies. In addition, the neutron scattering length varies fairly randomly between elements and isotopes of the same elements, allowing the study of light isotopes such as hydrogen. The nuclear force gives rise to scattering of the neutrons by the atomic nuclei, and is referred to as nuclear scattering. Neutrons interact with the nucleus via a simple point-like potential, so that the amplitudes of nuclear scattering are easily interpreted. In addition, neutrons have an intrinsic spin 1/2 magnetic moment so that they are sensitive to the internal magnetic field of materials originating from unpaired electrons. Neutron magnetic scattering thus allows spin correlations functions in magnetic materials to be accessed.

The rate of scattered neutrons per unit of incident flux ψ_0 corresponds to the cross section σ and is the fundamental quantity measured in a neutron scattering experiment. The rate I of neutrons detected in a solid angle $d\Omega$ with a final energy between E_f and $E_f + dE_f$ is given by :

$$I = \psi_0 \left(\frac{d^2\sigma}{d\Omega dE_f} \right) \Delta\Omega\Delta E_f \tag{1.1}$$

where ($\frac{d^2\sigma}{d\Omega dE_f}$) defines the partial differential cross section, which can be calculated using the formalism of scattering theory.

1.1.1 Scattering theory

For a complete derivation of the partial differential cross section, one can refer to Squires [9]. A scattering process is described by Fermi's golden rule. The rate of change between the neutron in an incoming state and a continuum of outgoing states is given by :

$$\sum_{k_f} W_{i \to f} = \frac{2\pi}{\hbar} \rho_{k_f} \langle \psi_i | \hat{V} | \psi_f \rangle|^2 \tag{1.2}$$

with $\hat{V}$ the operator describing the interaction responsible for the scattering and ρ_{k_f} the number of momentum states per unit range for neutrons in the final state with scattered wavenumber k_f. The incoming flux is expressed as :

$$\psi_0 = \frac{v}{Y} = \frac{\hbar k_i}{Y m_n} \tag{1.3}$$

with Y the normalisation volume, k_i the incident wavenumber and m_n the mass of the neutron.

Considering only neutrons scattered into the solid angle $d\Omega$, and using the expression for the flux ψ_0, the differential cross section is given by :

$$\frac{d\sigma}{d\Omega} = \frac{1}{\psi_0} \frac{1}{d\Omega} \sum_{\substack{k_f \\ \text{in } d\Omega}} W_{i \to f} = \frac{k_f}{k_i} \left(\frac{m_n}{2\pi\hbar^2} \right)^2 |\langle \psi_i | \hat{V} | \psi_f \rangle|^2 \tag{1.4}$$

Neutrons are scattered by the nucleus due to the strong nuclear force, which has a interaction range of the order of femtometers (fm). As this interaction range is much smaller than the neutron wavelength (Å), neutrons cannot probe the internal structure of the nucleus and thus scatter isotropically. In this context, the first Born approximation allows to replace the scattered wave function by a plane wave, by taking only the first term in the expansion of the wave function in powers of the interaction potential V(r). The first term of this series describe a single scattering process of the incident wave, and the following terms describe scattering processes of higher order known as multiple scattering. The Born approximation thus assumes that both the incident and scattered neutrons can be described as plane waves, with only one single scattering event of the incident wave from the interaction potential.

A scattering process can be inelastic, with the neutron either gaining or loosing energy to the scattering system. The neutron energy transfer is defined as :

$$\begin{aligned} \hbar\omega &= E_i - E_f \\ &= \frac{\hbar^2}{2m_n} (k_i^2 - k_f^2) \end{aligned} \tag{1.5}$$

The neutron momentum transfer to the scattering system $\hbar\mathbf{Q}$ is defined as :

$$\hbar\mathbf{Q} = \hbar\mathbf{k}_i - \hbar\mathbf{k}_f \tag{1.6}$$

In a scattering event, the state of the scattering system must also be taken into account. For a transition of the scattering from an initial state $|\lambda_i\rangle$ to a final state $|\lambda_f\rangle$, the partial differential cross section is thus given as :

$$\left(\frac{d^2\sigma}{d\Omega dE_f}\right)_{\lambda_i \to \lambda_f} = \frac{k_f}{k_i}\left(\frac{m_n}{2\pi\hbar^2}\right)^2 |\langle \lambda_i \psi_i | \hat{V} | \lambda_f \psi_f \rangle|^2 \delta(E_i - E_f + \hbar\omega) \tag{1.7}$$

with $\delta(E_i - E_f + \hbar\omega)$ an explicit expression for energy conservation.

Regarding magnetic scattering, the magnetic potential $\hat{V}_m$ contains the spin operator $\hat{\sigma}$. The spin state of the neutron must be thus specified in the partial differential cross section for a magnetic scattering event :

$$\left(\frac{d^2\sigma}{d\Omega dE_f}\right)_{\sigma_i \lambda_i \to \sigma_f \lambda_f} = \frac{k_f}{k_i}\left(\frac{m_n}{2\pi\hbar^2}\right)^2 |\langle \sigma_i \lambda_i \psi_i | \hat{V}_m | \sigma_f \lambda_f \psi_f \rangle|^2 \delta(E_i - E_f + \hbar\omega) \tag{1.8}$$

Turning to the interaction potential with respect to the neutron coordinate $\mathbf{r}$, it can be written for the whole scattering system as :

$$V(\mathbf{r}) = \sum_j V_j(\mathbf{r} - \mathbf{R}_j) \tag{1.9}$$

with $V_j(\mathbf{r} - \mathbf{R}_j)$ the potential of the neutron due to the j$^{\text{th}}$ nucleus.

1.1.2 Nuclear scattering

The interactions of neutrons with the j$^{\text{th}}$ nuclei of the sample can be described by the Fermi pseudo-potential :

$$V_j(\mathbf{r} - \mathbf{R}_j) = \frac{2\pi\hbar^2}{m_n} b_j \delta(\mathbf{r} - \mathbf{R}_j) \tag{1.10}$$

with b_j the nuclear scattering length of the j$^{\text{th}}$ nucleus . The scattering length of an element depends on its isotopes and, if present, on the direction of its nuclear spin with respect to the spin of the incident neutron.

For a fixed $\mathbf{k}_i$ and $\mathbf{k}_f$, the Fourier transform $V(\mathbf{Q})$ of the potential for the scattering system is

given as :

$$V(\mathbf{Q}) = \sum_j \frac{2\pi\hbar^2}{m_n} b_j e^{i\mathbf{Q}\cdot\mathbf{R_j}} \tag{1.11}$$

Coherent scattering contains the scattering cross-section obtained if all the scattering centres have the same average scattering length $\bar{b} = \sum_i f_i b_i$ with f_i the abundance of the isotope with scattering length b_i . For a mono-atomic sample, the coherent partial differential cross section is given by :

$$\left(\frac{d^2\sigma}{d\Omega dE_f}\right)_{coh} = \frac{k_f}{k_i}\frac{1}{2\pi\hbar}\bar{b}^2 \sum_{j,j'}\int_{-\infty}^{\infty} dt\, e^{-i\omega t}\langle e^{i\mathbf{Q}\cdot(r_j(t)-r_{j'}(0))}\rangle \tag{1.12}$$

showing that coherent scattering from a crystal depends on spatial and temporal correlations between the same nucleus, or different nucleus at different times. Nuclear Bragg peaks thus appear in the coherent part of the partial differential scattering cross section.

On the other hand, incoherent scattering is caused by randomly distributed deviations from the mean scattering length which is characterised by the variance $\overline{b^2} = \sum_i f_i b_i^2$ and is given by:

$$\left(\frac{d^2\sigma}{d\Omega dE_f}\right)_{inc} = \frac{k_f}{k_i}\frac{1}{2\pi\hbar}(\overline{b^2}-\overline{b}^2) \sum_{j}\int_{-\infty}^{\infty} dt\, e^{-i\omega t}\langle e^{i\mathbf{Q}\cdot(r_j(t)-r_j(0))}\rangle \tag{1.13}$$

showing that incoherent scattering arises from self-correlations of the same nucleus at different times.

The total scattering cross sections for coherent and incoherent scattering for an element are given as :

$$\sigma_{coh} = 4\pi\overline{b}^2 \tag{1.14}$$
$$\sigma_{inc} = 4\pi(\overline{b^2}-\overline{b}^2) \tag{1.15}$$

These values are tabulated for each isotope in [10].

Also tabulated in [10] are the neutron absorption cross sections σ_{abs} of elements and their isotopes, given for the typical thermal velocity $v = 2200$ m/s. Neutron absorption results from neutron-induced nuclear process which destroys the neutron and emits secondary radiation and is generally inversely proportional to the neutron velocity in the cold and thermal energy range.

1.1.3 Scattering from a crystal

In the case of periodic scattering centres, such as in a crystal with a reciprocal lattice defined by $\mathbf{a}^*$, $\mathbf{b}^*$ and $\mathbf{c}^*$ and lattice vector $\boldsymbol{\tau} = h\mathbf{a}^* + k\mathbf{b}^* + l\mathbf{c}^*$, there are Bragg peaks in the coherent differential cross section $\frac{d\sigma}{d\Omega}$ for momentum transfer $\mathbf{Q} = \boldsymbol{\tau}$.

This corresponds to satisfying Bragg's law in the case of a monochromatic beam :

$$n\lambda = 2d\sin\theta = \frac{4\pi}{|\boldsymbol{\tau}|}\sin\theta \tag{1.16}$$

Hence, the coherent differential cross section is given as :

$$\frac{d\sigma}{d\Omega} = N\frac{(2\pi)^3}{V_0}\sum_{\boldsymbol{\tau}}\delta(\mathbf{Q} - \boldsymbol{\tau})|F_n(\tau)|^2 \tag{1.17}$$

with N the number of unit cells in the sample, V_0 the volume of the unit cell, and F_n the static nuclear structure factor corresponding to $F_n(\tau) = \sum_j \overline{b_j}\, e^{i\boldsymbol{\tau}\cdot\mathbf{r}_j}\, e^{-W_j}$ with e^{-W_j} the Debye-Waller factor from thermal lattice fluctuations.

1.1.4 Scattering function

The quantity measured in neutron scattering can be related to the thermal average of operators expressed as correlation functions. Indeed, the partial differential cross section is proportional to the scattering function $S(\mathbf{Q}, \hbar\omega)$ after removing the instrumental effects. $S(\mathbf{Q}, \hbar\omega)$ contains a double sum over pairs of nuclei where each term of the sum corresponds to the correlation between the spatial position of one nucleus (or spin) at time $t = 0$ with the position of another nucleus (or spin) at a time t. $S(\mathbf{Q}, \hbar\omega)$ thus provides information on collective behaviours, and can be used to estimate the strength of couplings in the system.

Furthermore, the scattering function $S(\mathbf{Q}, \hbar\omega)$ can be related to the imaginary part of the dynamical susceptibility $\chi''(\mathbf{Q}, \hbar\omega)$ by the fluctuation-dissipation theorem :

$$S(\mathbf{Q}, \hbar\omega) = \frac{\hbar}{\pi}[n(\omega) + 1]\chi''(\mathbf{Q}, \hbar\omega) \tag{1.18}$$

with $[n(\omega) + 1]$ the Bose factor, given by $n(\omega) = \frac{1}{e^{\hbar\omega/k_B T} - 1}$. The dynamical susceptibility corresponds to the response of a system to a perturbation, and its imaginary part $\chi''(\mathbf{Q}, \hbar\omega)$ is related to the dissipation of energy by the perturbed system. The constant $\hbar$ will be dropped in following expressions of the scattering function.

1.1.5 Detailed balance

It can be shown that $S(\mathbf{Q}, \omega)$ has the analytical property [9] :

$$S(\mathbf{Q}, \omega) = e^{\frac{\hbar\omega}{k_B T}} S(-\mathbf{Q}, -\omega) \tag{1.19}$$

This is known as the principle of detailed balance.

For systems where there is no effect of the reversal of $\mathbf{Q}$, then $S(\mathbf{Q}, \omega) = e^{\frac{\hbar\omega}{k_B T}} S(\mathbf{Q}, -\omega)$. Let a positive energy transfer $\omega > 0$ be defined in a scattering process as a loss of energy for the neutron (and a gain for the system). The probability that the neutron creates an energy exchange in either direction is the same. However, for a temperature T, the probability of the system being initially in the higher energy state is lower than the probability of it being in the lower energy state by a factor $e^{\frac{\hbar\omega}{k_B T}}$. The scattering function corresponding to a neutron energy gain $S(\mathbf{Q}, -\omega)$ is thus less than the one corresponding to a neutron energy loss $S(\mathbf{Q}, \omega)$ by the same factor.

Figure 1.1 illustrates the principle of detailed balance for a system with a temperature comparable to the energy of the mode, i.e. $k_B T \sim \hbar\omega_0$.
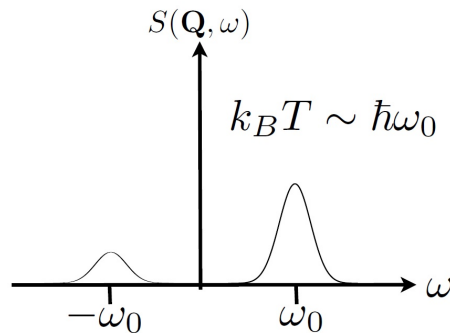
Figure 1.1: Scattering function as a function of ω for $k_B T \sim \hbar\omega_0$ showing the principle of detailed balance. [1]

---

[1] from "Neutron Scattering" lecture by Ross Stewart, ISIS neutron Facility, Rutherford Appleton Lab, Didcot, UK

1.1.6 Magnetic scattering

Neutron magnetic scattering will be discussed under the assumption of localised unpaired electrons, and considering scattering as due to spin only, so that itinerant systems are excluded. In this context, neutron magnetic scattering measures the spin correlations function, and thus can easily distinguish between phases with different symmetries of the correlation function (for example, between a paramagnet with diffuse scattering or an ordered phase with Bragg peaks). Neutrons are scattered by the spatially varying magnetic field from spins in the material. The dynamic scattering function is proportional to time and the spatial Fourier transform of the two-spin correlation function of the sample is :

$$S^{\alpha,\beta}(\mathbf{Q},\omega) = \frac{1}{2\pi}\sum_{\mathbf{R}}\int_{-\infty}^{+\infty}\mathrm{e}^{i\mathbf{Q}\cdot\mathbf{R}-\omega t}\langle S_0^\alpha(0)S_{\mathbf{R}}^\beta(t)\rangle dt \tag{1.20}$$

with R the spin positions. The measured Q-dependence of the scattering function can give insight on the spatial correlations of the spin correlations : if $S(\mathbf{Q},\omega)$ is resolution limited in $\mathbf{Q}$, then the spatial spin correlations are long-ranged, whereas if $S(\mathbf{Q},\omega)$ is broader than the resolution in $\mathbf{Q}$, the spin correlations are short-ranged.

Furthermore, the observed scattering is modified by two factors : the orientation factor and the magnetic form factor. The orientation factor exists because only some components of this tensor can be observed by neutron scattering. Indeed, the neutron only see magnetism with components perpendicular to the scattering vector Q, which is a consequence of Maxwell's law $\nabla \cdot B = 0$. The dynamic scattering function is thus multiplied by the orientation factor $\delta_{\alpha\beta} - \hat{Q}_\alpha\hat{Q}_\beta$ to remove the parallel components, with $\hat{Q}_{\alpha\beta}$ the components of the unitary vector $\hat{Q}$. The magnetic interaction vector thus has the form :

$$\mathbf{M}_{\perp\mathbf{Q}} = \hat{\mathbf{Q}} \times \big(\mathbf{M}(\mathbf{Q}) \times \hat{\mathbf{Q}}\big) \tag{1.21}$$

with $\mathbf{M}(\mathbf{Q})$ the Fourier transform of the sample magnetization $\mathbf{M}(\mathbf{r})$.

Neutrons are scattered by magnetisation densities rather than by point-like objects on a lattice, as unpaired localised electrons have spatially extended valence orbitals. The dynamic scattering function is derived from effective operators with localised spins on lattice vertices, so that a correction factor is needed in order to take into account the spatial spin densities. The validity of the approach is given by the Wigner-Eckart theorem, which shows that the matrix element can be decomposed into a product of two factors, one of which is independent from the angular momentum orientation. In this case the correction factor is the magnetic form factor squared $f^2(|\mathbf{Q}|)$, with f the Fourier transform of the normalised spin density of a single atom or ion. The magnetic form factor is ion specific [11], and within the hypothesis of a spherical spin density, follows a simple decreasing function as $|\mathbf{Q}|$ increases.

Nevertheless, not all electronic orbitals can be well approximated by a sphere, such as the e_g, $d(x^2 - y^2)$ orbital, for which the spin density is extended in the z-direction and has a faster decay in the xy-plane. Taking into account the particular shape of orbital can be necessary in order to properly account for an anisotropic form factor, and can be crucial for example in the case of Cu^{2+} where a single unpaired spin occupies a $3d(x^2 - y^2)$ orbital. For example, an anisotropic form factor had to be taken into account in La_2CuO_4 in order to analyse high energy spin waves obtained from neutron scattering [12].

The analytical approximation of the form factor obtained from the radial distribution of electrons is given as the sum of radial integrals, which are defined as :

$$\langle j_l(|\mathbf{Q}|) \rangle = \int_0^\infty R(r)^2 j_l(|\mathbf{Q}|r) 4\pi r^2 dr \tag{1.22}$$

where $j_l(|\mathbf{Q}|)$ are spherical Bessel functions with l=0,2,4,6 and $R(r)$ the radial part of the single electron wavefunction in the atom. An analytical approximation to the $\langle j_l(|\mathbf{Q}|) \rangle$ integrals for most common atoms and magnetic are tabulated as coefficients in the International Tables of Crystallography volume C [13]. Usually the dipole approximation is used to obtain the magnetic form factor from only the leading contribution in the limit of small momentum transfer $\mathbf{Q}$, with g the Landé splitting factor [11] :

$$f(|\mathbf{Q}|) = \langle j_0(|\mathbf{Q}|) \rangle + \frac{2 - g}{g} \langle j_2(|\mathbf{Q}|) \rangle \tag{1.23}$$

In the case of particular shape of orbitals, the anisotropic magnetic form factor is derived from the spherical Bessel functions by taking into account an angular dependence on the polar angles θ_Q and Φ_Q of the wavevector $\mathbf{Q}$ [14]. For the electron in the $d(x^2 - y^2)$ orbital relevant for Cu^{2+}, the following explicit expression can be used :

$$
\begin{aligned}
f(|\mathbf{Q}|) =& \langle j_0(|\mathbf{Q}|) \rangle - \frac{5}{7}(1 - 3\cos^2(\theta_Q)) \langle j_2(|\mathbf{Q}|) \rangle \\
&+ \frac{9}{56} \langle j_4(|\mathbf{Q}|) \rangle (1 - 10\cos^2(\theta_Q) + \frac{35}{3}\cos^4(\theta_Q)) \\
&+ \frac{15}{8} \langle j_4(|\mathbf{Q}|) \rangle \sin^4(\theta_Q) \cos(4\Phi_Q)
\end{aligned}
\tag{1.24}
$$

Figure 1.2 shows the anisotropic magnetic form factor squared for the $d(x^2 - y^2)$ orbital of Cu^{2+} depending on the direction of the wavevector $\mathbf{Q}$ compared to the angle-averaged form factor from the dipole approximation. Except for very small $|\mathbf{Q}|$, the anisotropy is large for $\mathbf{Q}//z$ and should be taken into account.
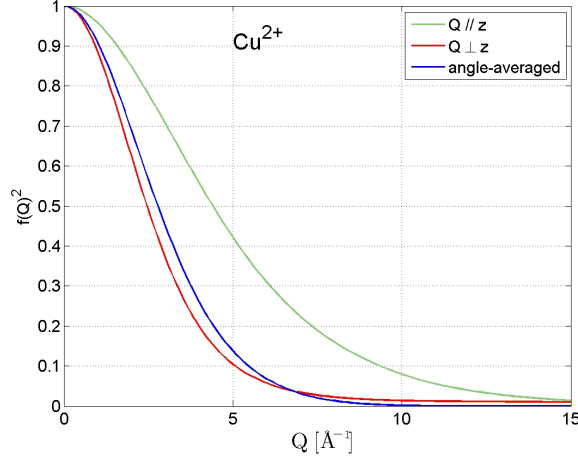
Figure 1.2: Wavevector dependence of the anisotropic magnetic form factor squared $f(|\mathbf{Q}|)^2$ for the $d(x^2 - y^2)$ orbital of Cu^{2+} from equation 1.24. In blue is the angle-averaged form factor, which corresponds to the form factor calculated from the dipole approximation. In green and red are the magnetic form factor for two directions of $\mathbf{Q}$ with the polar angle $\theta_Q = 0$ and $\Phi_Q = 0$ for $\mathbf{Q}//z$ (green) and $\theta_Q = 90$ and $\Phi_Q = 0$ for $\mathbf{Q} \perp z$ (red).

Including the orientation factor and the form factor described above, the magnetic scattered intensity from a single crystal is given by the partial differential cross section:

$$\frac{d^2\sigma}{d\Omega dE} = r_0^2 \frac{k_f}{k_i} f(|\mathbf{Q}|)^2 \sum_{\alpha,\beta} (\delta_{\alpha\beta} - \hat{Q}_\alpha \hat{Q}_\beta) S^{\alpha,\beta}(\mathbf{Q}, \omega) \tag{1.25}$$

with the magnetic scattering length $r_0 = \frac{\gamma_N e^2}{m_e c^2}$ where γ_N is the neutron gyromagnetic ratio [9]. In order to take into account the effect of temperature, this equation should be corrected by the Debye-Waller thermal factor $e^{(-2W)}$.

Similarly to nuclear elastic scattering from a crystal, a periodic arrangement of magnetic moments leads to magnetic elastic scattering with the following cross section :

$$\left(\frac{d\sigma}{d\Omega}\right)_{mag} = r_0^2 N_m \frac{(2\pi)^3}{V_{0m}} \sum_{\boldsymbol{\tau}_m} \delta(\mathbf{Q} - \boldsymbol{\tau}_m) \left| \hat{\mathbf{Q}} \times \left(\mathbf{F}_m(\mathbf{Q}) \times \hat{\mathbf{Q}} \right) \right|^2 \tag{1.26}$$

with N_m the number of magnetic unit cells in the sample, V_{0m} the volume of the magnetic unit cell. Magnetic peaks are found for $\mathbf{Q} = \boldsymbol{\tau}_m$ and the magnetic structure factor $\mathbf{F}_m(\boldsymbol{\tau}_m)$ is given by :

$$\mathbf{F}_m(\boldsymbol{\tau}_m) = \sum_j \frac{1}{2} g_j f_j(\boldsymbol{\tau}_m) \langle S_j \rangle e^{i\boldsymbol{\tau}_m \cdot \mathbf{r}_j} e^{-W_j} \tag{1.27}$$

with j the magnetic moments in the unit cell.

1.1.7 Neutron Sources (and neutron beam)

Neutron sources can roughly be divided into two categories, with neutrons either produced by nuclear fission or by nuclear spallation. An alternate way of classifying the sources are between continous or pulsed neutron beams, as the PSI spallation source produces a continuous neutron beam. A non-exhaustive list of neutron scattering institutes is given in table 1.1 and corresponds to the facilities relevant to this experimental work .

Table 1.1: List of relevant neutron scattering facilities

Neutron sources	production type	beam type
Institut Laue Langevin (ILL), France	fission	continuous
ISIS, Rutherford Appleton Laboratory, UK	spallation	pulsed
Paul Scherrer Institute (PSI), Switzerland	spallation	continous
FRM-II, Germany	fission	continous
ANSTO, Australia	fission	continous
J-Parc, Japan	spallation	pulsed
SNS, USA	spallation	pulsed

Typical neutron energies available from a neutron source are usually divided into three categories : hot, thermal and cold (described in table 1.2) corresponding to a Maxwellian distribution profile of neutron energies obtained from moderators.

Table 1.2: Classification of neutron beam by energy range, with examples of ILL instruments

Type	Energy [meV]	Temperature [K]	example
Cold	0.1-100	1-120	IN14, IN5
Thermal	10-100	120-1200	IN8, IN4
Hot	100-500	1200-6000	IN1

Ultracold neutrons (UCN), with neutron velocities as low as 5 m/s, can be used in particle physics, for example to measure the lifetime of neutrinos. The neutrons have too low energy to study bound states , and are thus outside the scope of this work.

1.1.8 Neutron spectroscopy

Neutron spectroscopy is concerned with measuring the partial differential cross section $\frac{d^2\sigma}{d\Omega dE}$. This is done by counting the number of neutrons scattered per unit time for a sample as a function of energy transfer $\hbar\omega$ and momentum transfer $\mathbf{Q}$ using a neutron detector. This requires to know the energy and wavevector of both the incident neutron and of the scattered neutron. There are several ways to measure the partial differential cross section, including triple-axis spectroscopy and direct time-of-flight spectroscopy.

Triple-axis spectroscopy

Triple-axis spectrometers are versatile instruments that measure a scattering event at a single value of $(\mathbf{Q}, \omega)$, with the initially polychromatic neutron beam undergoing three separate scattering events. The initial and final neutron energies are selected by Bragg diffraction on respectively a monochromator and an analyser. The choice of materials for the monochromator and analyser depends on the neutron wavelength, and the desired resolution. For thermal neutrons, a widely used monochromator is pyrolytic graphite (PG) oriented along [001], which is a special form of graphite with the layers randomly distributed around a common **c** axis. Other materials also commonly used in triple-axis spectroscopy are silicon and copper.

The name of the triple-axis technique comes from the existence of three rotation axis in the scattering configuration (schematically shown in figure 1.3) : to select the desired wavelength from Bragg scattering at the monochromator, both the monochromator and the spectrometer table have to be rotated around the first axis (A1/A2). The analyser/detector unit rotates around the second axis to select the sample scattering angle 2θ with respect to the direction of the incoming neutron wavevector $\mathbf{k}_i$ (A4). Around the third axis, the detector and the analyser are rotated separately to select the scattered wavevector $\mathbf{k}_f$ (A5/A6). An additional rotation of the sample table (A3) allows sample orientation in order to obtain the desired position in reciprocal space.
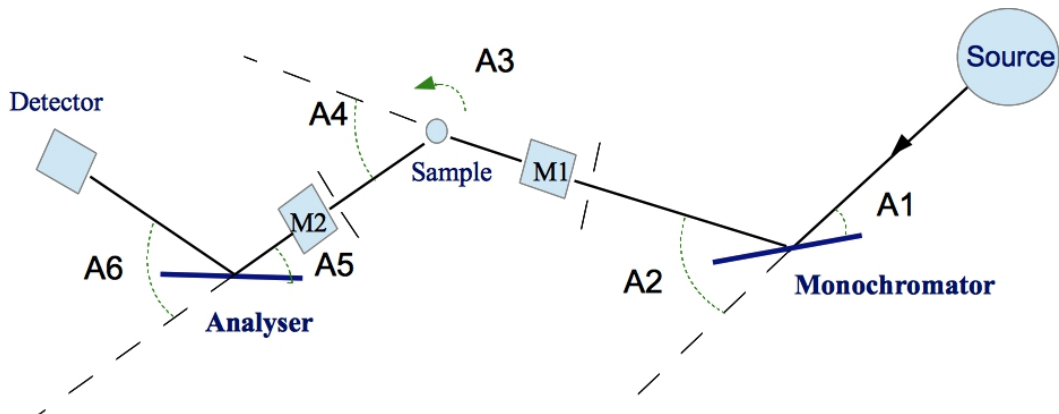
Figure 1.3: Schematic configuration of a conventional triple-axis spectrometer.

A neutron energy-loss scattering process corresponds to the scattering triangle shown in figure 1.4 with :

$$\mathbf{Q} = \mathbf{k}_i - \mathbf{k}_f = \boldsymbol{\tau} + \mathbf{q} \tag{1.28}$$

$$\hbar\omega = \frac{\hbar^2}{2m_n}(k_i^2 - k_f^2) = \hbar\omega_0(\mathbf{q}) \tag{1.29}$$

with $\boldsymbol{\tau}$ the reciprocal lattice vector and $\hbar\omega_0(\mathbf{q})$ the energy of an excitation for a reduced wavevector $\mathbf{q}$. The magnitude of the momentum transfer is given as a function of the scattering angle :

$$|Q| = \sqrt{k_i^2 + k_f^2 - 2k_i k_f \cos(2\theta)} \tag{1.30}$$
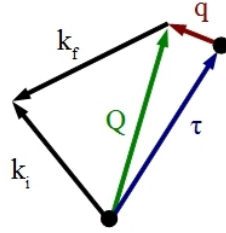
Figure 1.4: Schematic scattering triangle of a scattering process
.

Two types of scans are fundamental to triple-axis spectrometry to map the dispersion relation of excitations in condensed matter systems such as magnons or phonons : constant-$\mathbf{Q}$ scans and constant-energy scans. The former corresponds to keeping the momentum transfer $\mathbf{Q}$ constant while changing the energy transfer by small increments, which is done by modifying the Bragg scattering angle of either the analyser or the monochromator. In this type of scans, the sample angles A3 and A4 must also change. Constant-energy scans, on the other hand, correspond to varying the momentum transfer, while keeping the energy transfer constant, so that only A3 and A4 are changing.

Resolution Ellipsoid

Triple-axis spectrometer models assume perfectly monochromatic and divergence-free beams. In reality, this conditions are relaxed in order to obtain sufficient statistics. The selected energy at the monochromator is distributed around a mean value due to the finite mosaicity of the crystals and the divergence of the incident neutron beam, and similarly, a distribution of energy is obtained from the analyser. The measured phase space $(\mathbf{Q},\omega)$ is thus distributed around the nominally selected $(\mathbf{Q_0},\omega_0)$, and this distribution is known as the spectrometer resolution function $R(\mathbf{Q} - \mathbf{Q_0},\omega - \omega_0)$.

The measured intensity can thus be described as a 4D convolution of the dynamical scattering function with the resolution function of the spectrometer :

$$I(\mathbf{Q_0}, \omega_0) = \int R(\mathbf{Q} - \mathbf{Q_0}, \omega - \omega_0) S(\mathbf{Q}, \omega) d\mathbf{Q} d\omega \tag{1.31}$$

The resolution function of a triple-axis spectrometer depends on the relative sense of rotation at the instrument spectrometer axes and can be approximated using a Gaussian beam profile [15] :

$$R(\mathbf{Q} - \mathbf{Q_0}, \omega - \omega_0) = R_0 \, e^{-\frac{1}{2} \Delta v M \Delta v} \tag{1.32}$$

with Δv a four dimensional vector corresponding to the difference between nominal $(\mathbf{Q_0}, \omega_0)$ and measured $(\mathbf{Q}, \omega)$ and M the resolution matrix. The results are 4D resolution ellipsoids, with size and orientation depending on the resolution matrix.

The resolution matrix has been derived analytically by Cooper and Nathans [16] as well as by Popovici [17] , the latter taking into account the finite size of the sample and of the instrument. Several tools have been developed to calculate analytically and numerically the convolution of the dynamical scattering function with the resolution, including for example the Monte Carlo Matlab® routines "trixfit" based on the resolution calculations "rescal" [18].

Time-of-flight spectroscopy

Time-of-flight spectroscopy uses the neutron time-of-flight to obtain its energy via the de Broglie relation between wavelength and speed $\lambda = \frac{h}{mv}$. Inelastic time-of-flight is very efficient to explore large areas of $(\mathbf{Q}, \hbar\omega)$ space as scattered neutrons are collected over a wide range of neutron energy transfers. Two different geometries exist depending on whether the neutron energy is fixed for the incoming beam (direct) or the outgoing beam (indirect). In the direct geometry, a pulsed neutron beam is monochromated at a time t_c. At sample position neutrons are then scattered at a time t with momentum and energy transfers $\mathbf{Q}$ and $\hbar\omega$. Each neutron is then detected on a position sensitive detector (usually a ^{3}He detector) at a time $t + dt$, creating a map where each pixel represents at trajectory in 4 dimensional $(\mathbf{Q}, \hbar\omega)$.

Parabolas in Reciprocal space   From energy and momentum conservation, the trajectories are parabolas in reciprocal space. When the interest lies in $S(Q, \omega)$ (for a powder sample for example), from $Q^2 = k_i^2 + k_f^2 - 2k_i k_f \cos(2\theta)$ and using eq. 1.5 for a fixed E_i, with 2θ the scattering angle :

$$\frac{\hbar}{2m_n} Q^2 = 2E_i - \hbar\omega - 2\sqrt{E_i(E_i - \hbar\omega)} \cos(2\theta) \tag{1.33}$$

The available phase space for direct time-of-flight spectrometers can be derived from 1.33 for a fixed incident energy E_i and the detector coverage in scattering angle. The trajectories in reciprocal space are shown in figure 1.5 for $E_i = 12$ meV and scattering angles of 5, 25, 50, 75, 100 and 140 degrees. The detector coverage on an inelastic time of flight spectrometer thus defines the accessible area of the $S(Q, \omega)$ spectrum.
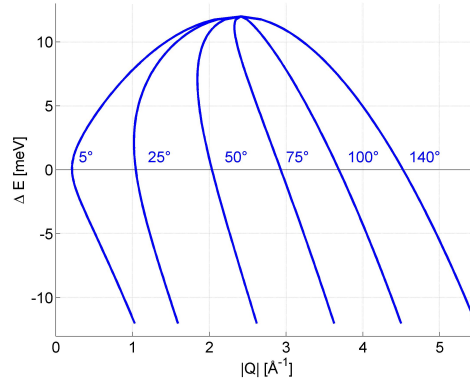
Figure 1.5: Trajectories in reciprocal space as a function of Q for an incident energy of 12 meV. For a detector coverage from 5 degrees to 140 degrees, the full area between the two outermost blue lines will be accessible on an inelastic time-of-flight spectrometer

.

As the detectors are Position Sensitive Detectors (PSD), both the polar and azimuthal angle of the scattered neutron are obtained with respect to $\mathbf{k}_i$. The components of $\mathbf{Q}$ can thus be separated into parallel $\mathbf{Q}_{||}$ and perpendicular $\mathbf{Q}_\perp$ to $\mathbf{k_i}$ so that the parabolas become :

$$\frac{\hbar}{2m_n}k_i^2 - \hbar\omega = \frac{\hbar}{2m_n}(|\mathbf{Q}_\perp|^2 + (k_i - |\mathbf{Q}_{||}|)^2) \tag{1.34}$$

In an inelastic time-of-flight experiment on a single crystal, the measured intensity corresponds to the intersection between the trajectories of the parabolas with the scattering function $S(\mathbf{Q}, \omega)$. The sample can be rotated in 2θ with 1-5 degrees steps in order to cover a larger four dimensional $S(\mathbf{Q}, \omega)$ range. This separation into perpendicular and parallel components is useful in particular in the case of low-dimensional systems, where the $S(\mathbf{Q}, \omega)$ is independent on one or more directions of $\mathbf{Q}$. In a 2D system, rod-like scattering will be observed along one direction as there is no dependence of the dynamical scattering function on the momentum transfer along this $\mathbf{Q}$ direction . In that case, a time-of flight spectrometer can be used with the $\mathbf{Q}_{||}$ direction parallel to the incident beam $\mathbf{k}_i$. $\mathbf{Q}_\perp$ then corresponds to the in-plane scattering. At a fixed $\mathbf{Q}_\perp$ point, $\mathbf{Q}_{||}$ varies with as the energy transfer changes. Since $S(\mathbf{Q}, \omega)$ is independent of this direction, the variation of $\mathbf{Q}_{||}$ does not impact the intensity of the magnetic scattering. One carefully chosen sample orientation thus allows to collect the full relevant $S(\mathbf{Q}, \omega)$ map for a 2D system by integrating the data over the irrelevant $\mathbf{Q}_{||}$ range.
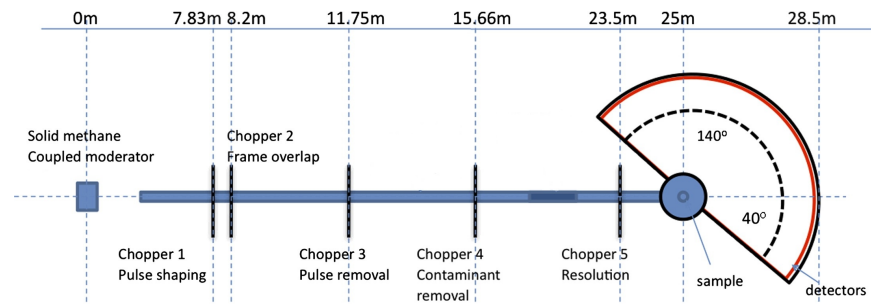
Figure 1.6: Schematic of the cold direct time-of-flight spectrometer LET from [19] showing the choppers for pulse shaping, contaminant removal, pulse removal and resolution. Chopper 1 and 5 are high-speed rotating disks that control the incident energy and the energy resolution.

Inelastic spectrometers are usually large in size, with long flight paths from moderator to detectors (20-30 m) and wide angle coverage by detectors (for example on LET, 4 m high position sensitive detectors are arranged in a cylindrical coverage from -40 to 140 degrees). The large angle coverage allows to access extended areas of reciprocal space, and as will be shown in this section, the energy resolution improves with larger distances.

TOF spectrometers at Spallation sources   Time-of-flight spectrometers are widely used in spallation sources, as the neutron are directly produced as a pulsed beam. A set of choppers is then used to shape the pulse, remove contamination and select the desired incident energy. A example of such a set of choppers is shown in figure 1.6 for the cold time-of-flight spectrometer LET at ISIS.

These chopper disks are carbon fibre composite disks with ^{10}B coating to absorb neutrons and have apertures for neutron transmission. For LET, chopper 1 and 5 are high speed 300Hz counter rotating discs to control the incident energy. The pulse-width matching between the two choppers allows the optimization of the flux for the desired resolution. Choppers 2, 3 and 4 are slower rotating choppers to prevent frame overlap and other spurious signal. In addition, the chopper system is designed to allow scattering from several incident energies to be collected within the same time-frame. This is known as multiplexing and is an efficient mode of data collection that takes full advantage of the 100ms pulse out of the moderator [19].

TOF spectrometers at fission sources   At fission sources such as the ILL, the neutron beam is continuous. Time-of-flight spectrometers thus need additional choppers (pulsing choppers) in order to create polychromatic neutron pulses from the continuous source. This is usually done in the first chopper group with counter-rotating disks which are de-phased with respect to the monochromating choppers in order to select the desired wavelength. Figure 1.7 shows a schematic time-distance diagram for the case of the cold time-of-flight spectrometer IN5 at ILL, which shows a schematic of the energy distribution of the neutron pulses as they pass through the different chopper groups, the sample and finally reach the detectors.
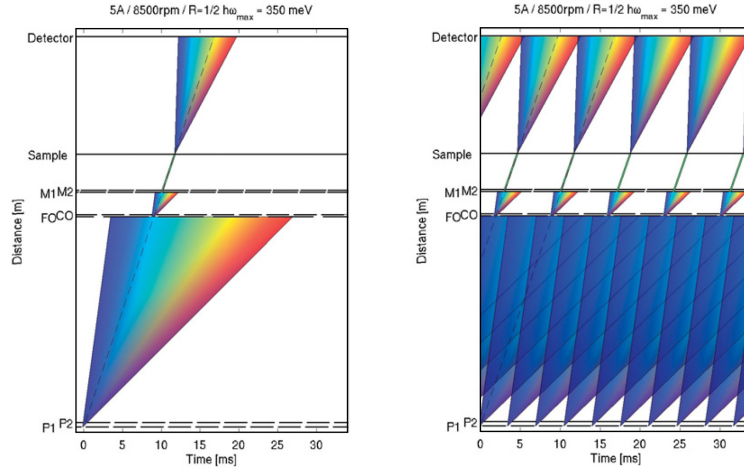
Figure 1.7: Distance-Time diagram for IN5 from [20]. Blue represents the most energetic neutrons and red the less energetic ones. Dashed diagonal line corresponds to E_i. P1 and P2 are the Pulsing choppers, FO and CO are respectively the Frame overlap chopper and the Contaminant order chopper. M1 and M2 are the Monochromating choppers. The left panel shows one pulse while the right panel shows the pulse repetition and clearly demonstrates the need for the frame overlap chopper.

Resolution   Faster neutrons are more difficult to resolve in time at the detector position, so that time resolution (and hence energy resolution) is better at larger energy transfers (slower neutrons) than for no energy loss (faster neutrons). The energy resolution of the instrument for a fixed E_i is typically given as the full-width half-maximum of the elastic line. Resolution is strongly dependent on how narrow in time the pulse is, on the energy distribution from the moderator, as well as on the sample-to-detector distance.

In a simple approximation, the energy resolution has two contributions: the distribution of energies of the moderator and the monochromating chopper burst. The neutrons with an energy E_c out of the moderator have a time width of $\Delta t_m(Ec)$. The time window of the monochromating chopper is Δt_c. The convolution of Δt_c and $\Delta t_m(Ec)$ give the time distribution Δt of the neutrons after the monochromating chopper. Approximating the distributions by Gaussians, this is given by .

$$\Delta t = \sqrt{\Delta t_c^2 + \Delta t_m(E_c)^2} \tag{1.35}$$

Taking into account the moderator-chopper distance $L1$, this quantity corresponds to the incident energy resolution. The energy resolution for the scattered beam must also take into account the chopper-sample distance $L2$ and the sample-detector distance $L3$.

The energy resolution at the detector can be obtained by combining these contributions [21] :

$$\frac{\Delta\hbar\omega}{E_i} = \left(\left(2\frac{\Delta t_c}{t_c}\left(1 + \frac{L1 + L2}{L3}\left(1 - \frac{\hbar\omega}{E_i}\right)^{\frac{3}{2}}\right)\right)^2 + \left(2\frac{\Delta t_m}{t_c}\left(1 + \frac{L2}{L3}\left(1 - \frac{\hbar\omega}{E_i}\right)^{\frac{3}{2}}\right)\right)^2\right)^{\frac{1}{2}} \quad (1.36)$$

For a fixed E_i, the resolution thus improves for large sample-detector distance $L3$ and as the energy transfer increases.

In terms of Q resolution, the dominant contribution is the pixel size of the position sensitive detectors. Other contributions are the divergence of the incident beam, the finite energy resolution and the physical size of the sample, which all lead to a Gaussian spread. The convolution of the square resolution function of the pixel size and the Gaussian spread gives a overall isotropic projection of the Q-resolution on the detector plane, unlike triple-axis spectroscopy, where the resolution is extended along one of the in-plane **Q** components.

Repetition-rate multiplication mode   One aspect of new-generation time-of-flight spectrometers is the possibility to use several incident energies from a single neutron pulse. This is obtained by synchronising the source pulse with the incident beam chopper so that a single pulse can have a distribution of neutrons with different discrete incident energies reaching the sample at separate times. At the detector position, the scattered neutrons are correlated to their respective incident energy using their time-of-flight. This mode allows simultaneous measurements of different resolution and kinematic parameters, which drastically reduces the experimental acquisition time.

1.1.9 Polarised neutron spectroscopy

It is not always possible to distinguish the nature of the observed neutron scattering. This can be the case when focusing for example on very weak diffuse scattering whose intensity is much weaker than the dominant nuclear scattering, or when the nature of the scattering is not obvious, for example if it is quasi-elastic. Incoherent scattering in a sample could also need to be identified, in particular for samples containing hydrogen (large incoherent scattering cross-sections). Polarised neutron spectroscopy is very efficient in addressing these problems as it is possible to combine the cross-sections obtained for different polarization directions in order to separate magnetic, nuclear and incoherent scattering contributions.

The general principle of polarised neutron scattering is to probe the spin transition of the scattered neutron. A neutron beam with a defined spin state needs to be produced, and the spin-state distribution of the neutrons after scattering needs to be analysed. This allows to measure the scattering amplitudes for each transition for an uniaxial polarised beam, given by the Moon-Riste-Koehler equations derived from the interaction potential for magnetic,

nuclear and incoherent scatterings [22]:

$$U_{|\uparrow\rangle \to |\uparrow\rangle} = b_{coh} - pM_{\perp z} + BI_z \tag{1.37}$$

$$U_{|\downarrow\rangle \to |\downarrow\rangle} = b_{coh} + pM_{\perp z} - BI_z \tag{1.38}$$

$$U_{|\uparrow\rangle \to |\downarrow\rangle} = -p(M_{\perp x} + iM_{\perp y}) + B(I_x + iI_y) \tag{1.39}$$

$$U_{|\downarrow\rangle \to |\uparrow\rangle} = -p(M_{\perp x} - iM_{\perp y}) + B(I_x - iI_y) \tag{1.40}$$

where z refers to the direction of the neutron polarisation and with b_{coh} the coherent scattering length, $M_\perp$ the magnetic interaction vector, p the magnetic pre-factor $p = \frac{\gamma_n r_0}{2\mu_B}$, I the nuclear spin operator and B the spin-dependant nuclear amplitude.

These equations show that coherent nuclear scattering is always non-spin-flip scattering ($|\uparrow\rangle \to |\uparrow\rangle$ or $|\downarrow\rangle \to |\downarrow\rangle$). In addition, the incoherent scattering cross section can be separated into the spin-dependant and independent part (the latter referred to as isotopic incoherent). Isotopic incoherent scattering results from a random disorder in the nuclear scattering lengths and hence is entirely non-spin-flip. On the other hand, the magnetic and nuclear spin scattering are non-spin-flip if the effective spin components are along the direction of the neutron polarization, and the scattering is spin-flip if the effective spin components are perpendicular to the polarization direction. Hence the nuclear-spin incoherent, which comes from randomly oriented nuclear spin, is present in both non-spin-flip and spin-flip channel with respectively 1/3 and 2/3 ratios. Regarding magnetic scattering, only spin components which are perpendicular to the scattering vector are visible in neutron scattering. In the special case where the neutron polarisation is along the scattering vector, magnetic scattering thus only appears in the spin-flip channels.

On multi-detector neutron spectrometer, a technique of longitudinal neutron polarisation analysis for three orthogonal directions of the neutron polarisation is generally used, called XYZ-polarisation analysis [23]. In the case of a paramagnetic sample, it provides unambiguous separation of the magnetic, nuclear and spin incoherent cross sections. For a planar multi-detector in the xy-plane, the incident polarisation is aligned alternately along x, y and z, and the separated scattering cross-sections within the hypothesis of a paramagnetic sample are given by a linear combination of the measured XYZ cross-sections :

$$\left(\frac{d\sigma}{d\Omega}\right)_{mag} = 2\left(\frac{d\sigma}{d\Omega}\right)_{SF}^x + 2\left(\frac{d\sigma}{d\Omega}\right)_{SF}^y - 4\left(\frac{d\sigma}{d\Omega}\right)_{SF}^z \tag{1.41}$$

$$= 4\left(\frac{d\sigma}{d\Omega}\right)_{NSF}^z - 2\left(\frac{d\sigma}{d\Omega}\right)_{NSF}^x - 2\left(\frac{d\sigma}{d\Omega}\right)_{NSF}^y \tag{1.42}$$

$$\left(\frac{d\sigma}{d\Omega}\right)_{nuc} = \frac{1}{6}\left[2\left(\frac{d\sigma}{d\Omega}\right)_{T_{NSF}} - \left(\frac{d\sigma}{d\Omega}\right)_{T_{SF}}\right] \tag{1.43}$$

$$\left(\frac{d\sigma}{d\Omega}\right)_{si} = \frac{1}{2}\left(\frac{d\sigma}{d\Omega}\right)_{T_{SF}} - \left(\frac{d\sigma}{d\Omega}\right)_{mag} \tag{1.44}$$

with T_{SF} and T_{NSF} corresponding respectively to the total spin-flip and total non-spin-flip measured cross-sections. The magnetic cross-section can thus be calculated in two independent ways.

Examples of such multi-detector diffractometers using XYZ polarisation analysis include the diffuse spectrometer D7 at the ILL [24] and the spectrometer DNS at the FRMII [25]. The working principle is as follows: a guide field sets the polarisation axis for the neutron beam, and then one of the spin states is selected by reflection from a super-mirror bender. This is followed by a Mezei-type precession coil neutron spin flipper, which flips the spin with respect to the guide field direction. The flipper is switched on or off depending on whether processes flipping the neutron spin or not are being measured. A set of coils around the sample position rotates the polarization into one of three orthogonal directions for XYZ polarisation analysis, and the outgoing polarisation is analysed by another set of super-mirror benders. A total of six cross sections are collected : spin flip and non-spin flip for each field orientation at the sample position. The different contributions to the total scattering cross section (magnetic, spin incoherent and nuclear and isotope incoherent) are then separated by the linear combination of the cross sections given in equations 1.41-1.44.

In a practical neutron experiment, several corrections have to be made during data reduction to correct for instrumental errors (detailed in [26]) : The polarisation efficiency of the instrument is obtained by measuring the scattering from amorphous quartz. As it gives only nuclear coherent scattering, there should be no spin-flip scattering for an ideal efficiency of the polariser, analyser and flipper. The detector efficiencies is then obtained by measuring scattering from vanadium, which has a negligible coherent cross section (for the most abundant isotope ^{51}V) and thus is considered to only scatter incoherently. A vanadium count in a detector is thus proportional to the efficiency and solid angle coverage of that detector. In addition, the background is estimated using transmission measurements of an empty sample holder and of a cadmium sample (which has a very large neutron absorption cross-section), weighted by the transmission of the sample.

Finally, the calibration with vanadium allows the normalisation of data in order to obtain the scattering in absolute units, i.e. as a cross section per solid angle and per formula unit (barns sr^{-1} f.u. $^{-1}$). Indeed, the incoherent cross section for the most abundant isotope of vanadium ^{51}V (99.75 % abundancy) is $\sigma_{inc} = 5.08$ barns so that the total cross section of vanadium is given by : $\left(\frac{d\sigma}{d\Omega}\right)_V = \frac{5.08}{4\pi}$

To obtain the sample cross section in absolute units, the sample counts N_S can thus be divided by the vanadium counts N_V, normalising by the vanadium cross section, the ratio of scattering centres between vanadium $n_{s(V)}$ and the sample $n_{s(S)}$ and the ratio of their transmission t_V and t_S :

$$\left(\frac{d\sigma}{d\Omega}\right)_S = \frac{N_S}{N_V} \frac{n_{s(V)}}{n_{s(S)}} \frac{t_V}{t_S} \frac{5.08}{4\pi} \tag{1.45}$$

1.1.10   Sample environment

At sample position on neutron spectrometers, several types of environments can be installed in order to control the temperature (cryostat, dilution fridge or cryo-furnace), the applied magnetic field (vertical or horizontal magnets) or the applied pressure (pressure cells). A detailed review of the range of available sample environments for neutron scattering experiments can be found in [27], and only high-pressure sample environments will be discussed further.

Pressure

In the context of neutron scattering, the realisation of high-pressure experiment is usually a challenge. Having a high-pressure set-up as sample environment will lead to a reduction of sample size, an increase of the quantity of absorbing and scattering materials in the trajectory of the neutron beam, constraints on operating temperatures and a reduction of accessible reciprocal space. The choice of a pressure cell type, of the pressure transmitting media in which the sample is immersed (to obtain hydrostatic pressure) and of a pressure marker (NaCl, Pb) is thus very dependent on the experiment. Only four different high pressure experimental set-ups will be described here, and a comprehensive overview of possibilities and constraints in high pressure neutron scattering experiments can be found in [28].

"Russian alloy" Clamp cell for time-of-flight with 10 kbar at 1.5K   Clamp cells are widely used in high-pressure neutron scattering experiment as they are compact and reliable. They consist of a piston cylinder pressure device. Pressure is applied ex-situ with an external press and the clamp cell is then locked mechanically. Due to the partial loss of pressure when the load is released after locking the cell and the temperature dependence of the applied pressure on the sample, accurate pressure can only be obtained from an in-situ neutron measurement of the Bragg peaks from a pressure marker such as NaCl or Pb. As the maximum reachable pressure from calibration is given at 300K, the decrease of pressure when the clamp cell is cooled (from thermal contraction of pressure medium) should be taken into account when choosing a particular pressure cell. The pressure cell chosen in the CrAs time-of-flight experiment described in section B.2 was a "Russian alloy" clamp cell, suitable for single crystal measurements up to 15 kbar. "Russian alloy" refers to a NiCrAl alloy with 57% Ni, 40% Cr and 3 % Al, which is non-magnetic and is used in high pressure experiments for its strength.

McWhan Clamp cell for triple-axis-spectroscopy with 23 kbar below 1K   The first McWhan pressure cell was developed by McWhan and collaborators in 1974 for pressure neutron scattering beyond 10 kbar. Its characteristic elements are a bi-conical Al_2O_3 cylinder containing the sample and two tungsten carbide pistons. Current design are clamped McWhan pressure cells, with pressure applied ex-situ with an hydraulic press. Al_2O_3 is suitable for neutron scattering experiments as it is non-magnetic and shows an 80 % transmission across the full bi-cone.

The Mcwhan design used at the ILL is shown in Figure 1.8 for the 20 kbar set-up with a CuBe sample capsule (number 16). Sample space is large for a high pressure cell device (5-10 times larger than for the Paris-Edinburgh pressure cell), as the sample capsule has 6mm diameter and 24mm height in the 20 kbar set-up. This sample environment was used in combination with a cooling device ("Triton") to reach dilution temperatures of 150mK in the context of the plaquette phase SCBO experiment described in section 2.5.

The pressure transmitter was Fluorinert, a perfluoro-carbon liquid which does not contain hydrogen (and thus a very weak incoherent scattering cross section) but with a limited hydrostatic pressure range of maximum 20-23Kbar (depending on composition, best is 1:1 FC84-Fc87).

The pressure marker was pure NaCl, for which the equation-of-state as a function of pressure and temperature is known. Tabulated value for the unit cell volume variation V/V_0 was obtained by Decker et al.[29] and extended to low temperatures by Skelton et al. [30].In practice, the salt (either powder or single crystal) is added with the sample and the scattering angle of a Bragg peak can be obtained in-situ from diffraction. The unit cell volume of NaCl under pressure V can then be extracted from the new d-spacing of the Bragg peak and compared to the ambient unit cell volume V_0 in order to get the tabulated pressure from the obtained $(V_0 - V)/V_0$ at a specific temperature.

Paris-Edinburgh (PE) pressure cell for diffraction with maximum 76 kbar from 5 to 300K
Paris-Edinburgh cells are hydraulic pressure cells with opposed anvils of sintered materials for compression. Their advantage is that pressure can be applied and changed in-situ. There exists a number of Paris Edinburgh pressure cell, each with different load frames, anvils, hydraulic fluid and cryogenic equipment.

Presented here is specifically the ILL Paris Edingburgh pressure cell VX5 which has a maximum pressure of 10GPa (at 300K) and a minimum temperature of 5K [32]. The load frame of the VX5 is a two column design, which must be taken into account for single crystal experiments, as the columns block the neutron beam and lead to a loss of about 30 degrees of accessible rotation on each side. The pressure cell is equipped with single-toroidal anvils of sintered cubic Boron nitride and a gasket of TiZr alloy with available sample space of 10-30 mm^3.

In neutron scattering, TiZr refers to an alloy with null neutron coherent scattering. The bound coherent scattering length of Ti and Zr are respectively -3.44 fm and 7.16 fm so that an alloy with 67.7 % Ti and 32.3 % Zr will not produce Bragg reflections [28]. However, there is incoherent scattering and some short range species-species order which create a background, which is significant in the case of a weak signal. Boron has a large neutron absorption cross section, and the Boron nitride anvils thus have very low neutron transmission.

The hydraulic fluid used is compressed helium, which is the only possibility for cooling below 110K. The pressure cell is cooled by a closed-cycle He gas cryostat, with a cooling time of 30hrs
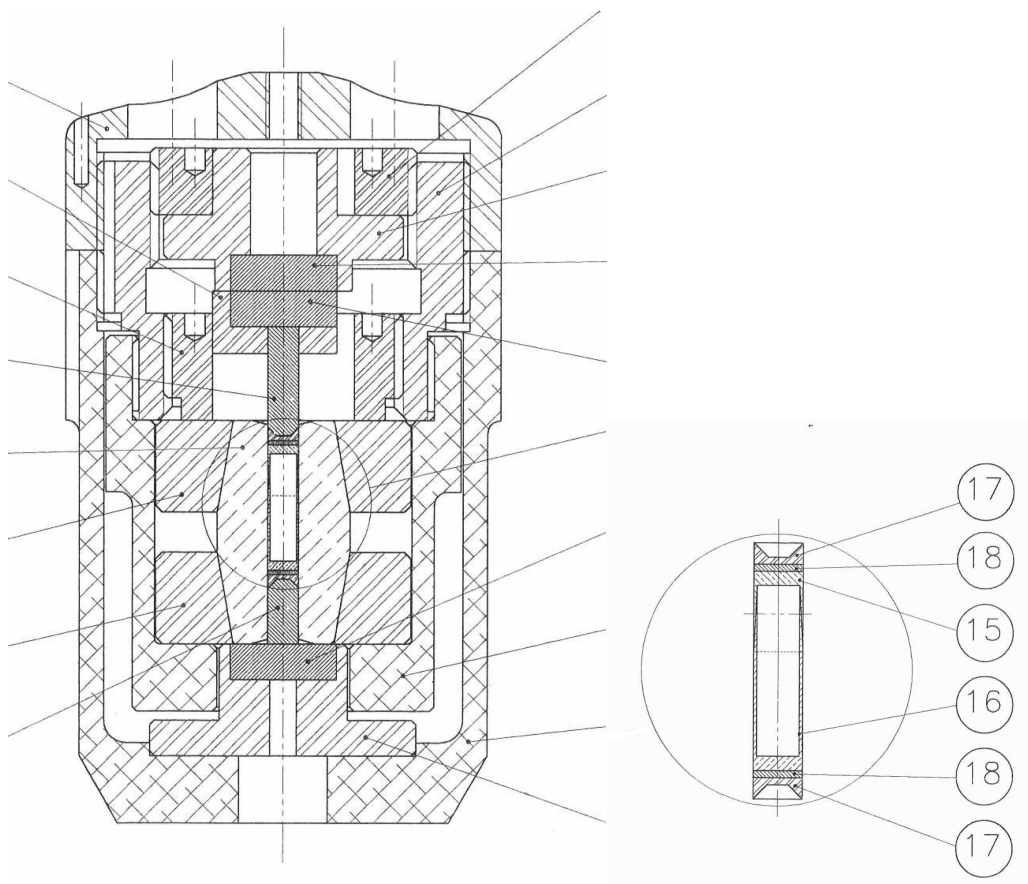
Figure 1.8: Technical drawing for the ILL McWhan pressure cell in the 20kbar set up. Courtesy of ILL, from design in [31]. Left : Full body of the MacWhan pressure cell. Right : Zoom on the sample capsule

from 300K to 5K. It has the option of a fast pre-cooling to 77K by flooding the sample space with liquid nitrogen, evacuating and then using the CCR to cool to base temperature (6-8hrs) The reduction of cooling time is crucial, as although pressure can be increased in-situ on the beam-line, the pressure cell temperature needs to be at 250-300K while the pressure load is increased.

The PE cell is suited for both powder sample and single crystal, as shown in section B.3. For the powder sample, the pressure transmitting medium is usually a 4:1 deuterated methanol:ethanol mixture and the pressure marker is a small piece of Pb, a strong neutron scatterer with a small incoherent cross section. The accurate pressure can be obtained from the known equation of state of Pb corrected by the thermal expansion [33]. Single crystals are instead embedded in a Pb matrix which also acts as the pressure transmitting media (due to its low shear strength), and the ensemble is then inserted in a CuBe ring to prevent radial rupture.

1.1.11 Neutron-related Units

In practice, a particular set of units are associated with neutron scattering, with cross sections usually discussed in barns (1 barn = 10^{-28}m^2 = 10^{-24}cm^2), with wavelength and wavevector in respectively in Å and Å^{-1} and energies in meV. From neutron kinematics, useful numerical relations between the neutron energy and its wavelength and wavevector are the following :

$$E[\text{meV}] = \frac{h^2}{2m\lambda^2} = \frac{81.81}{\lambda^2}[\text{meV.Å}^2]$$

$$E[\text{meV}] = \frac{(\hbar k)^2}{2m} = 2.072k^2[\text{meV.Å}^2]$$

Other techniques may use different units for energy, and a pratical energy conversion table between frequently used units is given below :

- $E = k_B T$ with T the temperature in K $\longrightarrow$ 1 meV=11.6 K

- $E = \mu_B B$ with B the magnetic field strength in T $\longrightarrow$ 1 meV=17.3 T

- $E = h\nu$ with ν the frequency in Hz $\longrightarrow$ 1 meV= 242 GHz

- $E = hc/\lambda$ with λ the wavelength in mm $\longrightarrow$ 1 meV=1.23 mm

- $E = hc\lambda^{-1}$ with λ^{-1} the wavenumber in cm^{-1} $\longrightarrow$ 1 meV= 8.07 cm^{-1}

with $\mu_B = 5.788 \cdot 10^{-5}$ [eV T^{-1}] the Bohr magneton and $k_B = 8.617 \cdot 10^{-5}$ [eV K^{-1}] the Boltzmann constant. As a reference, thermal neutrons, with typical v=2200 m/s, correspond to an energy of 25.3 meV, T=293 K and $\lambda = 1.8$ Å.

1.2 Samples

1.2.1 $SrCu_2(BO_3)_2$

The $SrCu_2(BO_3)_2$ single crystals were grown by travelling solvent technique at PSI. These crystals were intended for neutron scattering studies and thus have the chemical formula $SrCu_2(^{11}BO_3)_2$, with natural Boron replaced by the ^{11}B isotope in order to avoid the large neutron absorption cross section of ^{10}B : $\sigma_{abs} = 3835$ barns for the naturally 20% abundant ^{10}B isotope compared to $\sigma_{abs} = 0.0055$ barns for ^{11}B isotope, from tabulated values in [10].

The obtained crystals were rods with diameter of about 8mm and cut into ~ 15 mm long crystals. One of the sample mount was composed of a single crystal aligned on a aluminium mount with a mass of about 2.5g. In order to increase the quantity of sample in the beam, the other sample was a multi-crystal system on a CuBe mount with 7 crystals for a total mass of 10.3g, co-aligned with (110) and(001) in the scattering plane. For the pressure experiment, one of the SCBO crystal was cut into a rod with a diameter of 6mm and a 7mm height in order to tightly fit in the CuBe capsule[1] of the McWhan pressure cell, aligned using X-ray Laue with a and b in the scattering plane.

1.2.2 MPS_3

Growth method

Crystals of $FePS_3$ and $NiPS_3$ were prepared using the vapour transport method [2]. The method is described in details in [34] for $FePS_3$ and [35] for $NiPS_3$. Quartz tubes were subjected to a cleaning procedure of etching in acid, followed by rinsing with de-mineralized water. They were then heat-treated under vacuum at 1000°C for 30mn. Stoichiometric quantities of the pure elements ($\geqslant$ 99.998 %), for a total mass of 5g, were placed in the quartz tubes. The tubes were then evacuated, sealed, and placed in a horizontal two-zone furnace. The temperature of the two zones were independently controlled to a range between 620 and 750°C and a two-stage heating protocol was followed (duration 2-4 weeks) before the furnace was switched off and allowed to cool. The resulting tubes contain a large number of small platelets with a hexagonal motif and a metallic gray color with typical largest dimensions 10x10x0.2 mm^3.

Powder pellets of $FePS_3$ and $NiPS_3$

Due to the layered nature of the $FePS_3$ and $NiPS_3$ crystals, obtaining an anisotropic powder with no preferred orientation is difficult. The method used in order to limit this problem was to compress the powder from ground crystals into several cylindrical pellets, as detailed in [36]. Three cylinders were obtained with a volume of about 1cm^3 each. For neutron scattering spectroscopy, the pellets were stacked with mutually orthogonal axes in an attempt to reduce

---

[1]done by Björn Wehinger at the University of Geneva
[2]Done by Andrew Wildes at the Institut Laue Langevin

preferred orientation.

Single crystals of FePS$_3$

The largest crystals obtained were saved for neutron scattering experiments, and their quality was assessed using either X-ray Laue (EPFL), or neutron Laue (ANSTO). FePS$_3$ crystals form into platelets with the [001] axis normal to the plane. They have a typical thickness of 0.2mm.

Two co-aligned single crystals Using Laue neutron scattering, each crystal (labeled 4 and 5 in the batch for reference) was first confirmed to be a single-crystal [3] and the [110] direction could be identified. The two samples were wrapped in Al foil and glued to Aluminium pins. The two samples were co-aligned with (33$\bar{1}$) and (001) in the scattering plane.

17 co-aligned single crystals In order to have sufficient mass for a time-of-flight experiment, numerous platelet crystals of FePS$_3$ were co-aligned and glued on thin Aluminium sheets with amorphous CYTOP®fluoropolymer glue[37] with low hydrogen content and thus adapted for neutron scattering. The monoclinic c* axis is normal to the surface of the platelets. The alignment of the sample, done on a X-ray Laue diffractometer, had the (33$\bar{1}$) direction in the scattering plane, although the quality of the X-ray Laue images did not allow to distinguish between the monoclinic directions (33$\bar{1}$), (3$\bar{3}$$\bar{1}$) and (010). The scattering obtained from the co-aligned samples was thus a superposition of three domains. The final sample was composed of 8 Aluminum sheets parallel to each other with a total of seventeen crystals for an estimated total mass of 0.3g. An acceptable co-alignment of the 8 Aluminium sheets was done on Orientexpress at ILL.

High-field samples For the high-field measurements, a good quality single crystal was selected using X-ray Laue patterns. The samples were then cut out from this single crystal and oriented with respect to the field in order to get either **H//c*** or **H//b**. The sample for the **H//c*** orientation had a diameter smaller than 1mm, and a thickness of about 0.01mm. It was held by vacuum grease to a wooden flat holder and inserted in a standard plastic capsule. The second sample (**H//b**) was cut out in a rectangular shape with dimensions 1x2.5x0.1 mm^3 and held by vacuum grease in the plastic capsule.

---

[3]characterised by Garry McIntyre at ANSTO, Australia

1.2.3   Sample quality

The MPS$_3$ samples are very sensitive to external elements and strains. Using glue can change the magnetic properties of NiPS$_3$ [35], and NiPS$_3$ as well as FePS$_3$ powders appear to adsorb water. In addition, the crystals are difficult to grind into a truly randomized powder and the strain from grinding can introduce distortions. Although MPS$_3$ structures are indexed with a monoclinic space group, they can also be indexed with good accuracy with an hexagonal space group with (001) shared between the two space-groups. This makes it impossible to determine unique a and b axis from the Laue patterns. As there is no obvious deviation from a three-fold symmetry, the identified $(0\ k\ 0)$ direction could also be $(h\ h\ 0)$ or $(h\ \bar{h}\ 0)$. Figure 1.9.a shows an example of such a Laue X-ray pattern.

Finally, the FePS$_3$ crystals are usually twinned with a rotation within the (a, b) plane, so that the sample have 120°-rotated domains . All of these factors contribute to the necessity to carefully select and characterise samples before neutron experiments in order to minimize mosaicity, although experiment have to be carried out taking mosaicity and domains into account. Figure 1.9.a-b shows examples of the Laue pattern of FePS$_3$ crystals, while figure 1.9.c shows a scan of (001) for two co-aligned crystals, with a mosaicity of about 4 degrees.
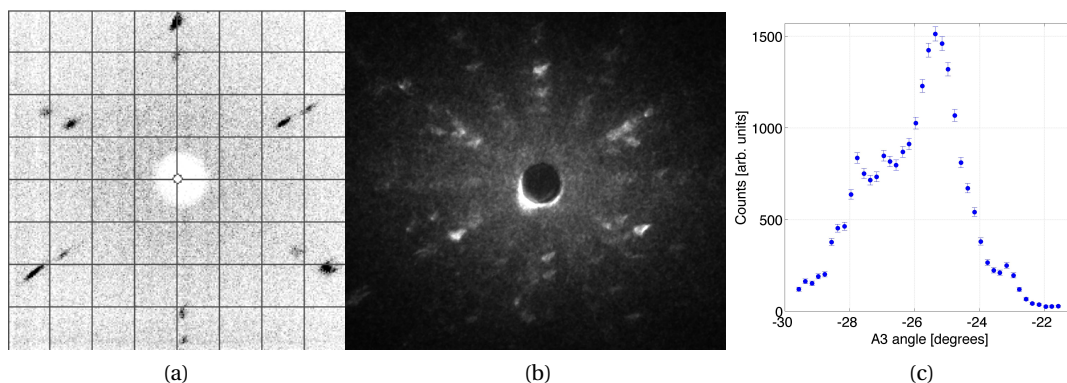

Figure 1.9: FePS$_3$ single-crystal examples of sample quality and mosaicity. a) X-Ray Laue pattern of a single crystal. b) Neutron Laue pattern for the composite 17-crystal mount. c) Neutron scan of the (001) Nuclear peak for the co-aligned crystals 4 and 5.

1.3 Linear Spin Wave theory

In ordered systems, the dispersion of magnetic excitations can be described and derived using linear spin wave theory. Relevant in the context of inelastic neutron scattering by spin-waves, linear spin wave theory [38, 9] taking into account an antiferromagnetic nearest neighbour interaction will be outlined below. In a classical picture, the spin waves are described as the synchronised precession of the spins in a magnetically ordered ground state, with a wave-like behaviour coming from the phase difference between the precessing spins.

In the bosonic approach to spin waves, the starting point is given by the Hamiltonian :

$$H = \frac{1}{2} J \sum_{i\delta} S_i \cdot S_{i,\delta} \tag{1.46}$$

with δ running over nearest neighbours and $J < 0$ the antiferromagnetic exchange constant.

The magnetic lattice is divided into two inter-penetrating sub-lattices A and B with respectively spin up or spin down. Lattice geometries allowing this division are referred to as bipartite lattices .

In order to transform the problem into a interacting-boson problem, the Holstein-Primakoff transformation expresses the spin operators in terms of Boson creation and annihilation operators for each sublattice [39] :

$$
\begin{aligned}
S_A^+ &= \sqrt{2S} \; a^\dagger \sqrt{1 - \frac{a^\dagger a}{2S}} & \quad S_B^+ &= \sqrt{2S} \sqrt{1 - \frac{b^\dagger b}{2S}} \; b \\
S_A^- &= \sqrt{2S} \sqrt{1 - \frac{a^\dagger a}{2S}} \; a & \quad S_B^- &= \sqrt{2S} \; b^\dagger \sqrt{1 - \frac{b^\dagger b}{2S}} \\
S_A^z &= S - a^\dagger a & \quad S_B^z &= -S + b^\dagger b
\end{aligned}
\tag{1.47}
$$

with the boson operators obeying the commutation relation $[a, a^\dagger] = 1$. The raising and lowering operators are defined as $S^\pm = S^x \pm i S^y$. In the linear spin wave approximation, only the first term of the expansion in $1/S$ is taken into account, so that only terms that are quadratic in terms of boson operator are kept in the Hamiltonian. The obtained Hamiltonian however is not diagonal, with coupled bosons on different lattice sites.

Fourier-transformed variables $a_{\mathbf{q}}$ and $b_{\mathbf{q}}$ are then defined for a periodic system as a function of momentum $\mathbf{q}$, and the following Hamiltonian is obtained :

$$H = -\frac{N}{2} z J S^2 + z J S \sum_{\mathbf{q}} [\gamma_{\mathbf{q}} (a_{\mathbf{q}}^\dagger b_{-\mathbf{q}}^\dagger + a_{\mathbf{q}} b_{-\mathbf{q}}) + (a_{\mathbf{q}}^\dagger a_{\mathbf{q}} + b_{\mathbf{q}}^\dagger b_{\mathbf{q}})] \tag{1.48}$$

with $\gamma_{\mathbf{q}} = \frac{1}{z} \sum_{\delta} e^{i\mathbf{q}\cdot\delta}$.

Unlike in the ferromagnetic linear spin wave theory, the obtained Hamiltonian from Fourier-transformed variables is still not diagonal, with coupling terms between $a_{\mathbf{q}}$ and $b_{\mathbf{q}}$. It can be diagonalised using the Bogoliubov transformation to new variables $\alpha_{\mathbf{q}}$ and $\beta_{\mathbf{q}}$, corresponding to quasi-particles :

$$
\begin{aligned}
\alpha_{\mathbf{q}} &= u_{\mathbf{q}} a_{\mathbf{q}} - v_{\mathbf{q}} b_{-\mathbf{q}}^{\dagger} & \beta_{\mathbf{q}} &= u_{\mathbf{q}} b_{\mathbf{q}} - v_{\mathbf{q}} a_{-\mathbf{q}}^{\dagger} \\
\alpha_{\mathbf{q}}^{\dagger} &= u_{\mathbf{q}} a_{\mathbf{q}}^{\dagger} - v_{\mathbf{q}} b_{-\mathbf{q}} & \beta_{\mathbf{q}}^{\dagger} &= u_{\mathbf{q}} b_{\mathbf{q}}^{\dagger} - v_{\mathbf{q}} a_{-\mathbf{q}}
\end{aligned}
\tag{1.49}
$$

where the coefficients $u_{\mathbf{q}}$ and $v_{\mathbf{q}}$ must be chosen so that $u_{\mathbf{q}}^2 - v_{\mathbf{q}}^2 = 1$. The parametrization $u_{\mathbf{q}} = \cosh\theta_{\mathbf{q}}$ and $v_{\mathbf{q}} = \sinh\theta_{\mathbf{q}}$ satisfies this condition. In order to obtain an diagonalised Hamiltonian, the angle $\theta_{\mathbf{q}}$ can be chosen so that cross terms such as $\alpha_{\mathbf{q}}\beta_{\mathbf{q}}$ vanish :

$$
\tanh 2\theta_{\mathbf{q}} = -\gamma_{\mathbf{q}}
\tag{1.50}
$$

The Hamiltonian can thus be expressed as :

$$
H = -\frac{z}{2}NJS(S+v) + zJS\sum_{\mathbf{q}}\sqrt{1-\gamma_{\mathbf{q}}^2}(\alpha_{\mathbf{q}}^{\dagger}\alpha_{\mathbf{q}} + \beta_{\mathbf{q}}^{\dagger}\beta_{\mathbf{q}})
\tag{1.51}
$$

with $v = \frac{2}{N}\sum_{\mathbf{q}} 1 - \sqrt{1-\gamma_{\mathbf{q}}^2} \sim 0.158$. The first term of the Hamiltonian corresponds to the zero point energy, and the second part gives the energy dispersion of the spin waves. The magnon modes are doubly degenerate with :

$$
\omega_{\mathbf{q}}^2 = (zJS)^2(1-\gamma_{\mathbf{q}}^2)
\tag{1.52}
$$

Quantum fluctuations have the effect of reducing the staggered magnetization from the fully saturated value. It can be obtained as the deviation of the average S^z component in equilibrium for one sublattice A from S : $\frac{\delta M_A}{N} = <S_A^z> - S = \frac{1}{2} - \frac{1}{N}\sum_{\mathbf{q}}(a_{\mathbf{q}}^{\dagger}a_{\mathbf{q}} + \frac{1}{2})\frac{1}{\sqrt{1-\gamma_{\mathbf{q}}^2}}$.

Spin wave theory can be generalised to include further couplings such as second and third nearest neighbour exchange interactions. In addition, the presence of anisotropies break rotational symmetry and a spin gap hence opens in the spin wave excitation spectrum at the Brillouin zone center. Furthermore, most lattice cannot be written as bipartite, and competing interactions for particular geometries lead to frustration. Spin-waves follow from the concept of quasi-particles, with a well-defined momentum and energy and are thus associated to magnons following Bose statistics. Although spin wave theory stems from ordered magnets, the interacting boson picture can be extended to the dynamical properties of gapped systems with no magnetic long-ranged order, with magnon quasi-particles corresponding in this case to singlet to triplet excitations.

2 The frustrated quantum magnet SrCu$_2$(BO$_3$)$_2$

2.1 Introduction

Quantum magnets displaying collective singlet ground states have raised a large interest, in particular as quantum spin fluctuations in low spin antiferromagnets are responsible for unconventional magnetic behaviours. While spin-1 systems with Heisenberg interactions were shown to have a gapped spectrum away from conventional spin wave theory [3], quantum fluctuations are expected to have the largest effect in spin 1/2 compounds with reduced dimensionality, such as the chain compound CuGeO$_3$ [40].

Such system are typically discussed using an interacting bosons picture. With singlet states described as a hard-core bosons, an isolated dimer lattice has a ground state with total spin S=0 and a triply-degenerate excited state with S=1 [41]. Within this bosonic picture, the triplet state is identified as a quasi-particle with S=1, called a triplon, and the singlet state is generally defined as the absence of a triplon. For weak inter-dimer interaction, there is no long-ranged magnetic order and the ground state consists of non-magnetic singlets. The triplon mobility then depends on the increase of inter-dimer coupling. The bosonic nature of the singlet and triplet is guaranteed by the fact than the spin operator of two different dimers commute. Hard-core bosons means that they cannot occupy the same quantum state, as opposed to free bosons. A hard-core constraint is thus added in order to exclude states with more than one quasi-particle per dimer :

$$s_i^\dagger s_i + \sum_\alpha t_{i,\alpha}^\dagger t_{i,\alpha} = 1 \qquad (2.1)$$

with s_i and $t_{i,\alpha}$ ($\alpha = x, y, z$) as bound operator for the singlet and triplet states with bosonic statistics. This constraint implies that each dimer can only be in a singlet state or in one of the three excited triplet states. Both inter and intra-dimer interactions are typically present in the realization of a dimerized spin lattice, which can be mapped in the bosonic picture by repulsive and hopping terms, with the applied magnetic field controlling the triplon density. Systems where the spin topology leads to frustration thus exhibit a reduced kinetic energy

of the excitations. Interestingly, Bose-Einstein-Condensation (BEC) has been discussed in quantum magnets, by drawing an analogy between a frustrated spin 1/2 dimerized system in an applied a magnetic field with a lattice gas of hard-core bosons [41, 42]. In this analogy, the magnetic field is treated as a chemical potential.

Furthermore, bound states of excited dimers are also likely to form. Considering two dimers in an excited state only coupled by an inter-dimer coupling J, all the doubly excited states S=0, 1 and 2 would have the same energy $2J$. However, the inter-dimer coupling lifts the degeneracy, and the S=2 quintuplet with ferromagnetic spins appears at higher energy (since the inter-dimer coupling favours antiferromagnetic coupling). On the other hand, the S=0 and S=1 states with neighbouring excited dimers have lower energy than well-separated excited dimers due to resonance, leading to a short-range attractive potential. Thus triplons are confined as bound states as long as the kinetic energy is lower than the interaction energy, with resulting interesting multi-magnon excitation spectra. Inelastic neutron scattering has been shown to be useful to investigate these excited states, for example in the near-ideal alternating Heisenberg chain Cu(NO$_3$)$_2$•2.5D$_2$O [43].

The quantum magnet SrCu$_2$(BO$_3$)$_2$ (SCBO) was proposed as a realization of the Shastry-Sutherland model of interacting dimers in two dimensions (topical review in [7]). The magnetic properties of this compound are due to Cu^{2+} ions in a network of orthogonal dimers with localised spin-1/2. This Cu^{2+} network is strongly frustrated and there is no magnetic long-ranged order down to very low temperatures at ambient pressure and no applied field. This material shows a combination of unique features and exotic states, among which a spin gap of $\Delta \sim 34$K to the localised excited singlet-triplet mode [44], and magnetization plateaus in high-field magnetization measurements [45, 46]. In addition, from the in-plane exchange parameters, estimated by susceptibility measurements to $J = 85$ K and $J' = 54$ K in [47], the value of the inter-dimer to intra-dimer exchange parameter ratio $\alpha = 0.635$ places SCBO close to a critical point, with drastic changes in the correlations above $\alpha \sim 0.7$. Furthermore, the specific heat, susceptibility, and dynamical structure factor observed in SCBO have similar anomalous properties to the one-dimensional fully-frustrated ladder systems[48], making it a rich test-bed for frustrated quantum magnetism. In this context, inelastic neutron scattering has been a well-suited and widely used probe of the complex behaviour of SrCu$_2$(BO$_3$)$_2$ [44, 47, 49, 50, 51, 52, 53, 54].

2.1.1 Shastry Sutherland Model

The two-dimensional Shastry-Sutherland model was constructed for a square lattice with a diagonal bond in such a way that it had a exactly solvable ground state [55]. It was later shown that the orthogonal dimer lattice of $SrCu_2(BO_3)_2$ is topologically equivalent to this model [44], with the nearest-neighbour bond of the Shastry-Sutherland model corresponding to the next nearest neighbour bond of SCBO :

$$H = J \sum_{nn} \vec{S}_i \cdot \vec{S}_j + J' \sum_{nnn} \vec{S}_i \cdot \vec{S}_j \tag{2.2}$$

Figure 2.1 shows the 2D lattice of the Shastry Sutherland model, with J and J' corresponding to the intra and inter-dimer coupling of SCBO.

Figure 2.1: Schematic representation of the Shastry-Sutherland model on the 2D lattice, described in [55] by an orthogonal Heisenberg Hamiltonian with nearest and next nearest neighbour interaction

In a dimerized system, the Hilbert space is spanned by the singlet $|s\rangle$ and three triplets :

$$|t_x\rangle = \frac{i}{\sqrt{2}}(|\uparrow\uparrow\rangle - |\downarrow\downarrow\rangle) \tag{2.3}$$

$$|t_y\rangle = \frac{i}{\sqrt{2}}(|\uparrow\uparrow\rangle + |\downarrow\downarrow\rangle) \tag{2.4}$$

$$|t_z\rangle = \frac{-i}{\sqrt{2}}(|\uparrow\downarrow\rangle + |\downarrow\uparrow\rangle) \tag{2.5}$$

The direct product of the dimer singlet on the strong bond J is an eigenstate of this Heisenberg Hamiltonian with orthogonal dimer:

$$|s\rangle = \prod_i |s\rangle_i = \prod_i \frac{1}{\sqrt{2}}(|\uparrow\downarrow\rangle_i - |\downarrow\uparrow\rangle_i) \tag{2.6}$$

It was shown by Shastry and Sutherland that this eigenstate is the ground state for the 2D orthogonal dimer lattice for an exchange coupling ratio $\alpha = \frac{J'}{J} < 0.5$. Numerical calculations extended the validity for α just below 0.7, even in the presence of weak interlayer coupling J'', hence also extending the validity of the model to three dimensions [47]. This exact dimer singlet state is also the ground state of the Majumdar-Ghosh model which is realised in a zig-zag chain only for the fully frustrated ratio $\alpha = 0.5$ [56].

As α goes to infinity, the Shastry-Sutherland lattice tends towards the two-dimensional square lattice with an Heisenberg Hamiltonian, which has an antiferromagnetic long-ranged order with no spin gap. The existence of a plaquette phase in the intermediary range of the α parameter will be discussed in 2.5.

2.1.2 Physical realisation

SrCu$_2$(BO$_3$)$_2$ crystallises with a tetragonal structure with spacegroup I$\bar{4}$2m. The lattice constants are $a = b = 8.995$ Å and $c = 6.47$ Å at room temperature. The crystal structure of SCBO is characterized by a layered structure of alternating CuBO$_3$ and Sr planes, as shown in figure 2.2. Within the magnetic CuBO$_3$ layer, the Cu^{2+} ions with spin-1/2 are located at crystallographically equivalent sites and are connected through the triangular BO$_3$ molecules. Each Cu^{2+} ion has one nearest neighbour and four next nearest neighbours with distances of respectively 2.905 Å and 5.132 Å at room temperature. A pair of Cu^{2+} nearest neighbours are connected through O sites and form a dimer, which itself is connected to another orthogonal dimer unit through a BO$_3$ molecule. These CuBO$_3$ planes are normal to the crystallographic [001] direction, with the dimers oriented along [110] and [$\bar{1}$10]. These magnetic planes are separated from each other by the intercalated Sr layers.
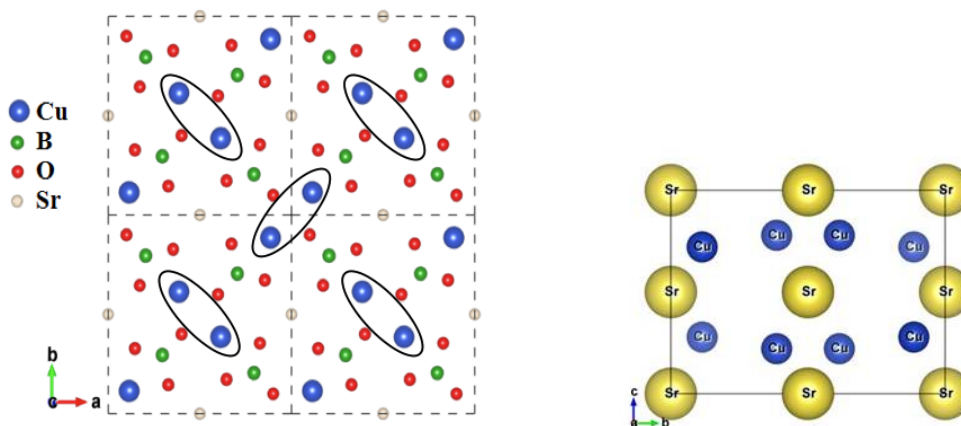

Figure 2.2: Schematic illustration of the crystal structure of SCBO. Left : CuBO$_3$ (a, b) plane. Right : (b, c) plane.

Below the structural transition temperature T_s=395K, the CuBO$_3$ planes are slightly buckled with a buckling angle of $\phi = 6°$, hence breaking mirror symmetry of the magnetic planes [50]. Between adjacent layers, there are thus two distances between Cu^{2+} ions : 3.593 or 4.233 Å, so that strictly speaking there are two interlayer coupling constants. In general, given the weak interlayer interaction (as will be discussed in 2.2), this difference is neglected and only one interlayer coupling J" is taken into account.

2.1.3 Dzyaloshinskii-Moriya interaction and staggered gyromagnetic tensor

If SrCu$_2$(BO$_3$)$_2$ was an exact realisation of the Shastry-Sutherland model, the triplet excitations would be fully localised with three-fold degenerate flat bands. Many features observed experimentally cannot be explained by the Heisenberg model for a Shastry-Sutherland geometry alone, such as the splitting of the singlet-triplet state observed both in Electron Spin Resonance (ESR) measurements [57] and neutron scattering [58] or the field-induced staggered moment seen in NMR [59]. In order to understand these experimental results in SCBO, the orthogonal dimer model Hamiltonian requires the inclusion of Dzyaloshinskii-Moriya interactions (DM) and a staggered gyromagnetic tensor, due to the buckling of the CuBO$_3$ planes below 395 K [50].

Flat CuBO$_3$ planes with mirror symmetry would have an inversion center at the center of the J bonds, hereby forbidding Dzyaloshinskii-Moriya interactions. The buckling of the planes causes a loss of mirror symmetry with respect to the (a, b) plane, and components of the Dzyaloshinskii-Moriya interaction are allowed. The Hamiltonian for the Dzyaloshinskii-Moriya interaction is given by

$$H_D = \sum_{(i,j)} \boldsymbol{D}_{ij} \cdot (\boldsymbol{S}_i \times \boldsymbol{S}_j) \tag{2.7}$$

Figure 2.3: Dzyaloshinskii-Moriya coupling in SCBO, figure from [60]. D represents the in plane intra-dimer Dzyaloshinskii-Moriya vectors. The inter-dimer D' has in-plane and out of plane components with $D_\perp$ vectors pointing out of the plane on each bond and $D'_{\parallel,s}$ the in-plane component. The green rectangle is the structural unit cell and black arrows represent the order of the spins for the DM term in the Hamiltonian.

Figure 2.3 from [60] shows the in-plane geometry with the DM vectors. Below the structural phase transition T$_s$=395K (i.e. in the low-symmetry phase), an in-plane intra-dimer Dzyaloshinskii-Moriya coupling D is allowed. Regarding the inter-dimer coupling, the DM coupling is labelled D', with a dominant out-of-plane component $D'_\perp$ and a weak in-plane component $D'_{\parallel,s}$. In [60], a linear combination $\tilde{D}_\parallel$ of the intra-dimer D and in-plane inter-dimer D'$_{\parallel,s}$ appear in the Hamiltonian, as they have been shown to be interdependant [61]. The Dzyaloshinksy-Moriya interaction in SCBO is not frustrated as the D vector alternates from bond to bond.

In addition, there are two inequivalent dimers in the plane (horizontal and perpendicular, see Figure 2.2.a). The unit cell thus contains four inequivalent spin sites, so that there are four inequivalent gyromagnetic tensors.
The gyromagnetic tensor on site 1 can be written as [50]:

$$\widehat{g}_1 = \begin{pmatrix} g_x & 0 & g_s \\ 0 & g_y & 0 \\ g_s & 0 & g_z \end{pmatrix} \tag{2.8}$$

with x along the 110 axis and z along the c-axis. g_x, g_y, g_z and g_s take into account the buckling angle of the CuBO$_3$ plane ϕ, with for example $g_x = g_\xi \cos^2\phi + g_\zeta \sin^2\phi$. The three other tensors are related to eq. 2.8 by symmetry operations. The diagonal terms are obtained from ESR experiments [57]: $g_x = g_y = 2.05$ and $g_z = 2.28$. The off-diagonal elements g_s are staggered (opposite on sites 1 and 2, and on sites 3 and 4) and are estimated to $g_s = 0.023$.

Taking into account a small magnetic field h_z applied perpendicular to the CuBO$_3$ planes and including the Dzyaloshinskii Moriya interactions, the Hamiltonian is given by :

$$H = \sum_{n.n.} J(S_i \cdot \boldsymbol{S}_j) + \sum_{n.n.n.} J'(\boldsymbol{S}_i \cdot \boldsymbol{S}_j) - g_z h^z \sum_i S_i^z + \sum_{n.n.} \boldsymbol{D}_{ij} \cdot (\boldsymbol{S}_i \times \boldsymbol{S}_j) + \sum_{n.n.n.} \boldsymbol{D}'_{ij} \cdot (\boldsymbol{S}_i \times \boldsymbol{S}_j) \tag{2.9}$$

2.1.4 Localised singlet-triplet mode

SrCu$_2$(BO$_3$)$_2$ is gapped to a localised singlet-triplet excitation around 3 meV. The singlet-triplet excitation is localised due to the frustrated geometry, as the kinetic energy of the triplon is reduced since the hopping of a triplet is only allowed through forming a closed path of triplets.

On the other hand, the Dzyaloshinskii-Moriya interaction is not frustrated (as opposed to the next nearest neighbour interaction), so that the degeneracy of the localized triplet is weakly lifted and the excitations have a weak dispersion. In addition, the triplet states for the two dimer orientations are not equivalent and so there are two dimer sub-lattices with triplet excitations. There are thus two degenerate upper modes with $S^z = \pm 1$, two degenerate lower modes $S^z = \pm 1$ and one $S^z = 0$ mode. A magnetic field along the c axis would split each $S^z = \pm 1$ modes into two branches.

Figure 2.4 illustrates the excitation spectra of SCBO measured using inelastic neutron scattering around $\Delta E = 3$ meV, corresponding to the energy of the singlet-triplet mode. The degeneracy of the triplon is weakly lifted by the DM interaction, and this is clearly visible, with a small dispersion of the singlet-triplet modes between 2.8 and 3.2 meV.
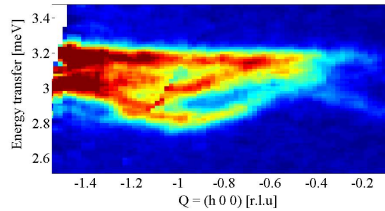

Figure 2.4: Excitation spectra measured on the cold time-of-flight spectrometer LET at 1.5K and zero applied field, showing the weak dispersion of the singlet-triplet modes at $\Delta E = 3$ meV

2.1.5 Neutron scattering studies of key features in SCBO

Inelastic neutron scattering is a key technique in order to gain insight on particular unique features of $SrCu_2(BO_3)_2$ through analysis of its excitation spectra :

- The effect of interlayer coupling on the excitations in SCBO can be studied in order to analyse time-of-flight inelastic neutron scattering data.

- SCBO has an unusual temperature damping behaviour, for which a correlated decay model has been proposed [51]. Further lifting the singlet-triplet mode degeneracy using a magnetic field is key in order to understand the damping behaviour of SCBO.

- Correlated hopping is thought to play a large role in the bound magnon excitations [62, 44]. Measuring the excitation spectra for higher energy transfers corresponding to bound magnon excitation energies allows to discuss these excitations.

- The proposed plaquette phase [53, 63] for the intermediary phase of SCBO depending the ratio α can be further investigated by inelastic neutron scattering, using pressure to tune the strength of the interactions.

- SCBO has been proposed as a topological magnon insulator [60], and the predicted Dirac-like dispersion of the triplon can be investigated experimentally using high-resolution neutron spectroscopy.

2.2 Effect of the Interlayer coupling

Most experimental and theoretical models of SrCu$_2$(BO$_3$)$_2$ consider that the system has a purely two dimensional character, which is equivalent to considering a negligible interlayer coupling [44]. Nevertheless, a value for the interlayer exchange constant J'' of 8K was estimated using bulk magnetic susceptibility and specific heat [47]. As there is a buckling of the CuBO$_3$ planes, creating a distance difference between Cu^{2+} ions of adjacent layers, there are in fact two exchange constants J'', which for simplicity are averaged using a mean field type approximation to obtain a unique J''. Compared to the main exchange coupling constant J of 84K, J'' is about an order of magnitude weaker. The interlayer coupling has been shown not to have an effect of the size of the spin gap [47], but magnetic excitations could be affected. Some arguments for of the negligible effect of J'' on the magnons can be found in [49], which claims little Ql dependence of the $n = 1,2$ and 3 excitations from an observation of a rod-like behaviour in inelastic time-of-flight measurements. Although rod-like scattering is characteristic of 2D materials (see 1.1.8), this study was only qualitative, and the interlayer coupling could still have a measurable effect.

This question is of crucial importance, as it is determinant in the analysis method of time-of-flight measurements. As shown in section 1.1.8, the excitation spectra for a 2D system obtained on time-of-flight spectrometer can be integrated along the irrelevant Q direction. In order to check the validity of the TOF analysis method, a set of inelastic experiments were carried out on cold and thermal triple axis spectrometers (table 2.1). The set of questions to answer with these experiments are the following : Is there an energy variation due to Ql in the singlet-triplet mode dispersion or within the multi-magnon continuum ? Is there an intensity dependence of the modes on Ql which cannot be explained by the magnetic form factor ? What is the value of the effective interlayer coupling J'' ?

Table 2.1: List of TAS experiment to evaluate the effect of interlayer coupling in SCBO

Instrument	Energy range	Sample	Type of scans
TASP	cold, E$_i$ ~ 5-8 meV	multi-crystal mount	Constant-Q scans
EIGER	thermal, E$_i$ ~ 16-30meV	single cystal	Constant-Q scans
IN8	thermal, E$_i$ ~ 16-30meV	single crystal	Constant-ΔE scans

2.2.1 Ql dispersion for the singlet-triplet mode

The first experiment was concerned with the possible Ql dependence of the dispersion of the singlet-triplet mode. As described in 2.1.4, the singlet-triplet mode is weakly split due to the Dzyaloshinskii-Moriya interaction, so that a cold instrument is necessary to obtain an energy resolution sufficient to resolve each of the three modes. The cold triple-axis spectrometer TASP at the Paul Scherrer Institute was set up with a vertically focusing PG(002) monochromator and a horizontally focusing PG(002) analyser with fixed $k_f = 1.2$ Å^{-1}. The incident energy E$_i$ was in the range 5-8 meV and the SCBO multi-crystal mount was aligned with (110) and

(001) in the scattering plane and cooled to 1.5K. Constant-Q scans were obtained for a set of Ql values at both a 2D Brillouin zone center and a Brillouin zone boundary (π, π). The measured excitations peaks were resolution limited (energy resolution given at 3 meV for $|Q| = 1$ Å by a full-width-half-maximum of 0.15 meV), so that they were modelled by three Gaussian functions. The resolution was nevertheless taken into account in details using the Popovici method available in the trixfit routines (refer to 1.1.8).

Figure 2.5 shows the results of the fits after taking into account the resolution of the instrument. For plotting purposes, the data at (1 1 0) and (1.5 1.5 0) has been multiplied by a scale factor of 5. Indeed, a lower intensity for $Ql = 0$ was observed compared to higher Ql values on TASP. This effect was only measured on this instrument, which hints toward a particular instrumental geometry leading to more neutron absorption in the direction corresponding to $Ql = 0$.

Figure 2.5: Fits of the TASP data for the 3meV singlet-triplet mode, shown with an offset. Constant-Q scans for a) $Q = $(11L) and b) $Q = $(1.5 1.5 L).

Figure 2.6 shows the energy center of each triplet mode extracted from the fits of the TASP dataset for both (11L) and (1.5 1.5 L) (resp. circles and squares).

Figure 2.6: Center of each of the singlet-triplet mode resulting from the fits of the TASP data for Q=(11L) (circles) and Q=(1.5 1.5 L) (squares).

No particular Ql dependence of the energy centers can be observed in these results and the variations observed are within the energy resolution. It thus appears that the interlayer coupling has no measurable effect on the dispersion of the singlet-triplet mode.
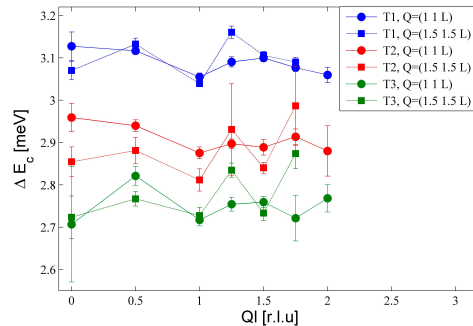
2.2.2 Ql dispersion for the Multi-magnon modes

Focusing on the Ql behaviour of the dispersion of the bound magnon modes at higher energy transfers, the same experimental and analysis method was applied using a thermal triple axis spectrometer. The thermal triple axis EIGER at the Paul Scherrer Institute was set up with a doubly focusing PG(002) monochromator and a horizontally focusing PG(002) analyser with fixed $k_f = 2.662$ Å^{-1}. The incident energy E$_i$ was in the range 16-30 meV and a single SCBO crystal was aligned with (110) and (001) in the scattering plane and cooled to 1.5K.

A set of Constant-Q scans were measured at (1 1 L) and (1.5 1.5 L) up to $\Delta = 12$ meV and the observed peak excitations were fitted with Gaussians, while taking into account the variation of the resolution with increasing energies using the Popovici method available in the trixfit routines, as for the analysis of TASP data. Figure 2.7 illustrates the results of the fits and the data quality for Q=(1 1 L). The singlet-triplet mode at 3 meV was fitted separately and found to be coherent with previous results.

Figure 2.7: Fit Result on EIGER data of the multi-magnon modes for Q=(1 1 L)

Figure 2.8 shows the energy centers ΔE_c of each mode at (1 1 L) in blue and (1.5 1.5 L) in red for the different Ql values measured. Overall, there does not appear to be any significant dispersion along Ql for any of the modes. It could be argued from the results that the ~ 9 meV mode has some dispersive behaviour, but it is more likely a combined effect of the decrease in resolution and lower statistics of the data for weak modes at higher energy transfers. For the bound magnon mode at 4.85 meV, which has the strongest intensity, it is clear that there is no dispersion along Ql that could be attributed to interlayer coupling, within the energy resolution of ~ 0.25 meV .

Figure 2.8: Energy centers ΔE_c of each of the multi-magnon mode (and singlet-triplet mode) resulting from the fits of the EIGER data for Q=(11L) (blue) and Q=(1.5 1.5 L) (red).
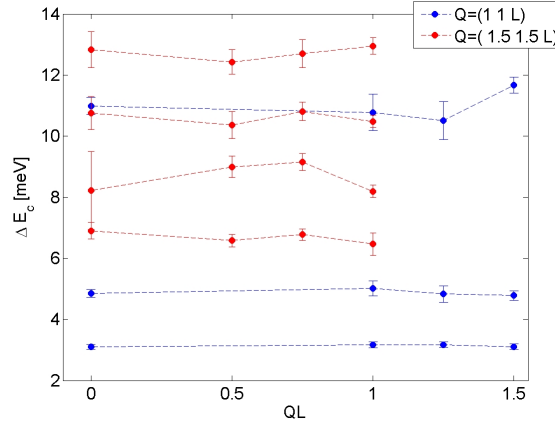
In summary, there does not appear to be any measurable effect of the interlayer coupling on the dispersion of the magnetic excitations in SCBO. No estimate of the effective coupling J'' could be obtained from these data, as the effect of the coupling was too weak to be detected. No conclusive information on the intensity of each mode as a function of Ql was obtained from these experiments, so that the possible modulation of intensity along Ql was measured on the thermal triple axis IN8 with constant Q-scans.

2.2.3 Intensity variation along Ql

Following the conclusions of a dispersion-less behaviour of the singlet-triplet mode and bound magnon excitations along Ql, the modulation of the intensity was measured on the thermal triple axis spectrometer IN8 at the ILL. The instrument was set up with a Si(111) monochromator, a PG(002) analyser and no collimation, with fixed $k_f = 2.662\,\text{Å}^{-1}$. The single SCBO crystal was aligned with (110) and (001) in the scattering plane and cooled to 1.5K.

Constant-energy scans are appropriate since there is is no observed Ql dispersion. A series of Ql scans were thus carried out for $L = -4$ to 4 at constant energies between $\Delta E = 3$ meV for the singlet-triplet mode and $\Delta E = 11$ meV for the multi-magnon modes for either (1 1 L) and (1.5 1.5 L). However, the magnetic scattering was contaminated by spurious signal, as illustrated in figure 2.9 for $\Delta E = 3$ meV. This is not unusual for a thermal neutron scattering experiment, as spurious signal can have various origins such as scattering from aluminium or contamination from the second or third harmonic of the incident energy from the monochromator. Furthermore, it is clear that these spurious signals are not magnetic in origin. Indeed, constant-energy scans were done at 15K, a temperature at which the magnons in SCBO are completely damped, and the same spurious peaks were observed (as shown by the black curve of figure 2.9). Nevertheless, due to this spurious scattering, not all the excitation modes observed on EIGER or TASP could be measured on IN8, as some modes could not have been

analysed reliably. Only scans for the singlet-triplet mode, the first bound magnon mode and a
mode at 9 meV were used in this intensity study.

Figure 2.9: Constant-Energy scan at $\Delta E = 3$ meV from IN8 experiment along Q=(11L) for 1.5K
and 15K

In addition, in order to remove the spurious scattering from the data, the 15 K data was
subtracted from the 1.5K data. Figure 2.10 shows the magnetic scattering as a function of Ql
for Q=(1 1 L) and $\Delta E = 3$ meV after subtraction of the spurious background.

Figure 2.10: Subtracted Intensity $I = I_{1.5K} - I_{15K}$ for $\Delta E = 3$ meV on IN8. The red line is the
result of the fit of the anisotropic magnetic form factor squared $f(\mathbf{Q})^2$ for (1 1 L), with a scaling
factor as the only free parameter.

In order to know whether the intensity variation differs from a simple form factor squared behaviour as $|Q|$ increases, the anisotropic magnetic form factor $f(\mathbf{Q})^2$ along $Q=(1\ 1\ L)$ for Cu^{2+} was calculated using the coefficient of $j_0(|Q|)$ and $j_2(|Q|)$ from the Crystallographic tables [13] and equation 1.24. 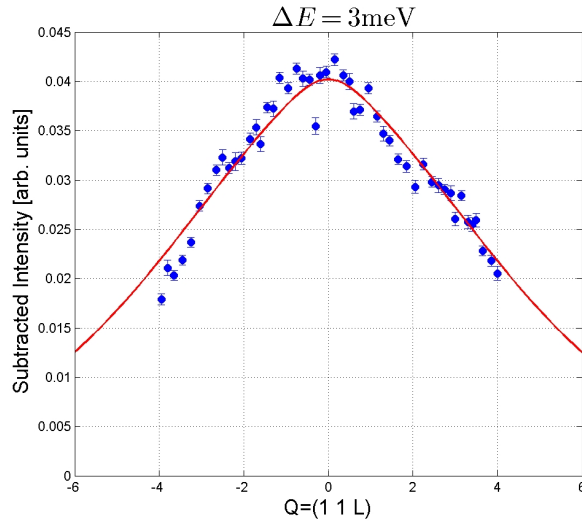The anisotropic magnetic form factor was then scaled to the data at $Ql = 0$ and the result is shown as the red line in figure 2.10.

The same procedure was also applied to the two multi-magnon modes by performing constant-energy scans at $\Delta E = 4.85$ and 9 meV. The scaling of the anisotropic form factor along Q=(1 1 L) to the subtracted dataset for these scans is shown in figure 2.11.
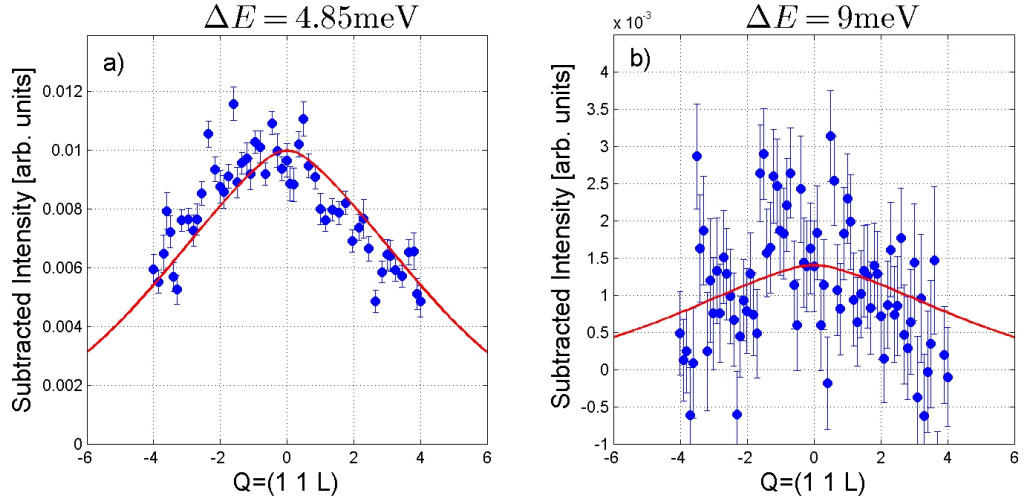

Figure 2.11: Subtracted intensity $I = I_{1.5K} - I_{15K}$ for a)$\Delta E = 4.85$ meV and b) $\Delta E = 9$ meV. The red line is a fit of the anisotropic magnetic form factor squared $f(\mathbf{Q})^2$ for Q=(1 1 L), with a scaling factor as the only free parameter.

Both figure 2.10 and figure 2.11.a-b show that, within the quality of the datasets, there is no measurable deviation of the intensity from a simple form-factor like behaviour. In particular for the singlet-triplet mode and the bound magnon mode at $\Delta E = 4.85$ meV, the system appears to behave like a two-dimensional system.

The interlayer coupling hence does not appear to have any effect of the intensity from the magnons in SCBO that can be observed in neutron scattering results. SCBO can thus be considered a proper 2D system for inelastic neutron scattering with typical resolutions larger than 0.15 meV at $\Delta E \sim 3$ meV and 0.25 meV at $\Delta E \sim 5$ meV. This has important consequences for the execution and analysis of time-of-flight neutron scattering experiment, as the data can be integrated over the measured Ql, which allows faster mapping of the 2D $S(\mathbf{Q}, \omega)$ and improved statistics. This method will be exploited in section 2.3 and section 2.4.1.

In conclusion, the interlayer coupling has no measurable impact on the neutron excitation spectra of $SrCu_2(BO_3)_2$, for instrumental Gaussian resolutions with typical full-width-half-maximum of 0.15 meV at 3 meV.

2.3 Damping of the singlet-triplet mode with temperature

The finite temperatures properties of SrCu$_2$(BO$_3$)$_2$ are particularly interesting, as the compound shows unusually fast temperature damping. Indeed, the magnetizations plateau, appearing in SCBO at fractional values of the saturation of the magnetisation [64], have already disappeared just above 1K. In addition, in inelastic neutron scattering, the singlet-triplet excitations were observed to damp rapidly with temperature and to be completely damped at 15 K, while the energy of the spin gap is 34K [52]. Figure 2.12 shows this strong magnon decay with temperature for 2K, 5.5K, 7.3K and 8.5K. In SCBO, the damping mechanism leads not only to a decrease of the mode intensities, but also to a small positive energy transfer shift and a broadening of the singlet-triplet excitations.

Figure 2.12: Damping of the singlet-triplet mode of SCBO from LET measurements along $Q = (h\,1\,0)$ for temperatures of a) 2K, b) 5.5K, c)7.3K and d) 8.5K.

Finite temperature drives changes in the spectral weight of the modes, which can be probed by inelastic neutron scattering, but it can also have an effect on the position and shape of the magnon spectrum, as discussed in [65]. In [66], thermal renormalization of a triplet excitation was studied in TiCuCl$_3$, with an observed shift in excitation energy with temperature without loss of magnon coherence. The shift in spectral weight to larger energies hence appears to be a many-body effect. Indeed, in the interacting boson picture, the hard-core constraint implies that each dimer can only be in a singlet state or one of the three triplet states. A reduction of the propagation of a triplet due to the occupation of some dimers by thermally excited triplets is thus expected, hereby reducing the dispersion bandwidth. In addition, anomalous dynamical line-shapes have been observed in strongly correlated states with temperature, for example in a 1D alternating Heisenberg chain realised in Cu(NO$_3$)$_2$•2.5D$_2$O [67].

Hence, the spin correlations in SCBO are very sensitive to a small increase in thermal energy. A real-space scenario has been proposed in [51, 68] in which correlated decay explains this unusual temperature damping. As discussed in section 2.1.4, the frustrated interaction of the Shastry-Sutherlad model on a 2D lattice induces localized singlet-triplet excitations. A neutron-excited singlet-triplet excitation will decay rapidly in the presence of a thermally excited singlet-triplet, while it will be long-lived if there are none nearby. This scenario of interacting bosons shows that the creation of a an excitation polarizes neighbouring singlets, leading to an extended boson covering several dimers. These extended bosons decay when they overlap with one another.

At low temperatures, there is only a small percentage of thermally excited triplets (2% at 6.8K and 9% at 10K), which means that the thermodynamical properties of SCBO are very sensitive to perturbations, as expected in a frustrated system. In [51], the experimental temperature dependence of the excitation was explained by an effective singlet-triplet radius of $R = 1.3a = 11.7$ Å. This corresponds to a polarisation of six of the neighbouring dimers (1.27 Å), which is similar to the polarisation obtained in theoretical studies calculating the influence of an introduced spin vacancy on one Cu^{2+} position on the dimerized singlet ground state [69]. Figure 2.13 from [51] illustrates this real-space image of extended bosons.

Figure 2.13: Real-space image of two overlapping singlet-triplet excitation from [51]. The magnetisation pattern is shown by up and down arrows around the central triplet with intensities proportional to the magnetisation.

In this context, the singlet population was compared to the temperature-dependent spectral weight of the singlet-triplet mode obtained from inelastic neutron scattering. The intensity of the excitation is proportional to the number of singlets, since the neutron excites a dimer from a singlet to a triplet state. It was found in [51] that the total spectral weight is consistent with the calculated singlet population $n_s(T) = \frac{1}{1+3e^{-\Delta/T}}$ for a spin gap $\Delta = 35$K. From this, it was concluded that, while the quasi-particle peak loses intensity well below the expected temperature, the spectral weight is transferred to a broad feature corresponding to fast-decaying triplets.

The excitations can thus be divided in two components : a sharp component corresponding to the long-lived singlet-triplet mode, and a broad component, corresponding to the fast decaying singlet-triplet. A finite temperature, a damped harmonic oscillator function (DHO) from linear theory can be used to model the dynamical structure factor $S(Q,\omega)$:

$$S(\mathbf{Q},\omega) = [n(\omega)+1]A(\mathbf{Q})\frac{4\omega\Gamma}{\pi}\frac{1}{(\omega^2-\Omega_0^2)^2+4\omega^2\Gamma^2} \tag{2.10}$$

This function has been developed for the study of anharmonic phonons [70]. In this case, $A(\mathbf{Q}) = \frac{Z(\mathbf{Q})}{\Omega_0}$, with $Z(\mathbf{Q})$ a dimensionless structure factor which corresponds to the imaginary part of the magnetic susceptibility $\chi'(\mathbf{Q})$. $[n(\omega)+1]$ is the Bose factor, and $\Omega_0^2 = \omega_0^2 + \Gamma^2$ are the renormalised frequencies, with Γ the damping parameter describing the line-width.

This function can be rewritten as a weighted difference of two Lorentzian functions, each corresponding to the Fourier transformation of an exponential decay $e^{-t/\tau}$ with $\Gamma_L = \tau^{-1}$ the half width at half maximum of the Lorentzian. The DHO function is then rewritten as :

$$S(\mathbf{Q},\omega) = \frac{1}{\omega_0\pi}[n(\omega)+1]A(\mathbf{Q})\left(\frac{\Gamma}{(\omega-\omega_0)^2+\Gamma^2} - \frac{\Gamma}{(\omega+\omega_0)^2+\Gamma^2}\right) \tag{2.11}$$

As shown in equation 1.25, the magnetic inelastic scattering intensity is proportional to the dynamical structure factor, and the DHO function describes the line-shape of the magnetic excitations. In addition, as discussed in [70], a DHO function satisfies both the detailed balance factor (described in 1.1.5) and the condition of an odd imaginary part of the susceptibility.

In order to describe instrumental data, the lineshapes are modeled with DHO functions convolved with a Gaussian resolution, which corresponds to a weighted difference of Voigt functions. At 2K, only long-lived triplet excitations are present, and the obtained excitations are resolution limited. The damping width Γ is zero, and the DHO function tends to a Dirac function with energies $\pm\omega_0$. At higher temperature, both the sharp and broad components are present, and the work in [51] showed that two DHO for each excitation mode, one with $\Gamma = 0$ and another with a finite damping width Γ_{DHO}, were necessary to reproduce the experimental dataset.

Figure 2.14 illustrates this model for $Q = (0.75\ 0.75\ 0)$, with 2K data and fit shown in green and 7.3K data and fit shown in black. The dashed lines correspond to the two components of the fits at 7.3K, three DHO functions with $\Gamma = 0$, and three DHO function with finite Γ_{DHO}.
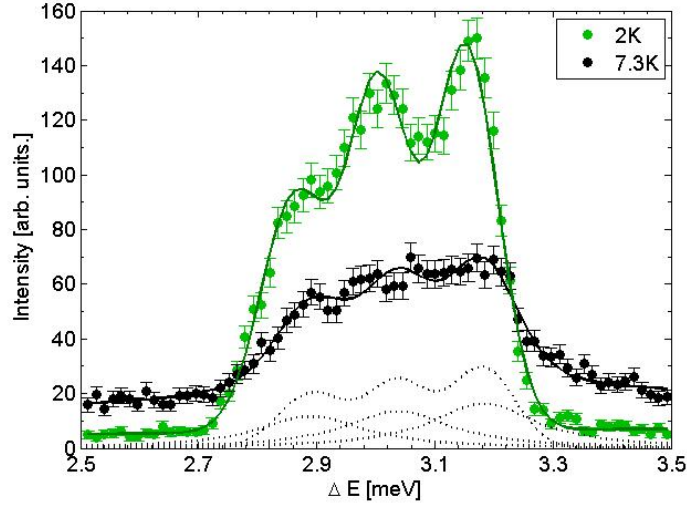
Figure 2.14: LET data and fits for $Q = (0.75\ 0.75\ 0)$ at 2K (green circles and curve) and 7.3K (black circles and curve). The dashed lines corresponds to 7.3 K and show the two components of the fits : three DHO functions with $\Gamma = 0$, and three DHO functions with finite $\Gamma_{DHO} \simeq 0.19$ meV.

In [51], the data were obtained using triple axis-spectrometers for a limited number of Q points, so that the analysis was done assuming no particular Q-dependence of the damping widths. The degeneracy of the singlet-triplet mode is slightly lifted by Dzyaloshinskii-Moriya interaction, so that there are three weakly split triplets for no applied field. The resolution of the data in [51] did not permit a clear difference between the damping of each triplet to be established. The exchange of spectral weight between the sharp and broad DHO was characterised in [51], but further information can be obtained from the large $S(\mathbf{Q}, \omega)$ maps measured by time-of-flight spectrometers. In addition, combining time-of-flight spectrometers with the application of a field, which splits the triplets further apart, allows a detailed study of the damping mechanism in SCBO.

2.3.1 Experimental details and analysis method

Datasets in applied fields of 0 T and 8 T were obtained on the cold time-of-flight spectrometer LET, at ISIS, UK with the SCBO multi-crystal mount sample with (110) and (001) in the horizontal plane. In 2.2, the magnon modes in SCBO were shown not to have any measurable Ql dependence, so that the Q-maps were obtained by aligning the sample such that $\mathbf{k}_i//\mathbf{c}$ and integrating over Ql. The incident energy was $E_i = 7$ meV.

For the 0T case, the sample was mounted in a simple orange cryostat with a bore radius of 100 mm. The excitation spectra were measured at 1.5 K, 2 K, 5.5 K, 7.3 K, 8.5 K and 10K. In the 8T case, the sample was mounted in a cryo-magnet with bore radius of 75mm. A crystal was removed from the multi-mount sample in order to accommodate the reduced size of the

sample space. The field was applied vertically, so that in this sample orientation the field was applied parallel to (1$\bar{1}$0).

The fitting procedure was the following : the one-dimensional energy scans as a function of Q were integrated over dQ, so that the dataset is effectively cut into Q squares. The 2K dataset, where only the sharp component is present, was fitted with only one DHO with $\Gamma = 0$ per mode, with the constraint $\sigma^1 = \sigma^{1'} = \sigma^2 = \sigma^3 = \sigma^{3'}$ where σ is the standard deviation of the Gaussian resolution. The numbers 1, 2 and 3 refer to the three triplet mode, and 1' and 3' are applicable only in the 8T case, for which there are 5 singlet-triplet modes.

From the 2K fits, one obtains the following constraints for the higher temperatures : The Gaussian resolution σ and the ratio between I^{T1}, I^{T2} and I^{T3}, as the spectral weight is not redistributed between each mode when temperature increases. In the 8T case, a ratio between T1 and T1', as well as between T3 and T3', for ω and the intensity were obtained and fixed. These peaks are almost degenerate, only separated at 8T by ~ 0.15 meV, so that they could not be fitted independently at 6.3K.

At higher temperatures, the datasets were then fitted with one DHO with $\Gamma = 0$ and one DHO with finite Γ per mode, with the following constraints : The energy centers are kept identical between the sharp and broad mode $\omega_{\text{sharp}} = \omega_{\text{broad}}$ and the integrated intensity ratio $\frac{I_{\text{broad}}}{I_{\text{sharp}}}$ is fixed from the results of each temperature in [51]. In summary, using the information of the 2K fits, the only independant parameters for the higher temperature fits are $\left(I^{T1}, \omega^{T1}, \Gamma^{T1}, \omega^{T2}, \Gamma^{T2}, \omega^{T3}, \Gamma^{T3}\right)$

2.3.2 Results at 0T applied field

The Gaussian resolution at $\Delta E \sim 3$ meV was estimated to be $\sim 0.06 \pm 0.01$ meV . This value was obtained by fitting the resolution-limited peaks of the singlet-triplet excitations at 2K fit from one-dimensional constant-Q cuts with dQ=0.15 [r.l.u.]. This resolution was then fixed for the subsequent fits at 7.3K

As shown in Figure 2.14, without any applied field, the three modes are only weakly separated by the Dzyaloshinskii-Moriya interaction, and the data quality at 7.3K was not enough to resolve the damping width for each triplet excitation peak separately as a function of Q. Each triplet however appeared to be damped with a similar averaged Γ width with $\Gamma^{T1} \sim 0.18 \pm 0.05, \Gamma^{T2} \sim 0.23 \pm 0.05$ and $\Gamma^{T3} \sim 0.20 \pm 0.04$ at 7.3K. In order to obtain a more reliable Q-map of the DHO damping linewidth, the line-widths of the three triplet were then assumed to be identical, hence leading to the additional constraint $\Gamma^{T1} = \Gamma^{T2} = \Gamma^{T3}$.

Figure 2.15 shows the obtained Q-map using this analysis method, with empty Q-squares (white) corresponding to either non-converging fits or the absence of data at this Q point. No particular Q-dependence is apparent in this Q-map, yet the challenge in resolving reliably the three modes at 0T is apparent. The average damping width (from converging fits only) is calculated to be $\Gamma_{DHO} = 0.198 \pm 0.08$ meV .
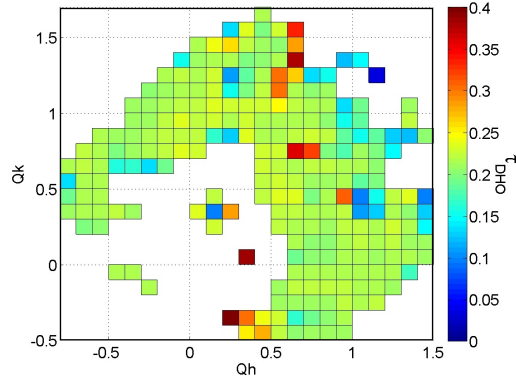
Figure 2.15: Q-map of the finite DHO damping width Γ_{DHO} for the LET dataset at 7.3K. Empty Q-squares correspond to non-converging fits or the absence of data at these Q-points.

From these results, it is thus apparent that a reliable Q-dependence of the damping linewidth Γ_{DHO} can only be obtained by lifting further the degeneracy of the three triplet modes. This can be done by applying a magnetic field, hereby further splitting the excitations into five modes. It is interesting to note that at 0T and 7.3K, the three triplets appear to have similar damping widths, within the incertitude of the fitting.[1]

2.3.3   Results at 8T applied field

As a magnetic field parallel to $(1\bar{1}0)$ is applied, the degeneracy of both the upper and lower mode is lifted by the Zeeman term, and there are five singlet-triplet modes. This field depen-dence will be detailed further in section 2.6.2. At 8T, the excitations are past the critical field, and the upper and lower modes are separated from the $S^z = 0$ central mode by about ± 1 meV.

Figure 2.16 shows an energy slice along $Q = (h\ 1\ 0)$ and an energy cut at $Q = (1\ 1\ 0)$ for both 2K (a,c) and 6.3K (b,d). The white lines in figure 2.16.a show the expected splitting into five modes for the 8T field applied along $(1\bar{1}0)$. As shown by Figure 2.17 and 2.16, the upper and lower $S^z = \pm 1$ modes are very close and appear as one broader peak with a maximum separation for $Q = (0.5\ 1\ 0)$ of ~ 0.15 meV and a minimum of zero at $Q = (1\ 1\ 0)$. This is taken into account in the analysis, although the damping widths of each weakly split mode are correlated, as the resolution is not sufficient to develop an analysis with five independent finite DHO widths.

The set of independent parameters of this analysis at 6.3K is thus $\left(I^{T1}, \omega^{T1}, \Gamma^{T1}, \omega^{T2}, \Gamma^{T2}, \omega^{T3}, \Gamma^{T3}\right)$, with the Gaussian resolution width and the relative integrated intensity of T1 with T1' and T3 with T3' fixed from the 2K fit results.

Interestingly, in the work described in [51], some fits were done with data obtained on a triple axis spectrometer for an 8T field applied along c. For an applied field along c, there is also an

---

[1]A similar analysis and fitting procedure at 0T applied field was done for 5.5, 7.3, 8 and 8.5K in the thesis work by Mattia Mena, with similar results.
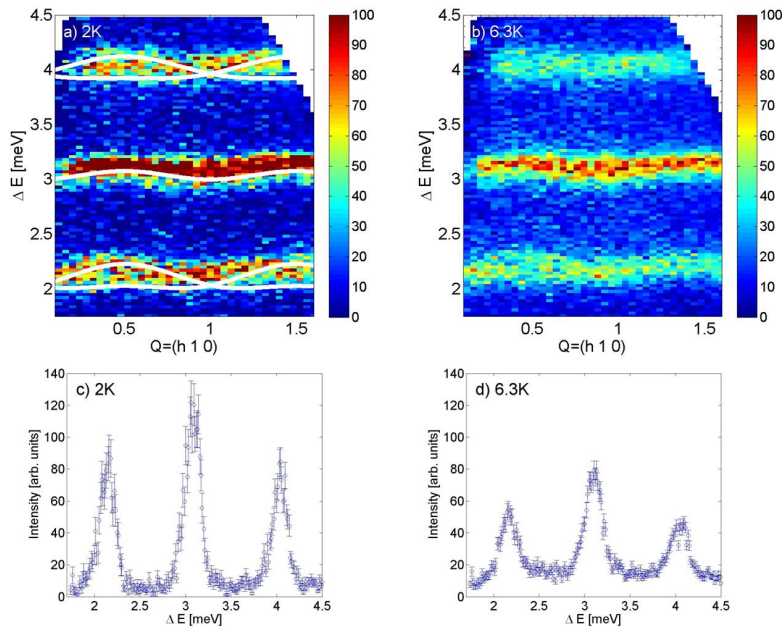
Figure 2.16: LET data at 8T applied field along (1-10). a) Energy slice at 2K along $Q = (h\,1\,0)$, with expected dispersion from calculated model in 2.6.2 with 8T field along (1-10) and g factor of $g_x = g_y = 2.05$. b) Energy slice at 6.3 K. c-d) One dimensional energy scans at $Q = (1\,1\,0)$ for T=2K and T=6.3K.
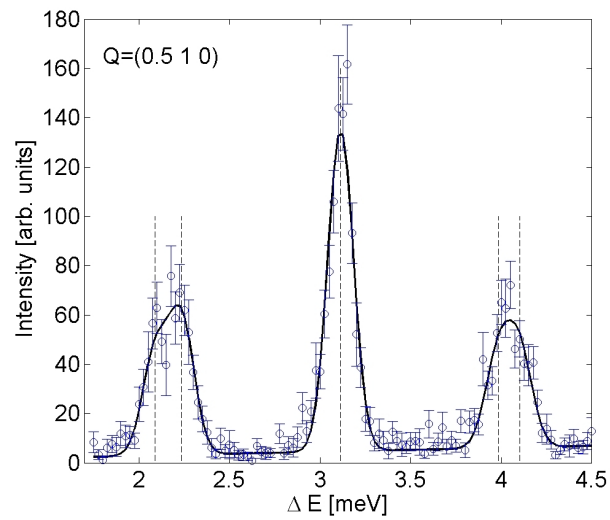
Figure 2.17: One dimensional Energy scan for $Q = (0.5\,1\,0)$ showing the maximum splitting of the lower and higher triplets into respectively T1 and T1' and T3 and T3'. The black line is a fit with five $\Gamma = 0$ DHO functions convolved with the resolution, and the dashed lines show the energy centers of these modes obtained from the fits.

additional weak splitting of the modes, maximum at Q =(110) with splitting of 0.37 meV and minimum at Q=(1.5 0.5 0) where the modes are degenerate. The fits had only been done at this latter Q point in [51], in order to avoid this further splitting.

In this case, the Gaussian resolution was estimated to be ~ 0.08 ± 0.01 meV from the 2K fit, with dQ=0.11 [r.l.u.] This resolution was then fixed for the subsequent fits at 6.3K. Figure 2.18 shows the following resulting parameters from the 6.3K fits along ($h\ h\ 0$): the energy centers ΔE_c, the Γ_{DHO} damping width, the integrated intensity of both the sharp and broad components, the sloping background parameters and the goodness of fits. These results show the coherence of the analysis, with a constant background variation with Q that can be explained by a geometrical inhomogeneity due to the use of a multi-crystal sample.
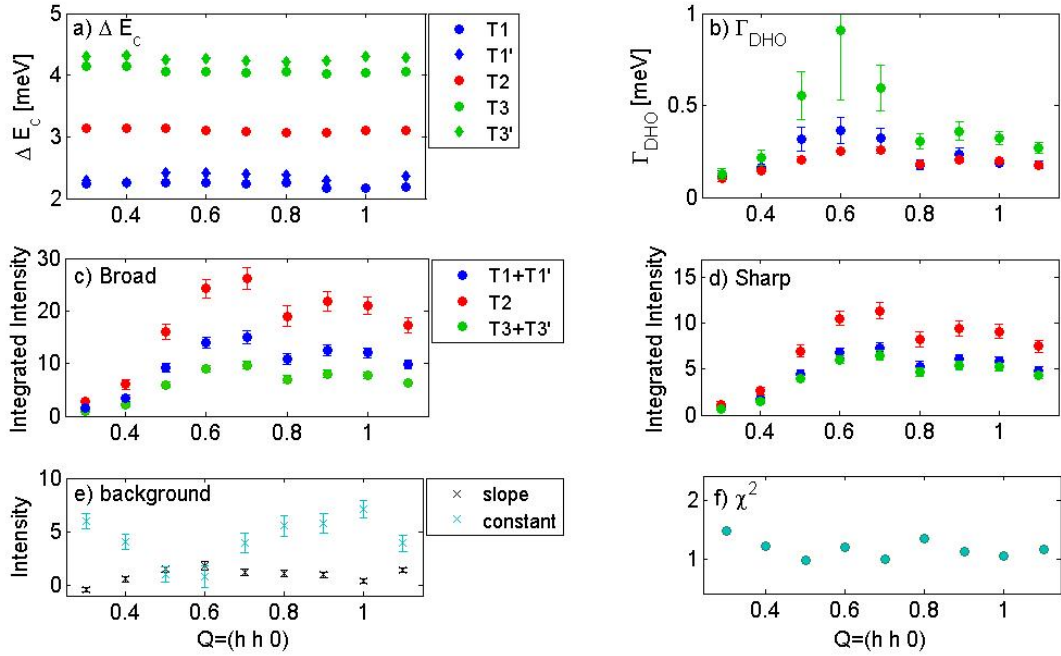
Figure 2.18: Results of DHO fits along ($h\ h\ 0$) at 6.3K. a) Energy centers of the five modes. b)Finite Γ damping width for the upper (green), middle (red) and lower (blue) triplet modes. c)Integrated intensity of the broad DHO modes with finite Γ. d) Integrated intensity of the sharp $\Gamma = 0$ resolution-limited modes. e)Parameters of the sloped background. f) Estimated goodness of fit χ^2.

In [51], a temperature dependence on the energy centers of the modes was observed with a shift of $\delta\omega$ ~ 0.05 meV between 2K and 7.3 K, both at zero field and 8T field for the three Q points measured. This is coherent with the results obtained in this study at 7.3K and no applied field (section 2.3.2) with an energy shift $\delta\omega$ for the lower, center and upper mode of respectively 0.044 ± 0.02, 0.042 ± 0.02 and 0.042 ± 0.03 meV, with no particular Q-dependence observed.

At 8T, the results obtained from the fits as a function of Q, shown in figure 2.19, show on the contrary that the energy shift is different between the upper, center and lower modes, although it still does not have any particular Q-dependence. For the lowest triplet mode (composed of two weakly split mode as described previously), the average shift of the energy center between 2K and 6.3K is 0.043 ± 0.01 meV. For the center mode, the average shift is smaller with $\sim 0.017 \pm 0.01$ meV while for the upper mode the average shift is very close to zero $\sim 0.005 \pm 0.1$ meV.
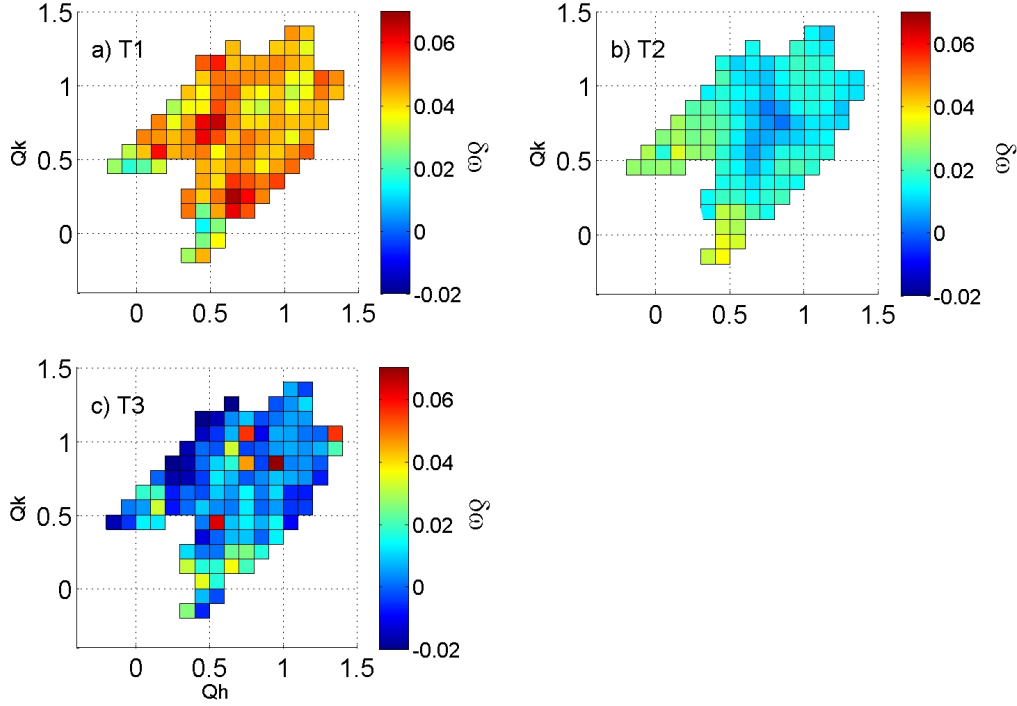
Figure 2.19: Q-dependence of the energy center shift $\delta\omega$ for each singlet-triplet mode obtained from fits of the 8T LET data at 6.3K. a) $\delta\omega$ for the lower mode T1. b)$\delta\omega$ for the center mode T2. c)$\delta\omega$ for the upper mode T3.

Figure 2.20 shows the Q-dependence of the finite Γ_{DHO} damping width obtained from the fits of the 8T LET data for each singlet-triplet mode. Three main observations can be made from these results:

- I) The Q-dependence of the DHO damping width appears to have the same overall behaviour for each of the triplet.
- II) The DHO damping width is larger around Q=(0.5 0.5 0) and roughly equal elsewhere for each of the singlet-triplet mode.
- III) The DHO damping width of the upper singlet-triplet mode is on average almost double the average widths of the two others modes. The latter have damping widths comparable to the 0T results. Table 2.2 shows the average damping width obtained for each singlet-triplet excitation.
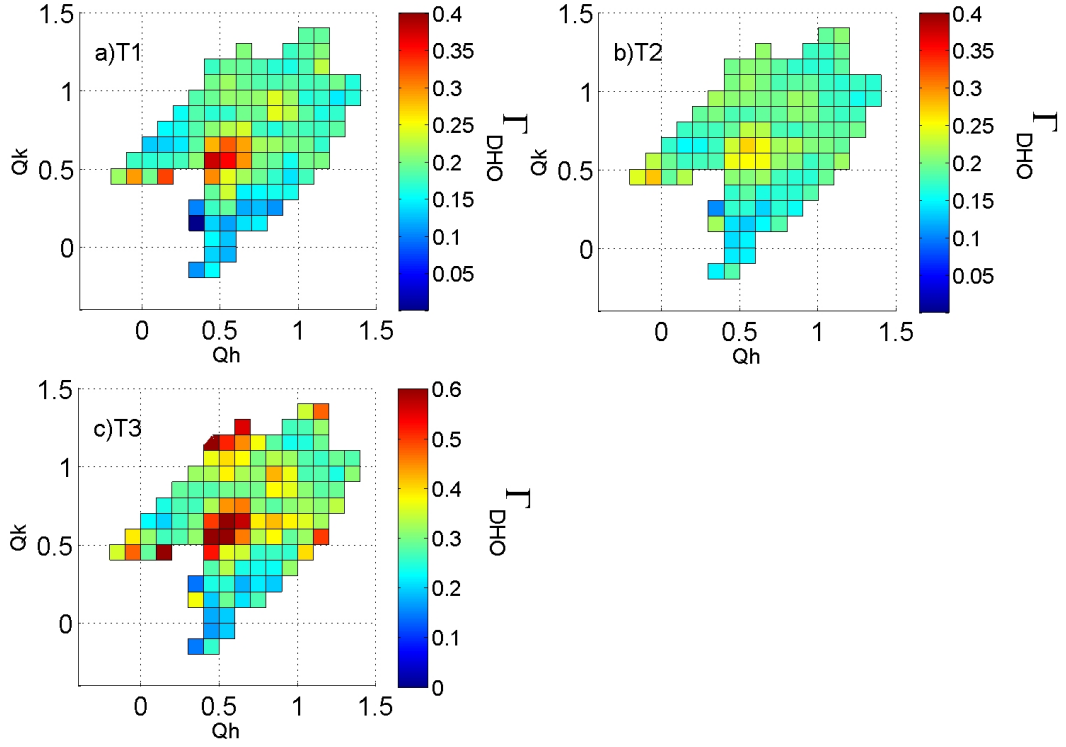
Figure 2.20: Q dependence of the Γ_{DHO} width for each singlet-triplet mode obtained from fits of the 8T LET data at 6.3K. a)DHO Damping width of the lowest mode T1. b) DHO Damping width of the center mode T2. c) DHO Damping width of the higher mode T3.

Table 2.2: Average Γ_{DHO} from both the 0T and 8T results. Only one Γ_{DHO} width is obtained at 0T as each triplet damping width is correlated. At 8T, the damping width of T1 and T1' (and T3 and T3') are correlated, so that three damping widths are obtained in total.

Average Γ_{DHO} [meV]	T1	T2	T3
8T	0.192 ± 0.02	0.194 ± 0.03	0.332 ± 0.05
0T	0.198 ± 0.08		

2.3.4 Discussion

I) Similar overall Q-dependent damping between the singlet-triplet modes   Each triplet appears to damp in qualitatively the same way, so that there is probably no particular distribution of each thermally excited triplet mode in real space. This confirms that the simple real space picture is overall correct even when taking Dzyaloshinskii-Moriya interaction into account, and that the DHO damping widths of each singlet-triplet mode can probably be correlated when no field is applied.

II) Faster Damping around (π, π) point Figure 2.21 show the data and fits at $Q = (0.5\ 0.5\ 0)$ where the Γ_{DHO} width is larger compared to another Q point $(0.75\ 0.5\ 0)$. Figure 2.22 shows the damping of the center peak at $Q = (0.6\ 0.6\ 0)$ which corresponds to the maximum Γ_{DHO} width obtained, compared to another Q point $(0.6\ 0.1\ 0)$. The Q-dependent effect is small, but it is consistent for the whole analysis. The effect is visually easier to observe in the centre peak as there is not splitting of the upper and lower modes into the weakly dispersive T1,T1' and T3 and T3'.
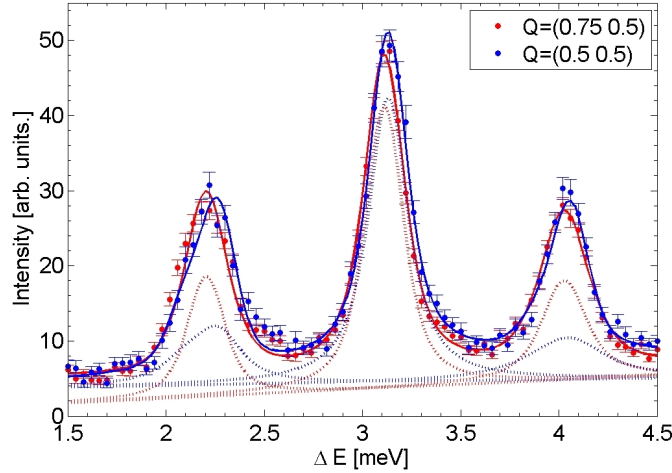
Figure 2.21: One dimensional cuts for $Q = (0.5\ 0.5)$ (blue circles) and $(0.75\ 0.5)$ with dQ= 0.175 at 6.3K. The red and blue lines show the fit result for the five modes with both the broad and sharp component. Red and blue dashed lines show only the broad component of the fitted five modes. The DHO width Γ_{DHO} is estimated to 0.14, 0.15 and 0.20 for $Q = (0.75\ 0.5)$ and 0.26, 0.29 and 0.41 for $Q = (0.5\ 0.5)$ for respectively T1, T2 and T3.
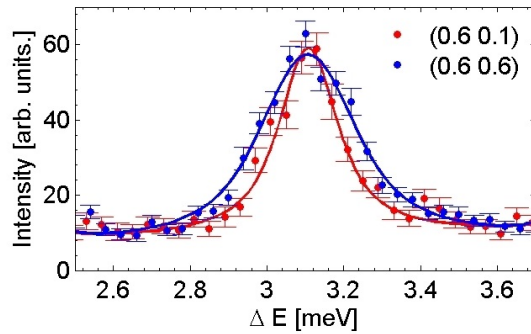
Figure 2.22: Center mode at 8T and 6.3K with fits, comparing two Q points : $(0.6\ 0.6\ 0)$, which shows the maximum DHO damping width Γ_{DHO}=0.27, and $(0.6\ 0.1\ 0)$, with Γ_{DHO}=0.17 meV.

A neutron-excited triplet is thus shown to be more likely to damp close to the Brillouin zone boundary (π, π) than in the other regions of Q-space, with fastest damping at $Q = (0.6\ 0.6)$. No theory currently explain this surprising behaviour, but it is an interesting effect of temperature and field in SCBO.

III) Faster Damping of the upper singlet-triplet mode T3   For the upper triplet T3, the n=2 bound magnon mode is in very close proximity (centered at 4.86 meV, as shown in 2.4.1). However, as shown by figure 2.23, the two modes appear sufficiently separated, such that the fitted damping line-width for T3 should not be affected. In [71], numerical results for the dynamical structure factor for a two-leg spin ladder system were obtained as a function of temperature and frustration. As a function of temperature, multi-magnon bound states lying at low energy transfers were shown to be increasingly populated, concomitant with the reduction of intensity of the triplon. This effect was expected to be strong close to a quantum critical point. This interpretation was extended to the Shastry-Sutherland model for α close to the phase transition, and can be relevant for SCBO. No low-lying bound-magnon modes were observed as temperature increased in SCBO in these measurements, and the bound magnon modes are still present at 6.3K with similar energy transfers compared to 2K. The exchange parameters of SCBO at this applied field may thus not be close enough a phase transition for this model to be applied in order to explain the temperature damping of the singlet-triplet modes.
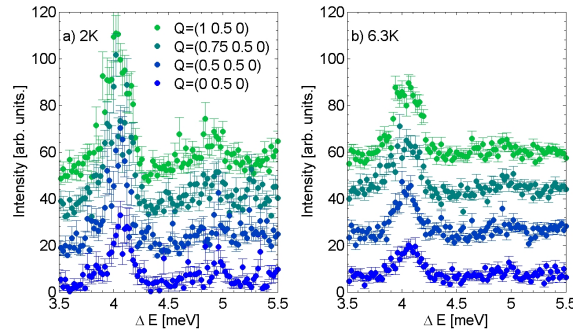
Figure 2.23: Energy cut at different Q points showing the energy range of the expected bound magnon modes at a)2K and b)6.3K.

A significant difference between the 0T and the 8T case is the damping of the upper triplet. When no field is applied, the upper triplet does not appear to damp faster than the other two modes, while it is clearly the case at 8T. A possible simple and phenomenological explanation for the faster damping of the upper triplet in field could be that it is due to the thermal population of each mode at 6.3K in field. Indeed, a fast damping could take place when a neutron-excited triplet with $S^z = \pm 1$ annihilates with a thermally excited triplet with $S^z = \mp 1$ giving a total $S^z = 0$. At 6.3K and 8T field, the population of thermally excited triplet is not equally distributed between the upper and lower modes, as they are separated by ~ 2 meV. The neutron-excited triplon of the upper mode is thus more likely to be in the polarised radius of an thermally excited triplet of the lower mode, and so it would decays faster. On average, the upper mode thus decays faster because such a triplet is more likely to appear in proximity to a thermally excited triplet of the lowest mode. At zero applied field, all the triplets are very close in energy transfer, with ~ 0.2 meV between the upper and lower modes, and thus this effect would be negligible.

Finally, it is interesting to discuss the shift of the energy centers $d\omega$ in this context. The shift is largest for the lower modes with $d\omega = 0.043$ meV. This value is similar to the value of the global energy shift obtained at 0T field for the three triplets fitted with interdependent parameters. For the center mode, $d\omega$ is reduced by a factor 2 (0.017 meV) at 8T, and it becomes nearly zero for the upper modes (0.005 meV). Figures 2.22.a-b illustrate visually this behaviour, which appears to be consistent with the thermal distribution of each mode at 6.3K and 8T. Indeed, one can imagine a real-space picture where the polarisation of space around a thermally excited triplet leads to the increase of the energy needed to excite another triplon with the same S^z value. The renormalisation of the excitation energy would thus depend on the thermal population of the triplets, with the largest energy shift for the most thermally populated lower modes.

In conclusion, the obtained Q-dependence of the damping width Γ_{DHO} strengthens the real-space correlated-decay model, with each excited triplet appearing to be equivalently distributed in space, but with different thermal population distributions due to the difference in energy of the $S^z = \pm 1$ and $S^z = 0$ modes in an applied field of 8T.

2.4 Bound magnon excitations

Beyond the energy of the localised singlet-triplet modes, multi-magnon excitations are present, with the two bound magnons mode appearing at $\Delta E \sim 5$ meV. The localised and dispersion-less behaviour of the singlet-triplet modes is explained by the conservation of parity due to the symmetry of the Hamiltonian, as the hopping of a triplet is only allowed through forming a closed path of triplets. The singlet-triplet excitations hops to the next-nearest neighbour dimer in the sixth order ot the perturbation, following the hopping process shown in figure 2.24.
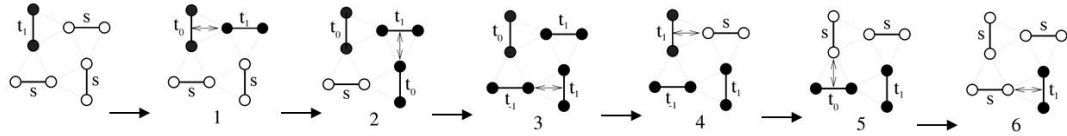

Figure 2.24: Lowest-order hopping process for a singlet-triplet excitation to the next-nearest neighbour. $|t_m\rangle$ represents an $S^z = m$ triplet state and $|s\rangle$ is a singlet. Figure reformatted from topical review [47].

This constraint was thought to be lifted for bound magnons due to correlated hopping defined as non-trivial two-particle hopping, shown experimentally by neutron scattering [44] and expected to lead to a continuum of excitations. However, with the increase of resolution of inelastic time-of-flight spectrometers, the bound magnon mode (n=2) was later shown to have also a fairly dispersion-less behaviour [62, 52], which was attributed to repulsive interaction between two triplet excitations. The question is then whether there is correlated hopping allowing dispersion in higher order bound magnon modes leading to a continuum of magnetic excitations or if the excitations are localized bound states of multiple triplets.

In order to investigate the multi-magnon excitations, two experiments were carried on time-of-flight spectrometers at ISIS, with either cold neutrons to reach the lowest bound magnon modes on LET and thermal neutrons on Merlin to give an upper bound to the magnons excitations.

2.4.1 n=2-4 bound states

To investigate the lower bound magnons modes, an experiment was performed on the cold direct time-of-flight instrument LET at ISIS using the multi-crystal mount with (110) and (001) in the horizontal plane. As discussed in 2.2, SCBO is properly two-dimensional with negligible effect of the interlayer coupling on the magnetic excitations. Hence the experiment was carried out with $\mathbf{k}_i // \mathbf{c}$ and the data could be integrated over the accessed Ql range. The dimension of the dataset is thus reduced from four dimensions with $Q = (Qh, Qk, Ql)$ and $\hbar\omega$ to three dimensions $Q = (Qh, Qk)$ and $\hbar\omega$. The incident energies were $E_i = 12$ meV and 17 meV with a resolution of respectively 0.27 meV and 0.45 meV at the elastic line. The sample was measured at 1.5K and the datasets were normalised by vanadium measurements in order to

obtain comparable intensities between the two incident energies.

Figure 2.25 shows energy slices along two different **Q** directions $Q = (hh0)$ and $Q = (h\bar{1}0)$ at 1.8K. Both Q-directions clearly show flat and dispersion-less modes at $\Delta E =\sim 4.8, 5.6$ and 6.5 meV, so that the behaviour of the multiple triplet modes appears to be composed of discrete excitations, still possibly ending in a continuum of degenerate excitations above $\Delta E \sim 7$ meV. The singlet-triplet mode at 3.1 meV is also shown for reference (with saturated intensity, as it has a much larger intensity compared to the bound magnons modes). The observed Q-dependent intensity below 3 meV corresponds to background only, with some spurious events from the tail of the elastic line which have no impact on the magnetic scattering.
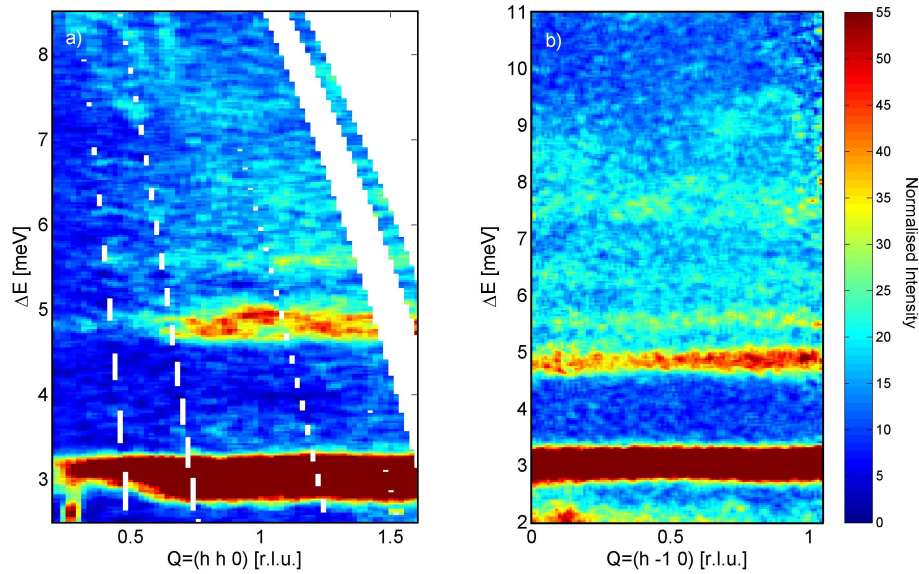
Figure 2.25: Energy slices at 1.8K for Q along $(hh0)$ and $(h\bar{1}0)$ showing discrete excitations with dispersion-less behaviour. a) LET data for E$_i$ = 12 meV integrated along Ql and binning $dE = 0.024$ and $dQ = 0.02$. b) LET data for E$_i$ = 17 meV integrated along Ql and binning $dE = 0.034$ and $dQ = 0.01$.

Furthermore, the energy slices of figure 2.25 show an unusual magnetic structure factor dependence on $|Q|$, beyond a simple magnetic form factor-like behaviour. In particular, at $Q = (0.5\ 0.5\ 0)$, the intensity is very weak compared to higher Q points. Triple axis spectroscopy at 1.5K and 1.5K for $Q = (110)$ showed that the n=1-4 modes are indeed magnetic, as they are already strongly damped at 15K. A simple model of pairs of isolated dimers in an orthogonal geometry cannot explain such a structure factor.

The equivalent Q points measured allow the mirror symmetrization of the data with respect to [0 1 0],[1 0 0] and [1 1 0], which reduces the dataset to the triangle shown in figure 2.28.b and improves statistics.
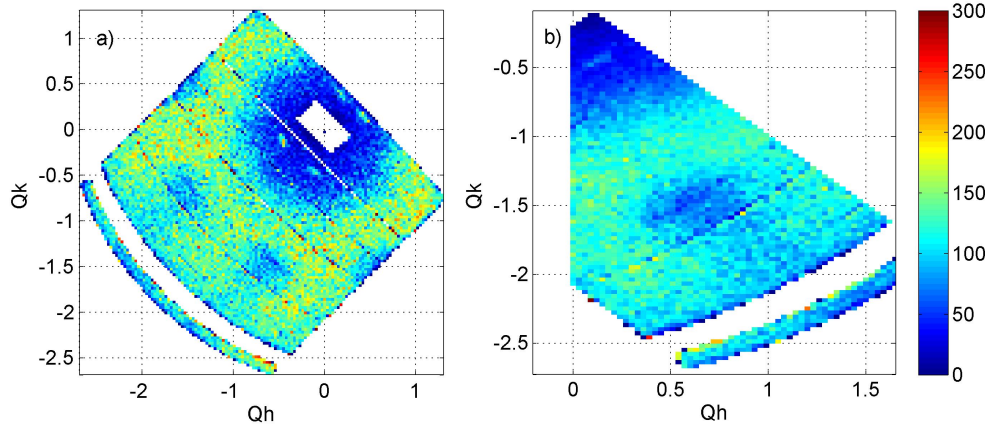
Figure 2.26: a) Constant-energy map from the LET Ql-integrated dataset as a function of Qh and Qk with energy integration over the singlet-triplet mode : [2.8,3.1] meV.
b) Reduced dataset after applying mirror symmetry over [0 1 0],[1 0 0] and [1 1 0].

To obtain the magnetic structure factor and quantitative values for the weakly dispersive multi-magnon modes, the reduced dataset for E_i=12 and 17 meV was binned into $Qh-Qk$ squares. The scattered intensity as a function of energy transfer for each (Qh,Qk) pair (Ql-integrated) were extracted and the excitations were then fitted with simple Gaussian functions (and a constant background). From these fits, the energy centers ΔE_c, the amplitude and the Gaussian widths of the measured multi-magnons modes could be obtained.

For reference, figure 2.27 shows an example of the typical reduced and normalised dataset used for the fits at the Q =(0.5 -1 0) for both E_i of 12 and 17 meV.

Figure 2.27: Normalised intensity as a function of energy transfer ΔE for Q = (0.5 -1 0) from the Ql-integrated, reduced and normalised dataset with a) E_i=12 meV and b) E_i=17 meV.

Figure 2.28 shows the $Qh - Qk$ maps of ΔE_c from which quantitative values of the weakly dispersive multi-magnons modes are obtained and shown in Table 2.3. The two bound-magnons mode is confirmed not to have any observable dispersive behaviour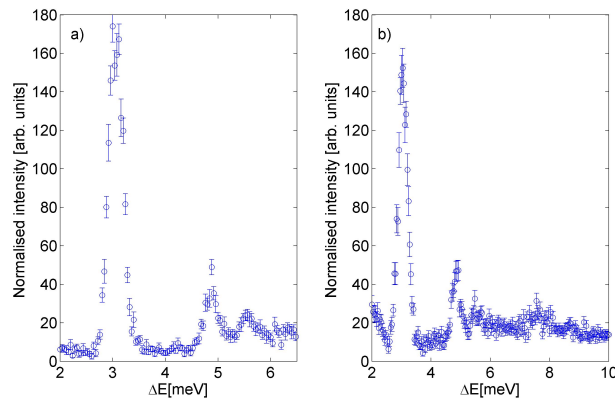, with an energy bandwidth of 0.17 meV, while the higher order bound magnons mode have slightly more dispersive behaviour, with 0.36 and 0.66 meV bandwidth for respectively n=3 and n=4.

Nevertheless, although the dispersion is weak, there is a Q-dependent dispersion of the modes leading to a broadening of the bandwidth. In particular, the n=2 bound magnon mode shown in Figure 2.28.a is clearly at higher energy transfers around Q=(0.25,-0.75) and Q=(0.5,-1.5). Given the instrumental resolution, it cannot be excluded that each of these nearly flat modes have an internal structure and dispersion that cannot be resolved with this energy resolution. In addition, the broadening of the bandwidth as the energy is increased is in favour of some correlated hopping allowed for the higher order bound modes.
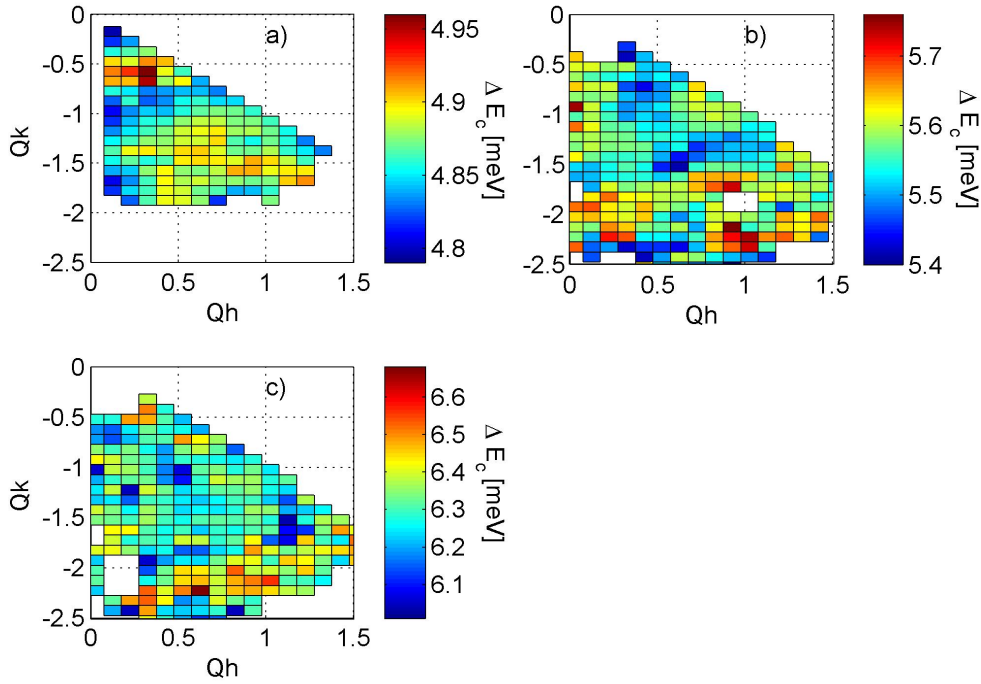
Figure 2.28: Energy center ΔE_c of SCBO multi- magnon modes n=2-4 from fits of LET Ql-integrated reduced dataset showing the weak dispersion of the mutli-magnon modes

Table 2.3: Dispersion of SCBO multi-magnons modes n=2-4 from Gaussian fits of constant-Q cuts from LET data

	n=2	n=3	n=4
Energy center [meV]	4.86 ± 0.02	5.57 ± 0.04	6.31 ± 0.07
Energy Bandwith [meV]	0.17	0.36	0.66

The weak dispersion of the n=2 bound magon state had been shown using the method of perturbative continuous unitary transformations [62], which contrasts with exact diagonalization calculations. This perturbative method, starting from a Heisenberg Hamiltonian with intra and inter dimer couplings, allows to obtain a continuous distribution of the excitation spectra. In [62], the weakly dispersive bound magnon mode was understood by level repulsion, linked to the small kinetic energy of the singlet-triplet mode. The individual bound states are thus expected to be flat due to their energetic repulsion. Figure shows the comparison between the LET dataset obtained in this experiment and the calculated spectral weight using perturbative analysis of an effective Hamiltonian in [62].
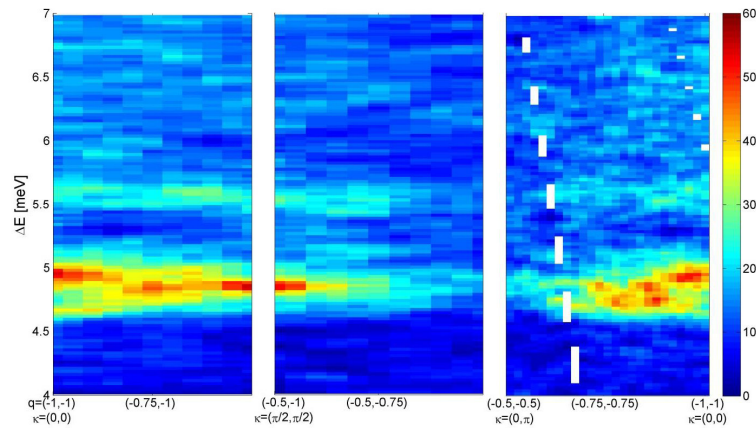
(a) Normalised LET dataset along the high symmetry directions and $E_i = 12$ meV
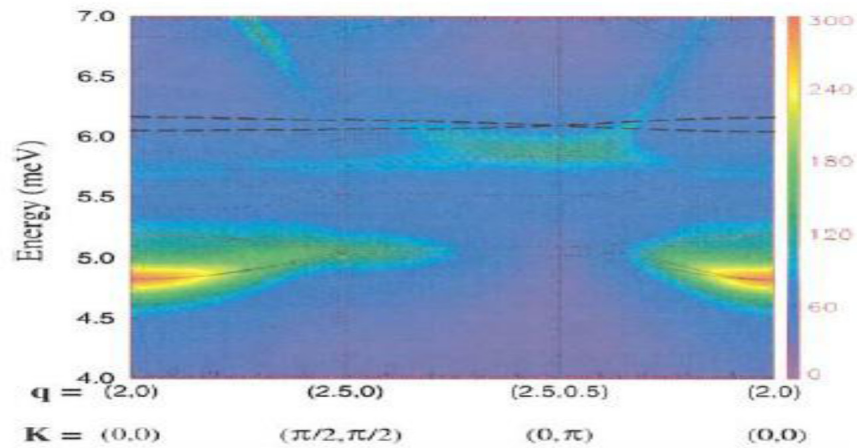
(b) Calculated spectral weightby perturbative unitary transformation of an effective Hamiltonian, figure from [62]

Figure 2.29: Comparing calculated spectral weight using perturbative unitary transformation of an effective Hamiltonian and the normalised LET dataset.

The agreement of the dispersion for the n=2 bound magnon is good but the discrete higher order magnons seen experimentally are not present in the numerical results. The spectral weight is similarly distributed overall but does not completely match the experimental data. Nevertheless, level repulsion appears as a coherent hypothesis for the n=2 bound magnon mode. The Hamiltonian used in [62] did not include the Dzyaloshinskii-Moriya interaction, so that anisotropies must have a significant effect on bound magnon beyond n=2.

To go further, the amplitude obtained from each Gaussian fit of the magnetic excitations can be linked to the Q-dependent magnetic structure factor, with the magnetic form factor squared included. Figure 2.30 shows the $Qh - Qk$ maps of the amplitude of the n=1-4 magnon modes, unfolded from the reduced dataset of fig 2.26.b.

Figure 2.30: Amplitude of SCBO multi- magnon modes n=1-4 from fits of LET Ql-integrated reduced dataset unfolded shown as a function of Qh and Qk.
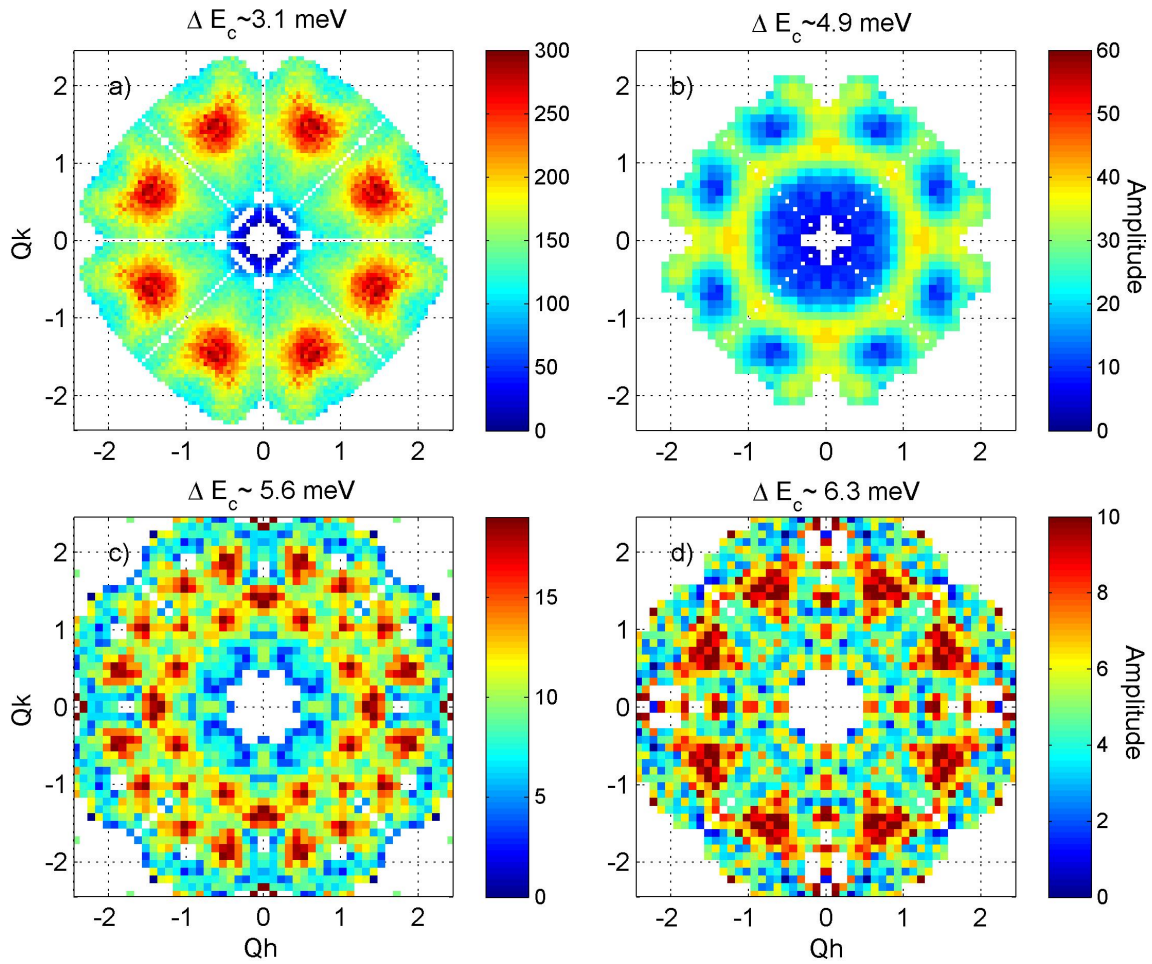
The magnetic structure factor is thus shown to have a strong $Qh - Qk$ dependence which goes much beyond a simple model of orthogonally arranged isolated dimers. Note that for the

singlet-triplet mode n=1 (Fig. 2.30.a), the Dzyaloshinskii-Moriya splitting into three modes has been ignored and that the resulting structure factor is averaged over the $S^z = -1, 0, 1$ singlet-triplet modes.

2.4.2 Upper bound on multi-magnon excitations

The excitation spectra obtained on LET hints towards an extension of the multi-magnons towards higher energy transfers, and the energy transfer range accessible on cold time-of-flight spectrometers was thus not sufficient to map the full extent of the magnetic excitations. In order to place an upper bound on the multi-magnon excitations, the excitation spectrum was measured on the thermal time-of-flight instrument Merlin at ISIS, using both E_i=35 meV and $E_i = 70$ meV at 2K. The multi-crystal sample mount was measured with $\mathbf{k}_i//\mathbf{c}$ and the data was Ql-integrated.

For E_i=35 meV, an asymmetrical background in $|Q|$ was observed in the raw dataset. Hence an empty sample holder was measured as a function of $|Q|$ and subtracted from the data. A background-subtracted energy slice is shown in figure 2.31.a along Q=(h -0.5 0). The flat dispersion-less character of the multi-magnon modes is observed again, although the background subtraction did not completely remove all spurious signal between 0 and 5 meV (as shown by the saturated dark red areas). Figure 2.31.b shows the intensity as a function of Q for six constant-energy scans with $3.45 \leq \Delta E \leq 21.5$ meV and this can be linked to the structure factor along $Q = (h$ -0.5 0) of the singlet-triplet mode, shown in figure 2.30 to be peaked at $Q = (1.5$ -0.5 0).
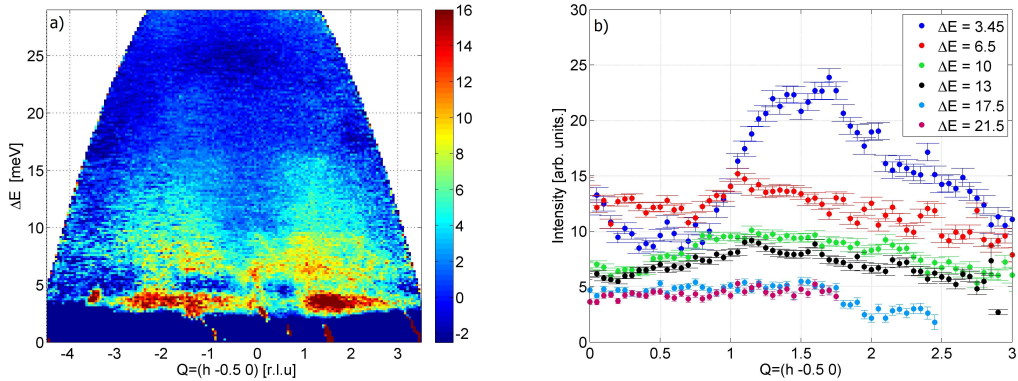
Figure 2.31: MERLIN Excitation spectra for E_i=35 meV with $Q = (h$ -0.5 0) at 2K. a) Multi-magnon excitation spectra along $Q = (h$ -0.5 0), with the background obtained from an empty measurement subtracted from the Ql-integrated dataset. b) Constant-energy cuts with $dE = 1$ meV : Intensity as a function of $Q = (h$ -0.5 0) for ΔE of 3.45 meV (blue), 6.5 meV(red), 10 meV(green), 13 meV (black), 17.5 meV(light blue) and 21.5 meV (magenta).

Overall, the structure factor for the energy transfers of 6.5, 10, 13 , 17.5 and 21.5 meV shows a

similar behaviour, with a broadly peaked profile around $Qh = 1.5$. A short measurement at 20K (not shown) was used to check that the inelastic scattering corresponded to magnetic excitations, as the magnons are completely damped above 15K.

From the $E_i = 35$ meV excitation spectra, it does not appear that the end of the multi-magnon excitations was reached, so that another measurement was carried out with E$_i$=70 meV. No background with an empty sample holder was measured in this case, so that the spectrum is dominated by a strong and broad elastic line, as shown in figure 2.33.a, corresponding to a resolution at the elastic line of 3.8 meV.

Figure 2.32.a shows the excitation spectra for $Q = (h\ h\ 0)$ while figure 2.32.b shows energy-integrated cuts along $Q = (h\ h\ 0)$. For both, at large Q, above $Q = (2.5\ 2.5\ 0)$, the spectrum appears dominated by a strong spurious background, with an intensity increasing as Q increases. Nevertheless, for the low Q data, the intensity up to the $\Delta E = 35$ meV cut seems to follow a similar broadly peaked behaviour to the E$_i$=35 meV lower energy excitations shown in figure 2.31.b. From these results, the intensity observed for Q smaller than $Q = (2.5\ 2.5\ 0)$ can be attributed to magnetic scattering.
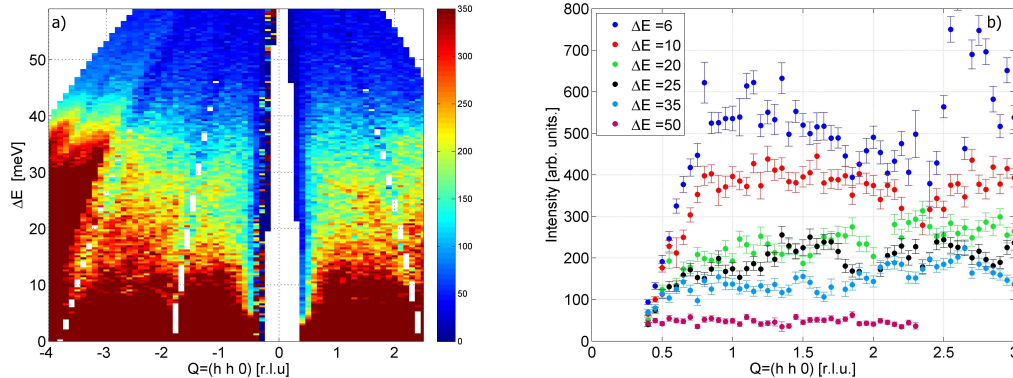
Figure 2.32: MERLIN Excitation spectra for E$_i$=70 meV with $Q = (h\ h\ 0)$ at 2K. a) Energy slice along $Q = (h\ h\ 0)$. The data has been Ql-integrated. b) Constant-energy cuts with $dE = 2$ meV: Intensity as a function of $Q = (h\ h\ 0)$ for ΔE of 6 meV (blue), 10 meV(red), 20 meV(green), 25 meV (black), 35 meV(light blue) and 50 meV (magenta).

In order to extract the multi-magnon excitations for different $Q = (h\ h\ 0)$ points, the constant-Q cuts of the E$_i$=70 meV data at the elastic line were fitted with a Lorentzian function for five Q points. Figure 2.33.a show the resulting fit for $Q = (1.5\ 1.5\ 0)$. The Lorentzian fits for each Q=(h h 0) with $0.5 \le h \le 2$ were then subtracted from the constant-Q cuts in order to obtain only the inelastic scattering, shown in figure 2.33.b.

The data of figure 2.33.b are presented with a vertical offset for each $Q = (h\ h\ 0)$ points and the black horizontal lines correspond to a constant fitted to the intensity above 50 meV, which can be identified as a background level. The magnetic intensity appears to have a slow decrease

from low to high energy transfers, reaching the level of the background around 43 ± 3 meV for each of the Q points studied.
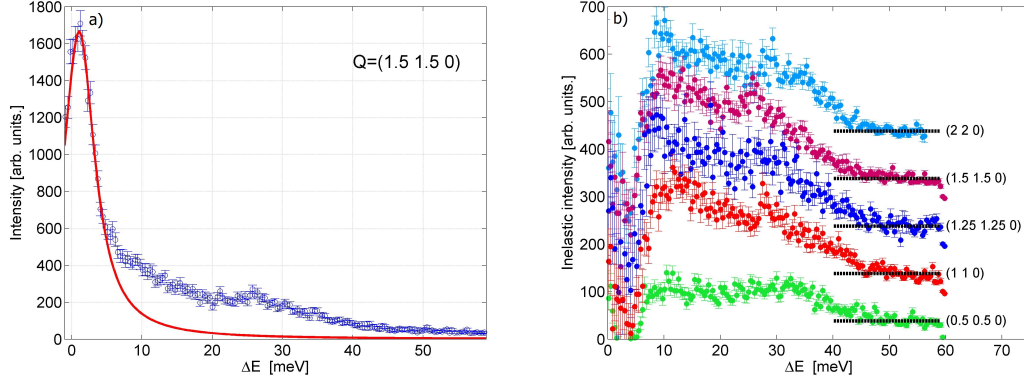
Figure 2.33: MERLIN Constant-Q cuts for E_i=70 meV at 2K. a) Intensity as a function of energy transfer ΔE for a constant-Q cut at $Q = (1.5\ 1.5\ 0)$ with $dQ = 0.2$. The red line is a Lorentzian fit of the elastic line. b) Inelastic intensity as a function of ΔE for constant-Q cuts at $Q = (h\ h\ 0)$ with $dQ = 0.2$ for $h = 0.5$ (green), $h = 1$ (red), $h = 1.25$ (dark blue), $h = 1.5$ (magenta) and $h = 2$ (light blue), shown with a vertical offset. A Lorentzian fit of the elastic has been subtracted from the data. The black lines correspond to a fit of the background intensity above 50 meV.

An estimate of the upper bound of the multi-magnon excitations is thus ∼ 43 meV, with the weak Q dependence of the intensity pointing towards very weakly dispersive discrete bound magnon modes for n larger than 4. Nevertheless, the background levels and spurious effect are strong in the $E_i = 70$ meV measurement, so that additional confirmation of the magnetic nature of the excitations would strengthen the conclusions. Indeed, the extension of the magnetic excitations to such large energy transfers (∼ 10 times the effective coupling J) is surprising. Confirming the magnetic nature of this scattering would require a technically challenging polarised neutron experiment.

In conclusion, careful characterization of the high-resolution excitation spectra obtained by inelastic neutron scattering show that the bound magnon modes n=2-4 are localised and appear as flat bands with very weak dispersion. Correlated hopping hence appears to be limited by possible level repulsion, but may nevertheless allows a dispersion of the magnon within the limited bandwidth of the bound magnon modes. Furthermore, the measured structure factor of the bound magnons modes have unusual $Qh - Qk$ dependence which cannot be explained by simple interacting bosons calculations with intra and inter-dimer coupling, and hence would require a calculation of the eigenvectors for an Hamiltonian which includes Dzyaloshinskii-Moriya interactions. Finally, the magnon excitations appear to extend well beyond the expected energy range, with magnetic scattering possibly up to $\Delta E = 43$ meV.

2.5 High pressure plaquette phase

The phase diagram of the Shastry-Sutherland model as a function of the ratio α of exchange parameters has raised a large interest. This is due partly to the proximity of a possible quantum critical point [72], and it has been studied using a combination of numerical, theoretical and experimental approaches [7, 53]. The dimer singlet phase for $\alpha \lesssim 0.7$ is well established. On the other hand, for a large intra to inter-dimer ratio ($\alpha \gtrsim 0.9$), an antiferromagnetic ordering has been observed [73, 74]. Quantum fluctuations are however thought to play a significant role, in particular regarding magnetization plateaux [75]. In between these two parameter ranges, for $0.7 \lesssim \alpha \lesssim 0.9$, a large number of possible intermediary phases have been proposed, with recent numerical results favouring a plaquette singlet phase with first order transitions between the phases [63].

In a recent work [53], an inelastic neutron scattering experiment confirmed the presence of a plaquette singlet state into the intermediary phase of SrCu$_2$(BO$_3$)$_2$ by tuning the system using hydrostatic pressure and measuring the excitation spectra with constant-Q scans for temperatures around 0.5K. Two possible plaquette phases were proposed, either a "full" plaquette with a diagonal bond, or a "void" plaquette phase.
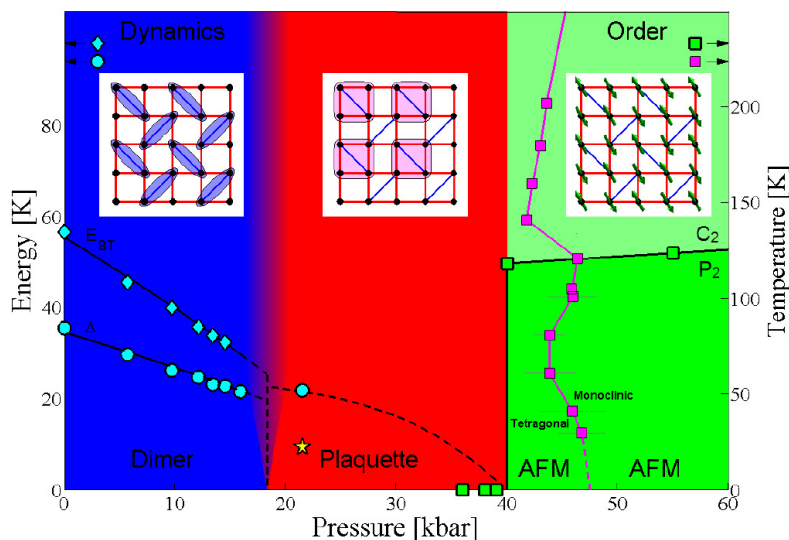
Figure 2.34: SrCu$_2$(BO$_3$)$_2$ phase diagram as a function of pressure and temperature from [53]. Also shown are the energy of the excitations as a function of applied pressure for the dimer singlet phase and the intermediary plaquette phase.

Figure 2.34 shows the phase diagram of SrCu$_2$(BO$_3$)$_2$ as a function of applied pressure and temperature proposed in [53]. The exact dimer phase remains until 16 kbar with a decrease of the spin gap from 3 mev to 2 meV as the applied pressure increases. Between 16 kbar and 20.5 kbar, SCBO was shown in [53] to enter a new intermediary phase, at which the spin gap softening appears to stop, as the gap energy remains unchanged at ~ 2 meV (labelled Δ).

In addition, a new excitation (called LE) appears at low energy transfers (around 1 meV) with a more dispersive behaviour (~ 0.4 meV bandwidth).

The 4-spin plaquette phase, expected as the new quantum phase between ~ 20 and 40kbar applied pressure, is described by the following Hamiltonian, for either a "void" or a "full" plaquette state :

$$H_{\text{void}} = J'(\vec{S}_1 \cdot \vec{S}_2 + \vec{S}_2 \cdot \vec{S}_3 + \vec{S}_3 \cdot \vec{S}_4 + \vec{S}_1 \cdot \vec{S}_4) \tag{2.12}$$

$$H_{\text{full}} = J'(\vec{S}_1 \cdot \vec{S}_2 + \vec{S}_2 \cdot \vec{S}_3 + \vec{S}_3 \cdot \vec{S}_4 + \vec{S}_1 \cdot \vec{S}_4) + J(\vec{S}_1 \cdot \vec{S}_3) \tag{2.13}$$

In the case of a "full" plaquette phase, a term $J(\vec{S}_1 \cdot \vec{S}_3)$, which corresponds to a diagonal bond between site 1 and 3, is added to the Hamiltonian of the "void" plaquette. Such isolated 4-spin plaquettes have a singlet ground state and two excitations at low energy transfers labelled $T1$ and $T2$ in [53]. The structure factor in the $Qh - Qk$ plane of these two excitations were computed in [53] for both the "full" and the "void" plaquette cases and are shown in figure 2.35.
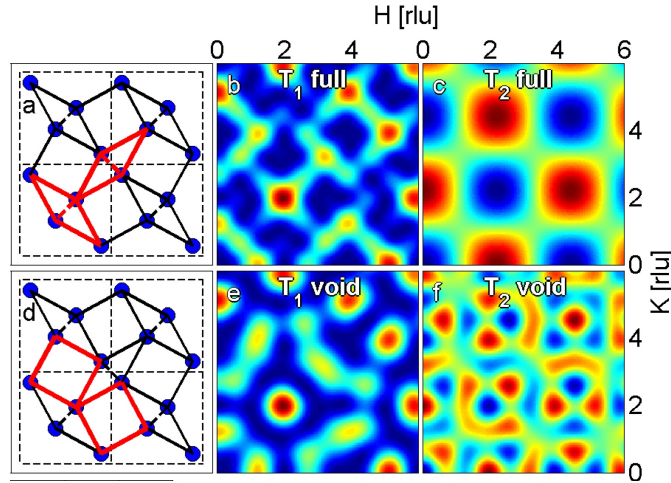
Figure 2.35: Calculated structure factor for the two plaquettes states. Figure from [53].

From the experimental results, the intensity of the excitations LE at ~ 1 meV and Δ at ~ 2 meV for the measured Q points were compared to the expected intensities from calculated structure factor. In [53], the sample was aligned with a and c in scattering plane, and although the measured structure factor slightly favoured the full plaquette phase, the evidence was only fully conclusive in confirming the presence of a plaquette phase in the intermediate α ratio.

This type of inelastic scattering experiments with high-pressure set-ups are technically challenging, and an attempt at measuring the Q-dependence of the intensity of the excitations was carried out to compare the intensity of the excitations with the calculated structure factor to identify the relevant plaquette phase for the intermediary range of α in SCBO.

The excitation spectrum in the intermediary phase was measured by inelastic neutron scattering on the thermal triple axis spectrometer ThALES at the ILL, using a McWhan pressure cell to reach an applied hydrostatic pressure of ∼ 24 kbar. The pressure set-up and calibration is described in 1.1.10. The sample was aligned with *a* and *b* in the scattering plane, and the whole pressure cell assembly was cooled to ∼ 200 mK. The optimal set-up to measure the LE excitation close to the elastic line was found to be with Graphite PG(002) monochromator and analyser, with radial collimation after the sample to improve energy resolution. Constant-Q scans were measured using $k_f = 1.5$ Å^{-1} to obtain a range of energy transfers from 0 to 3.3 meV, with typical counting times of 5 mn per point.

Figure 2.36 shows a constant-Q scan for *Q*=(2 2 0) at ∼ 24 kbar. It is clear from this scan that the intensity of the LE and Δ excitations are very weak and difficult to reliably differentiate from the background. In [53], although weak, the relative intensity of the excitation with respect to background were slightly larger. These weak intensities on the high-flux spectrometer ThaLES could be due to the instrumental difficulties, such as a very small portion of the sample being visible to neutrons.
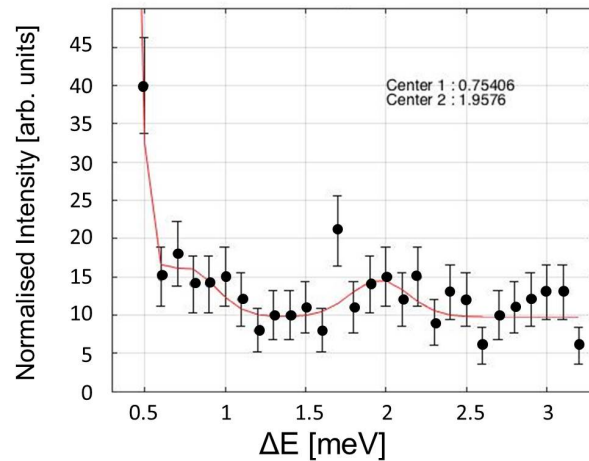
Figure 2.36: Constant-Q scan at *Q*=(2 2 0) for an applied pressure of ∼ 24 kbar and at 180 mK obtained on ThALES. The LE excitation is visible as a weak shoulder feature to the elastic line for $\Delta E = 0.75$ meV, and the Δ excitation is fitted at $\Delta E = 1.96$ meV

Overall, the excitation Δ was too weak to be reliably observed in this experiment, even at *Q* points where a maximum of the structure factor was expected in both proposed plaquette phase (such as *Q* =(020)). This could be due to the pressure cell masking the sample for certain *Q* directions, which was a known problem during this experiment (observed directly by a loss of intensity when measuring equivalent nuclear points). In addition, the Δ excitation observed in [53] was on average a factor two to three weaker than the strongest LE excitation, as shown in figure 2.37. Thus in this experiment, the Δ excitation cannot be analysed in order to extract the *Q*-dependence of the structure factor in the $Qh - Qk$ plane.
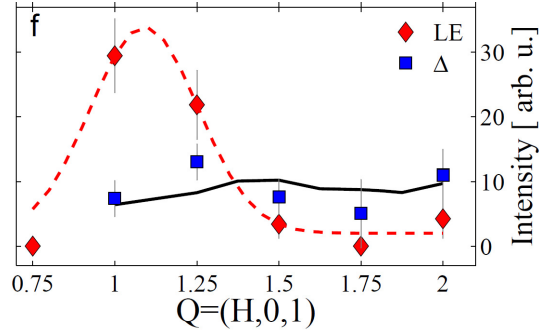
Figure 2.37: Intensity of the Δ and *LE* excitation along $Q = (h\ 0\ 1)$ from [53].

Regarding the LE excitation, a weak shoulder-like feature to the elastic line is apparent in constant-Q scans around $\Delta E = 1$ meV, and appears to be systematically above background. In particular, the direction $Q = (h\ h\ 0)$ was the least impacted by the potential masking of the sample by the pressure cell materials, and corresponds to a **Q** direction in $Qh - Qk$ space where there can be measurable differences between the magnetic structure factors. Hence the LE excitation was fitted with a Gaussian function with fixed width ($\sigma = 0.24$ meV) for a series of constant-Q scans along $Q = (h\ h\ 0)$ with $h =$0.75, 1 ,1.25, 1.5 and 2. The elastic line was also fitted with a Gaussian, with an additional constant background. In these fits, the Δ excitation was neglected, as it was found to be indistinguishable from background. The result of these fits along with the obtained energy centres and amplitude of the LE mode for these five Q points are shown in figure 2.38.
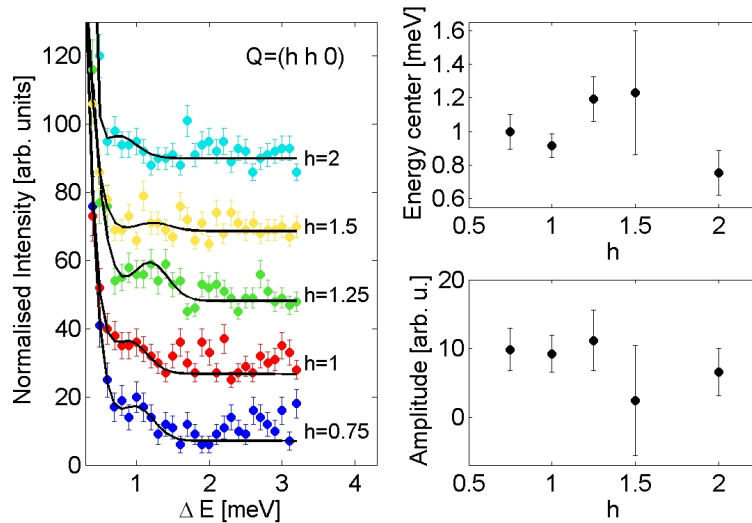
Figure 2.38: Constant-Q scans along $Q = (h\ h\ 0)$ with $h = 0.75, 1, 1.25, 1.5, 2$ [r.l.u] measured at T=180 mK. The data are shown with vertical offsets for clarity. The right panels show the obtained energy centres and amplitude of the LE excitation mode obtained from the Gaussian fits along ($h\ h$ 0).

These results should be interpreted with caution, due to the quality of the datasets. Nevertheless, the dispersive character of the LE excitation appears to be confirmed by this experiment, with a minimum of the dispersion at $Q =$(2 2 0) and a bandwidth of $\sim$ 0.5 meV. The amplitude of the modes along the $Q = (h\ h\ 0)$ direction can also be compared to the calculated structure factor from [53] shown in figure 2.35. In the case of the void plaquette, the T1 excitation would have little to no intensity along $Q = (h\ h\ 0)$, except at $Q =$(2 2 0). In the full plaquette case, the T1 intensity would be expected to be less Q-dependent along $(h\ h\ 0)$, with $Q =$(2 2 0) still remaining with the largest intensity. When comparing the inelastic neutron scattering intensities to the structure factor, it is important to note that the magnetic form factor squared should be taken into account, as it decreases as $|Q|$ increases, which could explain that no strong LE mode is seen for $h = 2$. Overall, the observed intensity around $h = 1$ is comparable to the intensity at $h = 2$, which would favour the full plaquette interpretation.

Nevertheless, these results are fairly unreliable given the technical difficulties faced in this experiment. To clearly distinguish between the two proposed plaquette phases, another attempt at measuring the excitation spectrum of SCBO while applying hydrostatic pressure would be necessary.

2.6   Dirac dispersion and topological magnons

Topological insulators are characterized by an insulating band gap and conducting gap-less edge states protected by symmetry. Hence they are insulating in the bulk but have exotic metallic phase at the surface due to topological order [76]. The quantum Hall effect is a famous example of rich physics emerging in reduced dimensionality system for a 2D gas of electrons in a large magnetic field, but it can also be observed in 3D materials due to topological effects [77]. Topological insulators have raised interest in the context of spintronics although spin transport by electrons leads to dissipation effects. On the other hand, spin waves are electrically neutral and thus have long range coherence, so that the magnon Hall effect is very promising for dispersion-less spin-based electronics. Topological phases of bosons have thus attracted interest in the context of analogues for the integer quantum hall effect, with protected edge states without dissipation. Indeed, there is a particular interest for quantum states with an insulating bulk but where magnons can be transported along edges or surfaces in materials, which are called topological magnons insulators.

The first realisation of an effectively 2D topological magnon insulator was observed in a Kagomé-lattice ferromagnet Cu[1,3-benzenedicarboxylate (bdc)] [78]. The crucial ingredient that gives rise to topological properties in magnon insulators is the Dzyaloshinskii-Moriya interaction from relativistic spin-orbit coupling, although accounting for dipolar interactions in the absence of DM interactions also led to similar topological magnonic edge mode [79]. Calculation using integer Chern numbers in bosonic Bogoluibov-deGennes systems shows the existence of a Dirac-like dispersion when the band gap closes at certain Q points. In the case of [1,3-benzenedicarboxylate (bdc)], non trivial bands were observed for out of plane Dzyaloshinskii-Moriya interaction, with Chern number of -1,0 and 1 for respectively the lowest, the center and the highest energy bands.

The Hall effect usually relies on the Lorentz force acting on a charge current. However, neutral quasi-particles (such as phonon or magnons) can carry heat current and thus can exhibit a thermal hall effect [80]. Chern bands in electronics systems are probed by doping the system to have the Fermi energy lying in the band gap, leading to a transverse electrical conductivity. In a bosonic system, instead, a temperature gradient is thought to populate the band differently at the edges. The rotational motion of the magnon is thus imbalanced, leading to a transverse triplon current carrying energy that can be measured as a thermal current. Indeed, the motion of a magnon wavepacket has a rotational motion along the edges, due to the Berry curvature corresponding to the topological structure of magnon bands, enhanced by band crossing [81]. Thermal conductivity hence comes from the edge magnon current when a temperature gradient is applied. The magnon thermal hall effect has been observed in an insulating ferromagnet $Lu_2V_2O_7$ with a pyrochlore lattice due to Dzyaloshinskii-Moriya interaction [82, 83].

As discussed in [84], the intrinsic Hall effect for magnons arises for specific lattice geometries and/or for specific underlying magnetic order. In addition, flat magnon bands hold unique

interest because the interaction energies between quasi-particles may dominate the kinetic energy, leading to novel correlated states. In this context, SCBO is a good potential system to have topological magnon effects, with Dzyaloshinskii-Moriya interactions expected to give rise to topological effects. A prediction of a Dirac-like dispersion in a critical field of ~ 1.4 T was made in [60], accompanying the creation of topologically protected edge modes, and thus possibly exhibiting a thermal Hall effect.

Previous ESR measurements [57] hinted towards the presence of a Dirac point with an observed crossing of the triplon modes around an applied field of 1.4T along (001) as shown by figure 2.39. The $S^z = 0$ mode is not visible with this technique.

(a) Magnetic excitations spectra at 1.6K   (b) Frequency-field diagram at 1.6K for **B//c**
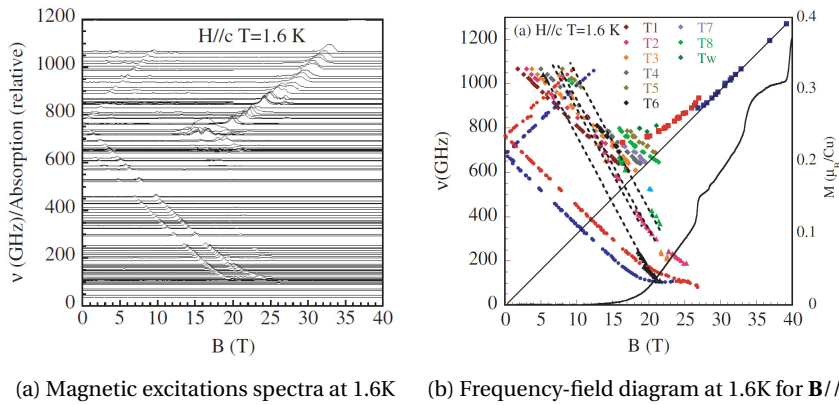
Figure 2.39: a) ESR Excitation spectra and b)ESR frequency-field diagram from [57], showing a crossing of the modes around 1.4T for **B//c**.

The estimated spin gap from ESR is 722 GHz=2.985 meV. Highest and lowest mode may deviate from a linear behaviour close to 0T. In addition, the other excitations (labeled T_i) in fig. 2.39.b appeared to be at higher energies around 1.4T, and they do start to cross the $S^z = \pm 1$ triplon excitations from ~ 5T. Far infra-red spectroscopy [85] also evidenced a crossing of the modes only in the case of a field parallel to (001), and showed a possible avoided crossing between the upper triplet with a singlet for a field of ~ 2.5T, explained by DM interaction.

In order to investigate the presence of a Dirac-like dispersion for an applied field of 1.4T in SCBO, the excitation spectra was measured using neutron inelastic scattering.

2.6.1   Experimental details and analysis method

The experimental challenge in measuring the dispersion of SCBO at the critical field to identify the presence or absence of a Dirac-crossing lies in the energy resolution needed in order to resolve the triplons. Indeed, in the absence of a field, the singlet-triplet mode is only weakly split by ~ 0.2 meV. The experiment was thus done on two cold time-of-flight spectrometers with an incident energy of $E_i = 4.2$ meV : AMATERAS, at J-Parc, Japan and IN5, at ILL using the single crystal mount with (100) and (010) in the horizontal plane.

Fields of 0.7, 1.4 and 2.1T were applied along (001) using a vertical cryo-magnet. The sample was inserted and cooled to 1.5K, and rotated about the vertical axis in order to cover a large area of reciprocal space (Horace-type scans). The area of reciprocal space accessed at $\Delta E = 3$ meV in the IN5 experiment is shown in figure 2.40 for an energy transfer of $\Delta E = 3$ meV, obtained by integrating over Ql and ± 0.05 meV. Although the datasets from the spectrometer AMATERAS are consistent with the IN5 dataset, the quality of the energy slices were not sufficient to discuss the possibility of a Dirac-like dispersion at the critical field, and thus were not used in the analysis.
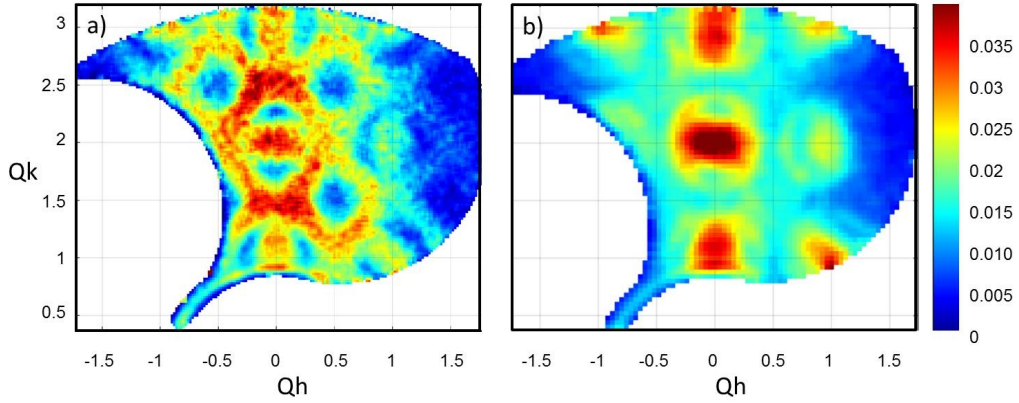
Figure 2.40: Constant-energy cuts for $\Delta E = 3$ meV integrated over ± 0.05 meV (and over Ql) on IN5 for a) 0T and b) 1.4T.

In order to interpret the observed dispersion in the inelastic spectra, the data were integrated over $Ql = [-1, 1]$, symmetrized with respect to (0 k 0) to improve statistics, and binned along the different **Q** directions shown in figure 2.41 with $dQ = 0.025$ and $dE = 0.01$ meV.
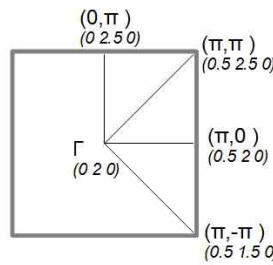
Figure 2.41: Four different **Q** directions in reciprocal space analysed from the IN5 dataset

An example of the resulting energy slice is shown in figure 2.42a for an applied field of 2.1T, and the fits were done for the one-dimensional cut obtained by integrating over Q with ± 0.05 r.l.u shown in figure 2.43. The peaks are resolution limited, so that the one-dimensional cuts with an applied field of 2.1 T were fitted with five Gaussians with identical Gaussian widths as the only constraints. The free parameters were thus: $\sigma(Q)$, $I_{1-5}(Q)$, $\omega_{1-5}(Q)$.

The intensity of the excitations (proportional to the dynamical structure factor) has no field dependence, so that I$_{1-5}$(Q) were fixed for the subsequent fits at the applied field of 1.4T (figure 2.44).

(a) Energy center ω_{1-5} for direction Γ to $(\pi, 0)$.

(b) Intensities I$_{1-5}$(Q) as a function of ζ for direction Γ to $(\pi, 0)$.

(c) Fits of energy center ω_{1-5} for direction Γ to (π, π).

(d) Intensities I$_{1-5}$(Q) as a function of ζ for direction Γ to (π, π).
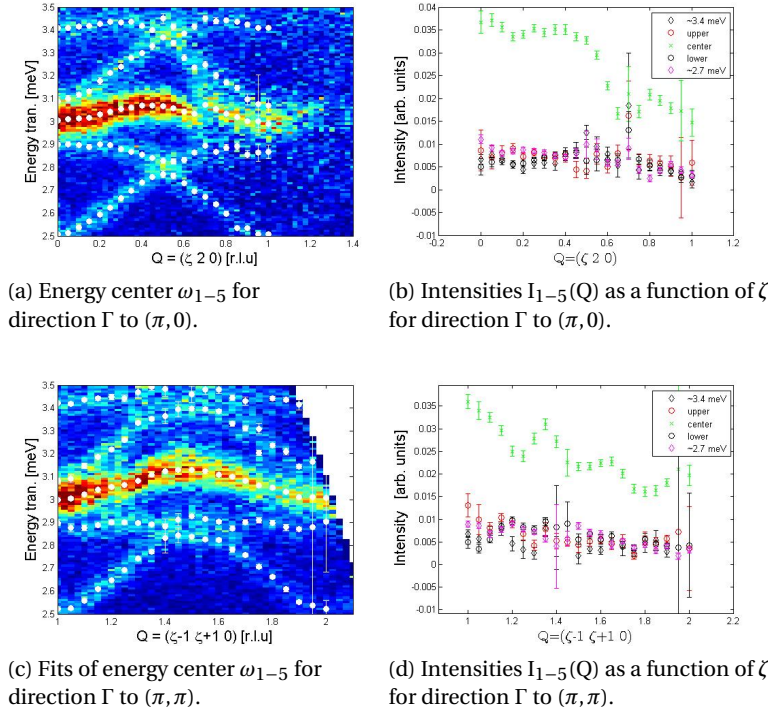
Figure 2.42: Results of fits for IN5 data for applied field 2.1T. a) and c) show energy slices along two particular directions with the fitted energy centers ω_0 of the five modes shown as white circles. b) and d) show the intensities I(Q) for each of the five modes for the same two Q directions.

Figure 2.43 shows one-dimensional cuts for $Q = (0.15\ 2\ 0)$ close to Γ and $Q = (0.75\ 2\ 0)$ at both applied field of 1.4T and 2.1T with the resulting fits (black curve). The result of the fits for the energy centers ω_{1-5} of the five modes at the critical field of 1.4T are presented in figure 2.44 for directions Γ to $(\pi, 0)$ and Γ to (π, π) both with and without the IN5 data, showing that there are only three modes apparent at the equivalent Brillouin zone centers Γ : $Q = (0\ 2\ 0)$, $(1\ 2\ 0)$ and $(1\ 3\ 0)$.

(a) Intensity as a function of energy transfer for $Q = (0.15\ 2\ 0)$ at 2.1T.

(b) Intensity as a function of energy transfer for $Q = (0.15\ 2\ 0)$ at 1.4T.

(c) Intensity as a function of energy transfer for $Q = (0.75\ 2\ 0)$ at 2.1T.

(d) Intensity as a function of energy transfer for $Q = (0.75\ 2\ 0)$ at 1.4T.
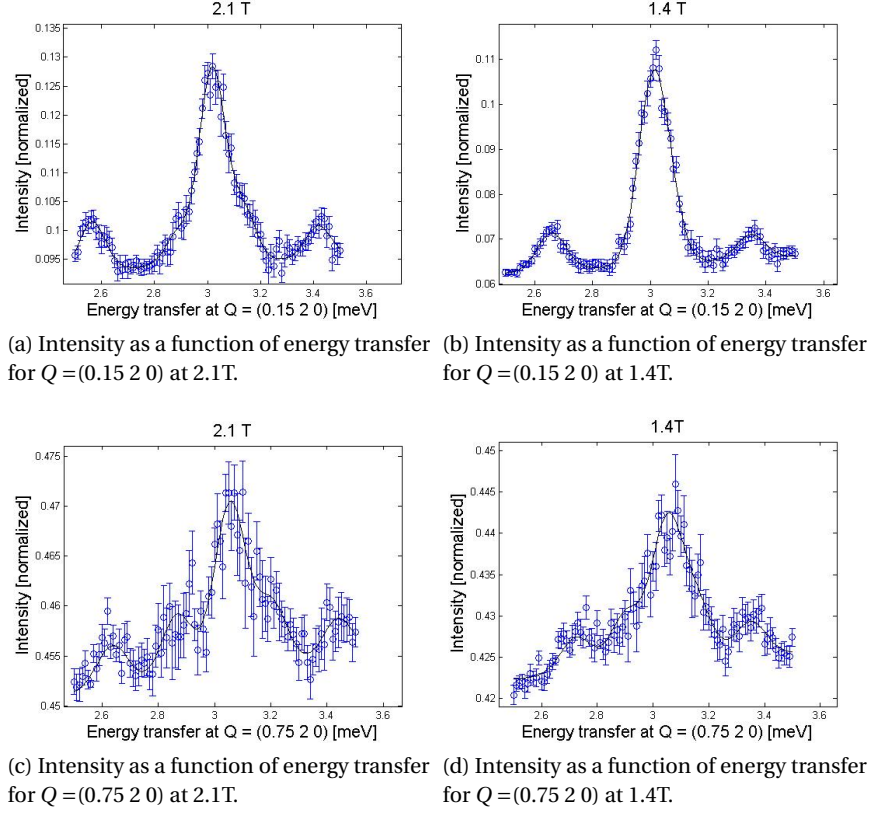
Figure 2.43: Comparing data and fits for 2.1T and 1.4T applied fields for $Q = (0.15\ 2\ 0)$ and $Q = (0.75\ 2\ 0)$.

2.6.2 Results and Discussion

The experimental results are compared with the dispersion obtained from the triplon Hamiltonian derived in [60], in which the behaviour of the triplon in momentum space corresponds to pseudo spin-1 objects coupled to a pseudomagnetic field. The Hamiltonian hopping matrix in [60] is given by :

$$M(\boldsymbol{k}) = [\Im - 2K\gamma_4(\boldsymbol{k})]\mathbf{1} + \boldsymbol{d}(\boldsymbol{k}) \cdot \boldsymbol{L} \tag{2.14}$$

with $\boldsymbol{d}(\boldsymbol{k})$ the pseudomagnetic field, $\mathbf{1}$ the 3x3 identity matrix, $\boldsymbol{L}$ a vector of 3x3 matrix and $\gamma_4(\boldsymbol{k}) = \cos(k_x)\cos(k_y)$. $\Im$ corresponds to the measured spin gap, i.e to an effective coupling constant. K corresponds to the strength of the second neighbour dimer-dimer interaction which locally shifts the triplon energies and creates a small dispersion with a Q dependence, but has no effect on topological properties (see supplementary materials of [60]). Intradimer and interdimer in-plane Dzyaloshinskii-Moriya interactions are interdependent and are taken into account with a linear combination $\tilde{D}_{\parallel}$, as detailed in 2.1.3. An out of plane inter-dimer DM interaction $D'_{\perp}$ is also included.

(a) Energy centers ω_{1-5} for direction Γ to $(\pi, 0)$ with IN5 data

(b) Energy centers ω_{1-5} for direction Γ to $(\pi, 0)$ without the data

(c) Energy centers ω_{1-5} for direction Γ to (π, π) with IN5 data

(d) Energy centers ω_{1-5} for direction Γ to (π, π) without the data
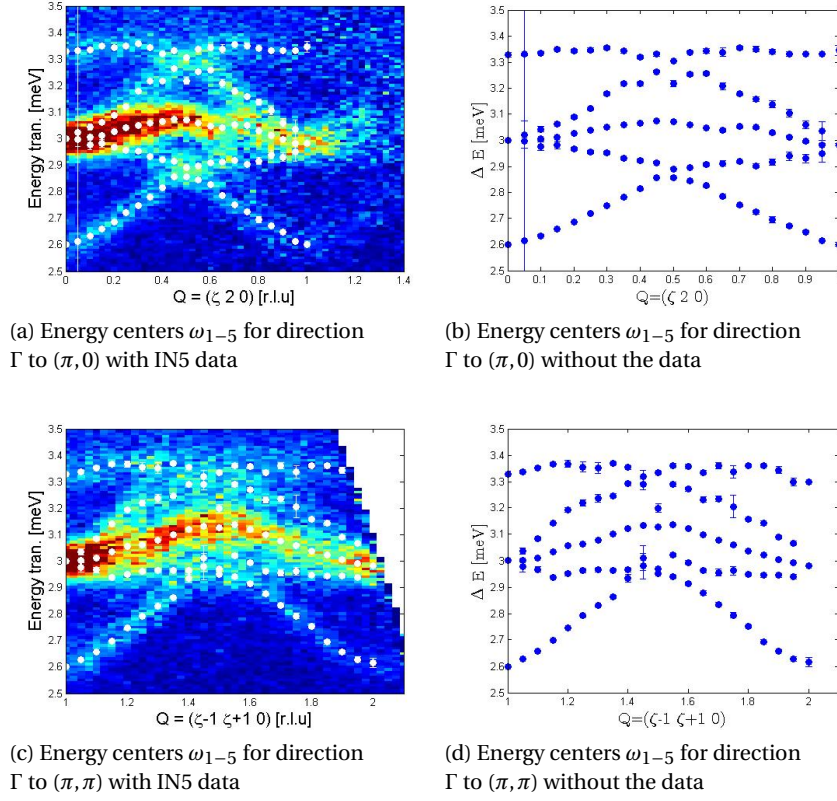
Figure 2.44: Results of fits both with and without IN5 data at the critical applied field of 1.4T

Figure 2.45 shows the triplet dispersion along the high symmetry directions Γ to (π, π) and Γ to $(\pi, 0)$. The experimental data was obtained on the cold time-of-flight instrument IN5 with the Brillouin zone center Γ measured at $Q = (0\ 2\ 0)$. The white curves correspond to the calculated eigenvalues of the hopping matrix M for $\Im = 3.075$ meV and no applied magnetic field. The parameters (in meV) are the following : $\Im = 3.075$, $K = 0.0013 \cdot \Im = 0.0384$, $dz = 0.03 \cdot \Im = 0.0922$, $dp = 0.023 \cdot \Im = 0.071$, $h_z = 0$. dz is the out of plane inter-dimer DM, and dp the hopping term $dp = dd\frac{Jp}{2J}$ with Jp the inter-dimer exchange parameter and dd the intra-dimer DM.

In SCBO, the application of a vertical magnetic field can tune the system through a topological transition. In the model described, the applied magnetic field h^z is included in the pseudomagnetic field $\boldsymbol{d}(\boldsymbol{k})$ which drives the transition. A small applied h^z opens a non-trivial bandgap with three well-separated bands. When the field reaches a threshold h_c, the three bands touch at the center of the Brillouin zone Γ, which becomes a spin-1 Dirac point and is characterised by $\boldsymbol{d}(\boldsymbol{k}) = 0$. When the field is increased further, a trivial band gap opens.

Figure 2.46 shows experimental data of the triplon bands as the field is increased to the critical field of 1.4T. The white circles correspond to the obtained energy centers ω_{1-5} from fits of
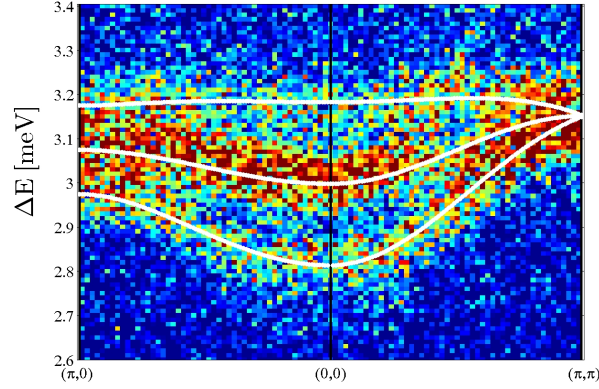
Figure 2.45: Triplon dispersion from IN5 data. White line correspond to the calculated eigenvalues of the dispersion.

the IN5 data and the red line corresponds to the calculated spin-1 Dirac cone dispersion for $h_z \cdot g_z = 0.06 \cdot \Im = 0.1845$ meV.

The two panels of figure 2.46 show two different areas of reciprocal space measured on IN5 which correspond to equivalent Γ to $(\pi, 0)$ and Γ to (π, π) directions. The eigenvalues of the dispersion for the two panels are thus equivalent, but the central modes have a different structure factor, as expected from the scattering intensities in the constant-energy slices shown in figure 2.40 at the two Brillouin zone center $Q = (0\,2\,0)$ and at $Q = (1\,2\,0)$. Figure 2.47 shows the same energy slices, calculated dispersion and fitted eigenvalues for an applied field of 2.1T, beyond the critical field, showing further separation of the triplon bands. From the results shown in figures (2.46 and 2.47), it appears that, within the resolution, the calculated dispersion matches the experimental data for the main features. In particular, in the crucial region close to the Γ point, the three modes appear to merge with a linear behaviour into the expected Dirac point at the applied field of 1.4T.

In order to see the evolution of the dispersion of the triplon as a function of an applied field along (001), figure 2.48a-d shows the experimental IN5 data with the calculated eigenvalues for applied fields of 0, 0.7, 1.4 and 2.1T.

Figure 2.49 shows the evolution of triplet excitations with applied vertical field at the Γ point $Q = (0\,2\,0)$, which clearly shows the crossing of the triplon bands at the critical field, and can be compared to electron spin resonance (ESR) measurements (figure 2.50).

Effect of Parameters at the critical field $\mathbf{h}^z$ Using the overall match between the fitted and calculated dispersions, the influence of the parameters at the critical field can be tested and understood. As previously stated, $\Im$ in this model Hamiltonian corresponds to an effective coupling which is responsible for the size of the spin gap. From the IN5 analysis, it is estimated
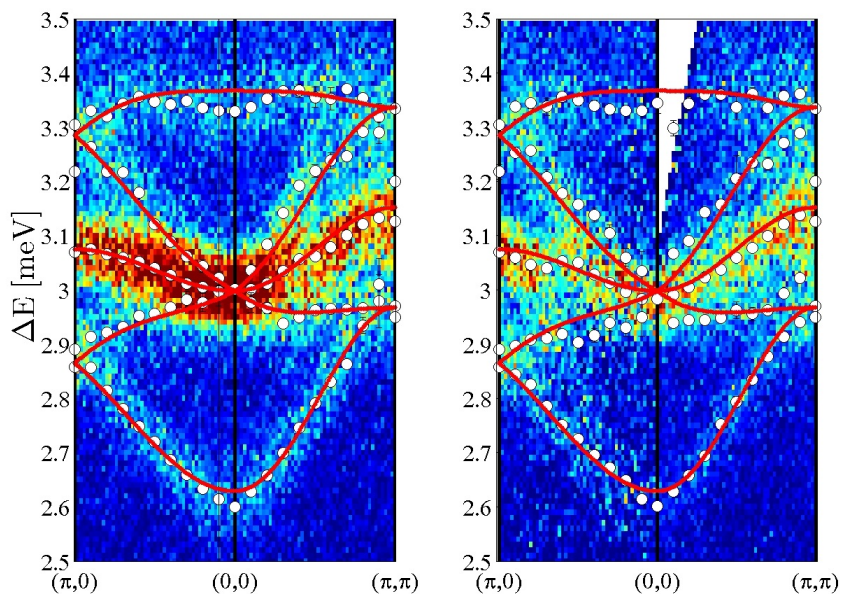
Figure 2.46: IN5 Energy slice and fits of the triplon dispersion (white circles) at the critical field of 1.4T. Red line corresponds to the calculated dispersion.
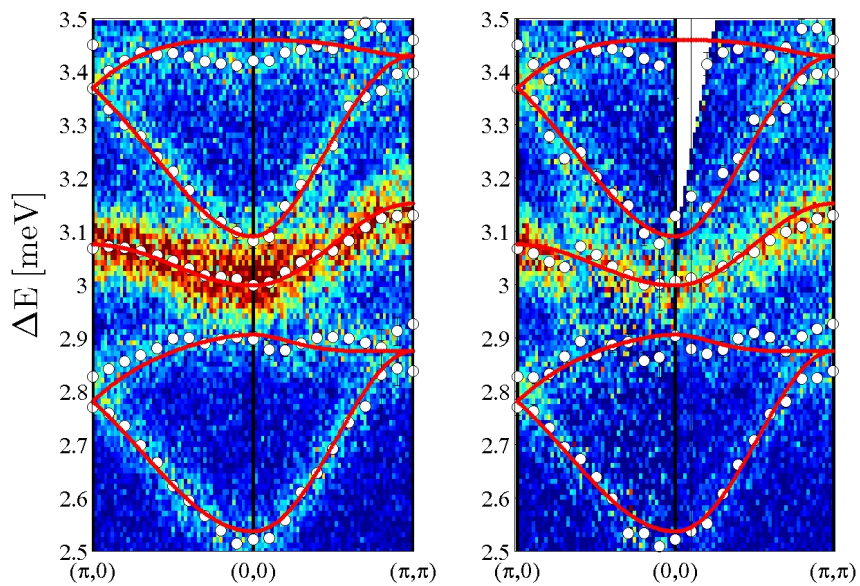
Figure 2.47: IN5 Energy slice and fits of the triplon dispersion (white circles) for an applied field of 2.1T. Red line corresponds to the calculated dispersion.
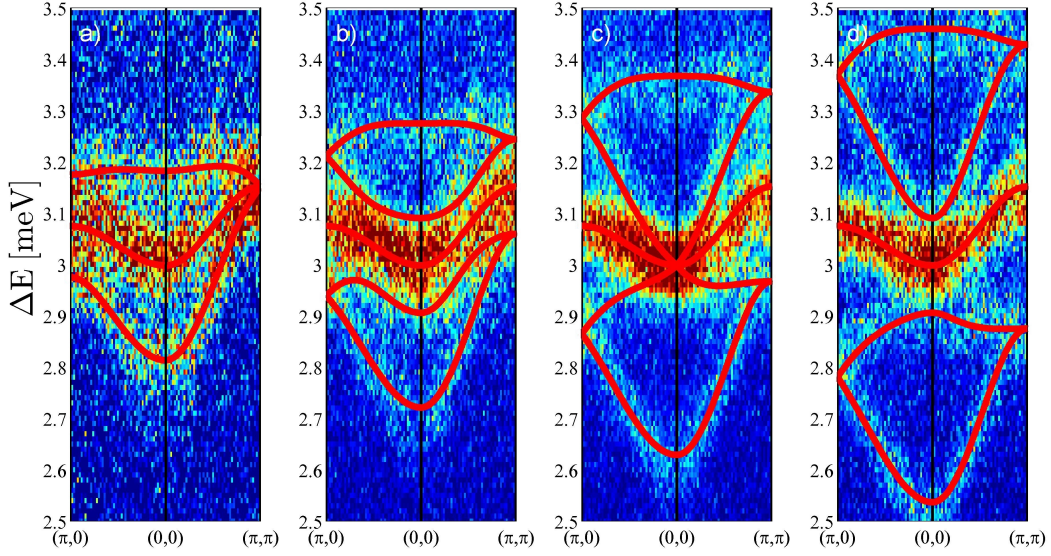
Figure 2.48: Calculated dispersion (red lines) superimposed on the IN5 excitation spectra around Γ at $Q =$(0 2 0). a) no applied field with three modes with lower and upper mode degenerate between $S^z = \pm 1$. b) At 0.7T, the degeneracy is lifted and the $S^z = \pm 1$ modes split. c) 1.4T : Critical field with Dirac crossing at the Brillouin zone center Γ. d) 2.1T : trivial band gap opens up and modes are split further.
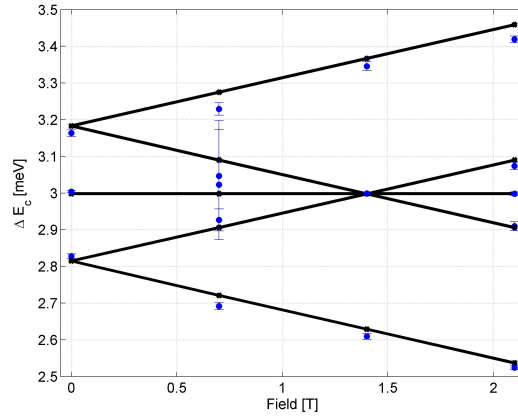
Figure 2.49: Energy centers ω_{1-5} of the triplet excitations for the 4 fields measured on IN5 at the Γ point $Q = (020)$ from Gaussian fits of the IN5 dataset (blue circles) and from the calculated eigenvalues (black lines).

in SCBO to $\Im = 3.075$ meV. K parametrizes the effect of the nearest triplon hopping. The $S^z = 0$ mode is flat if $K = 0$. This parameter is crucial in order to obtain the right calculated eigenvalues at $Q = (\pi, \pi)$ and $(\pi, 0)$ to match the experimental data, but has no impact on the presence or absence of a Dirac point.

Furthermore, the Dzyaloshinskii-Moriya interactions are crucial, as expected for topological magnon insulators[83], in order to obtain a Dirac crossing at Γ. Concerning the out-of-plane inter-dimer DM dz: if $dz = 0$, there are only three modes and no crossing of the bands, with very little dispersion. As dz is increased, the degenerate upper and lower modes split and start dispersing towards the S^z central mode. If dz increases further, the modes move again away from the central mode and there is no crossing. This parameter is very sensitive to variations and determinates the critical field as $h_c = \frac{2dz}{g_z}$. The second Dzyaloshinskii-Moriya parameter is the linear combination of the in-plane inter-dimer and intra-dimer DM, which corresponds to a hopping term dp in the effective Hamiltonian. If $dp = 0$, there is a crossing in the region of the Γ point, but it does not appear to correspond to a Dirac point, with no linear dispersion, and with possibly several band-crossing points. As dp is increased from zero, a Dirac cone starts to form. The value of this parameter can be increased well beyond the estimated value for SCBO, as there is still a Dirac crossing for $3 \cdot dp$. The eigenvalues of the dispersion are sensitive to this parameter at the $(\pi, 0)$ point, allowing its estimation from experimental data.

Differences between calculated and experimental dispersion   Although the agreement between the calculated eigenvalues for the dispersion and the data is good, there are features of the experimental dispersion that cannot be captured by the model. In particular for the lowest and uppermost mode, there is a weak dispersion of the upper band of about ∼ 0.05 meV that is not captured by the dispersion, most visible in the excitation spectra of figure 2.46 and 2.47. The largest deviation is at the Brillouin zone center Γ. Figure 2.50 shows the discrepancies between the fits and the calculated eigenvalues from the model.

The precise differences between the calculated eigenvalues and the energy centres from the fitted experimental dispersion at the Γ point $Q = (0\ 2\ 0)$ for the uppermost and lowest mode of the triplet excitation are summarized in Table 2.4. The deviations appear to increase slightly with increasing applied field.

Table 2.4: Energy center of the five modes for the 4 fields measured on IN5 at the Brillouin zone center $Q = (020)$ either calculated from the dispersion with adjusted parameters or as results of Gaussian fits of the IN5 data

Applied Field //c [T]	Calculated eigenvalues [meV]	Result of Gaussian fits [meV]
0	2.814	2.828 ± 0.006
	3.183	3.164 ± 0.010
0.7	2.721	2.692 ± 0.010
	3.275	3.229 ± 0.017
1.4	2.629	2.609 ± 0.008
	3.367	3.346 ± 0.012
2.1	2.537	2.524 ± 0.006
	3.459	3.419 ± 0.009

In addition, there are some surprising intensity variations of the triplon in the excitation
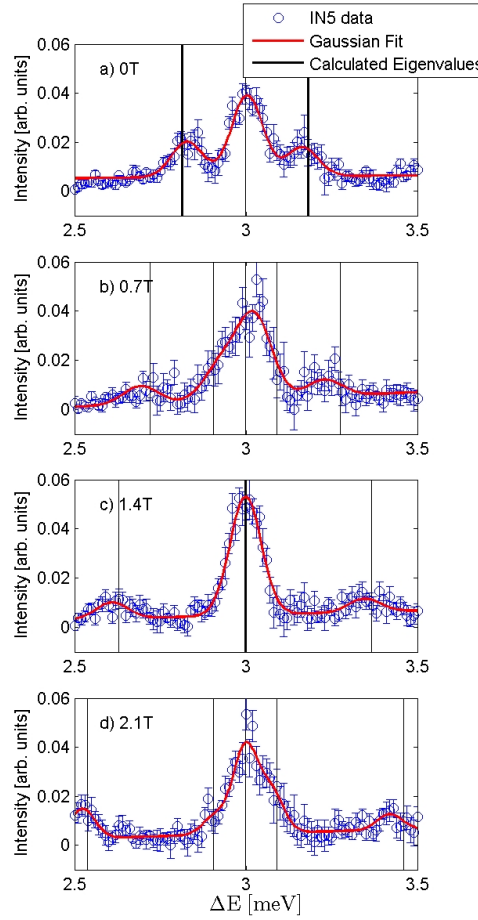
Figure 2.50: Brillouin zone center Γ corresponding to $Q = (0\ 2\ 0)$ for a) 0T, b) 0.7T, c) 1.4T, the expected critical field and d) 2.1T

spectra in applied field which cannot be explained fully by the model, visible for example in Fig 2.42b. These variations are also apparent in the raw data and do not appear to be an artefact of the measurements. In particular, for $\Delta E \sim 3.05$ meV, there is a sharp intensity drop at the following Q points : $Q = (0\ 2.32\ 0)$ and $Q = (0\ 1.68\ 0)$, which correspond to $\Gamma_{(020)} \pm (0\ 0.32\ 0)$, as well as at $Q = (\pm\ 0.67\ 2\ 0)$, which corresponds to $\Gamma_{(\pm120)} \pm (0.33\ 0\ 0)$. This hints towards an hybridization of the triplon, or an avoided crossing with another type of excitation that cannot be measured by neutron scattering, or to an excitation too weak compared to the background. Nevertheless the dispersion is well-reproduced using this set of interactions, in particular in the crucial region of the expected Dirac point.

Deviation from Dirac crossing   The exact confirmation of a Dirac point in $SrCu_2(BO_3)_2$ using neutron scattering is limited by the best resolution that can be obtained around $\Delta E = 3$ meV. It is nevertheless interesting to discuss the maximum possible deviation from a Dirac crossing. Using the ESR value of the out of plane DM interaction, the calculated critical field

$h_c = \frac{2dz}{g_z}$ is 1.316 T, so that the experimental data should show a very small gap at the Γ point due to the difference between the critical and applied field. The calculated gap for $dz = 0.867$ and h_z=0.1845 would then be ±0.016 meV.

To set an upper limit on the size of the deviation from a Dirac point, the data was fitted at the Dirac point $Q = (0\ 2\ 0)$ while fixing a deviation $\pm\delta E$ of the two modes from the energy centre of the $S^z = 0$ mode. Figure 2.51 shows the dependence of the goodness of the fit in χ^2 on the deviation δE with a minimum at δE=0.02 meV. This small deviation is coherent with the field difference between experimentally applied field and the calculated critical field for SCBO.
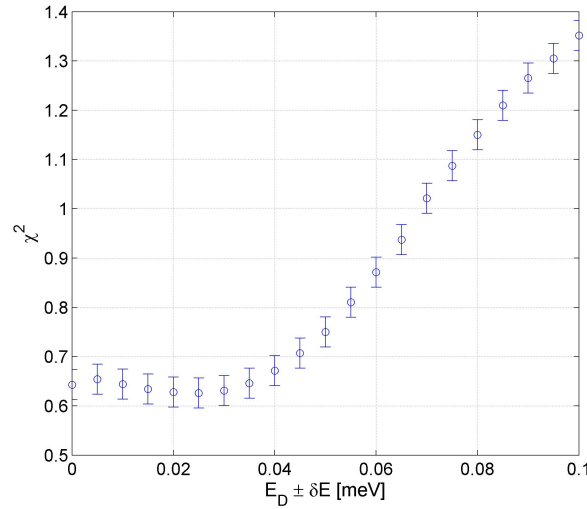
Figure 2.51: Dependence of the goodness of fit χ^2 on the deviation δE from the energy center E_D at the Dirac point position

In conclusion, from the high-resolution study of the triplet modes in an applied field along (001), the obtained dispersion confirms the validity of the model Hamiltonian derived in [60]. The main features of the excitation spectra of SCBO for the triplon modes is well reproduced by this Hamitonian. Within the accessible resolution of the measurements, the presence of a Dirac-like dispersion from the Brillouin zone center is confirmed, with a maximum energy gap at the Dirac point of 0.02 meV, corresponding to good accuracy to the difference between the calculated and the applied field.

During the writing of this document, we were made aware of a theoretical and experimental work carried out on the topological properties of SCBO [86]. This work is not in contradiction with our results and strengthens the conclusions regarding the non-trivial topological properties of SCBO in an applied field. Nevertheless, a weak additional dispersive mode was observed in their LET experimental data which is not clearly visible in the excitation spectra measured on IN5 for similar incident energies and resolutions. This dispersive mode was explained in [86] as a hybridization between a singlet bound state of two-triplons with the singlet-triplet modes.

2.7 Conclusions and Outlook

Three types of conclusions can be obtained from this experimental work on $SrCu_2(BO_3)_2$.

- The first is technique-oriented and concerns an optimal set-up for time-of-flight experiments and data analysis. Interlayer coupling was shown to be negligible when measuring excitation spectra, even for high-resolution experiments with typical resolution of 0.15 meV at $\Delta E = 3$ meV. The data can thus be integrated over Ql, which allows faster mapping of the 2D $S(\mathbf{Q},\omega)$ with improved statistics. This has little impact on other experimental techniques, although it does further confirm the 2D nature of magnetism in SCBO.

- The second type of conclusion is strongly experimental. These neutron scattering results on the multi-magnon excitation spectra, the magnetic structure factor of the bound magnon modes and the correlated decay of the singlet-triplet modes with temperature are very detailed experimental characterisation of $SrCu_2(BO_3)_2$. These results are, however, mostly ahead of the current theoretical modelling of the magnetic excitations in SCBO, hereby limiting their full interpretation.

In particular, the proposed correlated decay model was found to be a good phenomenological model to understand the unusual temperature damping of each of the singlet-triplet modes as a function of its thermal population. Nevertheless, the measured Q-dependence of the damping width, showing faster damping around $Q = (0.6\ 0.6)$ is a surprising result which is not currently fully understood.

Considering the multi-magnon excitations, careful characterization of the high-resolution excitation spectra showed that the bound magnon modes n=2-4 are localised as flat bands with very weak dispersions. Correlated hopping appears to be limited by possible level repulsion, although it may nevertheless allow the magnons to disperse within the limited measured bandwidth. Furthermore, the measured structure factors for the bound magnon modes were shown to have unusual $Qh - Qk$ dependence which cannot be explained by simple interacting-bosons structure factor calculations with intra and inter-dimer coupling only. Modelling of the bound magnon modes using an Hamiltonian which includes Dzyaloshinskii-Moriya interactions is thus likely be necessary to understand these results. Finally, the magnon excitations appear to extend well beyond the expected energy range, with magnetic scattering possibly up to $\Delta E \sim 43$ meV.

The results detailed in this chapter provide a very careful characterisation of collective magnetism in $SrCu_2(BO_3)_2$ to which further modelling of these aspects can be compared and assessed, testing further our understanding of fundamental quantum magnetism.

- This chapter also shows that inelastic neutron scattering is a powerful experimental technique to discuss theoretical predictions. The constant improvement of spectrometers allows deeper insights into magnetism by increasing the possibility to measure weak effects. This type of experimental work faces many technical challenges, particular in the case of complex

sample environments. Technical difficulties, such as the one encountered in this work to measure the excitations for an applied high pressure, may lead to unreliable results. Nevertheless, a further attempt to measure the excitations in the plaquette phase in SCBO will benefit from the lessons learned in the attempt reported here. Beyond these challenges, careful and detailed data analysis is also necessary in order to find identify interesting weak effects.

A Dirac-like dispersion had been predicted for SrCu$_2$(BO$_3$)$_2$ by careful modelling of the triplet excitations as a function of field, using an Hamiltonian that included the Dzyaloshinskii-Moriya interactions [60]. The high-resolution inelastic measurements of these modes allowed the refinement of the model parameters, making it directly comparable to the excitation spectra of SCBO at fields up to 8T. The comparison detailed in this work gave evidence that SCBO can be considered a topological magnon insulator, with a thermal Hall effect expected for an applied vertical field in the range $\sim 1.3 - 1.4$ T. Hence, in this part of the work, the theoretical prediction was shown to reproduce the experimental spectra with good accuracy in the crucial region (~ 3 meV) while small differences in the dispersion were shown to exist for the uppermost and lowest modes. Further calculations of the eigenvectors of the mode dispersion would permit a comparison with the measured intensity of the modes.

Outlook As discussed throughout this chapter, SCBO is an highly unconventional material, where frustration prevents magnetic order and where the increase of temperature does not lead to a renormalisation of the spin gap and conventional damping of the magnon. Insteade, magnon damping is driven by a Q-dependent and strongly unconventional mechanism which is dependent on the thermal population of each mode. In these type of compounds, anisotropies do play a large role and often tip the balance towards complex states of matter. They are to be understood as deviations from expected behaviours, and are often only observed when pushing the limits of experimental techniques, for example in terms of accessible reciprocal space, resolution or sample environment (pressure, field). In the broader picture, these weak effects are the ones to focus on, as studying in detail what drives these exotic behaviours deepens our understanding of the driving fundamental properties of matter. As often with low-dimensionality systems, generalities are hard to come by, as the dominant interactions and the strong correlations differ from compound to compound and create specific case studies, fascinating both on their own, or as a point of comparison. For example, other Shastry-Sutherland lattices do exist in materials, although spin-1/2 realisation are so far confined to SCBO. TmB$_4$ possesses such a lattice, and displays a rich frustration-driven magnetic phase diagram, where magnetisation plateaux makes it a possible magnetic analogue of the quantum Hall effect [87]. In another direction, strongly correlated spin ladder systems and their frustration-driven properties can and are compared to SCBO in order to discuss proximity and possibility of quantum critical points [71].

The interest in topological properties of materials and protected edge modes has now become a thriving field of research, and with the advent of possible topological magnons insulators, materials showing such unconventional behaviours may not be as scarce as what may have

been thought. Already thoroughly investigated and characterised materials such as SCBO may in this context reveal further surprising properties under specifically targeted investigation of their unconventional behavior. In this context also, the possibility of various neutron sample environments such as applied magnetic field and hydrostatic pressure allow to move in the parameter space of the magnetic phase diagrams in order to explore new areas previously only accessible in theoretical works or numerical simulations. Nevertheless, in the research field of frustrated magnetism and low-dimensional compounds, one should not remained confined to neutrons, and other experimental scattering and energy-dispersive techniques may well be significant contributors of our fundamental understanding of dynamical properties.

3 MPS$_3$

3.1 The family

Transition metal phosphorus trisulfides (MPS$_3$), with M=Mn,Fe,Ni and Co, are quasi-two dimensional antiferromagnets on an honeycomb lattice. They form in a monoclinic structure with space group C2/m. The transition metal atoms are placed at 4m position, and form a honeycomb lattice in the (a, b) planes, which are weakly bound by Van der Waals forces. The transition metal ions have a 2+ electronic ionization state and carry a localised magnetic moment. These compounds exhibit antiferromagnetic behaviour at low temperature and are considered good examples of quasi-two-dimensional materials in both their crystallographic and magnetic structure (see review in [88]). Within the MPS$_3$ family, substituting the transition metal ion for another has a drastic impact on its magnetic properties, with behaviours ranging from Heisenberg-like to strongly anisotropic (Ising or XY).
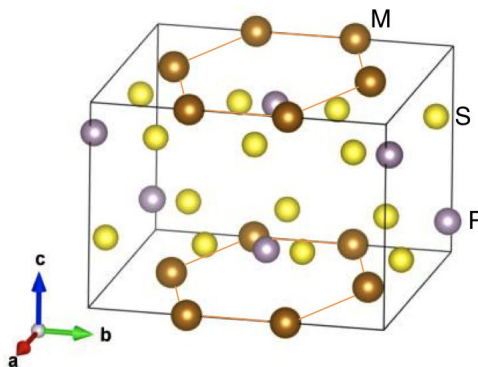

Figure 3.1: Common crystallographic structure of the MPS$_3$ compounds showing the honeycomb arrangement of the transition metal planes separated by the sulfur atoms

Crystallographically, the transition metal is in the center of an octahedron formed by sulfur atoms. All the MPS$_3$ structures show a close-packed stacking of sulfur anions in the ABC

sequence (CdCl2 type). [88, 89]. These atoms are connected to the two phosphorus atoms above and below the transition metal plane. Figure 3.1 shows the general crystallographic structure of the MPS$_3$ compounds. The plane are weakly bounded by Van der Waals forces due to the position of the sulfur atoms, and can be easily intercalated (for example with lithium[90]).

The magnetic layers are thus separated by the sulfur atoms, which reduces the strength of the interlayer magnetic interactions. It has recently been shown that both NiPS$_3$ ([91]) and FePS$_3$ [92] can be exfoliated to a monolayer. While the antiferromagnetic ordering of NiPS$_3$ was shown to be strongly influenced by interlayer coupling in [91], Raman spectroscopy showed that FePS$_3$ continues to exhibit Ising-type antiferromagnetic ordering even as a monolayer. Exfoliation of these compounds is thus an interesting testbed for fundamental magnetism, and these Van der Waals materials have also recently been singled out for their potential to be magnetic analogues to graphene [93].

In addition, this type of two-dimensional magnetic systems on a honeycomb lattice is interesting from a more theoretical point of view[94], as it has a low coordination number. Stability phase diagrams can be build depending on the strength and sign of the exchange parameter $J_{1,2,3...}$. In spin 1/2 systems, it could lead to large quantum fluctuations.

Although their crystallographic structure are very similar, each member of the MPS$_3$ family (M=Mn,Fe,Ni,Co) has very different magnetic properties.
MnPS$_3$ appears to be an Heisenberg antiferromagnet below T_N = 7 K with a propagation vector **k** = 0 and the moments pointing with an ~ 8° angle from the c^* axis [95]. The critical behaviour of the magnetic properties showed a deviation from an ideal Heisenberg-like behaviour, explained by a small XY anisotropy [96].
On the contrary, FePS$_3$ is anisotropic and has the properties of an Ising antiferromagnet below T_N = 123K with S=2 moments normal to the (a, b) plane. Each moment is ferromagnetically coupled to two of its nearest neighbours and antiferromagnetically coupled to its third, creating ferromagnetic chains coupled antiferromagnetically in the (a, b) plane [97].
NiPS$_3$ orders with a propagation vector **k** = [010] with the S=1 moments in the (a, b) plane, pointing mostly towards a. A Heisenberg Hamiltonian with weak XY anisotropy has been proposed for NiPS$_3$, although not fully consistent with the critical behaviour [35].

Within this family, there are still many open question about the magnetic properties of its members, related to their magnetic structure, magnetic excitations and critical properties. In particular, for FePS$_3$ and NiPS$_3$, the objectives were to use neutron scattering to provide new insight into their fundamental magnetism . Detailed scattering measurements and analysis of the excitation spectrum of FePS$_3$ were thus coupled to other experimental techniques in order to discuss the magnetic propagation vector, the exchange interactions driving the dynamical response as well as the critical properties at the Néel temperature. Insight on the anisotropies of NiPS$_3$ were also gained from inelastic neutron scattering on a powdered sample.

3.2 FePS$_3$

As mentioned in the previous section, FePS$_3$ orders below T$_N$ ~ 120 K in an antiferromagnetic structure with the S=2 high-spin Fe^{2+} moments normal to the (a, b) planes. In FePS$_3$, each moment is ferromagnetically coupled to two of its nearest neighbours and antiferromagnetically coupled to its third, resulting in antiferromagnetic coupled ferromagnetic chains.

3.2.1 Introduction to the magnetic structure, magnon dynamics and critical properties

Conversion between space groups

The structure of FePS$_3$ has a monoclinic space group $C2/m$, with cell parameters a_m=5.95, b_m=10.3 and c_m=6.72 Å, $\alpha = \gamma = 90, \beta = 107.16°$ [2]. Nevertheless, indexing the Bragg peaks can also be done using an hexagonal space group. Indeed, the X-ray refinement in [2] showed that the b/a ratio is precisely $\sqrt{3}$. In addition, the value of β necessary for an undistorted unit cell with trigonal symmetry can be calculated to be 107.16 degrees, equal to the cell parameter of FePS$_3$. Thus for FePS$_3$, in the monoclinic space group, the following conditions have been shown to be accurate to a good precision:

$$b_m = \sqrt{3} a_m$$
$$a_m = -3 c_m \cos(\beta) \tag{3.1}$$

Indexing either with the monoclinic space group or the hexagonal space group is therefore possible, with the [010] direction equivalent between the two, as shown in figure 3.2. The c^* axis is perpendicular to the (a, b) plane in both hexagonal and monoclinic system.
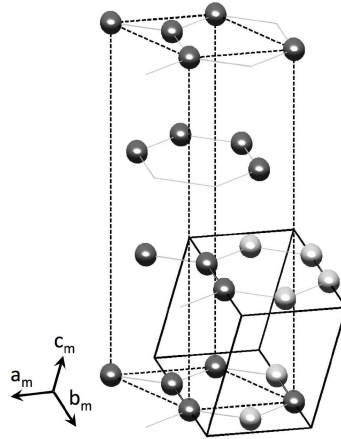

Figure 3.2: Monoclinic unit cell (solid lines) and hexagonal unit cell (dashed) lines for FePS$_3$. The spheres represent the Fe^{2+} ions. The dark spheres are included in the hexagonal unit cell, while the light spheres are included in the monoclinic unit cell but not in the hexagonal one.

Rotational twinning and magnetic domains

Due to the equivalent indexing between monoclinic and hexagonal space groups and the weak inter-plane binding, rotational twinning is likely to be present in FePS$_3$ samples in the form of multiple domains rotated by 120° about the c^* axis. As shown recently in [98] during crystal growth, every so often there can be a rotation of the structure by 120° about the normal to the (a, b) plane. Hence there are three possible in-plane orientations of the monoclinic unit cell, with the correspondence of the Miller indices between them given by the following rotation matrices :

$$
\begin{bmatrix} h \\ k \\ l \end{bmatrix}_m^{I} = \begin{bmatrix} -\frac{1}{2} & \frac{1}{2} & 0 \\ -\frac{3}{2} & -\frac{1}{2} & 0 \\ \frac{1}{2} & -\frac{1}{6} & 1 \end{bmatrix} \begin{bmatrix} h \\ k \\ l \end{bmatrix}_m^{II}
$$
$$
= \begin{bmatrix} -\frac{1}{2} & -\frac{1}{2} & 0 \\ \frac{3}{2} & -\frac{1}{2} & 0 \\ \frac{1}{2} & \frac{1}{6} & 1 \end{bmatrix} \begin{bmatrix} h \\ k \\ l \end{bmatrix}_m^{III}
\tag{3.2}
$$

Due to this rotational twinning, magnetic domains are expected in FePS$_3$ samples. The domains may have a different size distribution.

Ferromagnetic chains

There are three possible orientations for the ferromagnetic chains on a honeycomb lattice, with 120° rotation between them. Due to the presence of rotated magnetic domains, however, it can be difficult distinguish the correct orientation of the ferromagnetic chains, as illustrated by figure 3.3, which shows that magnetic scattering using a 120°-rotated domain would lead to a different ferromagnetic chain orientation.

The moment positions and orientations can be used to calculate the magnetic structure factor for each possible orientation of the ferromagnetic chains using :

$$
F_M(\mathbf{Q}) = \sum_j \mu_j \exp 2\pi i [hx_j + ky_j + l_z j]
\tag{3.3}
$$

The sum is done over all the moments in the magnetic unit cell which, for an Ising system, each have a magnetic moment $\pm\mu_j$. The orientation of the ferromagnetic chains shown in figure 3.3, with the chains along the monoclinic a axis, has non-zero magnetic structure factors for $Q = (0\ 1\ l \pm \frac{1}{2})$ and zero magnetic structure factors for $Q = (\frac{1}{2}\ \frac{1}{2}\ l \pm \frac{1}{3})$.
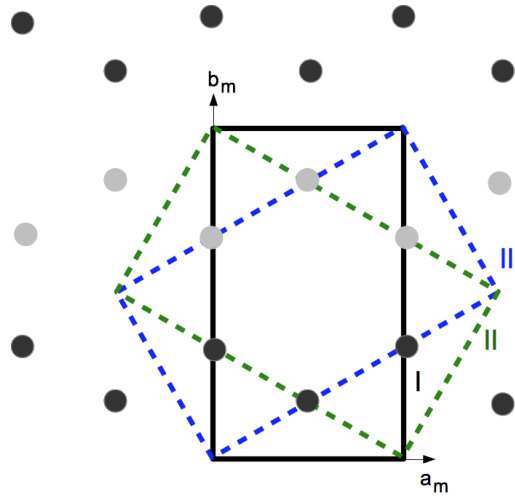
Figure 3.3: Ferromagnetic chains along the a_m axis. The black rectangle corresponds to the monoclinic unit cell drawn with respect to domain I. Black and grey circles represent the magnetic moments respectively parallel or anti-parallel to **c***. The green and blue dashed rectangles represent respectively the ±120°- rotated monoclinic unit cell with respect to domain II and III.

Propagation Vector

The propagation vector was shown to be **k**=[0 1 $\frac{1}{2}$] in [99], but later measurements [100] were thought to contradict this propagation vector, and a new magnetic propagation vector was proposed for FePS$_3$. In the latter work, the measured crystal was known to be twinned, and elastic scans were performed along ($\frac{3}{2}$ $\frac{1}{2}$ l), identifying peak a l= l_{nuc} ±0.34, as shown in figure 3.4. Using these elastic scans as well as Laue diffraction patterns, this study concluded that the propagation vector was $k = [\frac{1}{2}\frac{1}{2}0.34]$. This propagation vector is incommensurate, with $\delta = \pm0.34$ instead of $\delta = \frac{1}{3}$, and it was attributed in [100] to a short range ordering of moments between the layers. Such a propagation vector leads to a magnetic Bragg peak at both ($\frac{1}{2}$ $\frac{1}{2}$ -0.34) and ($\frac{1}{2}$ $\frac{1}{2}$ +0.34).
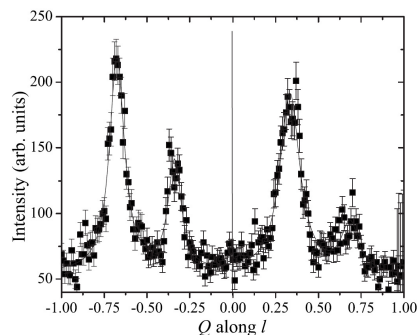

Figure 3.4: Elastic scans along ($\frac{3}{2}$ $\frac{1}{2}$ l) from [100], showing peaks at l_{nuc} ±0.34, which were attributed to one crystallite (labeled B)

Finally, previous studies of FePS$_3$ [34, 101] showed a broad feature in the neutron powder diffraction pattern for Q between 0.65 and 0.85 Å^{-1} (corresponding to $8 \lesssim 2\theta \lesssim 13°$ in figure 3.5). Figure 3.5 from [34] shows that the lowest magnetic Bragg peak for the propagation vector $\mathbf{k} = [01\frac{1}{2}]$ is expected at $Q =(0\ 1\ \frac{1}{2})$ with $|\mathbf{Q}|$=0.78 Å^{-1}, so that this propagation vector was unable to account for the broad feature. This was an argument in favor of $\mathbf{k} = (\frac{1}{2}\frac{1}{2}0.34)$ propagation vector [100]. Indeed, using the propagation vector $\mathbf{k} = (\frac{1}{2}\frac{1}{2}0.34)$, this scattering was shown to be indexed as a series of peak with l between -2/3 and 1/3.
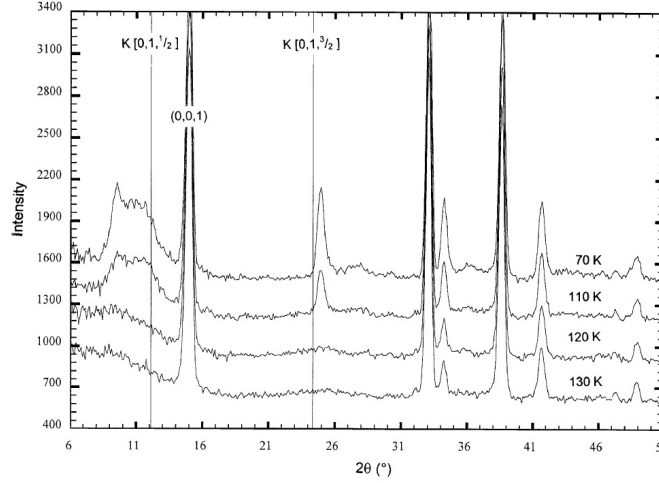

Figure 3.5: Neutron powder diffraction scans of FePS$_3$ from [34] shown with a vertical offset. A vertical line around $2\theta \sim 12°$ shows the lowest magnetic peak for the propagation vector $\mathbf{k} = (01\frac{1}{2})$

The magnetic dynamical structure factor

The dynamical structure factor was derived for a two-dimensional honeycomb lattice from linear spin wave theory in [97]. The magnetic structure was decomposed into four interlocking Bravais lattice with 120° between $\mathbf{a}_h$ and $\mathbf{b}_h$, with $b_h = 2a_h$.

Even though FePS$_3$ is thought to be Ising-like, the exchange interactions were modelled using an Heisenberg Hamiltonian with a large single-ion easy-axis anisotropy :

$$H = -\sum_{i,j} J_{i,j} S_i \cdot S_j - \Delta \sum_i (S_i^z)^2 \tag{3.4}$$

The exchange interaction $J_{i,j}$ depend on the proximity to the neighbouring moments. Four different exchange parameters are taken into account, with three intra-planar parameters for the nearest neighbour interaction $J_{1,2,3}$ and the inter-planar couplings J' and J''. Figure 3.6 shows these distances schematically with J_1 and J_2 the nearest and next nearest neighbour along the ferromagnetic chains, and J_3 the exchange interaction between the chains. J' and J'' are the inter-plane exchange parameters, which are set to zero in this two-dimensional model.
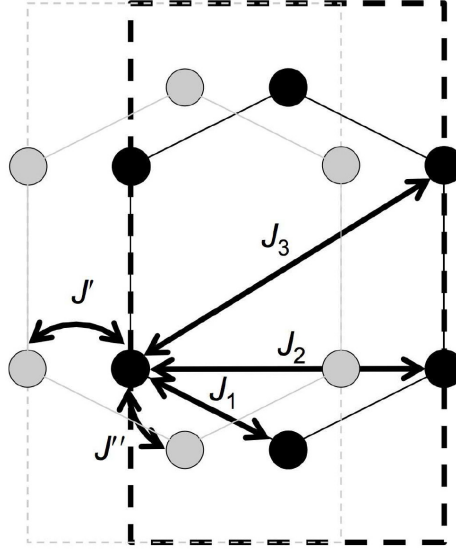
Figure 3.6: Exchange parameters shown as a function of the distances between the Fe^{2+} moments. Black circles represent the moments on one (a, b) plane and grey circles represent the moments on another (a, b) plane displaced along the c axis. J_1, J_2 and J_3 are the intra-plane exchange parameters and J' and J'' are the inter-plane exchange parameters.

Following the work in [97], using the Holstein-Primakoff transformation and Fourier transforming, the effective Hamiltonian can be written in the following form :

$$
H_M = 2S \begin{bmatrix} A & B* & C & D* \\ B & A & D & C \\ C & D* & A & B* \\ D & C & B & A \end{bmatrix}
$$

$$
\begin{aligned}
A &= 2J_2\cos(2\pi h) - \Delta - J_1 + 2J_2 + 3J_3 \\
B &= J_1\exp(\tfrac{2\pi i}{3}[2h + \tfrac{k}{2}])(1 + \exp(-2\pi i h)) \\
C &= 2J_2(\cos(\pi k) + \cos(2\pi[h + \tfrac{k}{2}])) \\
D &= \exp(\tfrac{2\pi i}{3}[2h + \tfrac{k}{2}]) \\
&\quad \times (J_1\exp(-2\pi i[h + \tfrac{k}{2}]) + J_3(2\cos(\pi k) + \exp(-2\pi i[2h + \tfrac{k}{2}])))
\end{aligned}
$$

(3.5)

with h, k and l given with respect to the magnetic unit cell.

Diagonalising the Hamiltonian gives two pairs of degenerate magnon modes with dispersion:

$$
\begin{aligned}
\omega_Q^2 &= r \pm \sqrt{s} \\
r &= A^2 + |B|^2 - C^2 - |D|^2 \\
s &= 4|AD^* - CD^*|^2 - |BD^* - DB^*|^2)
\end{aligned}
$$

(3.6)

The explicit expressions for the eigenvectors of this Hamiltonian can be found in [102], derived for a similar form of Hamiltonian which is also applicable for FePS$_3$.

Figure 3.7 shows the dispersion along high-symmetry directions obtained from the 2D Hamiltonian and the exchange parameters in [97]. These exchange parameters were obtained in [97] by fitting the neutron inelastic data from a powder sample. The data were integrated over **Q**, which corresponds to the powder average of the dispersive spin waves, using the dynamical structure factor derived from the Hamiltonian.
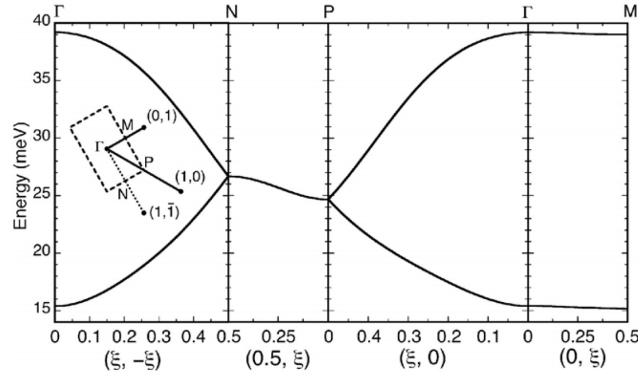

Figure 3.7: Simulated dispersion along high symmetry directions derived from the Hamiltonian on two-dimensional honeycomb lattice. The inset shows the two-dimensional Brillouin zone. Figure from [97].

Theses directions are given with respect to the magnetic unit cell. It can be converted to in-plane monoclinic units using:

$$\begin{bmatrix} h \\ k \end{bmatrix}_m = \begin{bmatrix} 1 & 0 \\ 1 & 1 \end{bmatrix} \begin{bmatrix} h \\ k \end{bmatrix}_h \tag{3.7}$$

Figure 3.8 shows the result of the analysis in [97] done by fitting the powder data, from which the intra-planar exchange parameters were estimated. The gap of ∼ 16 meV is well reproduced using these fitted exchange parameters. The nearest neighbour exchange is ferromagnetic and the anti-ferromagnetic behaviour is due to exchange between the third nearest neighbours. Within this analysis, the second nearest neighbour exchange J_2 is ferromagnetic, although very close to zero. The anisotropy is large compared to the exchange parameters $J_{1,2,3}$, which is consistent with an Ising-like behaviour. Furthermore, the strength of the obtained coupling constants hinted towards a quasi one-dimensional ferromagnetic behaviour.

These estimated exchange parameters in FePS$_3$ were based on powder neutron scattering data where individual magnon dispersions cannot be measured. In order to test their validity, the results were compared with susceptibility measurements and stability conditions for an Ising Hamiltonian from mean field calculations.
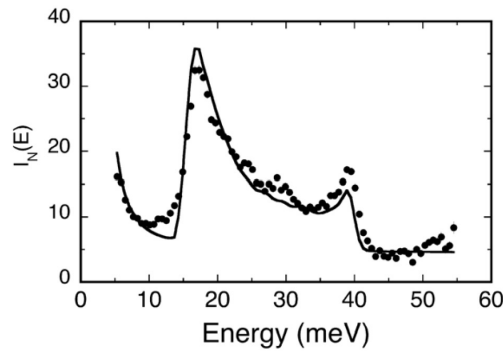
Figure 3.8: Inelastic neutron scattering for a powder sample of FePS$_3$ with fits of the Q-integrated magnons from the analysis in [97].

Critical properties

The critical properties on FePS3 have been discussed in previous studies [103, 104, 105, 106, 97]. The evidence for a first order transition is two-fold: First, in [103], the temperature dependence of the magnetic hyperfine field measured by Mössbauer spectroscopy combined with the observed temperature dependence of the lattice parameters measured by X-ray diffraction both point to a first order transition. Figure 3.9 from [103] shows that the change of lattice parameters with temperature is discontinuous, although the monoclinic space group $C2/m$ remains valid at all temperatures. The results of differential scanning spectrometry [104] also contribute to strengthen the conclusions for a first order transition, with a sharp peak in heat capacity around T$_N$. The sharp peak in the temperature dependence of the specific heat, characteristic of a first order transition, was also measured in [106, 107] and shown to be well reproduced by taking into account a magneto-elastic effect.
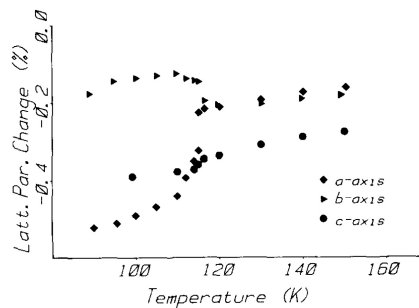
Figure 3.9: The relative deviations of the lattice parameters of FePS$_3$ from the room temperature values obtained from X-ray diffraction. Figure from [103].

On the other hand, a study the effect of magnetic ordering on the spin-dependent Raman scattering from phonons showed a strong enhancement of the quasi-elastic component [105]. This was interpreted as critical scattering due to an increase of short-range spin fluctuations close to the Néel temperature. Broad inelastic scattering above T$_N$ was also observed in inelastic neutron spectroscopy in [97].

3.2.2 Neutron experiment and discussion

To summarise, discrepancies on the magnetic structure were shown to exist in the literature [99, 100], with two different magnetic propagation vector proposed to explain neutron diffraction studies.

In addition, a first model of the powder excitation spectra was proposed by [97] based on a two-dimensional model. An extension to three dimensions and confirmation of the expected dispersion by measuring the full S($\mathbf{Q}, \omega$) would allow to test and refine this model.

Furthermore, the nature of the phase transition has been under discussion in FePS$_3$. The phase transition was concluded to be first order based on Mössbauer spectroscopy [103] and calorimetry measurement[104, 106], strengthened by the change in lattice parameters accompanying the onset of magnetic order. However, Raman spectroscopy for temperature around the Néel temperature T$_N$ ~ 120K showed strong inelastic scattering attributed to magnetic critical scattering [105].

A set of questions can thus be asked about this member of the MPS$_3$ family for which neutron scattering experiments will provide insight:

- What are the consequences of rotational twinning in FePS$_3$?

- Is the propagation vector $\mathbf{k} = [\frac{1}{2}\frac{1}{2}0.34]$ or $\mathbf{k} = [01\frac{1}{2}]$?.

- What is the impact of interlayer coupling on the magnetic excitation spectra ?

- Can the Heisenberg Hamiltonian with single ion anisotropy be used to model the magnetic excitation spectra ?

- Is FePS$_3$ a quasi two-dimensional material or close to a one-dimensional system ?

- What is the nature of the phase transition in FePS$_3$? What are the critical properties of FePS$_3$?

A set of experiments were hence carried out in order to answer these questions (see table 3.1), with either a single crystal, co-aligned crystals in order to increase the sample size or powdered samples.

Table 3.1: List of neutron scattering experiments for FePs3 with sample list

Instrument	Problematic	Sample
IN3	rotational twinning	single crystals 4 and 5 - rotated
D10	magnetic propagation vector	single crystal 5
TAIPAN	interlayer coupling	single crystals 4 and 5
IN8	interlayer coupling	single crystals 4 and 5
IN20	interlayer coupling	single crystals 4 and 5 - rotated
Merlin	Excitation spectra and exchange parameters	17 co-aligned crystals
IN4	Critical properties	powder pellets
D7	Critical properties	powder pellets

Due to rotationnal twinning, a distribution of 120°-rotated magnetic domains are expected in single crystals of FePS$_3$. An elastic neutron scattering experiment was thus carried out using using two co-aligned FePS$_3$ crystals with (110) and (001) in the scattering plane, in order to obtain a characterisation of the domains in these specific crystals. The two co-aligned crystals were cooled to 10K and magnetic Bragg scattering was measured on the IN3 triple axis spectrometer at ILL, with a graphite PG(002) for both the monochromator and the analyser and 40' collimation.

Figure 3.10 shows the obtained elastic scans along $(\frac{1}{2}\ \frac{1}{2}\ l)$, $(0\ 1\ l)$ and $(\frac{\bar{1}}{2}\ \frac{1}{2}\ l)$. These scans correspond to three different rotations of the co-aligned single crystals : 0°, +60° and -60° about the (001) direction (domains I, II and III) and the observed peaks thus confirm the presence of magnetic domains rotated by 120° from each other in the (a, b) plane. The peaks in the scans along $(\frac{1}{2}\ \frac{1}{2}\ l)$ and $(\frac{\bar{1}}{2}\ \frac{1}{2}\ l)$ are estimated to be at $l \sim N + \frac{1}{3}$ and are absent at $N - \frac{1}{3}$, with N an integer. For the scan along $(0\ 1\ l)$, the Bragg peaks are at $l \sim N \pm \frac{1}{2}$. Precise values for l could not be obtained due to the instrumental resolution of the IN3 spectrometer and the large sample mosaicity (discussed in 1.2.3). In addition, it is clear from figure 3.10 that these samples have domains with significant population differences, with the scans along $(0\ 1\ l)$ showing an intensity one order of magnitude larger than the other two scans.
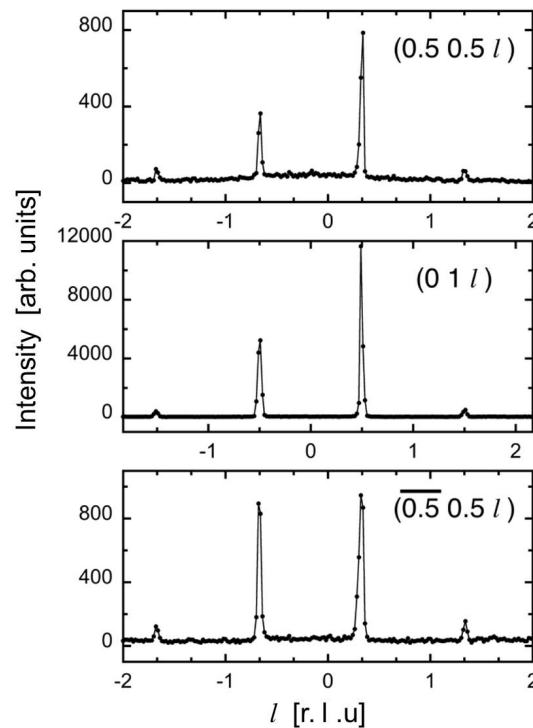

Figure 3.10: Elastic scans along l corresponding to three 60° rotation of the sample about **c**∗ obtained on IN3 at 10K.

Several conclusions can be drawn from this dataset. First, the presence of 120°-rotated magnetic domains in a single crystal is confirmed, which is important in the understanding of neutron excitation spectra. Indeed, in an inelastic neutron experiment, all the domains would contribute to the scattering and the measured data would be the sum of the cross sections from all the domains.

In addition, it is clear from this that carefully choosing the domain from which to scatter is necessary in order to obtain high quality datasets. Indeed, choosing the sample orientation where the largest domain is aligned with (010) and (001) in the scattering plane (orientation II for this specific crystal) will yield a better signal-to-noise ratio for the measured spin waves, as shown in section 3.2.2.

Finally, it allows to explain the discrepancy in the literature between the two magnetic propagation vector proposed in [100, 99], as discussed in more details in the next section.

Magnetic structure

The data obtained on IN3 and shown in Figure 3.10 has notable differences with the study described in [100] which concluded on a propagation vector $\mathbf{k} = [\frac{1}{2}\frac{1}{2}0.34]$. Such a propagation vector would lead to a magnetic Bragg peaks at both ($\frac{1}{2}$ $\frac{1}{2}$ -0.34) and ($\frac{1}{2}$ $\frac{1}{2}$ +0.34) which is clearly not the case in the dataset obtained on IN3 for single crystals shown in figure 3.10.

In addition, the Bragg peaks measured and indexed in [100] using the propagation vector $\mathbf{k} = [\frac{1}{2}\frac{1}{2}0.34]$ can also be indexed using the propagation vector $\mathbf{k} = [01\frac{1}{2}]$ from [99] by rotation between the magnetic domain I,II and III (using equation 3.2). Table 3.2 shows a few examples of these peaks, indexed in [100] using $\mathbf{k} = [\frac{1}{2}\frac{1}{2}0.34]$, but that can also be indexed by $\mathbf{k} = [01\frac{1}{2}]$ by rotating to another domain.

Table 3.2: Examples of indexing of magnetic peaks in [100] which can be explained using the propagation vector $\mathbf{k} = [01\frac{1}{2}]$ by 120° rotation in (a,b) plane from either domain II or domain II to domain I

hkl indexed in [100]	hkl by ±120° rotation	hkl$_{nuc}$ ± $\mathbf{k}$
$(\ \frac{1}{2}\ -\frac{1}{2}\ -0.66)_{III}$	$(\ 0\quad 1\ -\frac{1}{2})_I$	$(020) - \mathbf{k}$
$(\ \frac{1}{2}\ -\frac{11}{2}\ -0.66)_{II}$	$(-3\quad 2\quad \frac{1}{2})_I$	$(-310) + \mathbf{k}$
$(-\frac{1}{2}\ -\frac{5}{2}\quad 0.34)_{III}$	$(-1\quad 2\quad \frac{1}{2})_I$	$(-110) + \mathbf{k}$
$(\ \frac{3}{2}\quad \frac{1}{2}\ -0.34)_{II}$	$(-1\quad 2\quad \frac{1}{2})_I$	$(-110) + \mathbf{k}$
$(\ \frac{3}{2}\quad \frac{1}{2}\ -1.34)_{II}$	$(-1\quad 2\ -\frac{1}{2})_I$	$(-130) - \mathbf{k}$

Hence from these results the correct propagation vector would be $\mathbf{k} = [01\frac{1}{2}]$ as concluded in [99]. Nevertheless, three issues still need to be discussed in order to confirm this propagation vector. The first is that one Bragg peak indexed in [100] , ($\frac{1}{2}\frac{3}{2}$ -0.34) cannot be indexed using any 120° in-plane rotation. The most likely explanation is a miss-indexing of the peak in the previous work, or a spurious signal at this position, as one unique mismatch would not be

expected from a wrong propagation vector. The second issue is that the work by [100] found an incommensurate propagation vector with $\delta = \pm 0.34$ instead of $\delta = \frac{1}{3}$, attributed to a short range ordering of moments between the layers . This is not taken into account in the $\mathbf{k} = [01\frac{1}{2}]$ propagation vector. However, given the overall mosaicity of all the FePS$_3$ samples measured (between 4-10 degrees), it is unlikely that any diffraction study can be precise down to ± 0.01 [r.l.u]. Furthermore, an incommensurate propagation vector would be due to either a periodic variation of the moment size, or non-collinear components of the moments, which would both be unlikely for FePS$_3$, a good 2D Ising system with high spin Fe^{2+} moments.

Finally, an argument against the propagation vector $\mathbf{k} = [01\frac{1}{2}]$ was its inability to index the broad scattering feature observed in [100] for a powdered sample at Q between 0.65 and 0.85 Å^{-1}, as the first allowed magnetic Bragg peak is $(0\ 1\ \frac{1}{2})$ at 0.78 Å^{-1}. The feature begins at a Q which can be indexed with $(0\ 1\ 0)$. However, these measurements were done using powdered sample, and it is likely that grinding FePS$_3$ crystals destroys long-range order along the $\mathbf{c}^*$ axis, while keeping the in-plane structure. Indeed, materials in these family of compounds have been shown to be very soft and prone to distortions (for example NiPS$_3$ in [35]). This broad feature, which is only present in powdered samples, can thus be explained as a Bragg rod along $\mathbf{c}^*$ appearing at (010) and extending along l. This interpretation restores $\mathbf{k} = [01\frac{1}{2}]$ as a coherent propagation vector.

The magnetic structure was further confirmed from measurements on the diffractometer D10 at ILL, using one single crystal (labelled 5). The nuclear structure was refined from 2K data and the structural parameters were obtained, with a residual $_wR_{f2} = 10.7\%$ and $\chi^2 = 5.29$ for the space group $C2/m$ with lattice parameters $a = 5.94(4)$ Å, $b = 10.26(2)$ Å, $c = 6.60(6)$ Å and $\beta = 108.3(7)°$. The obtained structural parameters are consistent with the literature [2], within the limited accuracy of the refinement due to crystal size and mosaicity.

Regarding the magnetic structure refinement[1], the BasIreps program of the FullProf suite [108] was used to determine the irreducible representations compatible with the crystal symmetry and the propagation vector $\mathbf{k} = [01\frac{1}{2}]$, and the symmetry operators for the resulting four representations are shown in table 3.3.

Table 3.3: Symmetry operators for the four possible irreducible representations in the case of the propagation vector $\mathbf{k} = [01\frac{1}{2}]$

	Symmetry 1	Symmetry 2	Symmetry 3	Symmetry 4
	1: (0,0,0)	2: (0,y,0)	-1: (0,0,0)	m: (x,0,z)
IRep(1)	1	1	1	1
IRep(2)	1	1	-1	-1
IRep(3)	1	-1	1	-1
IRep(4)	1	-1	-1	1

Irep(4) was found to be the only one leading to a good match between the measured Bragg

---

[1] refinement carried out by Andrew Wildes, ILL

peak intensities and the calculated structure factor, and the result of both the nuclear and magnetic refinement at 2K are shown in figure 3.11. The results of the nuclear refinement were used as fixed parameters (structural and thermal) in the magnetic refinement. The refined moment direction was found to be approximately normal to the (a, b) planes, with a moment amplitude of $4.52 \pm 0.05 \, \mu_B$, obtained with residuals $_w R_{f2} = 21$ % and $\chi^2 = 24.9$. These results are consistent with previous studies[99, 100] and the expected moment from the $S = 2$ high-spin state of Fe^{2+}.
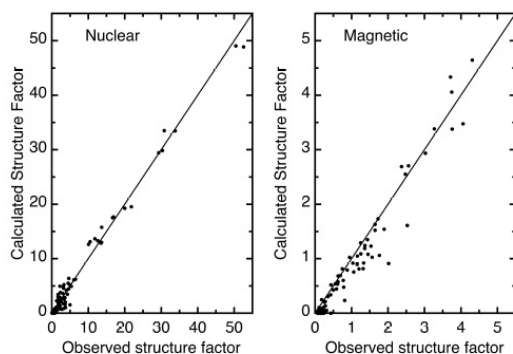

Figure 3.11: Observed versus calculated nuclear (left) and magnetic (right) structure factor from refinement using neutron diffraction data obtained on D10.

The magnetic propagation vector is thus confirmed to be $\mathbf{k} = [01\frac{1}{2}]$ and not $\mathbf{k} = [\frac{1}{2}\frac{1}{2}0.34]$, with the orientation of the ferromagnetic chains along the monoclinic a axis. This confirms the validity of the magnetic structure proposed in [99], and the presence of domains explains the data and interpretation proposed in [100].

Furthermore, all studies of single crystals of FePS$_3$ need to take into account rotational twinning, in particular for characterizing excitation spectra. The distribution between each of the three 120°-rotated domains can be estimated using diffraction studies on either nuclear or magnetic peaks. For example, a population ratio between the domains of 0.78:0.13:0.09 was estimated for a specific crystal (labelled 5) using the integrated intensity of nuclear peaks measured on the diffractometer D10.

Interplanar dispersion

FePS$_3$ is considered a quasi-two dimensional material and thus the interlayer coupling is expected to be negligible. In [97], the modelling of the density of states from spin wave calculation was done based on a two-dimensional Hamiltonian, which represents relatively well the density of states. However, it could be possible to have a dispersion along **c***, which would complicate analysis of the excitation spectra from a powdered sample.

There are two different inter-planar exchange parameters J' and J'', with exchange pathways between the sulphur layers which are between different sublattices. The distance only differs by less than 0.2 % (difference estimated in [89] to be within 0.005 Å), which is within the tolerance of the hexagonal indexing. Furthermore, the effect of the interlayer coupling is expected to be weak, so that the neutron scattering analysis will only take into account one averaged parameter for the interlayer coupling (referred to as J').

In order to evaluate J' from the measured dispersion along **c***, triple axis experiments were performed on thermal spectrometers with single crystals of FePS$_3$ oriented with (110) and (001) in the scattering plane. Constant-**Q** scans were performed to follow the dispersion of the spin waves along the Ql direction. Measurements focused either on $\Delta E \sim 16$ meV, corresponding to the spin gap energy, and on the maximum energy spin waves at $\Delta E \sim 40$ meV, as was expected from the calculated dispersion in [97] shown in figure 3.7.

The dispersion along two particular **Q** directions were studied : $Q = (\frac{1}{2}\ \frac{1}{2}\ l)$ and $Q = (1\ 1\ l)$ in monoclinic unit cell, which correspond for a +120° in-plane rotation to respectively (0 1 $l + \frac{1}{6}$) and (0 2 $l + \frac{1}{3}$) and for a -120° in-plane rotation to respectively ($\bar{\frac{1}{2}}\ \frac{1}{2}\ l + \frac{1}{3}$) and ($\bar{1}\ 1\ l + \frac{2}{3}$). For the first **Q** direction, a peak is expected at the eigenvalue of 16 meV corresponding to a contribution from only one of the domains, while for the second **Q** direction, a peak is expected for an eigenvalue of 40 meV, with a contribution from each of the domains. In addition, there is a broad bump around 25 meV which corresponds to the superposition of the dispersive spin waves from the different domains.
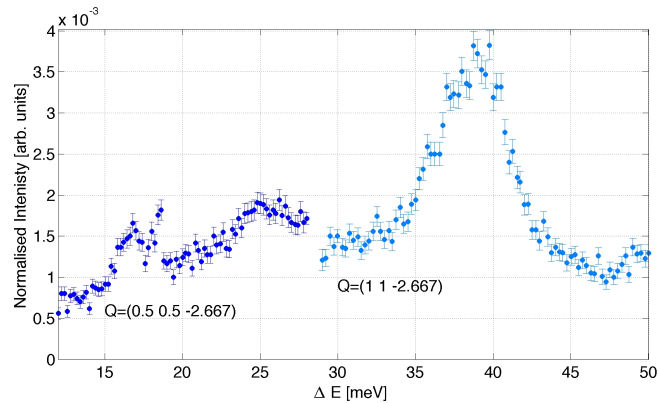

Figure 3.12: Inelastic neutron scattering on IN8 for $Ql = -2.667$ [r.l.u.]. The energy transfer ΔE range is 12 to 28 meV for $Q = (0.5\ 0.5\ -2.667)$ and 29 to 50 meV for $Q = (1\ 1\ -2.667)$.

Figure 3.12 illustrates the type of scattering measured at the Brillouin zone centers (0.5 0.5 -2.667) and (1 1 -2.66) on the IN8 spectrometer in ILL with a graphite PG(002) analyser and no collimation. A Si(111) monochromator was used for the measurements of the spin gap at $\Delta E \sim 16$ meV with k_f=2.662Å^{-1}, while the high energy spin waves at 40 meV were measured using a Cu(200) monochromator with a $k_f = 4.1$ Å^{-1}. Although presented on the same figure, the resolution of the 16 meV feature and the 40 meV features are not at all similar, due largely to the change of monochromator and the different values of Q.

In order to increase the relative intensity of the 16 meV mode with respect to the broad scattering from spin waves in other domains, another experiment was carried out on the thermal triple axis IN20 with the sample rotated by 60 degrees such that the largest domain was in the scattering plane. Figure 3.13.b shows the 16 meV mode measured on IN20 at $Q =$(0.5 0.5 l) corresponding to (0 1 $l+\frac{1}{6}$) for the largest domains, while figure 3.13.a shows the 40 meV mode measured at Q=(1 1 l) obtained on IN8. Figure 3.13.a-b both show that there is no clear dispersion along l, as the energy centres of each peaks appear constant as Ql varies from a Brillouin zone center (BZC) to a Brillouin zone boundaries (BZB).
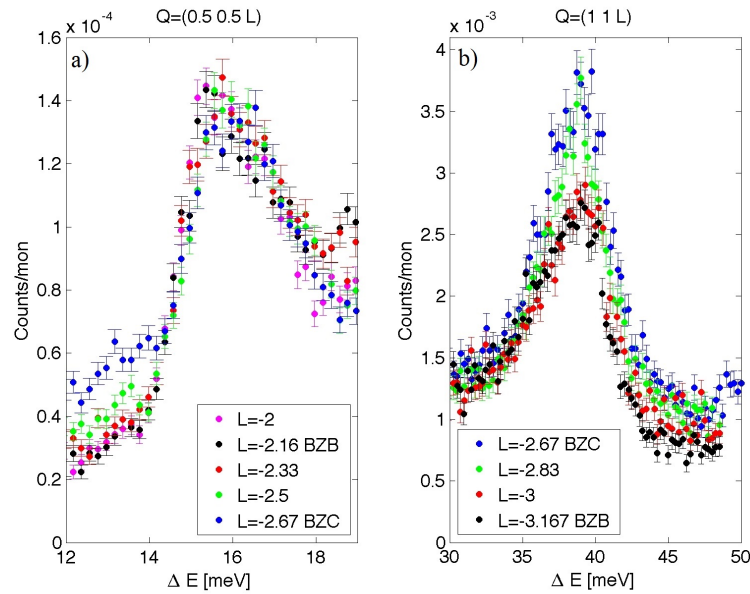

Figure 3.13: a)Intensity of the $\sim$ 16 meV mode measured at $Q = $ (0.5 0.5 l) with varying Ql between Brillouin Zone centers (BZC) and Brillouin zone boundaries (BZB) on IN20. The sample was rotated by 60 degrees to measure the magnetic scattering from the largest magnetic domain. b)Intensity of the $\sim$ 40 meV mode at $Q = $ (1 1 l) with varying Ql between Brillouin Zone centers (BZC) and Brillouin zone boundaries (BZB) on IN8.

In order to put an upper bound on the dispersion along Ql and to quantifying the interlayer coupling J', each dispersion mode was fitted using a damped harmonic oscillator (equation 2.10). The renormalised Q-dependent frequencies Ω_0 are given by the eigenvalues of the Hamiltonian and the structure factor $A(\mathbf{Q})$ is given by the eigenvectors of the effective Hamilto-

nian in equation 3.5. This function was then convolved with the instrumental resolution using the Monte Carlo algorithm trixfit (refer to 1.1.8), with the interlayer exchange parameter J' as the only free parameter in the calculation of the eigenvalues. An additional broad Gaussian background was added in order to account from the magnetic scattering from the spin waves of the other two domains.

Figure 3.14 shows the results of the fits for both the 16 meV mode from IN20 data and the 40 meV mode from the IN8 data for some of the measured Q points. It can be seen that the asymmetrical shape of the modes is well represented when taking into account the instrumental resolution. The damping width Γ was constrained to the same value for all the fits with a resulting estimate of $\Gamma \sim 0.58 \pm 0.1$ meV.
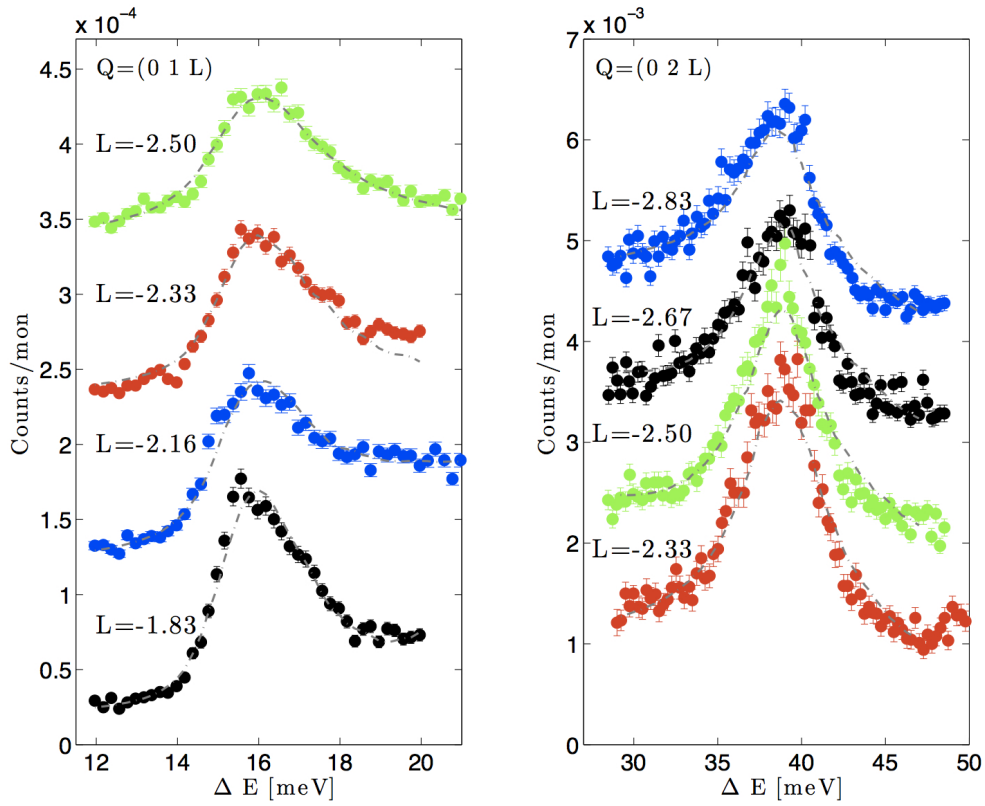

Figure 3.14: Fit results for of $S(\mathbf{Q},\omega)$ convolved with the instrumental resolution fonction. The interlayer coupling J' was a free parameter of the dispersion. a) Fits of the IN20 Constant-Q scans for Q=(0 1 l) of the $\sim$ 16 meV mode. b) Fits of the IN8 Constant-Q scans for Q=(0 2 l) of the $\sim$ 40 meV mode. This peak is a superposition of the 40 meV excitation of the three domains at in-plane Q=(0 1), (1 1) and ($\bar{1}$ 1).

For each of the constant-**Q** scans measured on IN8 and IN20, each peak was fitted for independent interlayer exchange coupling J'. The resulting J' values obtained from each independent fit is shown in figure 3.15, and an estimation of J'= -0.0073 ± 0.0003 meV was obtained by fitting the J' distribution with a constant.
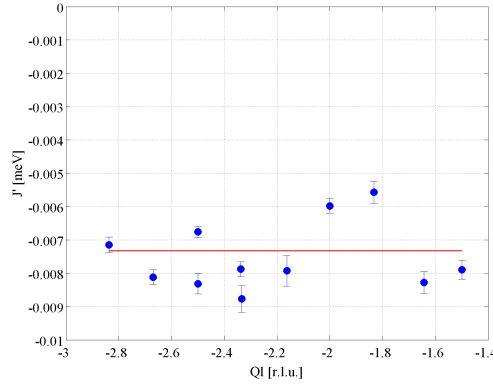
Figure 3.15: Interlayer exchange coupling J' as a function of Ql obtained from fits of $S(\mathbf{Q}, \omega)$ convolved with the instrumental resolution from both the IN8 ~ 40 meV mode and the IN20 ~ 16 meV mode. The red line is the fitted average parameter for J'

The obtained interlayer exchange coupling J' is negative, coherent with the expected anti-ferromagnetic coupling in between the planes. In addition, we conclude from the very weak exchange parameter J' obtained that the spin waves are close to dispersionless in the Ql direction. This is also clearly shown by the eigenvalues for both ~ 16 and ~ 40 meV modes obtained from the fits and presented in figure 3.16, where the dashed lines show the calculated weak dispersion along Ql for $J' = -0.0073$.
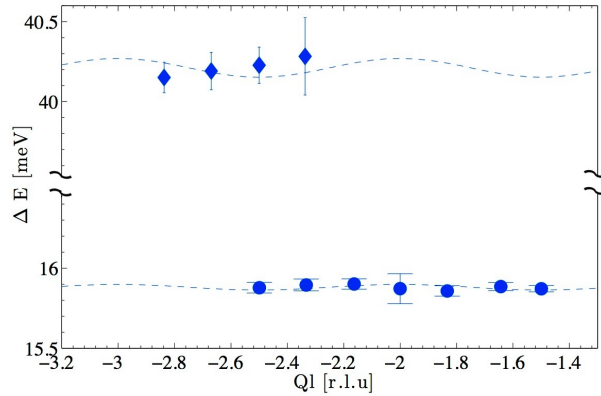
Figure 3.16: Fitted energy centers as a function of Ql of the ~ 16 meV and ~ 40 meV modes obtained from IN8 and IN20 data. The dashed lines show the calculated dispersion for the obtained average $J' = -0.0073$.

FePS$_3$ is thus shown to be a good approximation of a two-dimensional system, and studies of the excitation spectra can thus focus on the in-plane high symmetry directions showing a more dispersive behaviour, and the data can be integrated over Ql.

Excitation spectra in the (a,b) plane

The magnetic excitation spectra of FePS$_3$ in the (a, b) plane were measured on the Merlin thermal time-of-flight spectrometer at ISIS, using the sample made of seventeen co-aligned crystals (described in 1.2.2). As FePS$_3$ was shown to have negligible interlayer coupling, the sample was oriented with $\mathbf{k}_i//\mathbf{c}^*$ and the data were integrated over Ql in order to obtain the magnetic excitation spectra along and perpendicular to $(0\ k\ 0)$ (discussion of this method in 1.1.8). Multiplexing was possible on the Merlin spectrometer, and thus the scattering for two incident energies were collected at the same time : 31.8 meV and 75 meV at a temperature of 7 K. The datasets were are analysed in monoclinic units as energy slices of $S(\mathbf{Q}, \omega)$ either along $(0\ k\ 0)$ or perpendicular to $(0\ k\ 0)$, the latter corresponding to slices along $Q = (h\ k\ -h/3)$ for several values of k.

Figure 3.17.a shows a slice in reciprocal space at $k = 1$ for the incident energy E_i=75 meV. This corresponds to the high symmetry direction $(0, 0)$ to P shown in the inset of figure 3.7. The dispersion along this direction was expected to be highly dispersive from the results of [97], and this single crystal data show that it is indeed the case. The colorbar is in arbitrary units and will be the standard for the colorplots of all the energy slices from the Merlin dataset.
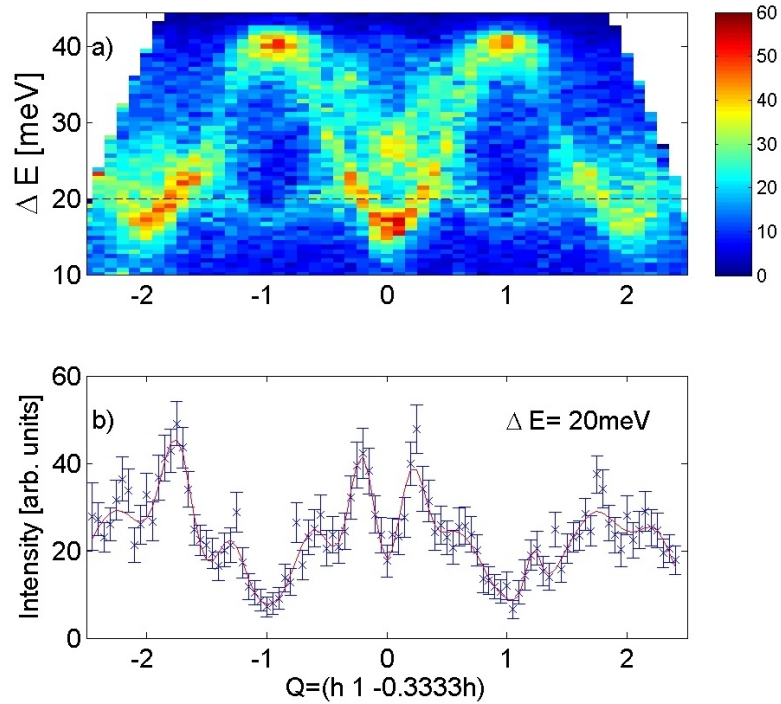

Figure 3.17: a) Merlin energy slice along $Q = (h\ 1\ -0.333h)$ for an incident energy E_i of 75 meV and a temperature of 7K.
b) One-dimensional cut of the energy slice along $Q = (h\ 1\ -0.333h)$ at constant energy transfer $\Delta E = 20$ meV with energy integration $dE = \pm0.5$. The red line is a fit of the spin waves by Gaussian functions.

One dimensional cuts were extracted from these energy slices and fitted with Gaussian functions in order to extract the spin wave energies ΔE_c as a function of Q. Figure 3.17.b shows an example of the fit of a one-dimensional cut for (h 1 $-0.333h$) at an energy transfer of $\Delta E = 20$ meV with an energy integration of $dE = \pm 0.5$ meV.

Figure 3.18a-c shows the results of the fits of the spin wave dispersion energies, represented as white circles superimposed on the energy slices along a) (h 1 -0.33h) for $E_i = 75$ meV, b) (h 1.5 -0.33h) for $E_i = 75$ meV and c) (0 k 0) for $E_i = 31.8$ meV. For Figure 3.18a-b, the fits were done for constant-energy scans with $dE = \pm 0.5$ meV, while for the perpendicular direction (0 k 0) shown in figure 3.18.c, the fits were done for constant-Q scans with $dQ = \pm 0.075$ [r. l. u.].
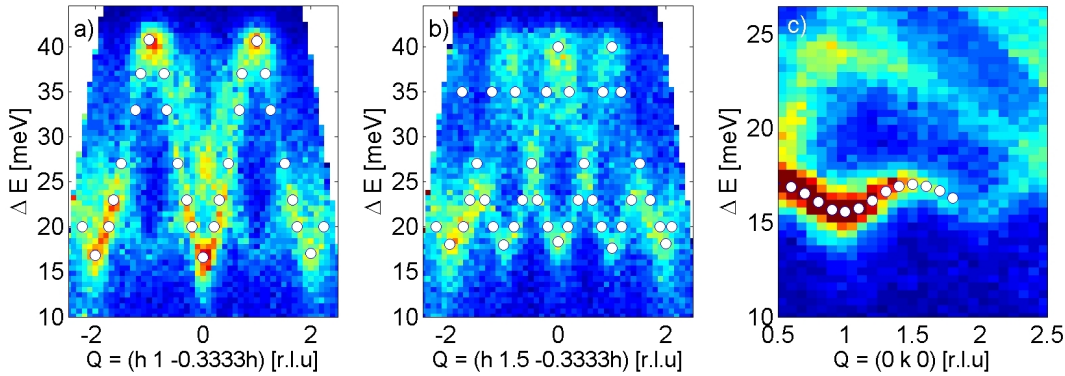

Figure 3.18: Merlin Energy slices at 7K along three high symmetry directions with results of the fits of the spin wave energies shown as white circles. a) Energy slice along (h 1 -0.33h) for an incident energy $E_i = 75$ meV. b) Energy slice along (h 1 -0.33h) for an incident energy $E_i = 75$ meV. c) Energy slice along (0 k 0) for an incident energy $E_i = 31.8$ meV.

In figure 3.18a and c, there is some inelastic scattering signal for which the extracted energies were not taken into account in the refinement of the exchange parameters. Indeed, they appear inconsistent with the expected spin wave dispersion : around $h = 0$ and $\Delta E \sim 25$ meV for figure 3.18.a and dispersive modes up to $\Delta E \sim 25$ meV in figure 3.18.c. These features are due to the spin wave dispersion of the two other magnetic domains, which have been shown in section 3.2.1 to be rotated by 120° in the (a, b) plane.

Additional spurious scattering that cannot be explained by spin waves of the other domains is also present in figure 3.18.c as an arc of intensity from ~ 24 meV at (0 0.5 0) to 17 meV at (0 2.5 0) and extra scattering in the top right-hand corner. However, this scattering was also present for an empty sample holder, so that they can be identified as instrumental background and not as magnetic contributions.

From the work done in [97], the spin wave dispersion was expected to be extremely weak in the energy slice along (0 k 0). However, figure 3.18.c shows that the spin wave dispersion is larger than expected, although still relatively weak. It seems that FePS$_3$ is no so close to being one-dimensional material as what was previously thought, with more exchange interaction than expected between ferromagnetic chains.

The obtained spin wave energies were then fitted with the expression for the spin-wave dispersion given in eq. 3.6 obtained from the diagonalisation of the effective Hamiltonian. In this case the model is extended to three dimensions in order to take into account the averaged weak interlayer coupling $J' = -0.0078$ meV obtained in the previous section.

The model for a three-dimensional magnetic unit cell is shown in Figure 3.19, comparing one of the magnetic sublattice to the monoclinic unit cell. The in-plane vectors of the magnetic unit cell $\mathbf{a}_{mag}$ and $\mathbf{b}_{mag}$ are identical to the previously used $\mathbf{a}_h$ and $\mathbf{b}_h$ in [97], and the transformation matrix for the Miller indices between a magnetic sublattice and the monoclinic unit cell is :

$$
\begin{bmatrix} h \\ k \\ l \end{bmatrix}_m = \begin{bmatrix} 1 & 0 & 0 \\ 1 & 1 & 0 \\ 0 & \frac{1}{2} & 1 \end{bmatrix} \begin{bmatrix} h \\ k \\ l \end{bmatrix}_{mag}
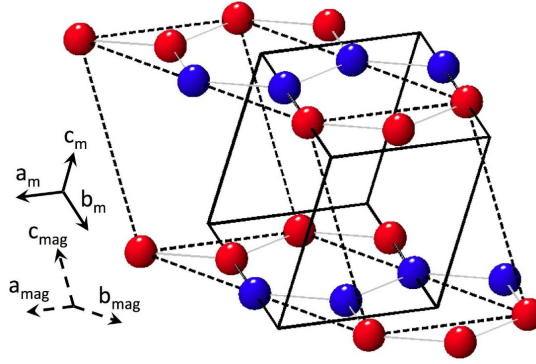\tag{3.8}
$$

Figure 3.19: One of the four interlocking primitive sublattices used to calculate the dynamical structure factor, compared to the monoclinic unit cell. Red and blue spheres correspond respectively to spin up and spin down moments. $a_{mag} = a_h = a_m$ and $b_{mag} = b_h = 2a_h$ correspond to the two dimensional hexagonal unit cell used in [97] with $\gamma_{mag} = 120°$. The lattice parameter $c_{mag} = \frac{a_m}{3}\sqrt{7 + \tan^2 \beta}$, with $\alpha_{mag} = 126.7°$ and $\beta_{mag} = 83.1°$.

The overall form of the effective Hamiltonian H_M is the same as the 2D Hamiltonian on a honeycomb lattice in [97], and adding the interlayer coupling J' only leads to the following modifications of the components A, C and D in the Hamiltonian given in eq 3.5 :

$$
\begin{aligned}
A &= 2J_2\cos(2\pi h) - \Delta - J_1 + 2J_2 + 3J_3 + 4J' \\
B &= J_1\exp(\tfrac{2\pi i}{3}[2h + \tfrac{k}{2}])(1 + \exp(-2\pi i h)) \\
C &= 2J_2(\cos(\pi k) + \cos(2\pi[h + \tfrac{k}{2}])) + J'\cos(\pi[k + 2l]) \\
D &= \exp(\tfrac{2\pi i}{3}[2h + \tfrac{k}{2}]) \\
&\quad \times (J_1\exp(-2\pi i[h + \tfrac{k}{2}]) + J_3(2\cos(\pi k) + \exp(-2\pi i[2h + \tfrac{k}{2}]))) \\
&\quad + 2J'\exp(\tfrac{\pi i}{3}[h + k])\cos(\pi[h + k + 2l])
\end{aligned}
\tag{3.9}
$$

111

The obtained best exchange parameters are listed in Table 3.4 and compared with the results that had been obtained from the fit of the density of states in [97]. Figure 3.20 shows the resulting dispersion for four directions of the excitation spectra using the new exchange parameters, showing overall agreement of the calculated dispersion with the data.

Table 3.4: Exchange parameters in meV obtained from the excitation spectra from single crystals on Merlin compared to the exchange parameters from [97]

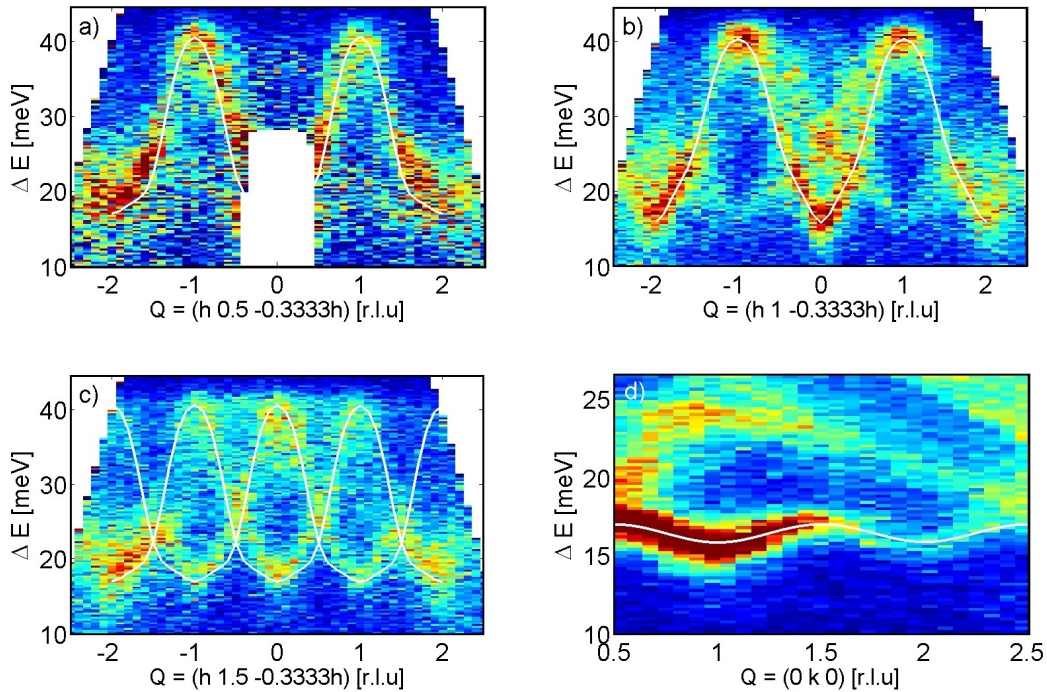|	J_1	J_2	J_3	J'	Δ
Best fit parameters	1.46(1)	-0.04(3)	-0.96(5)	-0.0073(3)	2.66(8)
Parameters from [97]	1.49 (3)	0.04 (3)	-0.6(2)	-	3.7(3)

Figure 3.20: Merlin Energy slices at 7K along four high symmetry directions with the calculated dispersion using the best fit exchange parameters shown as white curves.

These new exchange parameters were then used to simulate $S(\mathbf{Q}, \omega)$ for one domain, using an artificially broadened Damped Harmonic Oscillator function such as the one described in equation 2.10. The damping Γ width was increased in order to take into account the instrumental resolution. In order to compare with the scattering neutron intensity, the calculated intensities were multiplied with the isotropic Fe^{2+} magnetic form factor squared. Figure 3.21 shows the result of the simulation for one domain along Q directions that can be compared directly with the energy slices shown in Figure 3.20. In addition, the dashed lines represent the expected spin wave dispersion of the other two domains.
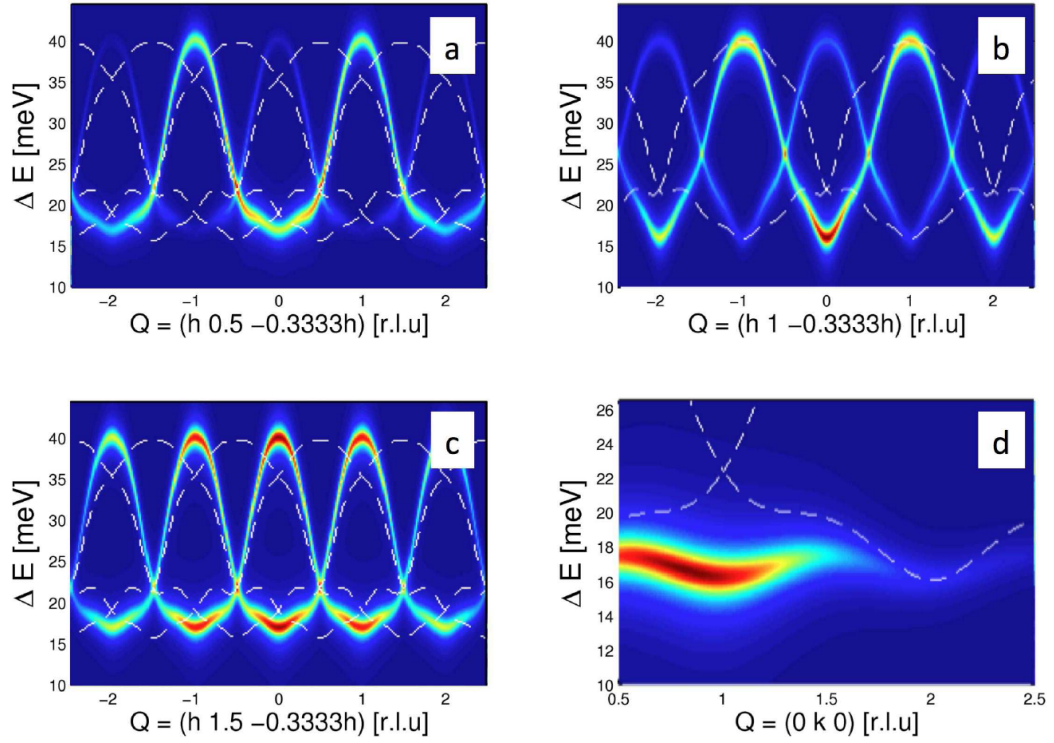
Figure 3.21: Simulation of S($\mathbf{Q}, \omega$) for one magnetic domain using the best estimates for the exchange parameters in FePS$_3$. The dashed lines correspond to the simulated dispersion of the spin waves from the other two domains.

Overall the agreement is good, with the modelled intensity variation corresponding roughly to what was observed in the experimental data, in particular for the dispersion along (0 k 0) and (h 1 -0.33h) in figure 3.20.b and d. Some discrepancies with the dispersion observed in the neutron data exists do exist, visible in particular in the wider and rounder shape of the calculated dispersion along (h 0.5 -0.33h) and (h 1.5 $-$0.33h) shown in 3.20.a and c. This cannot be resolved within this set of exchange parameters, and appears to come from the increase of J_3. A balance between J_3 and the anisotropy Δ cannot thus be completely obtained, so that they may be compensating for additional weak effects that are not taken into account when using this particular Hamiltonian to describe the spin waves in FePS$_3$. In particular, the construction of this Hamiltonian only takes into account equivalent exchange parameters for equivalent distances between the moments. However, each moment is ferromagnetically coupled to two of its nearest neighbour and antiferromagnetically to the third. Considering non-equivalent exchange interactions between equidistant neighbours could be a possibility in order to reproduce more closely the measured magnetic dynamical structure factor.

To conclude this study of the magnon dynamics, FePS$_3$ is found to be a good model compound for a quasi two-dimensional anti-ferromagnet, with an interlayer coupling that has a negligible effect on spin waves dispersion. In addition, modelling the exchange interactions using an

Heisenberg Hamiltonian with a single ion anisotropy appears to reproduce the essential characteristics of the excitation spectra obtained using inelastic neutron scattering, and the exchange parameters previously evaluated from the density of states in [97] could be refined. Furthermore, FePS$_3$ is shown not to be as close to a 1D compound as expected. Indeed, the obtained exchange coupling between third nearest neighbour J_3 is estimated to a substantially larger value than for the powder data, with the magnitude of the anisotropy correspondingly decreasing. Although weak, the spin waves clearly show a dispersive behaviour along $(0\,k\,0)$ as shown in figure 3.20.d.

Critical properties

In order to expand the discussion on the phase transition in FePS$_3$, the temperature dependence of both the magnetic Bragg peaks,the spin gap and the quasi elastic scattering in powdered samples were studied on the thermal time of flight spectrometer IN4 and the polarised diffractometer D7 at the ILL.

Concerning the experiment on the thermal time-of-flight spectrometer IN4 , the FePS$_3$ powder pellets were stacked in Al foil with mutually orthogonal axis in an attempt to minimize preferred orientation and inserted in a helium cryo-refrigerator. Initial measurements showed no difference in the inelastic spectra as a function of sample rotation, so that the rotation was kept fixed for the subsequent measurements. The temperature dependence of the magnetic Bragg peaks was measured using a wavelength of 3 Å, while the inelastic response were measured using a wavelength of 1.1 Å, giving a resolution of 3.8 meV at the elastic line.

The intensity of the $Q = 1.61$ Å^{-1} Bragg peak was integrated over the full energy range for each measured temperature between 1.5K and 150K with an incident wavelength of 3 Å. The resulting temperature dependence of magnetic order parameter was then fitted using the 2D Ising model on a honeycomb lattice which was derived for S=1/2 in [109], following the work in [100] :

$$M(T) = \left(1 - \frac{16z^3(1+z^3)(1+z^2)3}{(1-z^2)^6}\right)^{\frac{1}{8}}$$
(3.10)

with $z = \mathrm{e}^{-2K}$ for $K = \frac{2SJ}{k_B T}$. The critical exponent $\frac{1}{8}$ corresponds to a typical Ising power law computed for the Onsager's exact solution for the 2D Ising model on a square lattice.
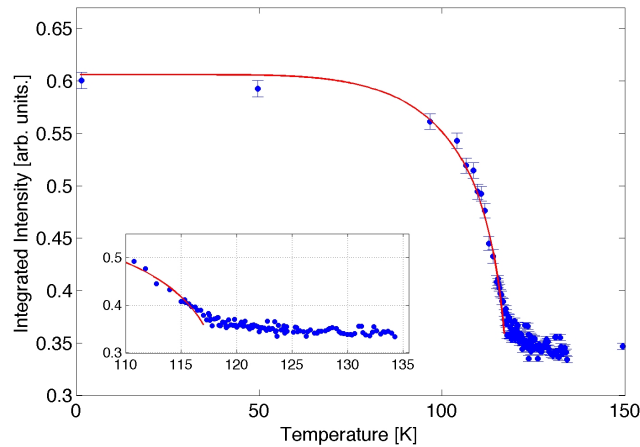

Figure 3.22: Temperature dependence of magnetic order obtained from integrating the measured intensity corresponding to the Bragg Peak at $Q = 1.65$ Å^{-1}. The red line is a fit of the data by the equation 3.10 with parameter $2SJ = 6.19 \pm 0.01$ meV (71.83 K).

This model only takes into account one exchange parameter J for a nearest neighbour anti-ferromagnetic interaction, which is known not be sufficient to describe fully the interactions in FePS$_3$. Nevertheless, the obtained $J = \frac{6.19}{2S} = 1.55$ meV for $S = 2$ is close to the best fit value shown in Table 3.4, so that this model describes well the temperature dependence of the magnetic order parameter in FePS$_3$.

The inelastic scattering was also measured on IN4 with $\lambda = 1.1$Å for temperatures between 1.5K and 294K. Figure 3.23 shows the obtained excitation spectra as a function of $|\mathbf{Q}|$ at 1.5K. The expected scattering from magnon is clearly visible at low Q, with a spin gap of ~ 16 meV, and the excitations extend up to ~ 40 meV. However, as Q increases, the spectrum becomes clearly dominated by non-magnetic excitations from ~ 10 meV, which can be attributed to phonon excitations.
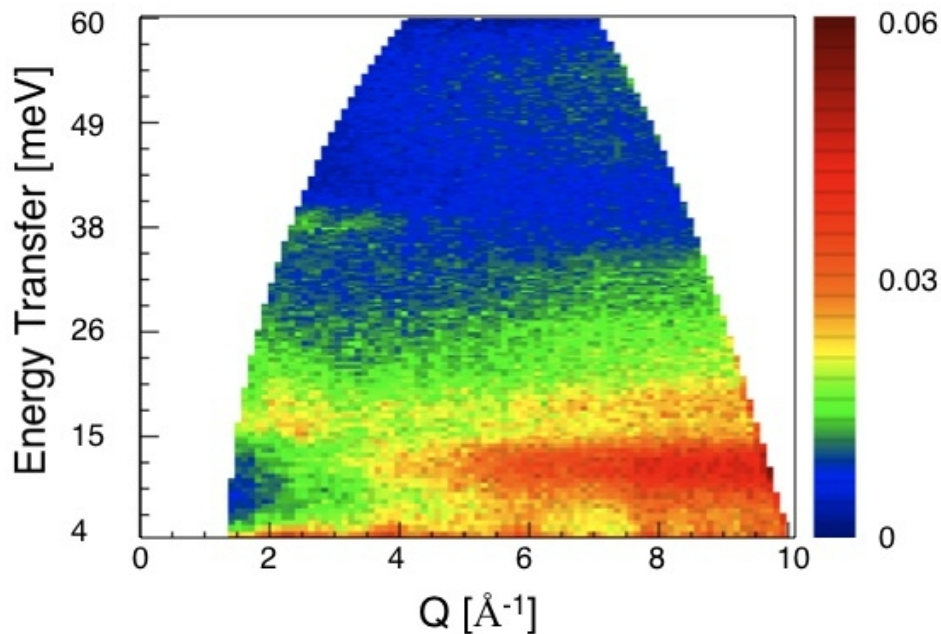
Figure 3.23: Inelastic spectra at 1.5K as a function of $|\mathbf{Q}|$ obtained on IN4 with wavelength 1.1A. The high Q part of the spectrum is clearly phonon dominated.

In order to establish the temperature dependence of the spin gap, the phonon contributions to the inelastic spectra were estimated and subtracted from the dataset, to obtain only the magnetic scattering such as shown by figure 3.24 for 1.5K. The obtained spectrum is phonon-free and the magnon density of state is clearly separated from the background. Nevertheless, there is additional spurious scattering around ~ 7 meV between 3 and 6 Å, which is likely an artifact of the analysis.
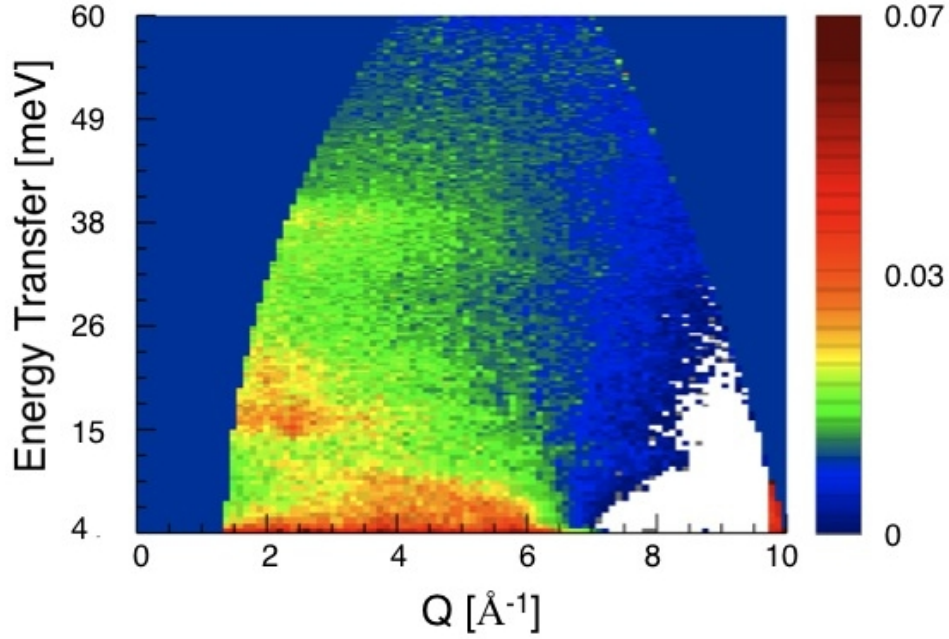
Figure 3.24: Magnetic excitation spectra at 1.5K as a function of |Q| obtained on IN4 with wavelength 1.1A after phonon substraction showing the density of states of the spin waves between ~ 16 meV and ~ 40 meV.

The phonon subtraction was performed for each measured temperature using the following procedure, which will be detailed in the case of the 1.5K spectra.

The coherent differential scattering cross section for one phonon scattering is given in [9] as :

$$
\left(\frac{d^2\sigma}{d\Omega d\omega}\right)_{coh} = \frac{k_f}{k_i}\frac{(2\pi)^3}{v_0}\sum_{\boldsymbol{\tau}}\sum_{j,\mathbf{q}}\frac{1}{\omega_j}\left|\sum_i \frac{\bar{b}_i}{\sqrt{m_i}}\exp(-2W)\exp(i\mathbf{Q}\cdot\mathbf{R}_i)(\mathbf{Q}\cdot\mathbf{e}_i^j)\right|^2
$$
$$
\times [n(\omega)+1]\delta(\omega-\omega_j)\delta(\mathbf{Q}-\mathbf{q}-\boldsymbol{\tau}) \tag{3.11}
$$

which includes the dynamical structure factor $\left|\sum_i \frac{\bar{b}_i}{\sqrt{m_i}}\exp(-2W)\exp(i\mathbf{Q}\cdot\mathbf{R}_i)(\mathbf{Q}\cdot\mathbf{e}_i^j)\right|^2$ showing that the intensity is proportional to a factor $(\mathbf{Q}\cdot\mathbf{e}_i^j)^2$ with $\mathbf{e}_i^j$ the polarization vector of the phonon mode. Thus the intensity of the phonon mode follows a quadratic dependence on |**Q**|. This factor also means that only the component of the displacement along the direction of momentum transfer is probed by neutrons. In addition, the intensity of a phonon depends inversely on its energy as shown by the $\frac{1}{\omega_j}$ factor, and the Bose factor $[n(\omega)+1]$ is also energy dependent.

The higher Q excitation spectrum shown in figure 3.23 follows this characteristic intensity dependence, and thus it can be clearly attributed to phonons. All these factors will be taken into account in order to model the phonon intensity as a function of |**Q**| and ω. The exact dispersion of the phonons in FePS₃ were not calculated (although phonon dispersion curves

117

were derived in [110]), and a phenomenological energy dependence was obtained for each temperature.

To summarize the procedure, the elastic line was first fitted with a Lorentzian function at low temperature and low Q. The phonon modes were then obtained by fitting constant-**Q** cut of the inelastic spectra with Gaussian functions at low temperature and for a high Q. The Q-dependence of the phonon modes was then obtained by fitting a constant-energy cut of the inelastic spectra at low temperatures. Finally, these parameters were fixed, and the intensity of the obtained phonon excitations was scaled as a function of temperature.

The fitting procedure of the inelastic scattering at constant-Q was done at $Q = 6.7\,\text{Å}^{-1}$, chosen as large as possible in order to have no magnetic scattering in the spectra. Indeed, as detailed in 1.1.6, the magnetic intensity is proportional to the magnetic form factor squared $f(|\mathbf{Q}|)^2$ and thus decreases as $|\mathbf{Q}|$ increases. Figure 3.25 shows the isotropic magnetic form factor squared $f(|\mathbf{Q}|)^2$ for Fe^{2+} from which it is clear that there is only phonon scattering in the constant-Q cut at $Q = 6.7\,\text{Å}^{-1}$.
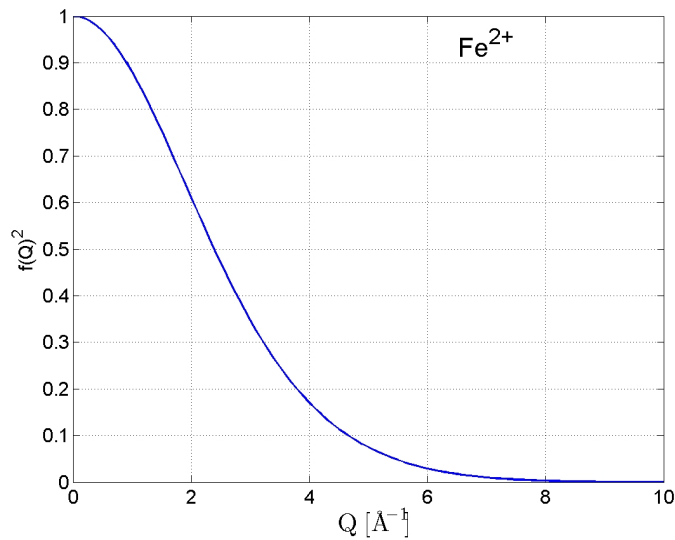
Figure 3.25: Isotropic magnetic form factor for Fe^{2+}. At $|Q| = 6.7\,\text{Å}^{-1}$, the magnetic form factor squared is reduced to less than 1.5%

Figure 3.26 shows the result of the fit of to phonon modes for the constant-Q cut at $Q = 6.7$ Å^{-1} (with $dQ = 0.1\,\text{Å}^{-1}$) with Gaussian functions, with the line-shape of the elastic peak fixed from a Lorentzian fit done at low Q. Indeed, the elastic line of the time-of-flight spectrometer IN4 has an asymmetric line-shape, and the phonon excitation around 10 meV can be well separated from the elastic line by fixing its fitted parameters. From this we obtain the intensity of the phonon modes as a function of energy for $Q = 6.7\,\text{Å}^{-1}$.

Figure 3.26: Result of the fit of the constant-Q cut at $Q = 6.7 \, \text{Å}^{-1}$ (dark blue line). The individual phonon modes are fitted with Gaussian functions (green curves). The elastic line (cyan curve) was fitted by a asymmetrical Lorentzian function fixed from low Q cuts.
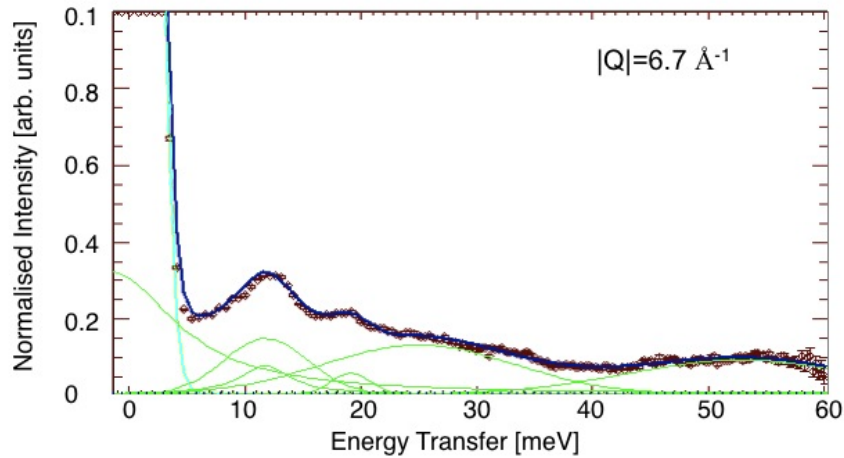
In order to obtain the variation of the phonon scattering intensity as a function of Q, the phonon mode at 50 meV was fitted with a quadratic function. Figure 3.27 show the Q^2 dependence of the phonon intensity.
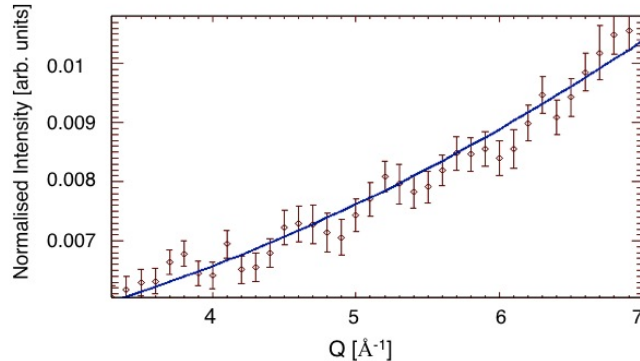
Figure 3.27: Fit of the 50 meV phonon mode as a function of Q for the phonon-dominated region.

Finally, the Bose factor can be computed as a function of energy and temperature. As the temperature increases, this factor will be very important in order to properly account for the phonon modes. For each data points in $(2\theta, \omega)$ space, the corresponding $|\mathbf{Q}|$ was calculated. Fixing the previous results for the energy-dependence, the Q-dependence and the Bose factor, the phonon intensity is then calculated as a function of $|\mathbf{Q}|$ and ω for each data points, and subtracted from the measured scattered intensity. Converting the obtained spectra into $(|\mathbf{Q}|, \omega)$ space, a phonon-free excitation spectrum is obtained, such as the one shown in figure 3.24. This procedure was followed for each temperature, modifying the Bose factor accordingly.

In order to obtain the temperature dependence of the magnetic density of states, the phonon-subtracted dataset in $(2\theta, \omega)$ space was integrated over the low 2θ angles (13-28 degrees), corresponding to $Q < 4.2$ Å^{-1}. Figure 3.28 shows the resulting inelastic spectra for a few selected temperatures, which only contains magnetic scattering. The gap appears to be renormalised towards lower energies as the temperature increase, and to go rapidly towards zero close to the Néel temperature. There is some apparent residual scattering at 150K around 10 meV, which can be attributed to strong ferromagnetic quasi-elastic scattering coming up against the kinematic constraints of the measurement.
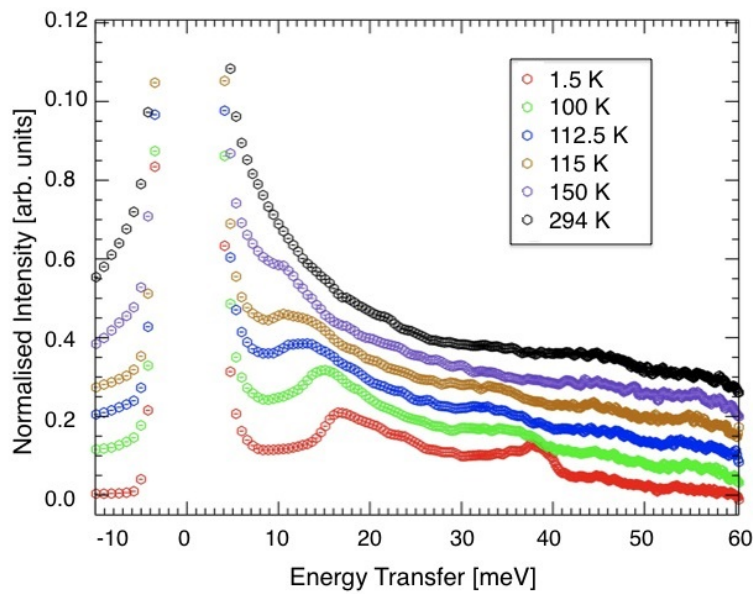

Figure 3.28: Magnetic scattering as a function of energy transfer after phonon subtraction for selected temperature : at base temperature at 1.5K (red), at temperature close to the Néel temperature, and well above the Néel temperature at 294 K (black).

Figure 3.29 shows the evolution of the spin gap as a function of temperature, obtained from the IN4 data after phonon subtraction and integration over the low 2θ angles. The gap appears to fall rapidly close to the Néel temperature, and broad and intense quasi elastic scattering starts to develop above T$_N$. From this it is not obvious whether the gap goes down to zero close to the critical temperature, due to the overlap with strong quasi-elastic scattering, for which the DHO width can be estimated to be $\Gamma_{QE} \sim 10$ meV.

The resulting temperature dependence of the spin gap can be compared with the inelastic spectra obtained on Merlin for an E_i of 31.8 meV. Figure 3.30 shows energy slices along (h 0.5 $-0.33h$) for four temperatures, two below the Néel temperature (7K and 109K) and two above (133K and 300K). The arc of weak scattering around 23 meV stays constant with temperature, and was shown to be spurious by measurements of an empty sample holder.
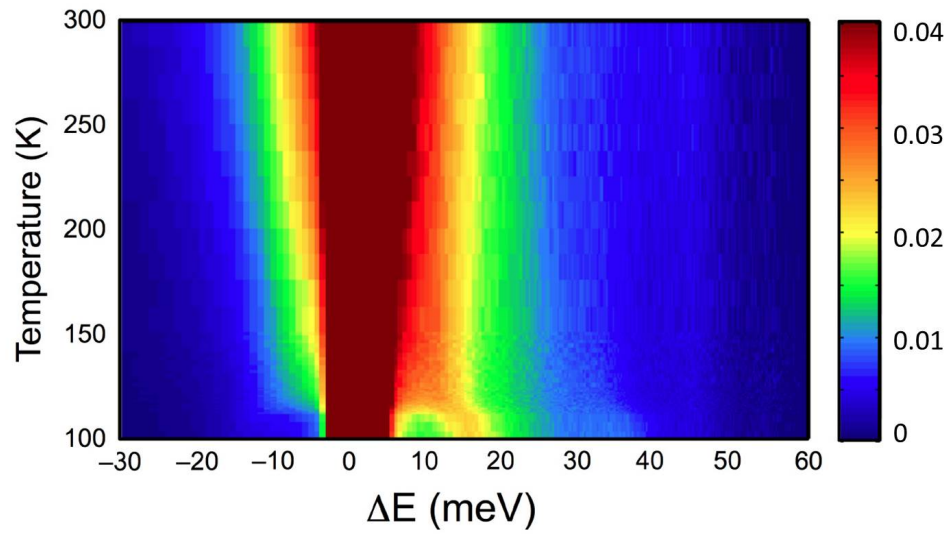
Figure 3.29: The low angle inelastic spectra as a function of temperature, after phonon-substraction, showing the evolution of the spin gap and the quasi-elastic scattering close to the Néel temperature.
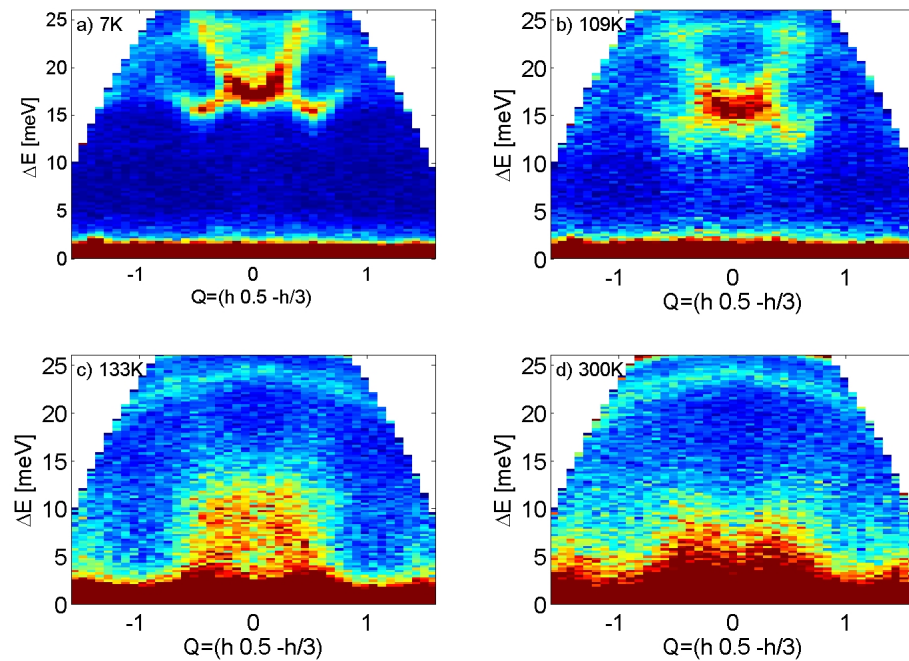

Figure 3.30: Energy slices of the E$_i$ = 31.8 meV Merlin dataset on a single crystal (experiment describe in 3.2.2), showing the spin wave dispersion along Q=(h 0.5 -h/3) at four temperatures: a) 7K, b) 109K, c) 133K and d) 300K.

The inelastic spectrum along (h 0.5 $-0.33h$) shown in figure 3.30 helps to clarify the temperature dependence of the gap just above the critical temperature. Indeed, the gap does completely disappear, as shown by figure 3.30.c at 133K. Combining with the IN4 results, the spin gap is thus shown to renormalise from 16 meV to ~ 10 meV as the temperature increases from 1.5K to ~ 115K, and then it drops down rapidly to zero close to the critical temperature. This drop of the spin gap appears to be concomitant with the onset of strong quasi-elastic scattering, which dominates the spectrum well above the critical temperature.

To focus on the nature and the temperature dependence of the quasi-elastic scattering around the Néel temperature, a polarised neutron experiment was carried out using the diffuse scattering spectrometer D7 at ILL, using the powder-pellets sample of FePS$_3$ inserted in a helium cryo-refrigerator. The instrument was configured with an incident wavelength of 3.2 Å, corresponding to E_i=9.61 meV. As no energy analysis was used, and with a wavelength cut-off set based on the sample width (~ 13 mm), each detector measured the scattering energy-integrated between -45 and 9.61 meV. All the data was scaled using the D7 calibration method (see 1.1.9), with the size and shape of the quartz and vanadium approximately matching the sample. The scattering from the sample was also converted to absolute units (barns sr^{-1} f.u. $^{-1}$).

Initial measurements were performed with XYZ polarisation analysis at 1.4K, 140K and 300K, in an attempt to separate the magnetic scattering and the combined nuclear coherent and isotropic incoherent scattering from the nuclear spin incoherent scattering. However, as the sample showed preferred orientation, the magnetic scattering was not independent on the direction of **Q**, and the separation failed at 1.5K and 140K. At 300K, the impact of preferred orientation was lower, and figure 3.31 shows the three cross sections obtained.
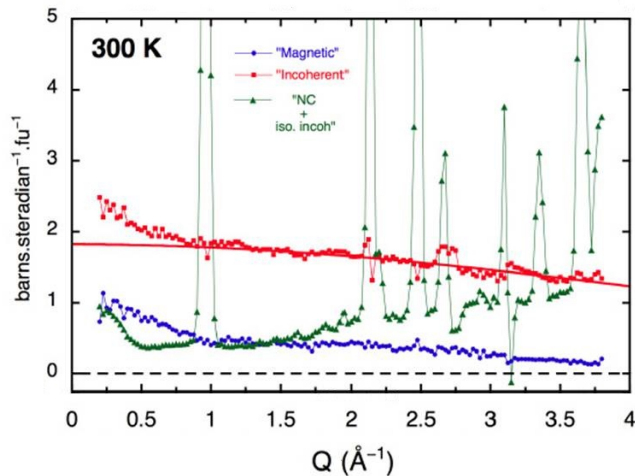

Figure 3.31: Magnetic (blue), incoherent (red) and combined nuclear coherent and spin incoherent scattering (green) cross sections obtained on D7 for FePS$_3$ at 300K.

Figure 3.31 shows a surprising large nuclear spin incoherent cross section compared to the contribution of FePS$_3$ alone, which can be calculated from tabulated values[10] to be 0.0075 in barns sr^{-1} f.u. $^{-1}$. A usual source for large incoherent cross-section would be hydrogen, and thus it is likely that water has been adsorbed in the powder samples of FePS$_3$ (frequent in this family of compounds, in particular for NiPS$_3$[111, 112]).

Due to the large preferred orientation, the experiment was then carried out with the polarization directed along **Z** only . In this case, the spin flip cross section corresponds to 2/3 of the nuclear spin incoherent cross section added to the magnetic cross section for the magnetization perpendicular to **Q** and **Z**. The temperature dependence of the spin-flip cross section measured is shown in figure 3.32, which shows the expected loss of intensity of the magnetic Bragg peaks at T$_N$. In addition, the intensity of the lowest Bragg peak is transferred to strong scattering intensity in the forward direction just above T$_N$.
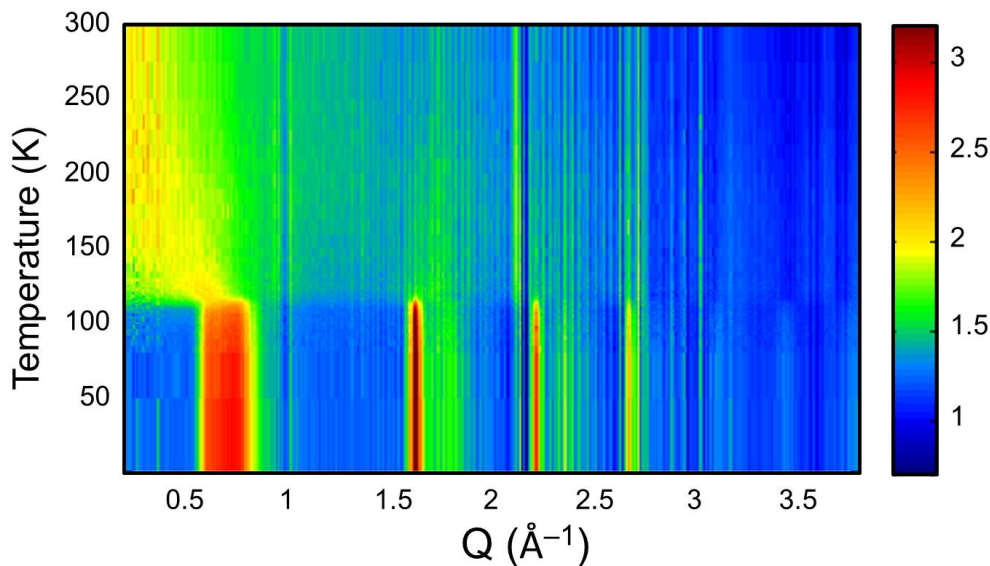
Figure 3.32: Spin-flip cross section as a function of temperature for FePS$_3$ with polarisation along **Z**

In order to study this transfer of intensities towards lower Q, the spin-flip cross section was integrated over two Q-ranges as a function of temperature. The first Q-range corresponds to integrating over the magnetic Bragg peak around $Q \sim 1.65$ Å^{-1} and the other corresponds to the low $Q < 0.4$ Å^{-1}, well below the lowest magnetic Bragg peak. Figure 3.33 presents these integrated intensities as a function of temperature, which clearly shows that the onset of the low Q scattering corresponds to the decrease of the magnetic Bragg peak intensity.

As the strong magnetic scattering above T$_N$ is at far lower Q than any magnetic Bragg peak, it can be attributed to an increase of ferromagnetic short ranged correlations. As the long-range magnetic order disappears at T$_N$, it thus appears to concomitant with an increase of

Figure 3.33: Spin-flip cross sections integrated over two different Q range: in blue is shown the integrated intensity of a magnetic Bragg peak for $1.5 < Q < 1.7$ Å^{-1} while in red the integration is done over the $Q < 0.4$ Å^{-1} range.

ferromagnetic short-range order. These results are consistent with previous inelastic scattering spectra obtained in [97], from which a transition to strong one-dimensional ferromagnetic fluctuations was suggested.

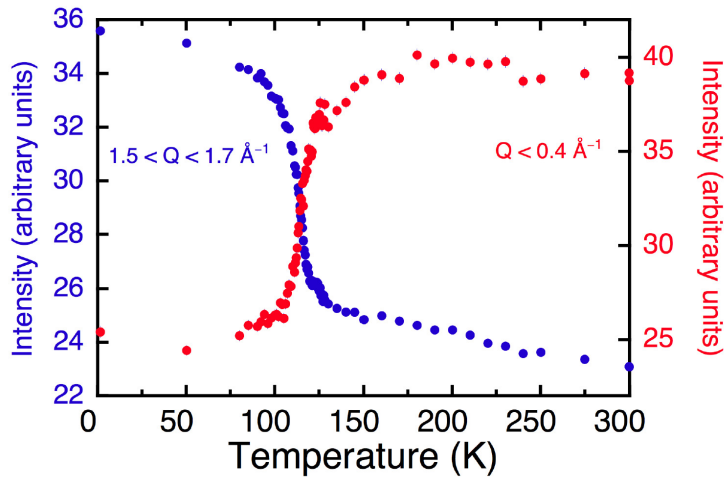Regarding the critical properties of FePS$_3$, the magnetic order transition is shown to be well modelled by a 2D Ising model on a honeycomb lattice. In addition, the spin gap measured as a function of temperature is shown to drop abruptly to zero close to T_N, concomitant with an increase of strong quasi-elastic scattering. Polarized neutron results indicate the onset of ferromagnetic short-ranged correlations close to T_N so that the quasi-elastic scattering appears to be largely magnetic. As evidenced by the drop of the spin gap close to T_N, it appears that the magnetic anisotropies in FePS$_3$ follow a first order transition, which is coherent with the previous measurements of specific heat, lattice parameters changes and Mössbauer spectroscopy [103, 106, 104]. There is no long-range magnetic order above T_N, however quasi-elastic short-ranged magnetic correlations appear close to the transition temperature and persist up to room temperature. As discussed in 3.2.1, there are strong ferromagnetic interactions along the chains at low temperatures, and weak antiferromagnetic interactions between the chains. The short-ranged ferromagnetic correlations appearing at the critical temperature could then well be along this chain direction, with no correlations between the chains. One can imagine either one-dimensional ferromagnetic short-ranged order, or two dimensional short-ranged order due to the collinear stacking of the chains perpendicular to the (a, b) plane. Neutron scattering on powdered samples cannot confirm or infirm either of these hypothesis, although they are consistent with the observed magnetic scattering around T_N.

3.2.3 High-field magnetisation

A tricritical point, derived in thermodynamical theoretical studies of 2D Ising system on a honeycomb lattice in a transverse field[113, 114, 115], may exist in FePS$_3$ at large fields (above 50T). Investigation of the magnetisation of FePS$_3$ at such high fields requires pulsed fields such as the ones available at the High magnetic Field lab of Los Alamos National Laboratory, USA.

Beyond the 2D Ising model on a square lattice solved by Onsager[116], the unsolved 2D Ising model in external non-zero magnetic field, despite its apparent simplicity, is a model that predicts possible tricritical points and quantum phase transition. Of particular interest is the 2D honeycomb lattice in a transverse field, which has the lowest coordination number ($z = 3$) for 2D lattices. The thermodynamics of this type of lattice have been studied using the following Hamiltonian :

$$H = -\sum_{i,j} J S_i^z \cdot S_j^z - \Delta \sum_i (S_i^z)^2 - \Omega \sum_i S_i^x \qquad (3.12)$$

with J the magnetic exchange parameter, Δ a single ion anisotropy and Ω an external transverse field. Using this model for $S = 2$, a tricritical point was reported in [115, 113, 114] depending either on the ratio of the anisotropy to the exchange or on the transverse field applied to the exchange, with possible quantum phase transition. The importance of the field direction is shown in [117], with calculations using a random field instead of a transverse field yielding no tricritical point. Figure 3.34 shows an example of the predicted tricritical point in [113] for a 2D Ising system with $S = 2$ in a transverse field, with a possible tricritical point at the junction between first order and second order phase transitions between a disordered phase and ordered phases, for a ratio $\Delta/J = -1.32$ and a ratio $\Omega/J \sim 1.1$.

FePS$_3$ is a potential candidate compound for testing these theories, as it has an honeycomb lattice and a large single ion anisotropy, and has been shown to behave as a 2D material. FePS$_3$ has more exchange interactions, so that it is difficult to estimate whether the ratio of anisotropy to the exchange corresponds to the value necessary for tricritical point. An rough estimation of the critical field can be obtained in [115], given by

$$\Omega = S \frac{8}{5\sqrt{5}} J(z-1) \qquad (3.13)$$

with z the coordination number. In the case of FePS$_3$, using an estimate of $J = J_1 = 1.46$ meV, $S = 2$ and $z = 3$, the estimated critical field is 4.18 meV, which corresponds to ~ 72 T. Using the results in [113], the estimated field would rather be $\sim 28 T$. An estimated value for the ratio anisotropy to exchange parameter in FePS$_3$ is $\Delta/J = -1.82$.

Evidence for a critical point in a Kagomé lattice with $S = 5/2$ had been found in the antiferromagnet KFe$_3$(OH)$_6$(SO$_4$)$_2$ [118], with a corresponding theory described in [119] predicting a tricritical point at T$_c$=47.3K and H$_c$=12.9 T. The signature of a possible tricritical point in this
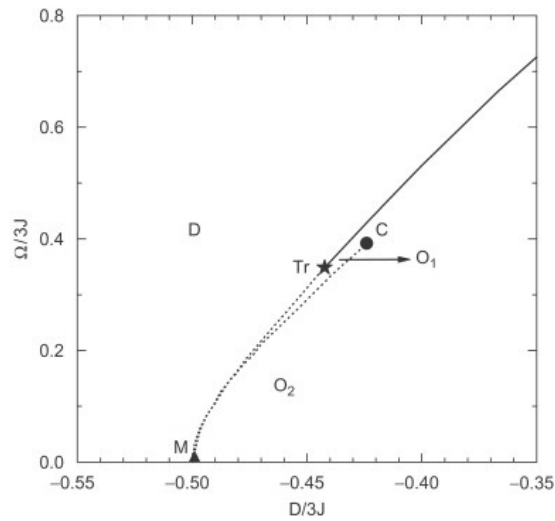
Figure 3.34: Ground-state phase diagram as a function of anisotropy ratio ($D/3J$) and the transverse field ratio ($\Omega/3J$) calculated in [113]. The tricritical point Tr is between a disordered phase D and two ordered ferromagnetic phases O1 and O2. The dotted line denotes a first-order transition, and the solid line a second-order transition.

compound was found by combining magnetization measurements and neutron spectroscopy to understand the nature of transitions as function of field and temperature, making high field measurements a starting point for searching for a tricritical point in FePS$_3$.

In FePS$_3$, no tricritical point is expected for a longitudinal field. The high field magnetization in this orientation was already measured in [120, 121] for a maximum applied field of either 38 and 45 T. These previous results show a transition as a two step process, with an hysteresis smaller than 2T for base temperature, as shown by Figure 3.35 from [121]). These results have been reproduced in [120].

An experiment to measure the magnetisation in a 65 T pulsed field was carried out at the High magnetic Field lab of Los Alamos National Laboratory, USA. The extraction technique was used, with a probe measuring dM/dt for two configurations, either with the sample inside the probe's coil or without the sample (corresponding to measuring the background). The data was then time-integrated for both configurations. Background subtraction was done by simple subtraction of the two configurations (with and without the sample). The magnet was calibrated and checked using 10T pulse, adjusting the gain to optimize the signal to noise ratio. The 65T pulses lasted about 10 ms. For faster cooling down to 4K, the sample space was flooded with liquid helium.

Two samples with different alignment were measured, one with a field applied along the moment direction **c***, and one with the field applied in the (a, b) plane, along **b**.
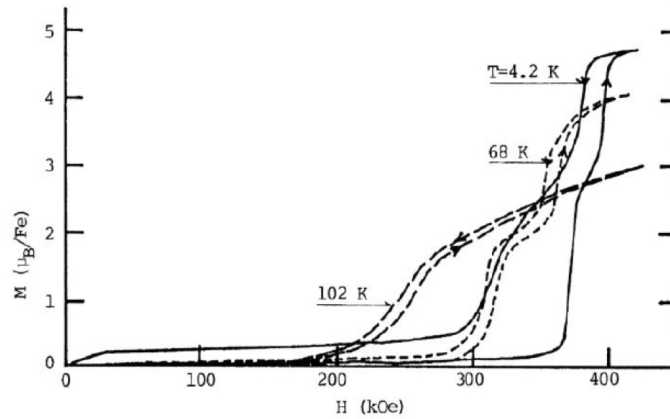
Figure 5 : Magnetization curves of FePS$_3$ at 4.2 K, 68 K and 102 K. The applied magnetic field are parallel to the Z-direction.

Figure 3.35: Results for **H**//**c*** from [121] with a maximum pulsed field up to 45 T showing a two step process with a small hyteresis

Applied Field along c*   Figure 3.36 shows the magnetisation as a function of applied field at 4K and 100 K for respectively a 65 T pulsed field and a 50 T pulsed field. At 4K, a very large hysteresis is present, with a transition at 44.05 T when the field increases, and a transition at 23.9 T when the field decreases. At 100K the hysteresis is still present, but the magnetisation does not show any sharp transitions. These results show large discrepancies with the two-step process with a small 2 T hysteresis previously measured in [99].

Figure 3.36: Magnetisation as a function of applied field **H**//**c*** at 4K and 100K showing a very large hysteresis at base temperature. The direction of the arrows shows whether the data was obtained upon an increase or a decrease of the applied field.

Applied Field along b   For the second sample, the magnetisation was measured for a transverse field **H//b**, with maximum pulsed fields between 30 and 65T. Figure 3.37 shows the magnetisation curve as a function of maximum applied field. Focusing on the 65 T pulse, when the field increases a l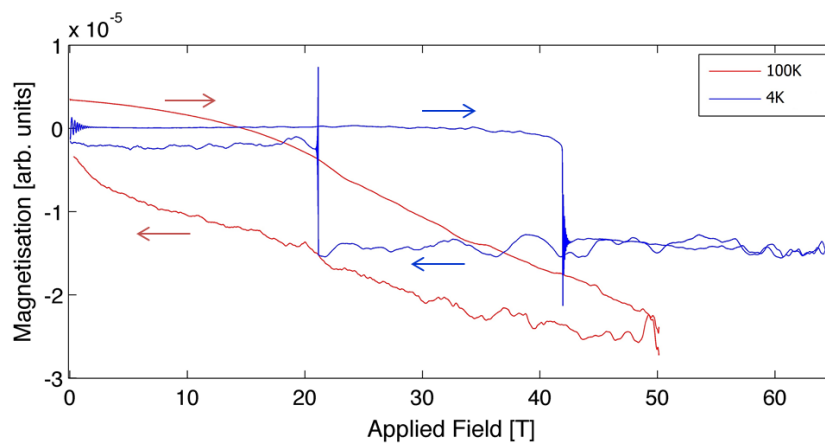inear behaviour is observed up to 35 T, followed by a broad transition up to 45 T, and another linear behaviour from 45 T to the maximum field. When the field decreases, we observe a linear behaviour down to 21.5 T, a sharp transition, and a linear behaviour back to zero. The sharp transition as the field decreases is not observed for a maximum applied field of 30, 38, 44 or 47 T. This transition only appears for 50,55 and 65 T, with a different amplitude and at slightly varying fields.
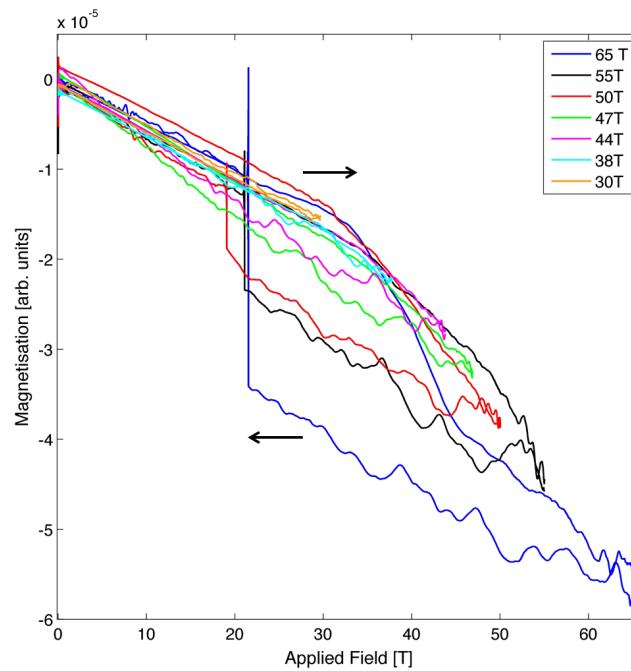
Figure 3.37: Magnetisation as a function of field for different maximum field. Applied Field along **b**.

These variations as a function of maximum applied field for pulses $\geqslant$ 50 T are shown in figure 3.38 for maximum applied fields of 50, 55 and 65T. No sharp transition appeared for a maximum applied field lower than 50T. The transition field increases as the maximum applied field increases and the variation of magnetisation is also larger with larger maximum field.

Figure 3.39 shows the temperature dependence of the magnetisation for three different temperatures (4, 25 and 50K). Although smaller (5T), there is still an hysteresis at higher temperatures, but the transitions appears to be a gradual two step process instead of a sharp transition. The behaviours when the field is ramped up and down seems to become more symmetrical.

As mentioned in the set-up, the sample were immersed in liquid ^{3}He(for faster cooling) for both **H//c*** or **H//b** measurements. To check the reproducibility of the measurements, a 65T pulsed magnetization measurement was done after warming up to 200K, and cooling
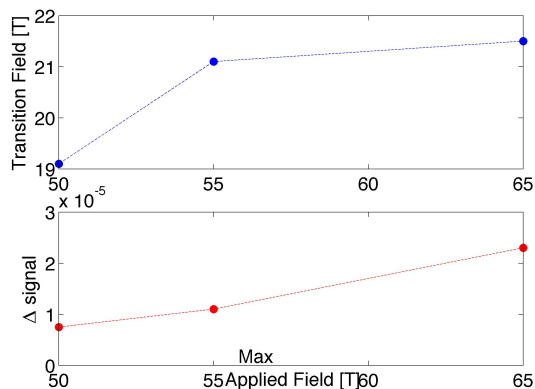
Figure 3.38: Transition field and amplitude of the transition as a function of the maximum applied field for sample 2. Applied Field along **b**.
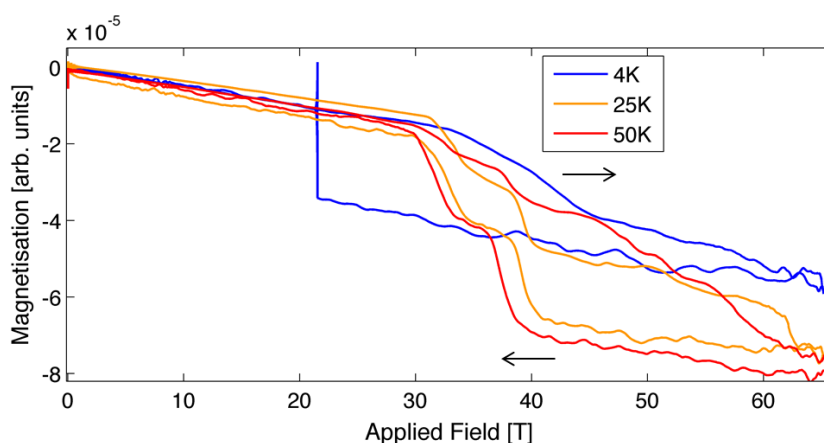
Figure 3.39: Magnetisation as a function of field for different temperatures (4K, 25K, 50K). Applied Field along **b**.

back to 4K without flooding sample space with liquid helium. In that case, the sample is surrounded by gaseous helium. This 4K measurement is shown in figure 3.40, compared to another 4K pulse for which there was liquid helium around the sample. Surprisingly, these two magnetisation profiles show very large discrepancies : in the 4K data without liquid helium around the sample, the size of the hysteresis is drastically reduced to $\sim 5T$, and the transitions show a symmetrical slow two-step process at higher transition fields compared to the other measurements. Hence it appears that heat exchange with liquid helium plays an important role in the thermodynamic properties of FePS$_3$.
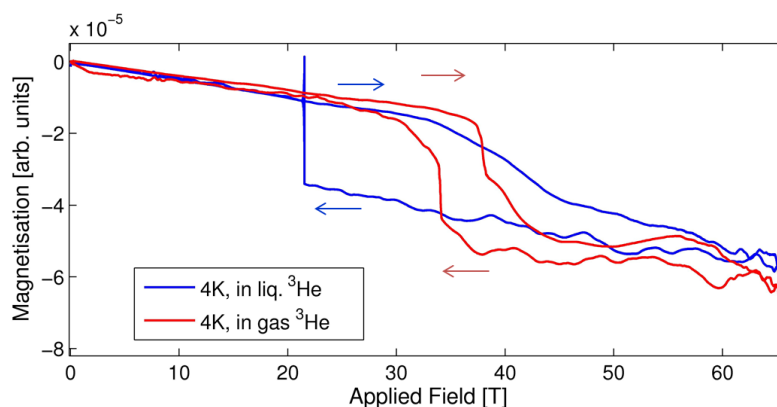
Figure 3.40: Magnetisation for 4K and 65T pulse at different time during the experiment. Applied Field along **b**.

Dependence of magnetisation on the presence of liquid or gaseous helium   A follow-up experiment was carried out[2] at the High magnetic Field lab of the Los Alamos National Laboratory in order to compare the effect of the presence of either liquid or gaseous helium in sample space on the transitions.

In figure 3.41, the data obtained for **H//c*** shows that when the liquid helium is replaced by exchange gas, the sharp transition with a large hysteresis is replaced by with a smaller hysteresis and a two step smooth transition at 35 and 39T for increasing applied field and 41 and 39.5T for decreasing field. The magnetisation behaviour observed in [121, 120] was thus retrieved in the gaseous helium case. From these results, it appears that the transition field and behaviour of these transitions, as well as the size of the observed hysteresis is very dependent on the heat exchange with the environment. Note that the magnetisation data do not return to the same value at zero field. As this was not observed in the first experiment, it is likely to be an artefact of the analysis.

The magnetisation was also measured both in liquid and gaseous helium for the other field orientation **H//b**, and the results for a maxiumum applied field of 65 T are shown in figure 3.42. In that case the magnetisation data in gaseous showed qualitatively similar transitions to the liquid helium case. This contrasts with previous results shown in figure 3.40, where the magnetisation at 4K after boiling off the liquid helium resulted in a smooth two step process with a small hysteresis, closer to what was measured at 25 and 50K . It is therefore likely that the sample was not effectively in thermal equilibrium at 4K before the field pulse in the first experiment.

In conclusion, for an applied field along **b**, the magnetisation data is characterised at low temperatures by a smooth transition as the field increases, and a sharp transition as the field decreases. As the temperature is increased, the sharp transition moves to higher field, and

---

[2]by Andrew Wildes
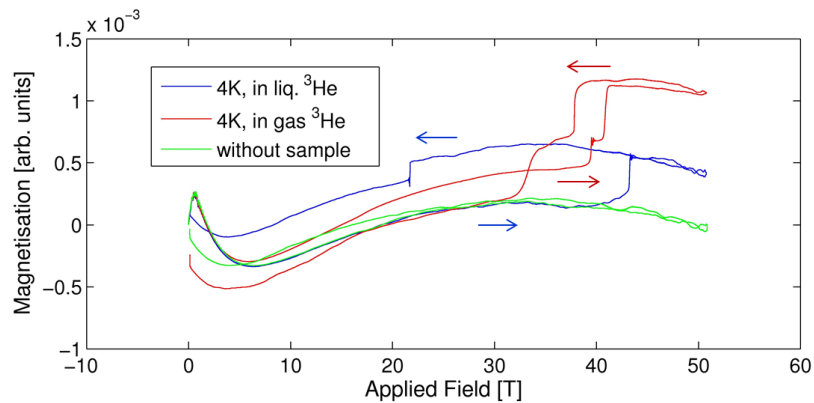
Figure 3.41: Magnetisation for a 50T pulse depending on whether the sample is in liquid or gaseous helium. Applied Field along **c***.
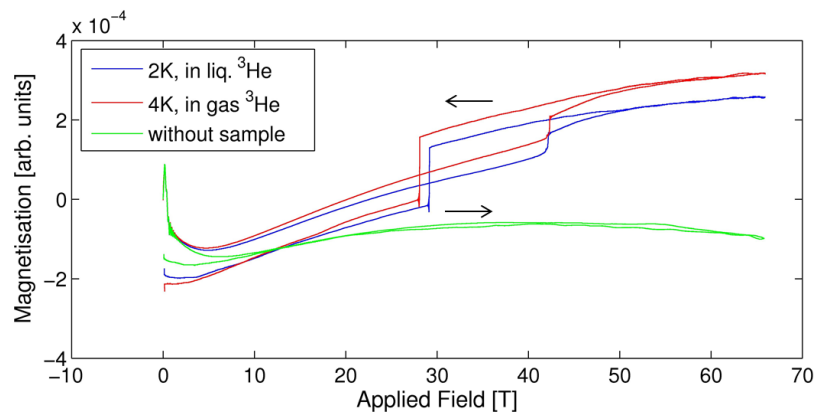
Figure 3.42: Magnetisation for a 65T pulse depending on whether the sample is in liquid or gaseous helium. Applied Field along **b**.

the hysteresis reduces in magnitude, with smoother two-step transitions appearing (shown in figure 3.39). This change with temperature from a sharp to a smooth transition suggests that a tricritical point may be present within this temperature range, with a first order transition at low temperature and a second order transition at higher temperatures (above 25 K).

In this case, the applied field was oriented along **b**, and thus perpendicular to some of the ferromagnetic chain. As discussed in 1.2.3, the identified $(0\ k\ 0)$ direction from a Laue pattern could also be identified as $(h\ h\ 0)$ or $(h\ \bar{h}\ 0)$. In addition, there are 120°-rotated magnetic domains in the sample due to rotational twinning, so the field is perpendicular to the ferromagnetic chains from only one domain. Characterisation of the domain population of the measured sample would allow to quantify this.

Moreover, it would be interesting to measure the magnetisation for a transverse field along the direction of the ferromagnetic chains (along **a**), to observe whether it has a strong impact on

the magnetisation properties. This would also allow to compare with the model derived in [113] for a tricritical point between disorder and ferromagnetic order.

Furthermore, the difference between liquid and gaseous helium shows the impact of non-adiabatic measurements on magnetisation. In liquid helium, the heat exchange is more efficient, so that the sample is likely to cool down during the field pulse, leading to drastically different magnetisation behaviour. On the other hand, a more adiabatic measurement can be done in exchange gas, with little heat exchange between the sample and its environment.

3.3 NiPS$_3$

3.3.1 Introduction to the magnetic structure

Similar to MnPS$_3$, the paramagnetic susceptibility of FePS$_3$ is shown to be largely isotropic [35] above the Néel temperature T$_N$=155K. The magnetic structure is similar to FePS$_3$, with ferromagnetic chains that are antiferromagnetically coupled. However, the $S = 1$ moments are pointing in the (a, b) plane in NiPS$_3$, creating a zigzag-type magnetic order, similar to the two-dimensional XY antiferromagnet BaNi$_2$(AsO$_4$)$_2$ [122] and the $S = 1/2$ compound Na$_2$IrO$_3$, which has been proposed as a realisation of the Kitaev-Heisenberg model [123].

The study of the magnetisation and magnetic structure in [35] combined susceptibility measurements and neutron diffraction on both powder and single crystals. The results showed discrepancies with previously published results. In particular, the susceptibility above T$_N$ was shown to be isotropic, unlike the anisotropic behaviour measured in [124, 125]. Furthermore, the magnetic propagation vector was confirmed to be $\mathbf{k}$ =[0 1 0] with the moments pointing mostly along a, unlike the previous conclusion in [88] of moments along c. Figure 3.43 from [35] shows the proposed magnetic structure of NiPS$_3$ with various orientations, along with the results of the refinement of the magnetic structure.
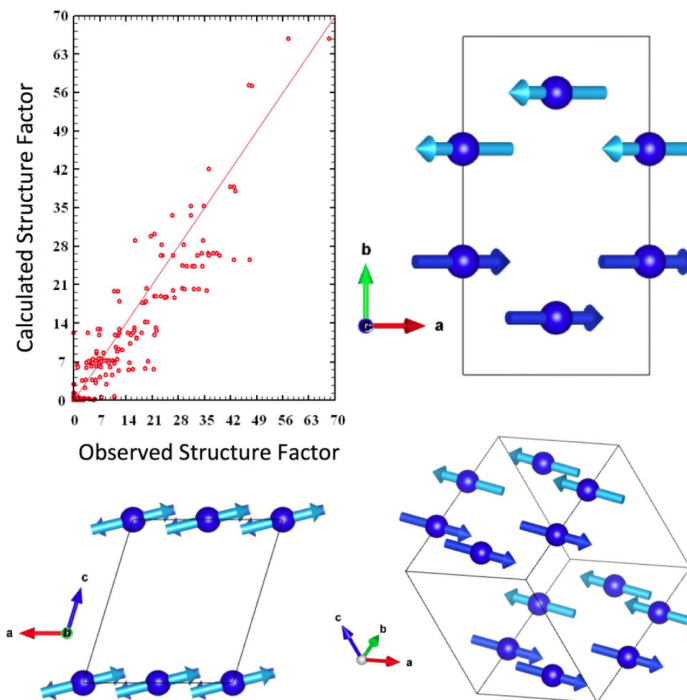

Figure 3.43: Figure from [35] showing the observed versus calculated structure factor of NiPS$_3$ using the best model, along with the obtained magnetic structure viewed with different orientations.

133

These discrepancies are explained by two sources of errors. The first is preferred orientation of powder samples due to the softness of the materials which leads to a sliding of the weakly bound planes when grinding, which is also thought to be the case for FePS$_3$ in the results in 3.2.1 and 3.2.2. The second difficulty with these sample is their sensitivity to glue, which leads to modification of the susceptibility depending on whether or not the sample is glued to a support. Careful considerations of these difficulties in [35] confirmed the magnetic propagation structure as **k** =[0 1 0], as previously identified in the review [88], however the moments are shown to point mostly along a. In addition, the strongly anisotropic susceptibility observed in [124, 125] were explained by the strain of the glue which conserves the magnitude of magnetization but increases measured anisotropies.

3.3.2 Spin waves

Based on anisotropic susceptibilities measured in the 45 to 65 K range, an Heisenberg Hamiltonian with a single-ion anisotropy was used to describe the system in [125]. The nearest neighbour exchange parameter J and single ion anisotropy D were calculated using from a modelling of the anisotropic susceptibility to be $J = -5$ meV and $D = 1.39$ meV. The nearest neighbour interaction is stated as antiferromagnetic despite the similar magnetic structure of NiPS$_3$ to FePS$_3$. In addition, the study in [35] showed that the compound was much less anisotropic than previously though. Nevertheless, this rough estimation suggests that the spin waves will disperse in the 15-20 meV energy range, which is a range suitable for thermal neutron experiments. In addition, an excitation was found at $\Delta E \sim 65$ meV energy transfer from Raman spectroscopy and were interpreted as anomalously broad two magnon process [126]. Neutron inelastic scattering is well suited in that case to measure and check whether this 65 meV feature is indeed magnetic.

A set of four successive experiment was carried out in order to investigate of the spin wave dynamics on 10.5g powder samples : triple axis spectrometry on TAIPAN (ANSTO), polarised time-of-flight spectrometry on D7 at ILL and thermal time-of flight experiments on MARI (ISIS) and IN4 (ILL). Only results from MARI and IN4 will be shown and discussed. The common sample for these experiments was composed of three compressed pellets of NiPS$_3$ powder stacked with 90 degrees rotation to each other in order to limit the effect of preferred orientation discussed in 3.3.1.

The first conclusive experiment was carried out on the direct thermal time of flight instrument MARI at ISIS. The three pellets were stacked in Al foil and cooled to 4.7K. The slices of energy as a function of $|Q|$ were obtained at incident energies E_i of 15, 30, 110 and 200 meV in order to check both the low energy excitation and the 65 meV energy transfer range. In addition, the high incident energy scans allowed access to the lowest Q range, at the cost of resolution in energy.

Figure 3.44a shows the intensity as a function of $|Q|$ for an incident energy of 30 meV . There are strong phonon modes at large Q and a broad feature around $Q = 1.2$ Å^{-1} and $\Delta E = 3.5$ meV,

which could correspond to the weak signal observed on D7. In addition, there appears to be a very steep dispersive magnon mode centred at $Q = 0.6\,\text{Å}^{-1}$ which starts to appear at $\Delta E = 6$ meV. The position $Q = 0.6\,\text{Å}^{-1}$ corresponds to a strong magnetic Bragg peak.

(a) Incident energy $E_i = 30$ meV (~ 65 hrs)

(b) Low Q data for $E_i = 200$ meV (~ 40 hrs)

(c) Full Q range for $E_i = 110$ meV (~ 25 hrs)
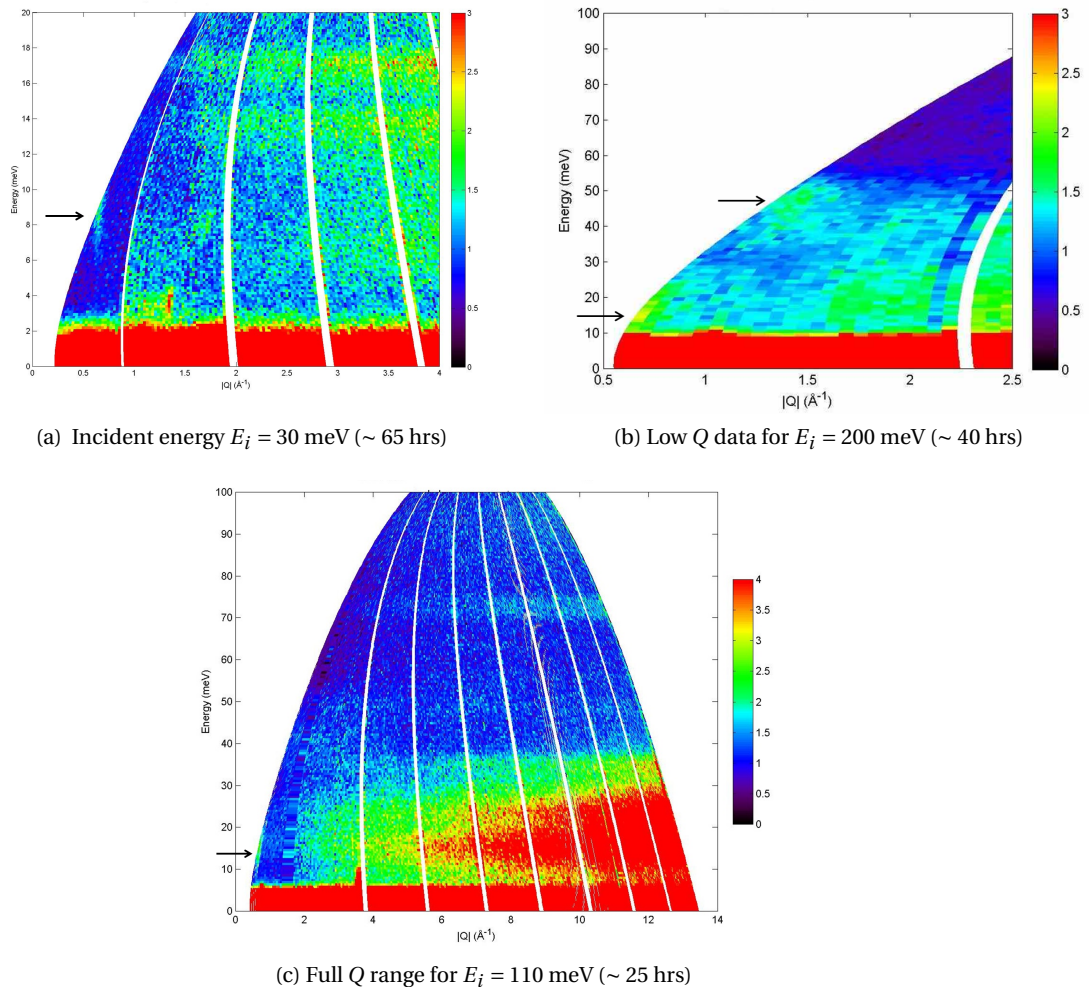
Figure 3.44: NiPS$_3$ scattering intensity as a function of $|Q|$ for three incident energies E_i on MARI : a) 30 meV, b) 200 meV and c) 110 meV). The arrows show the observed inelastic scattering attributed to the magnetic excitations in NiPS$_3$

The results of the scan for an incident energy of 200 meV are shown in figure 3.44b, zoomed on the low $|Q|$ scattering. This confirms the presence of a magnetic scattering at very low Q (close to the kinematic limits) which appears to disperse to $Q = 1.2\,\text{Å}^{-1}$ at $\Delta E \sim 45$ meV. This mode appears to be limited to 55 meV. It is likely that the scattering starting at $Q = 1.5\,\text{Å}^{-1}$ from ΔE=10-30 meV corresponds to the beginning of the phonon mode. Furthermore, figure 3.44c shows the results for an intermediate incident energy of 110 meV. It is clear from this that there are no excitations at the estimated bound magnon energy of 65 meV in the Q range accessed.

Finally, an additional experiment was done on the thermal time of flight spectrometer IN4 at ILL. As the minimum scattering angle is higher on IN4, the kinematic constraints did not allow the low Q magnetic scattering to be measured, so that the aim of this experiment was to check the 3.5 meV feature around 1.2 meV seen on MARI. The sample was composed of the three compressed pellets stacked in Al foil held in a Cadmium slab. Angle between the beam and the Cd slab was about 45 degrees. Two incident energies E_i were measured : 8.74 meV and 31 meV, for a set of 5 temperature between 1.7K and 300K in order to discriminate phonons and magnons. The resulting map (E_i=8.74 meV at 1.7K is shown on figure 3.45) shows no evidence of magnetic scattering in the accessible Q range. The 3.5 meV feature observed at Q=1.2 Å^{-1} on MARI can then be attributed to a spurious event.
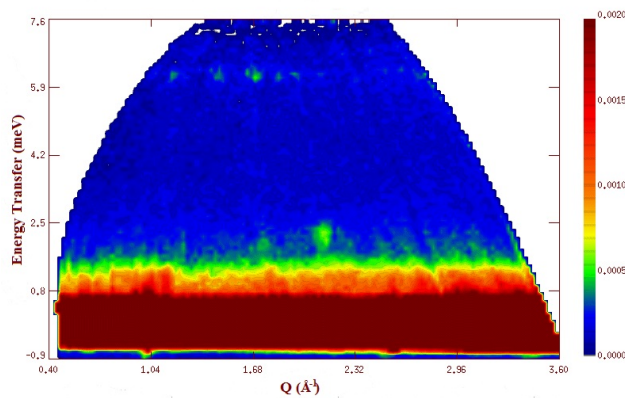
Figure 3.45: Incident $E_i = 8.75$ meV for NiPS$_3$ on IN4 (~ 15 hrs) showing no evidence of any magnetic scattering in accessible $(\hbar\omega, Q)$ range

From this set of experiments, it can be concluded that the spin waves in NiPS$_3$ are strongly dispersive and present only at very low Q. A rough estimation of the spin gap from the results on MARI would be 6 meV. The excitation appears to disperse from 6 meV at $Q = 0.6$ Å^{-1} to 1.2 meV with a maximum energy transfer of 55 meV. No evidence of the bound magnon mode seen in Raman spectroscopy could be found in any of these experiments. The best suited instrument in order to reach these very low Q values in the interesting energy transfer range would be a time of flight spectrometer for small scattering angle inelastic scattering such as BRISP at the ILL. This would allow to check for the presence of a spin-gap below 6-8 meV, expected to be small based on the largely isotropic susceptibilities measured in [35]. A complementary measurement on the time-of-flight spectrometer MAPS at ISIS with a large incident energy of $E_i \sim 500$ meV would allow to focus on the spectral weight at larger energy transfers.

3.4   Conclusions and Outlook

Several conclusions can be reached from focusing on the magnetic excitation spectra of $FePS_3$. The magnetic structure of $FePS_3$ has been clearly shown to have the propagation vector $\mathbf{k} = [01\frac{1}{2}]$, confirmed by refinement of the structure from diffraction measurements. These new neutron scattering results, compared to pre-existing data clarified the discrepancies between propagation vectors proposed in the literature. In addition, rotational twinning has been shown to lead to 120°-rotated magnetic domains about the c^* axis, so that any further study of the dynamical or critical magnetic properties of $FePS_3$ should take these domains into account both for planning experiments and analysing data. Rotational twinning is likely to happen in other members of the MPS_3 family, which may thus have a non negligible effect on collective magnetism.

Taking into account the magnetic domains, the excitation spectra of $FePS_3$ was then successfully modelled by a Heisenberg Hamiltonian with a single ion anisotropy on an honeycomb lattice extended to three dimensions. This brought insight on the strength and nature of the interactions in $FePS_3$. The interlayer coupling was shown to be very small, making this compound a good 2D model system. Furthermore, the overall spectra was well reproduced by the model after refinement of the coupling constants J_1, J_2, J_3 and of the single ion anisotropy Δ. $FePS_3$ appears to be further from a 1D model than what was previously expected, with weak couplings between the ferromagnetic chains. Although a fully satisfactory equilibrium between the interaction J_3 and the anisotropy Δ could not be found, this simple Hamiltonian was shown to explain well the measured spin waves.

The properties of $FePS_3$ at the phase transition are also particularly interesting. Previous contributions from various experimental techniques already existed, each probing different properties. Around the Néel temperature, $FePS_3$ appears to have properties which follow a first order transition. In particular, the temperature-dependence of the spin gap shows a sharp drop to zero close to T_N, so that the magnetic anisotropy disappears following a first order transition. Furthermore, the temperature-dependence of the magnetic order parameter was confirmed to follow the behaviour of a 2D Ising model on a honeycomb lattice. On the other hand, polarized neutron results identified the magnetic nature of the quasi-elastic scattering close to T_N. The hypothesis of a transition from a 2D magnetic long-ranged order to 1D ferromagnetic short-ranged correlations is consistent with the measured quasi-elastic spectra. Powdered samples do not allow to check the direction of the ferromagnetic short-ranged correlations, so that single-crystal measurements should be considered. The expected scattering has been shown to be at low Q and to extend up to $20-30$ meV, so that a thermal time-of-flight spectrometer with a low angle coverage would be necessary, with an analysis further complicated by the magnetic domains. Nevertheless, insight on the correlations could be obtained by measuring the quasi-elastic excitations along and perpendicular to $(0\ k\ 0)$ around the transition temperature in a well-characterised single crystal, for which the population ratios between the domains are known.

Finally, magnetization measurements at high pulsed magnetic fields do hint towards the presence of a tricritical point in FePS$_3$ in the 40-50 T range, with the measured transitions strongly dependent on heat exchange between the sample and the bath. Drastic differences between the magnetisation as a function of applied field exists upon an increase of temperature, with varying transition fields, large hysteresis, and amplitude variations observed for the two sample orientations tested (along $\mathbf{c}^*$ and along $\mathbf{b}$). Measurements with the field in the (a, b) planes, but along the ferromagnetic chain direction (along $\mathbf{a}$) would also give further insight on these transitions. Experiments beyond magnetisation could be attempted, although the required fields are out of the reach of current magnets designed for neutron scattering.

Interestingly, although the crystallographic structure of NiPS$_3$ is very close to FePS$_3$, the inelastic neutron scattering experiments showed that the energy range of the excitations in NiPS$_3$ was unlike what was expected from previous measurements of MnPS$_3$ and FePS$_3$. Magnetic scattering was only observed at low Q, and although kinematic constraints limited this study, the spin waves in NiPS$_3$ were shown to be strongly dispersive up to 40 meV and appear gapped. The ~ 6 meV spin gap gives some insight on possible anisotropies in NiPS$_3$ at low temperatures. Further measurements are needed in order to resolve the spin waves density, using thermal time-of-flight instruments with good resolution for a high incident energy and a small angle coverage in order to access low Q and energy transfers both around 5 meV and up to 40 meV. Single-crystal experiment could be considered, provided sufficiently large good single crystals can be obtained.

This work largely focused on FePS$_3$ with additional work on NiPS_3, but the interest in the magnetic structure, the dynamical and critical properties is not limited to these two transition metals, and other members of the MPS$_3$ family such as CoPS$_3$ may be equally interesting. In addition, synthesising compounds with a ratio of two different transition metals may lead to increased anisotropies or to induced frustration, opening further the possibilities for this family. An example of such compounds is Mn$_{1-x}$Fe$_x$PS$_3$ with $0 \leq x \leq 1$, where measurements of magnetisation and specific heat for different doping ratios demonstrated the existence of a rich magnetic phase diagram [107].

The materials discussed in this chapter behave largely as conventional magnets with magnetic order below a transition temperature. In addition, they are not spin 1/2 so that quantum fluctuations are not at the largest. However, studying the fundamental properties of conventional magnets still raise a large interest, in particular regarding reduced dimensionality. Albeit conventional, magnetic order and magnetic excitations investigations test fundamental magnetism in order to understand the balance between the strength of the exchange couplings and their origin by confronting real materials to model systems. In addition, interesting new behaviours and exotic states of matter upon the application of magnetic field, pressure or at a transition temperature cannot be excluded, and are worthy of both theoretical and experimental investigation. As in the investigated MPS$_3$ family, the variation of the transition metal leads to drastic changes in the magnetism, which illustrates the sensitivity of magnetic properties to their environment. In addition, turning to the application side, two-dimensional magnetic

compounds with weak Van der Vaals forces on a honeycomb lattice have been proposed as potential "magnetic graphene", placing such reduced-dimensionality systems in the context of novel devices, where magnetic properties have to be very well characterized and controlled [93]. The competing interactions becomes crucial in these cases, as well as the temperature dependence of magnetic order, and well-understood two-dimensional test materials are in that respect particularly sought after.

A Ferromagnetism in dilute Mn-doped ZnO

A.1 Introduction to ZnO-DMS

Dilute Magnetic Semiconductors (DMS) have transition ions substituting for the host semiconductor material. Due to the coupling of the localised d electrons of the magnetic ions to the extended electrons of the semiconducting band, DMS have a variety of promising properties [127]. Among these, ferromagnetic DMS have attracted interest as possible components for spintronic devices. In the effort towards controlled electron spin current, some important properties are high Curie temperature and large magnetisation, which makes ZnO a promising candidate in this context [128].

The experimental finding of room-temperature ferromagnetism in Mn^{2+} doped ZnO [129] was followed by a theoretical treatment of high temperature ferromagnetism in dilute magnetic oxides and nitrides [130]. This prediction included a rich magnetic phase diagram as a function of the bound polaron overlap $\gamma^3\delta$ and the dopant concentration x, containing both insulating and metallic ferromagnetic, antiferromagnetic and spin glass phases. Transition-metal doped ZnO (TM-ZnO) were suggested to be promising hosts for room-temperature ferromagnetism, due to the large bound polaron radius expected.

However, the room-temperature ferromagnetism results were disputed and an abundance of contradicting views on DMS arose, with ferromagnetism found in some Mn and Co-doped ZnO studies [131], and not in others [132] (for a review of reported results, see [133]). The main question in all these cases concerns the nature of ferromagnetism in transition-metal doped zinc oxide [134, 128, 135] and whether it depends on the fabrication method[127]. Indeed, in the context of potential spintronics applications, it is crucial to distinguish whether the ferromagnetic properties come from an homogeneous distribution of the transition-metal ion, or from a segregated phase within the semi-conducting matrix[135]. In addition, the experimental difficulty of the detection of non-homogeneous spin distribution and potential contamination further complicates the debate [136]. The most commonly used probe of the presence or absence of clustering, phases and impurities in the samples are XRD patterns[137, 131, 129]. For this, however, elemental contrast between Mn and Zn is poor.

Polarised neutron scattering is a powerful technique for distinguishing between short-ranged nuclear and magnetic order so that it is well-suited to clarify the question of the nature of ferromagnetism in Mn-doped ZnO. They can be combined with standard XRD measurements and magnetisation measurements in order to explain the discrepancies between the results of previous studies of Mn-doped ZnO.

A.2 Sample characterisation

Sample Growth

ZnO crystallises in the wurzite structure, with each Zn^{2+} cation coordinated tetrahedrally by 4 O^{2-} anions. Mn^{2+} is in principle highly soluble in the host matrice, substituting for Zn^{2+} and hole-doping the material. O^{2-} vacancies are also present. Issues such as secondary phases and Mn^{2+} clustering have been encountered depending on the synthesis method, and several synthesis methods have been explored to minimize this effect, such as the decomposition of hydrozincite [138].

Powdered $Zn_{1-x}Mn_xO$ samples were prepared using two synthesis methods, a conventional solid state method and a soft chemistry route [1].
In the first method, Mn-doped ZnO was synthesized by the solid state reaction from Mn carbonate and Zn oxide. A stoichiometric mixture of ZnO and $MnCO_3$ was ground in acetone and annealed in an $8\%H_2$ in N_2 atmosphere at 400°C. The composition of the sample was measured by EDX (Energy dispersive X-ray spectroscopy) and the Mn doping was estimated to $x = 2$ %. The second synthesis method involved decomposition of Mn-doped zinc carbonate produced by hydrothermal treatment of an aqueous solution of Mn nitrate, Zn nitrate and urea, similarly to the method in [138]. The obtained Mn-doped Zn carbonate was then decomposed into Mn-doped ZnO by heat treatment at 400°C in a forming gas ($8\%H_2$ in N_2), introducing oxygen vacancies to have a larger δ parameter. The actual concentration of Mn in the ZnO materials was measured by X-Ray fluorescence with a $30\mu m$ size probe. These measurements show that Mn doping of x=0.59(1), 1.14(1), 1.57(2) and 3.28(2) atomic % were obtained (see Table A.1). As the hydrozincite decomposition proceeds at low temperature, the homogeneity of the transition metal's distribution in the hydrozincite matrix is preserved, provided the concentration of the transition metal is lower than its solubility in ZnO. No gradient in the Zn distribution could be seen in the XRF measurements, so that the sample were homogeneous. Finally, a pure ZnO sample, for which no magnetic scattering is expected, was used as a control. Table A.1 shows a summary of the samples with their corresponding Mn^{2+} concentrations and an abbreviation system for reference.

---

[1] sample synthesis by A. Magrez and D. Fejes at the GCMP, EPFL

Table A.1: List of growth method and Mn^{2+} concentration for each sample, with reference code

Code	Growth method	Mn^{2+} doping %
S_2	solid state	~ 2
$H_{3.28}$	decomposition of hydrozincite	3.28 ± 0.02
$H_{1.57}$	decomposition of hydrozincite	1.57 ± 0.02
$H_{1.14}$	decomposition of hydrozincite	1.14 ± 0.01
$H_{0.59}$	decomposition of hydrozincite	0.59 ± 0.01
ZnO	from supplier	0

XRD Measurements

Most of the works on ferromagnetism in MnZnO used X-ray diffraction (XRD) as their main technique to evaluate the Mn homogeneity in the ZnO matrix [131, 129, 132]. In our case, XRD measurements were carried out on an Empyrean diffractometer (Panalytical)[2]. The X-rays were generated by the K_α emission line of copper, so that the diffraction patterns were measured with Cu K_α radiation ($\lambda = 1.54$Å).
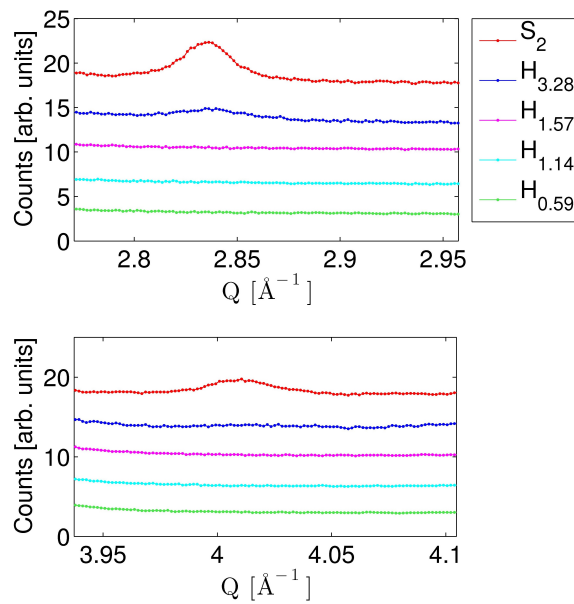
Figure A.1: X-Ray diffraction patterns for the five Mn^{2+} doped samples. The top panel shows the diffraction profile around Q=2.83 Å^{-1} (2θ=40.6°), which corresponds to the (2 0 0) Bragg peak position of MnO. The bottom panel shows the diffraction profile around Q=4 Å^{-1} (2θ=58.8°), corresponding to the (2 2 0) Bragg peak position of MnO.

Fig. A.1 shows the XRD measurements of the Mn^{2+} doped samples around respectively Q=2.83

---

[2]by A. Magrez, GCMP, EPFL

$Å^{-1}$ and Q=4 $Å^{-1}$, corresponding to expected positions for the (200) and (220) Bragg peaks of MnO. The presence of MnO is clearly observed in S_2, the sample grown by the solid state method. In $H_{3.28}$, there may be an indication of the presence of MnO at the scattering angle corresponding to (200) with a very broad signal, but no clear peak appears at the expected Q position for the (220) Bragg peak. For the rest of the samples ($H_{1.57}$, $H_{1.14}$ and $H_{0.59}$), there is no indication of the presence of MnO.

Magnetic susceptibility

DC magnetic susceptibility was measured using a SQUID magnetometer (Quantum Design MPMS). The magnetisation as a function of field was measured at 5K using a conventional hysteresis field sweep between ±5 T.

Fig. A.2 presents the results of the SQUID magnetisation measurements as a function of magnetic field at 5K. The magnetisation of S_2 in Fig. A.2.a shows a clear hysteresis from which a 6480 Oe coercive field can be deduced. Similarly, a smaller hysteresis can be observed in Fig. A.2.b for $H_{3.28}$, with an estimated coercive field of 301 Oe. Very close examination of the magnetisation for the lower doping $H_{1.57}$, $H_{1.14}$ and $H_{0.59}$, shown in the insets of A.2.c-e, shows no clear hysteresis, with an upper limit on the coercive field of 19, 10 and 5 Oe for $H_{1.57}$, $H_{1.14}$ and $H_{0.59}$ respectively.

With the hypothesis of paramagnetism, the magnetisation as a function of field can be modelled by a Brillouin function [139] :

$$M = \frac{1}{2}gN\mu_B \left[(2J+1)\coth\left[(2J+1)\frac{g\mu_B B}{2K_B T}\right] - \coth\left[\frac{g\mu_B B}{2K_B T}\right] \right] \tag{A.1}$$

with :

- J the total angular momentum quantum number
- N represents the number of ions in the sample
- T the temperature [K]
- B the applied field [T]
- μ_B Bohr magneton [J/T]
- K_B Boltzmann constant [J/K]
- g Landé factor g=2

In the case of Mn^{2+}, J= 5/2 and a Brillouin function with N as a free parameter (and a weak constant background) was used successfully to model the data as shown in Fig A.3a-c ,thus confirming the paramagnetic behaviour.
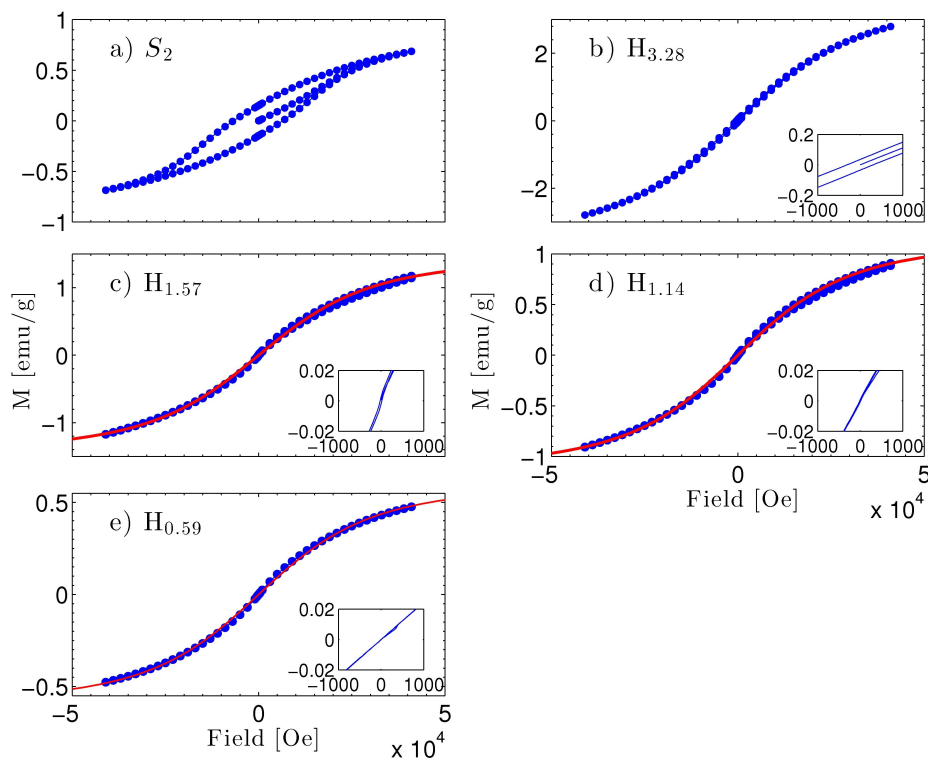
Figure A.2: Magnetisation as a function of field at 5K. Panel a corresponds to the sample grown with the solid state method S_2, while panels b-e concern the samples grown via the decomposition of hydrozincite $H_{3.28}$, $H_{1.57}$, $H_{1.14}$ and $H_{0.59}$. Calculated Brillouin function for S=5/2 is shown in red for panels c-e. The inset shows the region around H=0; only S_2 (a) and $H_{3.28}$ (b) show any hysteresis.

A.3 Polarised neutron scattering results

The polarized neutron experiments were performed on two polarized diffractometers, D7 [24] at ILL, France and DNS[25] at FRMII, Germany. On DNS, the incident wavelength was 4.13 Å, while two incident wavelength were used on D7: λ =3.1 and 4.8 Å. The samples all weighed ~ 10g and were loaded in aluminium cans of 20mm diameter and 6 cm height. A set of coils around the sample position rotated the polarization into one of three orthogonal directions for XYZ polarization analysis[23], and the outgoing polarization was analysed by another set of supermirror benders. A total of six cross sections were collected : spin flip and non-spin flip for each field orientation at the sample position. The different contributions to the scattering cross section (magnetic, spin incoherent and nuclear and isotope incoherent) were then separated by a linear combination of these cross sections. All the data was scaled using the D7 calibration method (see 1.1.9) and converted to absolute units (barns sr^{-1} f.u. $^{-1}$). The scaling to absolute unit was checked to be correct within 10%. This check was done by fitting the powder diffraction pattern from the ZnO crystallographic information file (cif)

(a) Brillouin function fitted to $H_{1.57}$

(b) Brillouin function fitted to $H_{1.14}$

(c) Brillouin function fitted to $H_{0.59}$
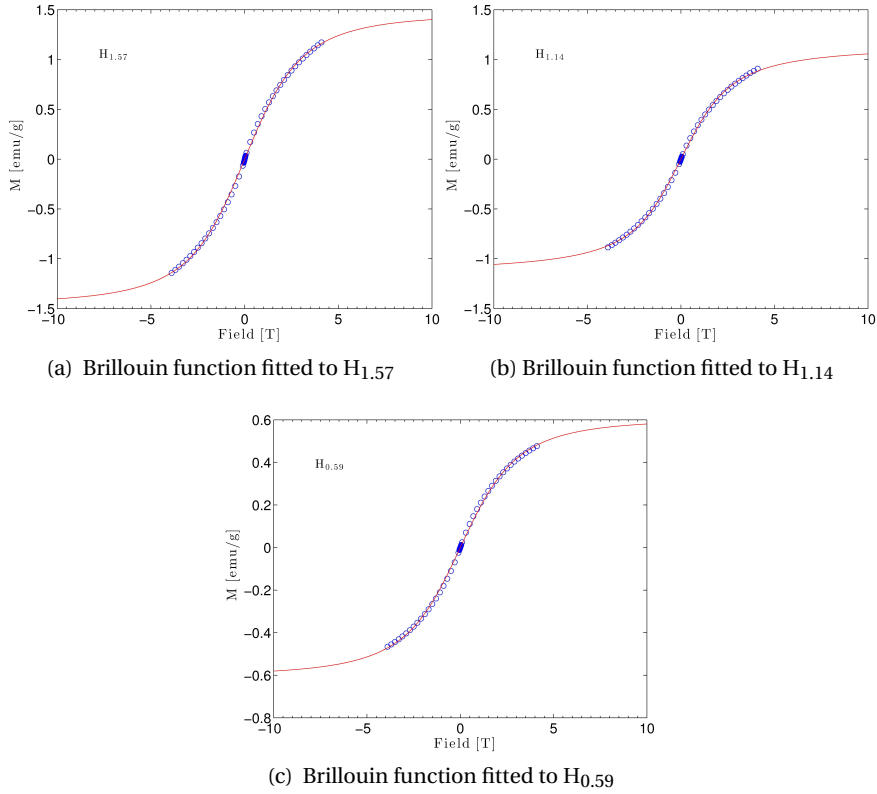
Figure A.3: Calculated Brillouin function with the prefactor and a weak background constant ($\sim 10^{-4}$) as free parameters

to the D7 data in absolute units for pure ZnO, with resolution and a scaling factor as free parameters. The obtained scaling factor was 0.93.

The polarised neutron data were analysed to separate the magnetic, nuclear and spin incoherent cross sections, allowing a comparison of the samples with respect to the synthesis method and the Mn^{2+} doping level. Figure A.4 shows the nuclear cross section for each of the sample, including the pure ZnO reference. The ZnO nuclear Bragg peaks are resolution limited, and thus were used to obtain the instrumental resolution. An upturn starting at Q lower than 0.7 is observed, which is possibly due to multiple scattering.

The strong Bragg peaks at Q =2.23 , 2.43 and 2.54 Å^{-1} correspond respectively to the ZnO nuclear structure peaks (1 0 0), (0 0 2) and (1 0 1). The inset shows a zoom of the nuclear and isotope incoherent scattering away from the Bragg peaks, which contains both diffuse scattering from substitutional disorder as well as small peaks not expected from the ZnO structure. Sample $H_{0.54}$ features weak peaks at Q =1.25 and 1.95 Å^{-1} while sample $H_{1.14}$ and $H_{1.57}$ have the same weak peaks at Q = 1.25 and 1.95 Å^{-1} and an additional sharper peak at 1.73 Å^{-1}. MnO has no Bragg peak within this Q-range. In order to identify these weak peaks, a
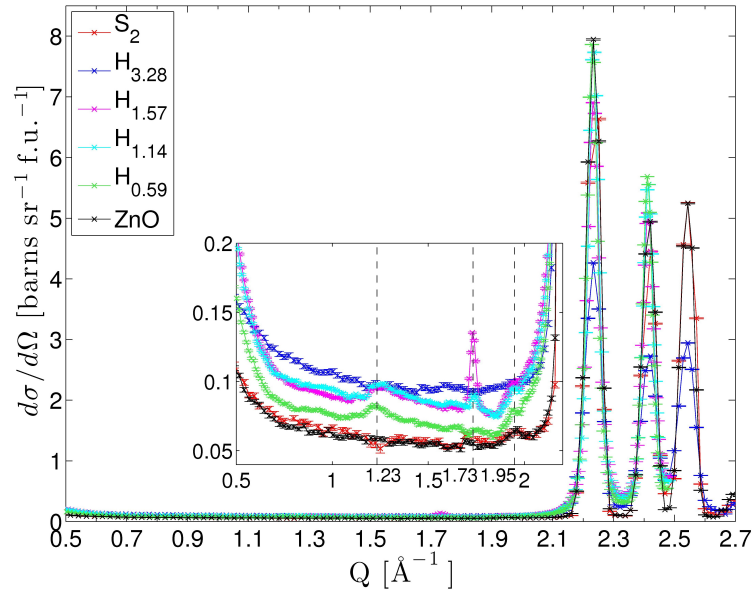
Figure A.4: Nuclear and isotope incoherent cross section for all the samples. The strong Bragg peaks at Q =2.23 , 2.43 and 2.54 Å^{-1} correspond to ZnO nuclear structure peaks. The inset is a zoom on the low Q scattering, showing very weak Bragg peaks probably corresponding to impurity phases

powder diffraction pattern was simulated for various possible impurity phases of Mn:ZnO [3] within the same Q-range: Chalcophanite,Mn_2O_3 cubic and orthorombic, MnO_2, $Mn(OH)_2$, $ZnMnO_3$, Hydrozincite, $ZnMn_2O_4$, MnOOH, $Zn(OH)_2$ and MnO_2xH_2O. However, none of these impurity phases corresponds to the observed weak peaks, so that they may come from an external contamination, with no expected effect on the magnetism.

In addition, the inset of the low Q scattering data shows that sample $H_{3.28}$ has the strongest nuclear diffuse scattering cross-section, followed by $H_{1.57}$ and $H_{1.14}$ with very similar cross sections, and then $H_{0.54}$. Finally, S_2 shows the lowest cross sections, which is equivalent to the scattering of the pure ZnO sample. The magnitudes of diffuse scattering are evidence that the hydrozincite samples do have site disorder, while the solid state sample has very little diffuse scattering, which is consistent with separate phases. In addition, no clear features corresponding to nuclear short range order were observed in the nuclear cross-section.

The main polarised neutron scattering results are presented in Fig. A.5, which shows the magnetic cross section as a function of Q obtained for all samples. The magnetic cross sections are presented in Fig. A.5. Panel a and b of Fig. A.5 shows that the magnetic cross section of S_2 and $H_{3.28}$ have clear features at $Q \sim 1.24$ Å^{-1}, which is the expected Q position for the $(\frac{1}{2}\frac{1}{2}\frac{1}{2})$ MnO magnetic Bragg peak. These features are broader than simple Bragg peaks, and reflect a

---

[3] done by G.J. Nilsen at STFC, UK

segregation of MnO inside ZnO with a distribution of particle size that cannot be established exactly. To address this, the data were fitted using two Voigt functions, assuming a Gaussian resolution extracted from the width of the nuclear peaks and a Lorenzian broadening. One results in a narrow and more intense peak at Q=1.24 Å^{-1}, corresponding exactly to Q for the $(\frac{1}{2}\frac{1}{2}\frac{1}{2})$ of MnO, while the second gives a smaller and broader peak around $Q = 1.48$ Å^{-1}. This type of scattering has been observed previously in studies of MnO nanoparticles [140] with a particle size distribution average of 100 Å. A rough estimation of the correlation length of the nanoparticles observed in S_2 are 43 ± 5 and 14 ± 4 Å while they are of 16.7 ± 3 and 4.8 ± 0.7 Å for $H_{3.28}$.
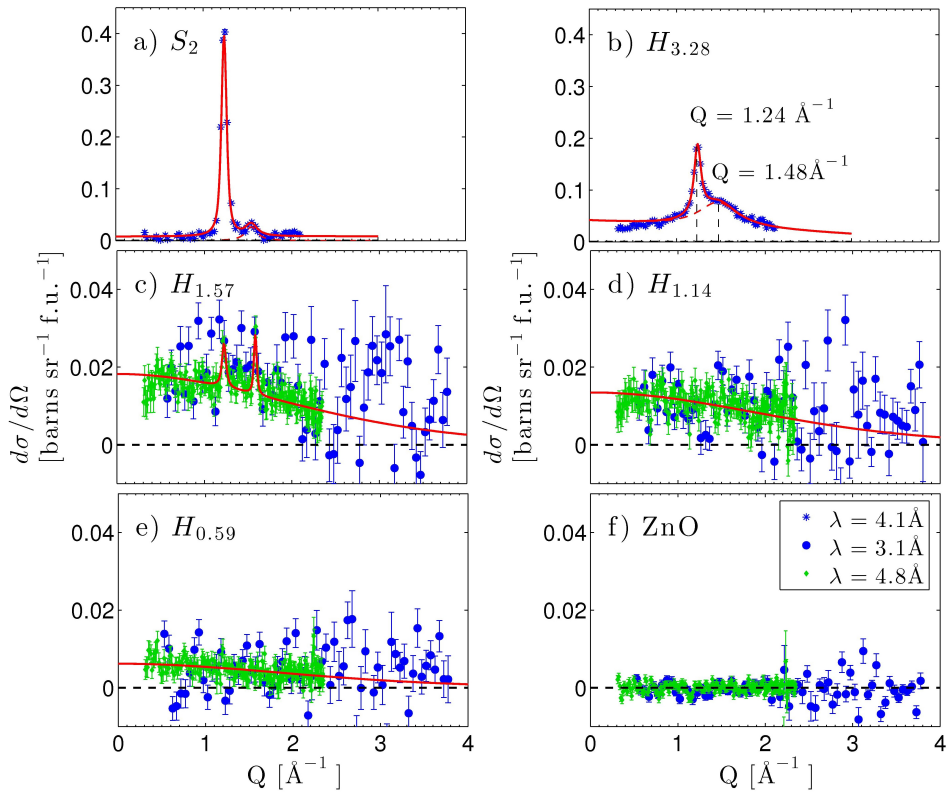
Figure A.5: Magnetic cross section. Blue stars correspond to $\lambda = 4.1$ Å(DNS), blue circles to $\lambda = 3.1$ Å(D7), while green diamonds correspond to $\lambda = 4.8$ Å(D7). Panel a shows to the sample grown with the solid state method, while panel b-e concern samples grown via the decomposition of hydrozincite. Pure ZnO is shown in panel f. The solid red line is a fit of the cross section using Voigt functions for the magnetic Bragg peaks and the Mn^{2+} form factor for the paramagnetic background.

The analysis of the magnetic scattering cross section for S_2 and $H_{3.28}$ shows clearly the presence of segregated MnO in the ZnO matrix. In addition, clear ferromagnetic behavior was observed in the magnetisation measurements (Fig A.2). It is therefore likely that ferromagnetism in
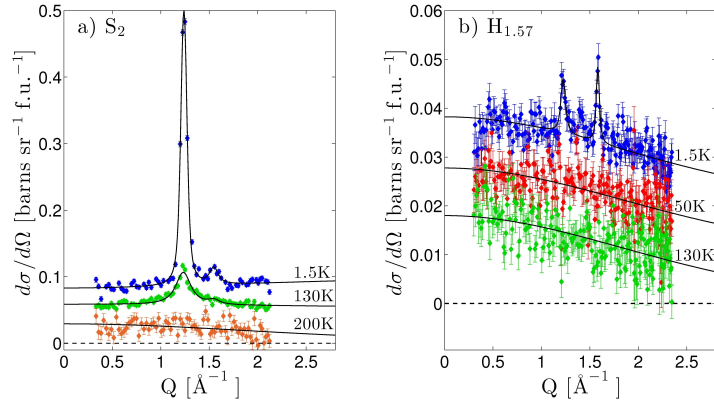
Figure A.6: a) Magnetic cross section of sample S_2 at three different temperatures : 1.5K (blue), 130K (green) and 200K (orange) and plotted with an offset. Black lines are fit of the data by two Voigt functions and the Mn2+ form factor b) Magnetic cross section of sample $H_{1.57}$ at three different temperatures : 1.5K (blue), 50K (red) and 130K (green) and plotted with an offset. Black lines are fit of the data by Voigt functions and the Mn^{2+} form factor.

these samples comes from uncompensated surface spins of the MnO nanoparticles, which had been observed in several studies[141, 140].

At 1.57% Mn^{2+} doping (Figure A.5.c), very weak and narrow peaks are observed again at the same Q position. Their intensity relative to the background is much lower than for the higher doping, and would correspond to a MnO volume fraction in ZnO matrice of 0.06%. These peaks disppear at 50 K (see figure A.6.b), well below $T_N \sim 122$K for MnO, and their peak width is smaller than the resolution width, hence they may be an artefact of the measurement.

For Mn^{2+} dopings of 1.57% and below (Fig. A.5.c-e), the spectrum is dominated by diffuse form-factor-like scattering, as expected for paramagnetic behavior. The cross section of the more lightly doped samples $H_{1.14}$ and $H_{0.59}$ show only paramagnetic behavior in the measured Q range, and were fittted with the Mn^{2+} form factor. Fig. A.5.f shows the magnetic cross section for the pure ZnO sample, which is zero as expected, providing a baseline for the other measurements.

Effective moment

Within the assumption of a paramagnetic behaviour, the Q-intercept of the magnetic cross section $\frac{d\sigma}{dQ}(Q=0)$ can be used to calculate the effective moment μ_{eff} from the spin-only equation for the magnetic cross section [9]:

$$\frac{d\sigma}{d\Omega}(Q=O) = \frac{2}{3}(\frac{\gamma r_0}{2})^2 g^2 S(S+1) \tag{A.2}$$

Table A.2: Effective moment of Mn^{2+} obtained from the Q=0 intercept of the magnetic cross sections

Mn^{2+} doping [%]	Estimated μ_{eff} [μ_B/atom]	Q=0 intercept
1.57	4.87 ±0.05	$1.82 \cdot 10^{-2} \pm 3 \cdot 10^{-4}$
1.14	4.91 ±0.05	$1.35 \cdot 10^{-2} \pm 3 \cdot 10^{-4}$
0.59	4.62 ±0.28	$6.18 \cdot 10^{-3} \pm 7 \cdot 10^{-4}$

with $\mu_{eff} = \sqrt{g^2 S(S+1)}$, we obtain :

$$\frac{d\sigma}{d\Omega}(Q = O) = 0.049 \cdot \mu_{eff}^2 \tag{A.3}$$

In the case of Mn:ZnO : x is the Mn^{2+} doping percentage :

$$\mu_{eff} = \sqrt{\frac{\frac{d\sigma}{d\Omega}(Q = O)}{x * 0.049}} \mu_\beta = 5.92 \mu_\beta \tag{A.4}$$

Table A.2 shows the Mn^{2+} effective moment μ_{eff} obtained from the form factor fits of the lightly doped samples, taking into account the Mn^{2+} concentration. Broadly speaking, the values are close to the expected $\mu_{eff} = \sqrt{g^2 S(S+1)} = 5.92 \mu_B$ for Mn^{2+}.

Volume fraction

From the integrated intensity of the ZnO nuclear peak (1 0 0) and the MnO magnetic Bragg peak (0.5 0.5 0.5) in the polarised neutron data, we can estimate the volume fraction V_f of MnO nanoparticles in the ZnO matrix for the samples that showed clear Bragg peaks in the magnetic neutron cross section.

The intensity of a nuclear Bragg peak is given by :

$$I_n = \frac{N}{V_0} \cdot \text{mult}_n \cdot LP_n \cdot F_n^2 \lambda^3 \tag{A.5}$$

with N the number of unit cells in the sample, V_0 the volume of the unit cell, LP_n the Lorentz polarisation factor, mult_n the multiplicity of Bragg reflection and F_n the nuclear structure factor.

The intensity of a magnetic Bragg peak is given by :

$$I_m = \frac{N_m}{V_{0m}} \cdot \text{mult}_m \cdot LP_m \cdot \frac{\gamma r_0^2}{2} \cdot g^2 F_m^2 \lambda^3 \tag{A.6}$$

with N_m the number of magnetic unit cells in the sample, V_{0m} the magnetic unit cell volume, LP_n the Lorentz polarisation factor, and F_m the magnetic structure factor.
The magnetic structure factor F_m includes $\mu_\perp$ and the magnetic form factor f.

The volume fraction is thus given by :

$$V_f = \frac{N_m V_{0m}}{N V_0} = \frac{I_m}{I_n} \frac{V_{0m}^2}{V_0^2} \frac{mult_n}{mult_m} \frac{LP_n}{LP_m} \frac{F_n^2}{F_m^2} \frac{1}{(\frac{\gamma r_0}{2})^2} \tag{A.7}$$

For the (1 0 0) nuclear Bragg peak of ZnO :

- multiplicity of 6
- $F_n^2 = 1.1933$
- for $\lambda = 4.13$Å(DNS data), the Q=(110) peak is at $2\theta = 92.52$ degrees so that $LP_n = \frac{1}{2 sin^2(\theta) cos(\theta)} = 1.385$
- Integrated intensity of normalised Gaussian function (resolution limited) obtained from fits of DNS data. For sample $H_{3.28}$, $I_n = 14.59$ and for sample S_2, $I_n = 24.26$
- ZnO has an hexagonal lattice with a=b=2.249 Åand c=5.229 Åso that $V_0(ZnO) = \frac{\sqrt{(3)}}{2} a^2 c = 47.802$ Å^3

For the (0.5 0.5 0.5) magnetic Bragg peak of MnO :

- multiplicity of 8 [142]
- for $\lambda = 4.13$Å(DNS data), the Q=(0.5 0.5 0.5) peak is at $2\theta = 48.1$ degrees so that $LP_m = \frac{1}{2 sin^2(\theta) cos(\theta)} = 3.297$
- Integrated intensity of the two Voigt function obtained from DNS data, thus taking into account both the sharp and broad magnetic peaks. For sample $H_{3.28}$, $I_m = 1.64$ and for sample S_2, $I_m = 0.89$
- MnO is cubic with a=4.41 Å, so that $V_0(MnO)= a^3 = 85.76$ Å^3. Magnetic unit cell volume is thus $V_{0m} = 8 V_0(MnO) = 686.13$ Å^3
- $\mu_\perp^2 = \frac{2}{3} <gS>^2 = \frac{50}{3}$ with $S = \frac{5}{2}$
- gyromagnetic ratio $\gamma = 1.913$ and classical electron radius $r_0 = 2.818 \cdot 10^{-15}$ m
- for $| Q |= \sqrt{3 \cdot (0.5 \cdot \frac{2\pi}{a})^2)} = 1.228$Å^{-1} (a=4.43 Å), the Mn^{2+} squared form factor is $f^2 = 0.812$
- The magnetic structure factor of MnO is $F_m =| \sum^{mag}(\tau_m) | \mu_\perp f = 32 \mu_\perp f$ [143]. $F_m^2 = 32^2 \cdot \frac{50}{3} f^2 = 1.707 \cdot 10^4 f^2 = 1.386 \cdot 10^4$

For $H_{3.28}$, the MnO volume fraction is estimated to $V_f = 8.6 \cdot 10^{-3} = 0.86\%$, while for S_2, the MnO volume fraction is estimated to $V_f = 2.8 \cdot 10^{-3} = 0.28\%$. These value take into account both the sharp feature corresponding to the $(\frac{1}{2}\frac{1}{2}\frac{1}{2})$ magnetic Bragg peak of MnO and the broader feature corresponding to the segregated MnO nanoparticles with a size distribution. In the case where only the sharp magnetic Bragg peak is considered in the integrated magnetic intensity, the MnO volume fraction becomes 0.14 % for $H_{3.28}$ and 0.23 % for S_2.

A.4   Conclusions

Previous experimental results had placed Mn:ZnO in the ferromagnetic phase of the magnetic phase diagram of the theoretical prediction mentioned in the introduction[130] for doping of 2.2% and for temperatures up to room temperature. This theory suggests that room temperature ferromagnetism and other magnetic phase in DMS are caused by the coexistence of defects and dopant cation at small doping. The band created by the defects hybridizes with the d orbital of the dopant, and spin are polarised via Hund's exchange. However, from these polarised neutron scattering results, we do not observe any spin glass or ferromagnetic phase in Mn:ZnO, which implies that either the defect concentration is too low, that the polaron radius $\gamma^3\delta$ is not sufficiently large, or that the bands are not close enough to hybridize. In that context, we thus conclude that Mn:ZnO is restricted to the paramagnetic region of the phase diagram for all cluster-free doping percentage even at 2K, at least in the case of these synthesis methods.

While magnetisation measurements showed clear evidence for ferromagnetism in S_2, the 2% doped sample grown by the solid state method, neutron polarisation analysis and XRD measurements confirm that there is segregation of manganese into MnO. However, while XRD does not clearly show the presence of MnO in $H_{3.28}$, the neutron scattering data demonstrated that the ferromagnetism appearing in the magnetisation measurements is strongly linked to the formation of MnO nanoparticles. Size estimates of the nanoparticles could also be obtained from fits of the polarised neutron data and are typically 20-50 Å. Lower Mn^{2+} doping result in paramagnetism with no indication of ferromagnetic short-range order, neither in polarised neutron scattering nor in magnetisation measurements. This leads to the conclusion that ferromagnetic correlations in these Mn^{2+} doped ZnO samples do not come from substitution of the zinc by manganese in the ZnO matrix. Instead, MnO nanoparticles form and the ferromagnetism most likely comes from unpaired spins at the nanoparticle boundaries.

Co doped ZnO has also been attracting attention in the context of spintronics, as it has the largest moment of the transition metals. As shown in several XRD and magnetisation studies of Co doped samples [144, 145] (with higher doping percentage than for Mn-doped ZnO : $\sim 1-20\%$), contradicting view exists on the origin of ferromagnetism in Co:ZnO, with a strong dependence on the fabrication method. Further polarised neutron scattering investigation would provide valuable information on the origin of ferromagnetism in Co-doped Zno, in particular whether there is segregation of the cobalt or if it substitutes homogeneously for the zinc.

B Incommensurate magnetic correlations in new superconductors

Doping-dependent phase diagrams of high temperature superconductors have shown that antiferromagnetic order is found in close vicinity to the superconducting phase in both cuprates and iron pnictide and chalcogenide systems[146, 147], so that looking at the interplay between magnetism and superconductivity is at the heart of research in unconventional superconductors [148]. The discovery of iron-pnictide and chalcogenide superconductors has sparked the studies of the interplay between magnetic structure, magnetic dynamics and superconductivity in this family of compounds. In iron pnictides and chalcogenides, the superconducting state appears either upon doping or by the application of pressure in a metallic parent compound, in contrast to cuprates where parents are usually in a correlated insulating state. Superconductivity has been found in a number of compounds involving 3d transition metals, and was recently discovered in binary pnictides MnP and CrAs under pressure [149, 150].

Discussed here are the incommensurate magnetic phases and excitations observed in three compounds, in which a transition to superconductivity appears as a function of either iron content, for the chalcogenide $Fe_{1+y}Te_{0.7}Se_{0.3}$, or as a function of applied pressure, for the binary pnictides CrAs and MnP.

B.1 $Fe_{1+y}Te_{1-x}Se_x$

Iron-based chalcogenides started attracting attention with the discovery of high temperature superconductivity in the doped iron compound RFeAsO [151, 152], further fuelled by their similarities to the high T_c cuprates. These similarities include a layered structure with a square lattice and a proximity of magnetic and superconductive states [153]. As in the cuprates, a spin resonance is observed in the excitation spectrum below T_c in both iron chalcogenide and pnictide compounds [147]. $Fe_{1+y}Te_{1-x}Se_x$ has the simplest layered crystallographic structure among the iron-based superconductors and displays a spin excitation spectrum with a spin resonance, an hourglass-shaped dispersion and a spin gap which accompanies the onset of superconductivity[154, 155, 156]. In addition to the Te/Se ratio as a tuning

parameter, the excess of iron (parameter y) located on interstitial sites strongly influences both the magnetic and the superconducting properties of $Fe_{1+y}Te_{1-x}Se_x$ [157] and its study provides new insights into the superconducting mechanism. In addition, parent compounds show peculiar magnetic behaviour upon the application of hydrostatic pressure such as ferromagnetism in antiferromagnetic $Fe_{1+y}Te$ [158], indicating a strong correlation between the crystal structure and the magnetic properties.

The excitation spectrum of $Fe_{1+y}Te_{0.7}Se_{0.3}$ for y=0.02 is characterised by an hourglass dispersion with the constriction of the incommensurate spectrum towards a commensurate wavevector $Q = (0.5\ 0.5\ 0)$ at the energy E_{hg}. In a previous inelastic neutron scattering study [156], the hourglass-shaped dispersion was shown to be most likely a prerequisite for superconductivity, while the consequences are the opening of a gap and a shift of spectral weight. Indeed, the hourglass dispersion was shown to exist above the transition temperature, and a possible natural explanation is that the inwards dispersion allows the spin gap to shift spectral weight towards the commensurate point, thereby lowering the exchange energy [159]. A consequence of this interpretation is that the commensurate energy E_{hg} sets an upper limit for the possible spin gap and hence for T_c.

Further investigations of the interplay between magnetism and unconventional superconductivity were thus performed by applying pressure, a parameter with the advantage of tuning superconductivity properties [160, 161] without sample composition changes, avoiding potential changes in doping-induced inhomogeneity and the hard-to-control level of excess iron. The evolution of the hourglass shaped dispersion under an applied pressure of 12 kbar was measured using a superconducting sample with composition $Fe_{1.02}Te_{0.7}Se_{0.3}$ in a Paris-Edinburgh pressure cell on the thermal neutron spectrometer IN8 at the ILL. The $Fe_{1+y}Te_{1-x}Se_x$ single crystals with different y excess Fe doping are in the tetragonal phase with the space group P4/nmm with cell parameters at ambient pressure of $a = b = 3.807$ Å and $c = 6.152$ Å.

The results are detailed and discussed in Lançon et al. [162] : it was shown that the pressure-induced 37% increase of T_c from 9.7 K to 13.3 K is concomitant with a change in the magnetic excitation spectrum, with a similar 38% increase of the hourglass energy E_{hg} from 5.3(5)meV to 7.3(6)meV. Figure B.1 illustrates this shift of the resonance energy with applied pressure.

In addition, figure B.1.a shows the typical excitation spectrum of $Fe_{1.02}Te_{0.7}Se_{0.3}$ at 2K, showing both the incommensurate rods of scattering, with a commensurate point at E_{hg} and $Q = (\pi, \pi) = (0.5\ 0.5)$, and the spin gap below $\Delta E \sim 4$ meV.

The temperature dependence of the spin gap was measured on the triple axis spectrometer IN14 at the ILL with $k_f = 1.5\,Å^{-1}$, using a single crystal of $Fe_{1.02}Te_{0.7}Se_{0.3}$ aligned with (100) and (010) in the scattering plane. From a constant-energy scan at $\Delta E = 7$ meV, the incommensurate excitation was estimated to be at $Q = (0.375\ 0.625)$ and the temperature dependence was measured at this Q point for $\Delta E = 1.5$ meV from 50K to 2K. Figure B.2 showing the opening of the spin gap from about 15 K, thus starting slightly above the transition temperature T_c=10K.
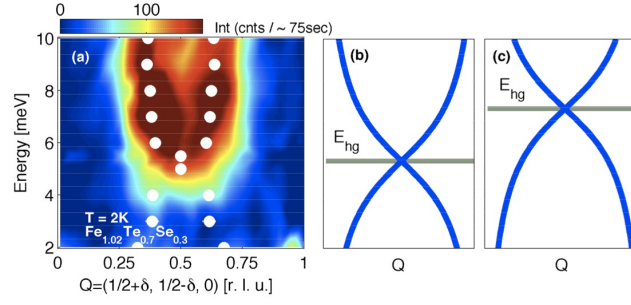
Figure B.1: (a) The magnetic dispersion measured in superconducting state of Fe$_{1.02}$Te$_{0.7}$Se$_{0.3}$ at T=2K at zero applied pressure. (b-c) Sketchs of the hourglass shape for zero applied pressure (b) and applied pressure (c), illustrating the increase of the commensuration energy E_{hg} in applied pressure
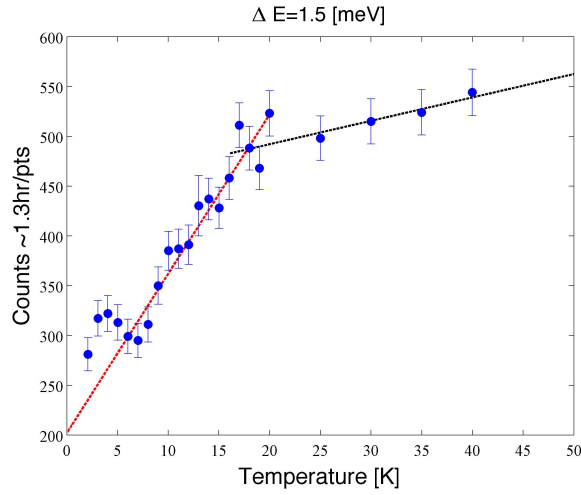

Figure B.2: Temperature dependence of the spin gap measured at Q =(0.375 0.625) at ΔE=1.5 meV on IN14. the line are guides to the eye

Furthermore, magnetic correlations at the in-plane magnetic wavevector $Q = (\pi, 0)$ were shown to survive as short-range order after the long-range antiferromagnetic order has been suppressed in non-superconductive samples by partially substituting Se by Te [163]. Indeed, the parent compound Fe$_{1+y}$Te has been shown to exhibit antiferromagnetic order with an in-plane magnetic vector of $(\pi, 0)$, contrasting with iron-pnictides where the magnetic order has an in-plane wavevector (π, π) . The hypothesis is that short-range order at $(\pi, 0)$ coexists with (π, π) spin fluctuations in Fe$_{1.02}$Te$_{0.7}$Se$_{0.3}$, thus hinting towards a similar mechanism between iron pnictides and iron chalcogenides [163].

The short range magnetic correlations at $Q = (\pi, 0)$ were measured for four single crystals of Fe$_{1+y}$Te$_{0.7}$Se$_{0.3}$ for excess Fe doping corresponding to compositions at the brink of super-conductivity, on the triple axis spectrometer IN3 at the ILL set up for elastic scattering with k$_i$ = k$_f$ = 2.62 Å^{-1}. Figure B.3 shows both a longitudinal (δ along Qh) and a transverse scan

(δ along Qk) of the $(\pi, 0)$ peak for a sample with $y \sim 0.05$ at 2K. The data was background-subtracted and the resulting peak profiles were both fitted with a Lorentzian function. No spin gap at 2K was observed for this sample at 2K on IN14, but magnetisation measurements using a SQUID magnetometer showed that the sample had a transition at 4K corresponding to a superconducting volume fraction of $\sim 14\%$.
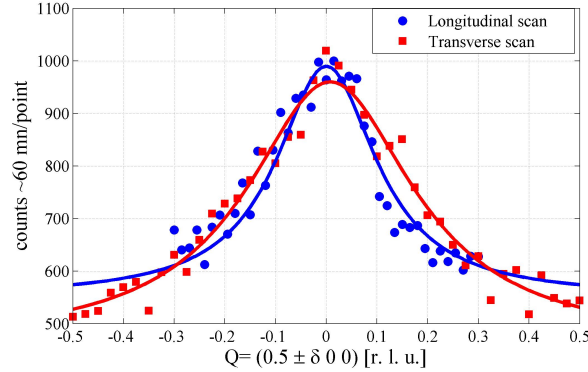

Figure B.3: Longitudinal and transverse scans of the $Q = (\pi, 0)$ feature at 2K for $Fe_{1+y}Te_{0.7}Se_{0.3}$ with $y \sim 0.5$.

From Figure B.3, it is clear that the $Q = (\pi, 0)$ peak corresponds to short range order correlations, with a peak width larger than the instrumental resolution. Similar to what was observed in [163], the feature is asymmetrical so that the range of the correlations are Q-dependent, with a Lorentzian width Λ for the longitudinal and transverse scans of respectively $\Lambda = 0.12$ and 0.21 [r. l.u].

The temperature dependence of the $Q = (\pi, 0)$ peak was measured for each of the four samples from 40 to 2K and is shown in figure B.4. Figure B.4.a corresponds to $Fe_{1+y}Te_{0.7}Se_{0.3}$ with $y \sim 0.05$ while Figure B.4.d corresponds to the superconducting sample $Fe_{1.02}Te_{0.7}Se_{0.3}$ previously measured on IN14. Figure B.4.b-c correspond to the temperature-dependence of two samples (labelled X6 and X7) very close to superconducting doping but which show no transition to superconductivity in magnetisation measurements. Their nominal excess Fe doping are respectively 0.11 and 0.05, and their actual Fe doping y is not known accurately.

For the samples corresponding to figure B.4.a-c, the $Q = (\pi, 0)$ peak is clearly present down to 2K, with an overal linear temperature dependence showing no particular transition. For the superconducting sample $Fe_{1.02}Te_{0.7}Se_{0.3}$, there is little to no evidence of the presence of this magnetic peak in this temperature range.

Overall, it appears that the actual excess Fe doping is difficult both to control and to characterize. Indeed, the composition of the sample was measured by EDX[1] (Energy Dispersive X-ray spectroscopy), taking five different points of the single crystals for the measurements,

---

[1]done with Arnaud Magrez at the EPFL, and compared to other EDX measurements done by Enrico Giannini at the University of Geneva
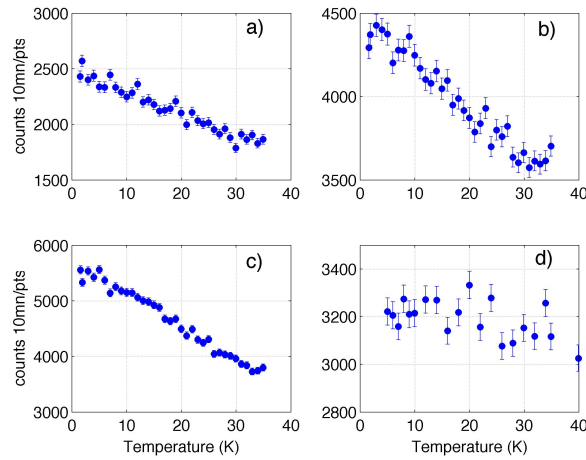
Figure B.4: Temperature dependence of the $Q = (\pi, 0)$ peak on IN3 for four samples of Fe$_{1+y}$Te$_{0.7}$Se$_{0.3}$. a) $y \sim 0.05$ with a superconductive volume fraction of 14% from SQUID measurements. b)-c) nominal excess Fe of respectively 0.11 and 0.05, no transition to superconducting phase observed in SQUID magnetisation. d) y=0.02, superconducting volume fraction of $\sim 94 - 100\%$

and the results showed that the samples did not appear homogeneous in their composition. In addition, the obtained Fe dopings were not consistent with previous EDX measurements. Furthermore, samples X6 and X7, with their compositions very close to the superconducting limit were shown not to have a superconducting phase by SQUID measurements (and by inelastic neutron scattering checking the absence of a spin gap). However, single crystals from the same batch were then measured again (12-24 months later) and were shown to have a superconducting phase for a fraction of the sample volume. The properties of these samples thus appear to be time-dependent [2], with possibly oxidation or water adsorption leading to chemical modifications.

From the study of short-range order magnetic correlations in Fe$_{1+y}$Te$_{0.7}$Se$_{0.3}$ single crystals, it thus appears that establishing a reliable phase diagram as a function of excess Fe is very challenging and any results must be interpreted with caution. Furthermore, the crystals appear highly inhomogeneous, with partial superconducting fractions observed in the $y \sim 0.05$ sample. The co-existence of short range order at $(\pi, 0)$ and with (π, π) spin fluctuations observed in [163] could thus well be linked to a two-phase description where the two magnetic correlations exists in two distinct volume fractions of the sample.

---

[2] observed by Enrico Giannini at the University of Geneva

B.2 CrAs

Superconductivity in the binary pnictide CrAs was discovered from resistivity and susceptibility measurements at 2.2K for an applied pressure $P_c > 7$ kbar, with a superconductive phase present up to a large applied pressure (>30 kbar)[149, 150, 164]. Figure B.5 from [150] shows the pressure-temperature phase diagram of CrAs.
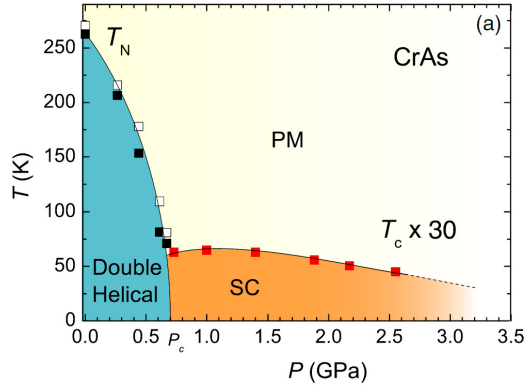

Figure B.5: Pressure-temperature of CrAs from [150], where T_c has been multiplied by 30 for plotting purposes.

CrAs has an orthorhombic structure with space group P*nma* with unit cell parameters $a = 5.649$ Å, $b = 3.463$ Å, $c = 6.208$ Å at room temperature. Below $T_N \sim 270$ K, the magnetic structure is double-helical with an incommensurate propagation vector along c with the magnetic moment of $\sim 1.7\mu_B$/Cr lying in the (a, b) plane. Understanding the magnetic interactions of CrAs would provide insight on the interplay between magnetism and superconductivity. A neutron diffraction study of the pressure evolution of the helimagnetic structure close to the critical pressure showed a reduction of the ordered moment and a Bragg-peak-width dependence on pressure, understood as competing ground states in vicinity of the superconducting phase [165].

An attempt at measuring the excitation spectra of CrAs in the helical phase without applied pressure and in the superconductivity phase around 10 kbar was carried out on the time-of-flight spectrometer CNCS at SNS for co-aligned single crystals of CrAs. Preliminary measurements on a powder sample had shown promising inelastic intensities.

Fourteen needle-shaped crystals of CrAS[3] were co-aligned on an Al holder with (010) and (001) in the horizontal plane for a total mass of about 100 mg. The sample was cooled to 1.7K and the excitation spectra were measured on the time-of-flight spectrometer CNCS for $E_i = 3.15, 12$ and 50 meV at ambient pressure. The sample was then inserted in a clamp pressure cell (described in 1.1.10) and a pressure of ~ 10 kbar was applied. The pressure cell was then cooled down to 1.7K and the excitation spectra were measured for $E_i = 12$ meV. The maps

---

[3]The crystals were grown by Athena S. Sefat at the Materials Science and Tech. division of ORNL and co-aligned by Andrey Podlesnyak at SNS

were obtained by doing "Horace-type" scans where the sample was rotated about the vertical axis with steps of 2 degrees, with a counting time of ∼ 4 mn per rotation.

Although the object of the neutron scattering experiment was to measure the inelastic spectrum, diffraction maps of CrAs in the $Qk - Ql$ plane could be obtained by integrating over the elastic line. Figure B.6 shows the resulting $Qk - Ql$ diffraction map for an integration over Qh=[-0.1 0.1] and over either $\Delta E = [-0.5, 0.5]$ meV for E$_i$=12 meV and $\Delta E = [-0.2, 0.2]$ meV for E$_i$=3.15 meV. The data has been symmetrized by folding over equivalent Q points to improve statistics. Strong powder rings corresponding to the Al holder are observed, and nuclear Bragg peaks are visible at (0 2 0) and (0 1 3), and magnetic incommensurate Bragg peaks are visible close to (0 0 0) and to (0 1 1).
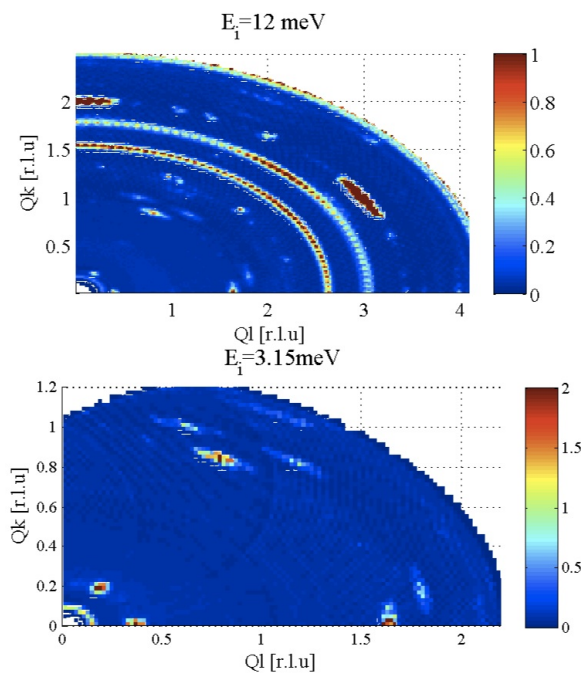
Figure B.6: Diffraction $Qk - Ql$ map of CrAs obtained on the time-of-flight spectrometer CNCS at 1.7K for two Q-coverages obtained with either E$_i$=12 and 3.15 meV

Figure B.7 shows energy slices of the data for E$_i$=12 meV and E$_i$=3.15 meV showing no inelastic scattering that could be attributed to magnons in CrAs. There appears to be inelastic intensity visible in the E$_i$=12 meV excitation spectra, but constant-energy maps clearly showed that it had a powder-like behaviour. The $|Q|$-dependence of the observed dispersion can be linked to the presence of helium in the sample space (used for cooling). This helium background was probably responsible for the strong inelastic scattering that had been observed in preliminary powder measurements.

In order to check the unlikely case where the excitations would be located at energy transfers above 10 meV, a partial set of rotation was carried out for E$_i$=50 meV with 9 minutes of counting
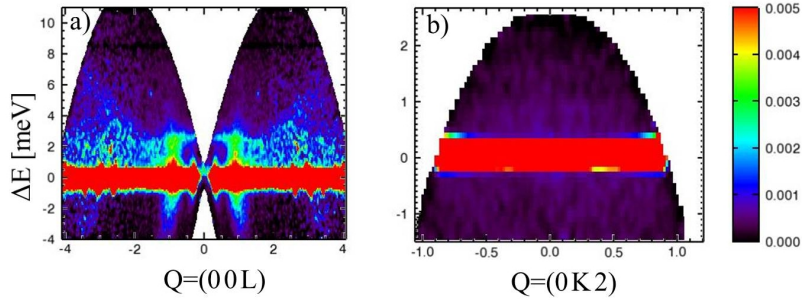
Figure B.7: Energy slice obtained on CNCS at ambient pressure and 1.7K for a)E_i=12 meV and b) E_i=3.15 meV

time per rotation. To reduce scattering from helium, the temperature was first increased to 20K, the sample space was pumped and then the sample was cooled back down to 1.5K. this procedure lead by a reduction of helium pressure by a factor 10. Figure B.8 shows the resulting spectrum, where no inelastic scattering is observed.
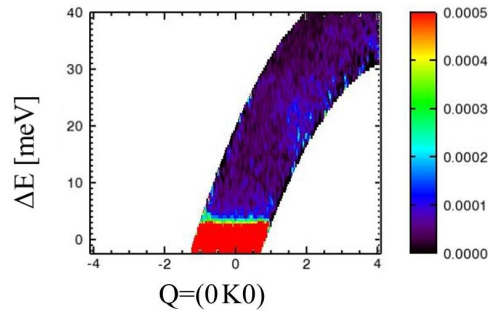
Figure B.8: Energy slice obtained on CNCS at ambient pressure and 1.7K for E_i=50 meV after reducing helium pressure in sample space.

Even at ambient pressure, no magnetic inelastic scattering could be detected on CNCS, possibly due to the small sample size resulting in intensities too weak to be measured. Nevertheless, measurements were done for CrAs at an applied pressure of about 10kbar , with E_i=12meV and at T=1.7K, with 9 mn counting time per rotation. Part of the $Qk - Ql$ diffraction map under pressure obtained by integrating over Qh=[-0.1 0.1] and over either $\Delta E = [-0.5, 0.5]$ is shown in figure B.9.

The $Qk - Ql$ map is dominated by rings attributed to the Bragg scattering from the pressure cell. A background measurement was done by measuring above the transition temperature, keeping the same set-up. However, the background-subtracted maps obtained still had a spurious character, although the ring intensity decreased by a factor 60. In B.9, the (0 1 3) nuclear Bragg peak is weakly visible close to the spurious ring. The Bragg peak has moved from $2\theta = 94$ degrees to $2\theta = 100$ degrees, so that there is significant reduction of lattice parameters with applied pressure.

Figure B.9: Diffraction Qk-Ql map of CrAs under 10 kbar applied pressure obtained on the time-of-flight spectrometer CNCS at 1.7K with E$_i$=12 meV

Overall, no inelastic excitations of CrAs could be measured on CNCS, most probably due to the small sample size. Before the inelastic spectrum can be successfully measured under pressure, ambient pressure measurements on larger samples should provide insight on the magnetic excitations in CrAs.

B.3 MnP

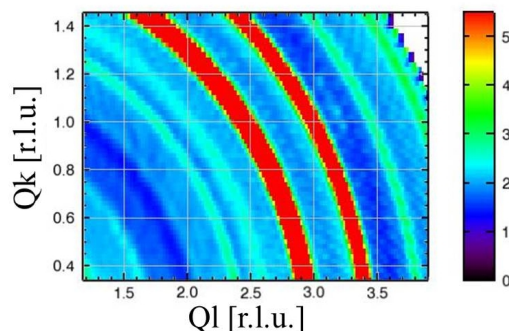A superconductivity phase was discovered by resistivity and susceptibility measurements in MnP, another binary pnictide, below ~ 1 K for an applied pressure of ~ 80 kbar [164], significantly larger than the P ~ 10 kbar applied pressure for the superconductivity phase in CrAs. Although both compounds have an helical magnetic phases at ambient pressure, CrAs has dominant antiferromagnetic correlations whereas ferromagnetic spin correlations dominate in MnP.

The orthorhombic P*bnm* spacegroup with a = 5.91 Å > b = 5.25 Å > c = 3.18 Å at room temperature is used for MnP, following [166] (equivalent to the P*nma* space group used in [167] with different axis labelling). MnP orders ferromagnetically below T$_N$=291 K, and a double helical magnetic structure appears as the temperature is cooled down further than 50K. Upon the application of pressure, this magnetic structure is suppressed and replaced by another magnetic phase which was interpreted as having antiferromagnetic order from susceptibility measurements [164]. For an applied pressure of ~ 80 kbar a superconducting dome appears.

Neutron diffraction experiments on both powdered and single crystal samples were performed under applied pressure in order to understand how the magnetism evolves with applied pressure to complete and check the proposed magnetic phase diagram of MnP.

The powdered sample was made by heating the mixture of Mn and P with the ratio of 1:1 in quartz tube, while the single crystal was grown by using the Bridgeman method [4]. The single

---

[4]The crystals were grown and prepared by Shinichiro Yano, from the Neutron Group of the National Synchrotron
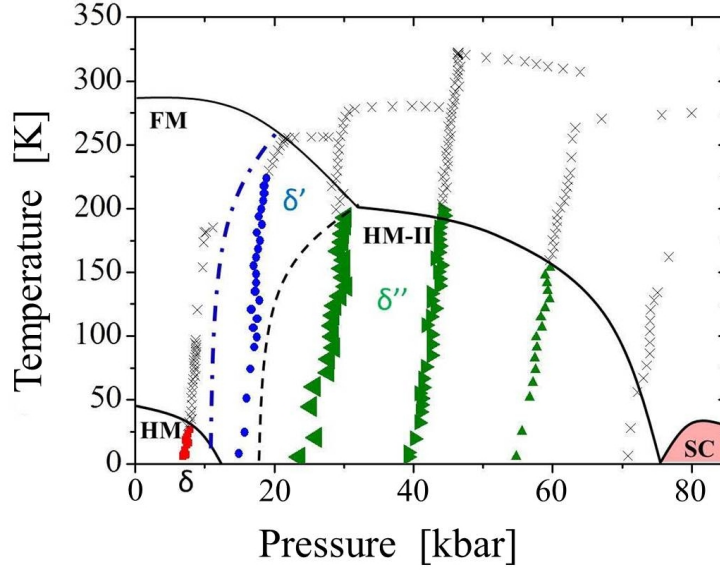
Figure B.10: The pressure-temperature phase diagram of MnP . Helimagnetic phase (HM), Superconducting phase (SC), Ferromagnetic phase (FM), and Antiferromagnetic phase (AFM) were proposed in [164] from susceptibility. The symbols shows the accessed points of the phase diagram in the D20 experiment, with the pressures calibrated from the Pb Bragg peaks (111) and (200). Color symbols red, blue, and green correspond respectively to the magnetic phases δ, δ' and δ" identified from the powder diffraction patterns.

crystal , with dimensions $\varnothing 4 \times 2$ mm, was aligned with (100) and (010) in the scattering plane.

The experiments were carried out using the high-intensity two-axis diffractometer D20 for the powdered sample and the thermal neutron diffractometer D23 for the single crystal at the ILL using a Paris-Edinburgh pressure cell. The particularity of this pressure cell is that applied pressure can be changed in-situ (described further in 1.1.10).

Powder neutron diffraction patterns were obtained the diffractometer D20 for $\lambda = 2.41$ Å. A methanol:ethanol mixture was added to the sample as a pressure-transmitting medium, creating a broad scattering feature in powder patterns around $30 \lesssim 2\theta \lesssim 50$. Figure B.10 shows the accessed points of the pressure temperature phase diagram as non-vertical lines, for which the temperature-dependent pressures were determined using Pb. The helimagnetic phase was identified from the powder diffraction patterns around an applied pressure of 7 kbar, but the expected antiferromagnetic order was not observed at 20 kbar applied pressure and above. In addition, a new phase δ' was observed in between the helimagnetic phase δ and the magnetic phase δ''.

Regarding the known δ phase, the magnetic satellite peak indexed as $(1 - \delta, 1, 0)$ was observed in the powder diffraction pattern for a pressure of ~ 7 kbar below 30K, with an intensity

reduced by a factor 17 from ambient pressure. The transition temperature is also reduced from 47 K at ambient pressure to 30K for 7 kbar applied pressure.

The new δ' phase discovered for an applied pressure of ~ 15 kbar at low temperatures, is characterised by four magnetic peaks appearing below 230 K, shown in the diffraction pattern of figure B.11. These peaks could be indexed with a propagation vector (0.25, 0.125, 0.25).
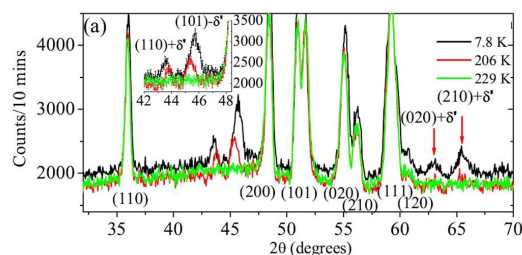
Figure B.11: Powder diffraction pattern of the new magnetic phase δ' for an applied pressure of 15 kbar (at ~ 10 K) showing the four magnetic peaks at 7.8K and 206 K (black and red curves) compared to the diffraction pattern at 229 K (green), just above the transition temperature.

The temperature-dependence of the nuclear peaks (110), (220) and of the magnetic peaks (110) + δ' is shown in figure B.12, obtained by fitting the resolution-limited peaks by normalised Gaussian functions. No transition to a ferromagnetic phase can be observed from the temperature dependence of the intensity of the nuclear peak, but the transition to the new magnetic phase around 230 K is clear from the magnetic peak (110) + δ'.
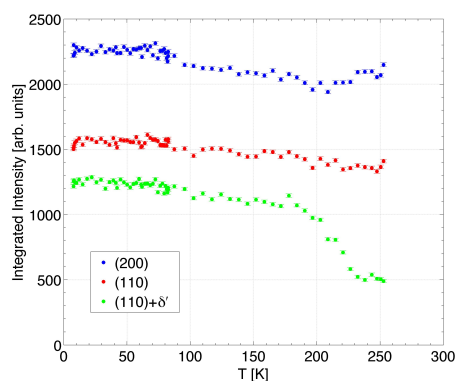
Figure B.12: Temperature dependence of the intensity of the nuclear peaks (110) and (200) and of the magnetic peak (110)+δ' for an applied pressure of ~ 15 kbar

The magnetic phase δ'' appearing for applied pressures above 20 kbar on the other hand is characterised by a broad magnetic scattering at low angles (around $2\theta = 3.7°$), while the four sharp magnetic peaks of the the δ' phase are not present in the δ'' phase. Figure B.13 shows the low angle part of the powder diffraction patterns for four different applied pressures by integrating over several temperature ranges. The value of the four applied pressures correspond to the measured pressures at low temperatures (~ 10 K) : 25, 39, 55 and 76 kbar.

As the background appears to be temperature dependant, the data were normalised to the nuclear Bragg peak (110) at 250K.
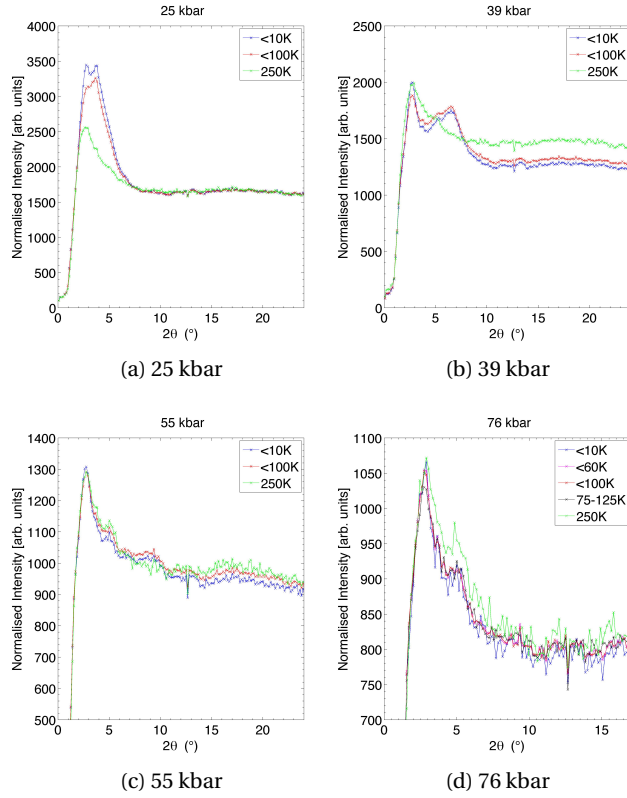
Figure B.13: Low angle part of the D20 powder diffraction pattern for an applied pressure of a) 25 kbar, b)39 kbar, c)55 kbar and d)76 kbar. Combining all scans with temperature below 10K (blue), below 100K (red) and around 250K (green), the data has been scaled with respect to the 250K (110) nuclear peak (at $2\theta = 36°$). For 76 kbar, there are additional curves for all data below 60 K (magenta) and between 75 and 125K (black)

As shown in figure B.14, the broad magnetic scattering feature appears to move from $2\theta = 3.7°$ at 25 kbar to $2\theta \sim 6°$ at 39 kbar, concomitant with a broadening and a significant decrease of ts intensity. At 55 kbar, a broad weak peak can still be identified around $2\theta \sim 9°$, while at 79 kbar no peak is visible. As this magnetic feature broadens and weakens with increased applied pressure, it cannot be completely excluded that it is present at 76 kbar with an intensity too weak to be detected from the background.

This feature can be attributed to short-range magnetic scattering and is consistent with a neutron pressure study [167] claiming that the δ'' phase is incommensurate along the c axis. In addition, under hydrostatic pressure, the lattice parameters only change significantly for the c axis, so that interaction between the Mn 3rd nearest neighbours is likely to play an important role in these magnetic structural changes.
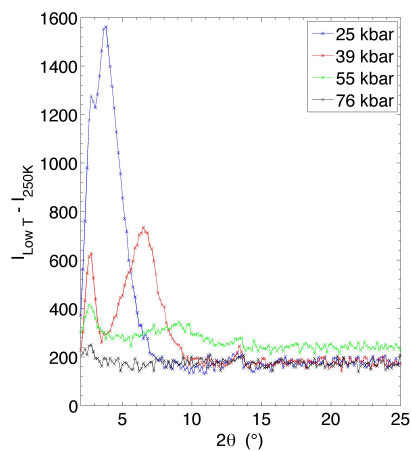
Figure B.14: Broad scattering feature scattering as a function of 2θ extracted by subtracting the high temperature datatset from the < 10 K dataset for an applied pressure of 25 kbar (blue), 39 kbar (red), 55 kbar (green) and 76 kbar (black).

Figure B.15 shows the temperature dependence of the broad magnetic scattering, obtained by integrating over the 2θ range of the observed scattering : [3.2,5] for 25 kbar, [5.5-8.5] for 39 kbar and [7.7-10.5] for 55 kbar. Regarding the highest applied pressure, the integrated range was [10-14] degrees, corresponding to a very weak possible peak consistent with the expected shift of the broad feature towards higher angles as pressure increases.
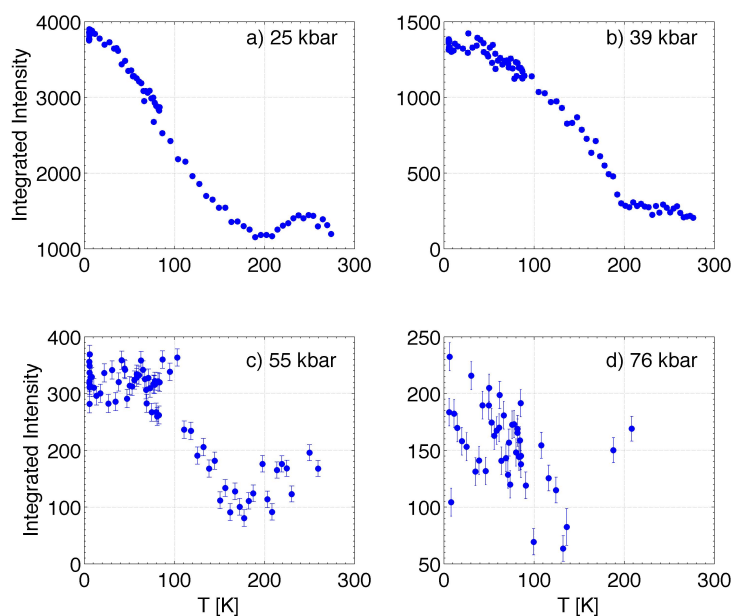
Figure B.15: Temperature dependence of the broad magnetic scattering observed in the δ'' magnetic phase as a function of applied pressure.

Appendix B. Incommensurate magnetic correlations in new superconductors

This temperature dependence allows to identify the transition temperature of the phase as a function of pressure, as shown the phase diagram of figure B.10, with a reduction of the transition temperature from ~ 200 K at 25 kbar to ~ 160 K at 55 kbar. In addition, the weak and broad feature observed at 55 kbar applied pressure is confirmed to correspond to the same magnetic scattering as at lower pressures since its temperature dependence follows the same behaviour. In the case of 76 kbar, the presence or absence of this feature cannot be determined, as the temperature dependence is not conclusive.

Finally, an attempt to find the propagation vector of the magnetic phases δ' and δ'' was carried out on D23 at a wavelength of 2.38 Å using a single crystal of MnP aligned with (100) and (010) in the scattering plane. No data for this experiment is shown, as no magnetic scattering was observed either in the δ' phase nor the δ'' phase.

Based on the powder diffraction, the intensity of the magnetic Bragg peaks in the δ' phase were expected to be high, but no peak was found in the (a, b) plane on D23, even when combining constant-Q scans with fixed 2θ scans. This result suggests that the propagation vector of this phase must have a component along the c axis, which cannot be accessed due to the small vertical opening of the Paris-Edinburgh pressure cell. A propagation vector $(0.25, 0.125, 0.25)$ can be proposed from the powder diffraction data.

Regarding the δ'' phase, magnetic peaks were searched at 39 kbar within the hypothesis of $\delta'' = (0.23 - 0.29, 0, 0)$, which corresponds to the $2\theta = 5.3 - 6.72$ values of the broad scattering seen in D20 powder diffraction patterns. Using 2θ fixed omega scan, and introducing an out-of-plane component by tilting within ± 3 degrees, no magnetic peaks were observed. These results support the idea that the incommensurability is along the c-axis.

From these sets of experiments, several conclusions are reached, confirming the complexity of the MnP pressure-temperature phase diagram: a new narrow magnetic phase is discovered at 15 kbar applied pressure, for which a propagation vector $(0.25, 0.125, 0.25)$ with a c-component is proposed. In order to solve this magnetic phase, further single crystal measurements with orientations including the c-axis in the scattering plane should be attempted. In addition, the δ'' magnetic phase from applied pressures of 25 kbar is shown to be incommensurate along c, and to extend at least to 55 kbar. This phase may even extend closer to the onset of the superconductivity phase, although it cannot be confirmed in the D20 experiment due to a too low signal compared to the background. Nevertheless, MnP is shown to be particularly interesting in the context of the interplay between complex magnetism phases and superconductivity.

Bibliography

[1] P. W. Anderson. Theory of magnetic exchange interactions: exchange in insulators and semiconductors. *Solid state physics*, 14:99–214, 1963.

[2] G. Ouvrard, R. Brec, and J. Rouxel. Structural determination of some MPS3 layered phases (M = Mn, Fe, Co, Ni and Cd). *Materials Research Bulletin*, 20(10):1181 – 1189, 1985.

[3] F. D. M. Haldane. Nonlinear field theory of large-spin Heisenberg antiferromagnets: semiclassically quantized solitons of the one-dimensional easy-axis Néel state. *Physical Review Letters*, 50(15):1153, 1983.

[4] J. P. Renard, L-P. Regnault, and M. Verdaguer. Experimental evidences for an Haldane gap in quasi one-dimensional antiferromagnets. *Le Journal de Physique Colloques*, 49(C8):C8–1425, 1988.

[5] K. Katsumata. Experimental studies of one-dimensional quantum spin systems. *Journal of Magnetism and Magnetic Materials*, 140:1595 – 1598, 1995.

[6] F. Mila. Quantum spin liquids. *European Journal of Physics*, 21(6):499, 2000.

[7] S. Miyahara and K. Ueda. Theory of the orthogonal dimer Heisenberg spin model for SrCu2(BO3)2. *Journal of Physics: Condensed Matter*, 15(9):R327, 2003.

[8] M. Mambrini and F. Mila. RVB description of the low-energy singlets of the spin 1/2 Kagomé antiferromagnet. *The European Physical Journal B-Condensed Matter and Complex Systems*, 17(4):651–659, 2000.

[9] G. L. Squires. *Introduction to the theory of thermal neutron scattering*. Cambridge university press, 2012.

[10] V. F. Sears. Neutron scattering lengths and cross sections. *Neutron news*, 3(3):26–37, 1992.

[11] S. W Lovesey. *Theory of neutron scattering from condensed matter*. 1984.

[12] R. Coldea, S. M. Hayden, G. Aeppli, T. G. Perring, C. D. Frost, T. E. Mason, S-W. Cheong, and Z. Fisk. Spin waves and electronic interactions in La2CuO4. *Physical review letters*, 86(23):5377, 2001.

Bibliography

[13] P. J. Brown. *International Tables For Crystallography*, volume C, chapter 4.4.5, pages 454–461. 2006.

[14] I. A Zaliznyak and S-H. Lee. Magnetic neutron scattering. *Modern Techniques for Characterizing Magnetic Materials, Springer, Heidelberg*, 2005.

[15] G. Shirane, S. M. Shapiro, and J. M. Tranquada. *Neutron scattering with a triple-axis spectrometer: basic techniques.* Cambridge University Press, 2002.

[16] M. J. Cooper and R. Nathans. The resolution function in neutron diffractometry. I. the resolution function of a neutron diffractometer and its application to phonon measurements. *Acta Crystallographica*, 23(3):357–367, 1967.

[17] M. Popovici. On the resolution of slow-neutron spectrometers. IV. the triple-axis spectrometer resolution function, spatial effects included. *Acta Crystallographica Section A: Crystal Physics, Diffraction, Theoretical and General Crystallography*, 31(4):507–513, 1975.

[18] D.A. Tennant and D. F. McMorrow. Rescal for Matlab: a computational package for calculating neutron TAS resolution functions. 1995. url: https://www.ill.eu/instruments-support/computing-for-science/cs-software/all-software/matlab-ill/rescal-for-matlab/.

[19] R.I. Bewley, J.W. Taylor, and S.M. Bennington. LET, a cold neutron multi-disk chopper spectrometer at ISIS. *Nuclear Instruments and Methods in Physics Research Section A: Accelerators, Spectrometers, Detectors and Associated Equipment*, 637(1):128 – 134, 2011.

[20] J. Ollivier and J-M. Zanotti. Diffusion inélastique de neutrons par temps de vol. *École thématique de la Société Française de la Neutronique*, 10:379–423, 2010.

[21] R. S. Eccleston. Time-of-flight inelastic neutron scattering. In A.-J. Dianoux and G. Lander, editors, *Neutron Data Booklet*. Institut Laue Langevin, 2002.

[22] R. M. Moon, T. Riste, and W. C. Koehler. Polarization analysis of thermal-neutron scattering. *Phys. Rev.*, 181:920–931, May 1969.

[23] O. Schärpf and H. Capellmann. The XYZ-difference method with polarized neutrons and the separation of coherent, spin incoherent, and magnetic scattering cross sections in a multidetector. *Physica Status Solidi (a)*, 135(2):359–379, 1993.

[24] J. R. Stewart, P. P. Deen, K. H. Andersen, H. Schober, J-F. Barthélémy, J. M. Hillier, A. P. Murani, T. Hayes, and B. Lindenau. Disordered materials studied using neutron polarization analysis on the multi-detector spectrometer, D7. *Journal of Applied Crystallography*, 42(1):69–84, 2009.

[25] W. Schweika and P. Böni. The instrument DNS: polarization analysis for diffuse neutron scattering. *Physica B: Condensed Matter*, 297(1):155–159, 2001.

[26] A. R. Wildes. Scientific reviews: Neutron polarization analysis corrections made easy. *Neutron News*, 17(2):17–25, 2006.

[27] I. F. Bailey. A review of sample environments in neutron scattering. *Zeitschrift für Kristallographie-Crystalline Materials*, 218(2):84–95, 2003.

[28] S. Klotz. *Techniques in high pressure neutron scattering.* CRC press, 2012.

[29] D. L. Decker. High-pressure equation of state for NaCl, KCl, and CsCl. *Journal of Applied Physics*, 42(8):3239–3244, 1971.

[30] E. F. Skelton, A. W. Webb, S. B. Qadri, S. A. Wolf, R. C. Lacoe, J. L. Feldman, W. T. Elam, E. R. Carpenter Jr, and C. Y. Huang. Energy-dispersive X-ray diffraction with synchrotron radiation at cryogenic temperatures. *Review of scientific instruments*, 55(6):849–855, 1984.

[31] D. B. McWhan, D. Bloch, and G. Parisot. Apparatus for neutron diffraction at high pressure. *Review of Scientific Instruments*, 45(5):643–646, 1974.

[32] J-E. Jørgensen and T. C. Hansen. Pressure-induced successive magnetic and structural phase transitions in Fe1.087Te. *The European Physical Journal B*, 88(5):1–8, 2015.

[33] Th. Strässle. In S. Klotz, editor, *Techniques in High Pressure Neutron Scattering*, chapter 13. CRC Press, 2012.

[34] K.C. Rule, D.J. Kennedy, S.J.and Goossens, A.M. Mulders, and T.J. Hicks. Contrasting antiferromagnetic order between FePS3 and MnPS3. *Applied Physics A*, 74(1):s811–s813, 2002.

[35] A. R. Wildes, V. Simonet, E. Ressouche, G. J. McIntyre, M. Avdeev, E. Suard, S. A. J. Kimber, D. Lançon, G. Pepe, B. Moubaraki, et al. Magnetic structure of the quasi-two-dimensional antiferromagnet NiPS3. *Physical Review B*, 92(22):224408, 2015.

[36] K. C. Rule, A. R. Wildes, R. I. Bewley, D. Visser, and T. J. Hicks. High energy excitations measured by neutron spectroscopy in FePS3. *Journal of Physics: Condensed Matter*, 21(12):124214, 2009.

[37] accessed : 2016-09-14. http://www.bellexinternational.com/products/cytop/.

[38] C. Kittel. Quantum theory of solids, SRP, 1987.

[39] T. Holstein and H. Primakoff. Field dependence of the intrinsic domain magnetization of a ferromagnet. *Physical Review*, 58(12):1098, 1940.

[40] M. Hase, I. Terasaki, and K. Uchinokura. Observation of the spin-Peierls transition in linear Cu^{2+} (spin-1/2) chains in an inorganic compound $CuGeO_3$. *Phys. Rev. Lett.*, 70:3651–3654, Jun 1993.

[41] T. Giamarchi, Ch. Rüegg, and O. Tchernyshyov. Bose-Einstein condensation in magnetic insulators. *Nature Physics*, 4(3):198–204, 2008.

[42] S. Haravifard, D. Graf, A. E. Feiguin, C. D. Batista, J. C. Lang, D. M. Silevitch, G. Srajer, B. D. Gaulin, H. A. Dabkowska, and T. F. Rosenbaum. Crystallization of spin superlattices with pressure and field in the layered magnet SrCu2(BO3)2. *Nature Communications*, 7, 2016.

[43] D. A. Tennant, C. Broholm, D. H. Reich, S. E. Nagler, G. E. Granroth, T. Barnes, K. Damle, G. Xu, Y. Chen, and B. C. Sales. Neutron scattering study of two-magnon states in the quantum magnet copper nitrate. *Phys. Rev. B*, 67:054414, Feb 2003.

[44] H. Kageyama, M. Nishi, N. Aso, K. Onizuka, T. Yosihama, K. Nukui, K. Kodama, K. Kakurai, and Y. Ueda. Direct evidence for the localized single-triplet excitations and the dispersive multitriplet excitations in $SrCu_2(BO_3)_2$. *Physical review letters*, 84(5876), 2000.

[45] J. Dorier, K. P. Schmidt, and F. Mila. Theory of magnetization plateaux in the Shastry-Sutherland model. *Phys. Rev. Lett.*, 101:250402, Dec 2008.

[46] K. Kodama, M. Takigawa, M. Horvatić, C. Berthier, H. Kageyama, Y. Ueda, S. Miyahara, F. Becca, and F. Mila. Magnetic superstructure in the two-dimensional quantum antiferromagnet SrCu2(BO3)2. *Science*, 298(5592):395–399, 2002.

[47] S. Miyahara and K. Ueda. Thermodynamics properties of three dimensional orthogonal dimer model for SrCu2(BO3)(2). *J. Phy. Soc. Japan (Suppl.) B*, 2000.

[48] A. Honecker, S. Wessel, R. Kerkdyk, T. Pruschke, F. Mila, and B. Normand. Thermodynamic properties of highly frustrated quantum spin ladders: Influence of many-particle bound states. *Phys. Rev. B*, 93:054408, Feb 2016.

[49] B. D. Gaulin, S. H. Lee, S. Haravifard, J. P. Castellan, A. J. Berlinsky, H. A. Dabkowska, Y. Qiu, and J. R. D. Copley. High-resolution study of spin excitations in the singlet ground state of SrCu2(BO3)(2). *Physical review letters*, 93(26):267202, 2004.

[50] S. Miyahara, F. Mila, K. Kodama, M. Takigawa, M. Horvatic, C. Berthier, H. Kageyama, and Y. Ueda. The effects of intra-dimer Dzyaloshinsky-Moriya interaction on the properties of SrCu2(BO3)2 in an external magnetic field. *Journal Of Physics-Condensed Matter*, 16:S911–S916, 2004.

[51] M. E. Zayed, Ch. Rüegg, Th. Strässle, U. Stuhr, B. Roessli, M. Ay, J. Mesot, P. Link, E. Pomjakushina, M. Stingaciu, et al. Correlated decay of triplet excitations in the Shastry-Sutherland compound SrCu2(BO3)2. *Physical review letters*, 113(6):067201, 2014.

[52] K. Kakurai, K. Nukui, N. Aso, M. Nishi, H. Kadowaki, H. Kageyama, Y. Ueda, L-P. Regnault, and O. Cépas. Neutron scattering investigation on quantum spin system SrCu2(BO3)2. *Progress of Theoretical Physics Supplement*, 159:22–32, 2005.

[53] M. E. Zayed, Ch. Rüegg, J. Larrea, A. M. Läuchli, C. Panagopoulos, S. S. Saxena, M. Ellerby, D. F. McMorrow, Th. Strässle, S. Klotz, et al. Observation of a 4-spin Plaquette singlet state in the Shastry-Sutherland compound SrCu2(BO3)2. *arXiv preprint arXiv:1603.02039*, 2016.

[54] N. Aso, H.i Kageyama, K. Nukui, M. Nishi, H. Kadowaki, Y. Ueda, and K. Kakurai. High energy-resolution inelastic neutron scattering experiments on triplet bound state excitations in SrCu2(BO3)2. *Journal of the Physical Society of Japan*, 74(8):2189–2192, 2005.

[55] B. S. Shastry and B. Sutherland. Exact ground state of a quantum mechanical antiferromagnet. *Physica B+ C*, 108(1-3):1069–1070, 1981.

[56] C. K. Majumdar and D. K. Ghosh. On next-nearest-neighbor interaction in linear chain. i. *Journal of Mathematical Physics*, 10(8):1388–1398, 1969.

[57] H. Nojiri, H. Kageyama, Y. Ueda, and M. Motokawa. ESR study on the excited state energy spectrum of SrCu2(BO3)2 – A central role of multiple-triplet bound states. *Journal of the Physical Society of Japan*, 72(12):3243–3253, 2003.

[58] O. Cépas, K. Kakurai, L-P. Regnault, T. Ziman, J. P. Boucher, N. Aso, M. Nishi, H. Kageyama, and Y. Ueda. Dzyaloshinski-Moriya interaction in the 2D spin gap system SrCu2(BO3)2. *Physical review letters*, 87(16):167205, 2001.

[59] K. Kodama, K. Arai, M. Takigawa, H. Kageyama, and Y. Ueda. Spin correlation and field induced staggered magnetization in the 2D orthogonal dimer spin system SrCu2(BO3)2. *Journal of magnetism and magnetic materials*, 272:491–492, 2004.

[60] J. Romhányi, K. Penc, and G. Ramachandran. Hall effect of triplons in a dimerized quantum magnet. *Nature communications*, 6, 2015.

[61] Y. F. Cheng, O. Cépas, P. W. Leung, and T. Ziman. Magnon dispersion and anisotropies in SrCu$_2$(BO$_3$)$_2$. *Phys. Rev. B*, 75:144422, Apr 2007.

[62] Ch. Knetter and G. S. Uhrig. Dynamic structure factor of the two-dimensional Shastry-Sutherland model. *Physical review letters*, 92(2):027204, 2004.

[63] P. Corboz and F. Mila. Tensor network study of the Shastry-Sutherland model in zero magnetic field. *Phys. Rev. B*, 87:115144, Mar 2013.

[64] F. Levy, I. Sheikin, C. Berthier, M. Horvatić, M. Takigawa, H. Kageyama, T. Waki, and Y. Ueda. Field dependence of the quantum ground state in the Shastry-Sutherland system SrCu2(BO3)2. *EPL (Europhysics Letters)*, 81(6):67004, 2008.

[65] B. Normand and Ch. Rüegg. Complete bond-operator theory of the two-chain spin ladder. *Phys. Rev. B*, 83:054415, Feb 2011.

Bibliography

[66] Ch. Rüegg, B. Normand, M. Matsumoto, Ch. Niedermayer, A. Furrer, K. W. Krämer, H.-U. Güdel, Ph. Bourges, Y. Sidis, and H. Mutka. Quantum statistics of interacting dimer spin systems. *Phys. Rev. Lett.*, 95:267201, Dec 2005.

[67] D. A. Tennant, B. Lake, A. J. A. James, F. H. L. Essler, S. Notbohm, H.-J. Mikeska, J. Fielden, P. Kögerler, P. C. Canfield, and M. T. F. Telling. Anomalous dynamical line shapes in a quantum magnet at finite temperature. *Phys. Rev. B*, 85:014402, Jan 2012.

[68] M. E. Zayed. *Novel states in magnetic materials under extreme conditions*. PhD thesis, Diss., Eidgenössische Technische Hochschule ETH Zürich, Nr. 19103, 2010, 2010.

[69] S. El Shawish and J. Bonča. Spin-polaron excitations in a doped Shastry-Sutherland model. *Phys. Rev. B*, 74:174420, Nov 2006.

[70] B Fåk and B Dorner. Phonon line shapes and excitation energies. *Physica B: Condensed Matter*, 234:1107–1108, 1997.

[71] A. Honecker, F. Mila, and B. Normand. Multi-triplet bound states and finite-temperature dynamics in highly frustrated quantum spin ladders. *Phys. Rev. B*, 94:094402, Sep 2016.

[72] T. Senthil, A. Vishwanath, L. Balents, S. Sachdev, and M. P. A. Fisher. Deconfined quantum critical points. *Science*, 303(5663):1490–1494, 2004.

[73] M.E. Zayed, Ch. Rüegg, E. Pomjakushina, M. Stingaciu, K. Conder, M. Hanfland, M. Merlini, and H.M. Rønnow. Temperature dependence of the pressure induced monoclinic distortion in the spin Shastry–Sutherland compound SrCu2(BO3)2. *Solid State Communications*, 186:13 – 17, 2014.

[74] S. Haravifard, A. Banerjee, J. van Wezel, D. M. Silevitch, A. M. dos Santos, J. C. Lang, E. Kermarrec, G. Srajer, B. D. Gaulin, J. J. Molaison, H. A. Dabkowska, and T. F. Rosenbaum. Emergence of long-range order in sheets of magnetic dimers. *Proceedings of the National Academy of Sciences*, 111(40):14372–14377, 2014.

[75] T. Momoi and K. Totsuka. Magnetization plateaus as insulator-superfluid transitions in quantum spin systems. *Phys. Rev. B*, 61:3231–3234, Feb 2000.

[76] J. E. Moore. The birth of topological insulators. *Nature*, 464(7286):194–198, 2010.

[77] L. Fu, C. L. Kane, and E. J. Mele. Topological insulators in three dimensions. *Physical Review Letters*, 98(10):106803, 2007.

[78] R. Chisnell, J. S. Helton, D. E. Freedman, D. K. Singh, R. I. Bewley, D. G. Nocera, and Y. S. Lee. Topological magnon bands in a Kagomé lattice ferromagnet. *Physical review letters*, 115(14):147201, 2015.

[79] R. Shindou, R. Matsumoto, S. Murakami, and J. Ohe. Topological chiral magnonic edge mode in a magnonic crystal. *Physical Review B*, 87(17):174427, 2013.

[80] Y. Onose, T. Ideue, H. Katsura, Y. Shiomi, N. Nagaosa, and Y. Tokura. Observation of the magnon hall effect. *Science*, 329(5989):297–299, 2010.

[81] R. Matsumoto and S. Murakami. Theoretical prediction of a rotating magnon wave packet in ferromagnets. *Phys. Rev. Lett.*, 106:197202, May 2011.

[82] L. Zhang, J. Ren, J-S. Wang, and B. Li. Topological magnon insulator in insulating ferromagnet. *Physical Review B*, 87(14):144101, 2013.

[83] T. Ideue, Y. Onose, H. Katsura, Y. Shiomi, S. Ishiwata, N. Nagaosa, and Y. Tokura. Effect of lattice geometry on magnon hall effect in ferromagnetic insulators. *Physical Review B*, 85(13):134411, 2012.

[84] H. Katsura, N. Nagaosa, and P. A. Lee. Theory of the thermal Hall effect in quantum magnets. *Phys. Rev. Lett.*, 104:066403, Feb 2010.

[85] T. Rõom, D. Hüvonen, U. Nagel, J. Hwang, T. Timusk, and H. Kageyama. Far-infrared spectroscopy of spin excitations and Dzyaloshinskii-Moriya interactions in the Shastry-Sutherland compound $SrCu_2(BO_3)_2$. *Phys. Rev. B*, 70:144417, Oct 2004.

[86] P. A. McClarty, F. Krüger, T. Guidi, S. F. Parker, K. Refson, A. W. Parker, D. Prabakharan, and R. Coldea. Topological triplon modes and bound states in a Shastry-Sutherland magnet. *arXiv preprint arXiv:1609.01922*, 2016.

[87] K. Siemensmeyer, E. Wulf, H-J. Mikeska, K. Flachbart, S. Gabáni, S. Mat'aš, P. Priputen, A. Efdokimova, and N. Shitsevalova. Fractional magnetization plateaus and magnetic order in the shastry-sutherland magnet tmb 4. *Physical review letters*, 101(17):177201, 2008.

[88] R. Brec. Review on structural and chemical properties of transition metal phosphorous trisulfides MPS3. *Solid State Ionics*, 22(1):3–30, 1986.

[89] G. Ouvrard, R. Brec, and J. Rouxel. Structural determination of some MPS3 layered phases (M= Mn, Fe, Co, Ni and Cd). *Materials research bulletin*, 20(10):1181–1189, 1985.

[90] V. Grasso and L. Silipigni. Low-dimensional materials: The MPX3 family —physical features and potential future applications. *Nuovo Cimento Rivista Serie*, 25(6):1–102, 2002.

[91] C-T. Kuo, M. Neumann, K. Balamurugan, H. J. Park, S. Kang, H. W. Shiu, J. H. Kang, B. H. Hong, M. Han, T. W. Noh, et al. Exfoliation and Raman spectroscopic fingerprint of few-layer NiPS3 Van der Waals crystals. *Scientific reports*, 6, 2016.

[92] J-U. Lee, S. Lee, J. H. Ryoo, S. Kang, T. Y. Kim, P. Kim, C-H. Park, J-G. Park, and H. Cheong. Ising-type magnetic ordering in atomically thin FePS3. *arXiv preprint arXiv:1608.04169*, 2016.

[93] J.-G. Park. Opportunities and challenges of 2D magnetic Van der Waals materials: magnetic graphene? *Journal of physics. Condensed matter: an Institute of Physics journal*, 28(30):301001, 2016.

[94] J. B. Fouet, P. Sindzingre, and C. Lhuillier. An investigation of the quantum J1-J2-J3 model on the honeycomb lattice. *The European Physical Journal B-Condensed Matter and Complex Systems*, 20(2):241–254, 2001.

[95] E. Ressouche, M. Loire, V. Simonet, R. Ballou, A. Stunault, and A. Wildes. Magnetoelectric MnPS$_3$ as a candidate for ferrotoroidicity. *Phys. Rev. B*, 82:100408, Sep 2010.

[96] A. R. Wildes, H. M. Rønnow, B. Roessli, M. J. Harris, and K. W. Godfrey. Static and dynamic critical properties of the quasi-two-dimensional antiferromagnet MnPS3. *Physical Review B*, 74(9):094422, 2006.

[97] A. R. Wildes, K. C. Rule, R. I. Bewley, M. Enderle, and T. J. Hicks. The magnon dynamics and spin exchange parameters of FePS3. *Journal of Physics: Condensed Matter*, 24(41):416004, 2012.

[98] C. Murayama, M. Okabe, D. Urushihara, T. Asaka, K. Fukuda, M. Isobe, K. Yamamoto, and Y. Matsushita. Crystallographic features related to a Van der Waals coupling in the layered chalcogenide FePS3. *Journal of Applied Physics*, 120(14):142114, 2016.

[99] K. Kurosawa, S. Saito, and Y. Yamaguchi. Neutron diffraction study on MnPS3 and FePS3. *Journal of the Physical Society of Japan*, 52(11):3919–3926, 1983.

[100] K. C. Rule, G. J. McIntyre, S. J. Kennedy, and T. J. Hicks. Single-crystal and powder neutron diffraction experiments on FePS3: Search for the magnetic structure. *Physical Review B*, 76(13):134402, 2007.

[101] K. C. Rule, T. Ersez, S. J. Kennedy, and T. J. Hicks. Identification of features in the powder pattern of the antiferromagnet FePS3 using polarization analysis with energy analysis. *Physica B: Condensed Matter*, 335(1):6–10, 2003.

[102] E. M. Wheeler, R. Coldea, E. Wawrzyńska, T. Sörgel, M. Jansen, M. M. Koza, J. Taylor, P. Adroguer, and N. Shannon. Spin dynamics of the frustrated easy-axis triangular antiferromagnet 2H-AgNiO2 explored by inelastic neutron scattering. *Physical Review B*, 79(10):104421, 2009.

[103] P. Jernberg, S. Bjarman, and R. Wäppling. FePS3: A first-order phase transition in a "2D" Ising antiferromagnet. *Journal of magnetism and magnetic materials*, 46(1):178–190, 1984.

[104] P. Ferloni and M. Scagliotti. Magnetic phase transitions in iron and nickel phosphorus trichalcogenides. *Thermochimica acta*, 139:197–203, 1989.

[105] T. Sekine, M. Jouanne, C. Julien, and M. Balkanski. Light-scattering study of dynamical behavior of antiferromagnetic spins in the layered magnetic semiconductor $FePS_3$. *Phys. Rev. B*, 42:8382–8393, Nov 1990.

[106] Y. Takano, N. Arai, A. Arai, Y. Takahashi, K. Takase, and K. Sekizawa. Magnetic properties and specific heat of MPS3 (M= Mn, Fe, Zn). *Journal of Magnetism and Magnetic Materials*, 272:E593–E595, 2004.

[107] T. Masubuchi, H. Hoya, T. Watanabe, Y. Takahashi, S. Ban, N. Ohkubo, K. Takase, and Y. Takano. Phase diagram, magnetic properties and specific heat of $Mn1 − x$FexPS3. *Journal of Alloys and Compounds*, 460(1):668–674, 2008.

[108] J. Rodríguez-Carvajal. Recent advances in magnetic structure determination by neutron powder diffraction. *Physica B: Condensed Matter*, 192(1):55–69, 1993.

[109] R. J. Baxter. *Exactly solved models in statistical physics*, chapter 11. Academic, New York, 1982.

[110] G. Benedek, G. L. Marra, L. Miglio, M. Scagliotti, and M. Jouanne. Lattice dynamics of layered crystals in the class MPX3 (M= Fe, Mn; X= Se, S). *Physica Scripta*, 37(5):759, 1988.

[111] E. Prouzet, G. Ouvrard, R. Brec, and P. Seguineau. Room temperature synthesis of pure amorphous nickel hexathiodiphosphate Ni2P2S6. *Solid State Ionics*, 31(1):79 – 90, 1988.

[112] P. Fragnaud, E. Prouzet, G. Ouvrard, J.L. Mansot, C. Payen, R. Brec, and H. Dexpert. Room temperature synthesis study of highly disordered a-Ni2P2S6. *Journal of Non-Crystalline Solids*, 160(1):1 – 17, 1993.

[113] G. Wei, H. Miao, J. Liu, and A. Du. Ground-state magnetic properties of the spin-2 transverse Ising model. *Journal of Magnetism and Magnetic Materials*, 320(6):1151–1156, 2008.

[114] W. Jiang, G-Z. Wie, and Z-H. Xin. Transverse Ising model with a crystal field for the spin-2. *Physica Status Solidi (B)*, 225(1):215–221, 2001.

[115] O. Canko, E. Albayrak, and M. Keskin. The quantum transverse spin-2 Ising model with a bimodal random-field in the pair approximation. *Journal of magnetism and magnetic materials*, 294(1):63–71, 2005.

[116] L. Onsager. Crystal statistics I. a two-dimensional model with an order-disorder transition. *Physical Review*, 65(3-4):117, 1944.

[117] D. F. de Albuquerque, I.P. Fittipaldi, and J.R. de Sousa. Absence of tricritical behavior of the random field Ising model in a honyecomb lattice. *Journal of Magnetism and Magnetic Materials*, 306(1):92 – 97, 2006.

Bibliography

[118] K. Matan, B. M. Bartlett, J. S. Helton, V. Sikolenko, S. Mat'aš, K. Prokeš, Y. Chen, J. W. Lynn, D. Grohol, T. J. Sato, M. Tokunaga, D. G. Nocera, and Y. S. Lee. Dzyaloshinskii-Moriya interaction and spin reorientation transition in the frustrated Kagomé lattice antiferromagnet. *Phys. Rev. B*, 83:214406, Jun 2011.

[119] A. S. Freitas and D. F. de Albuquerque. Existence of a tricritical point in the antiferromagnet $KFe_3(OH)_6(SO_4)_2$ on a Kagomé lattice. *Phys. Rev. E*, 91:012117, Jan 2015.

[120] K. C. Rule. *Magnetic Ordering in the Two Dimensional Antiferromagnet, FePS3.* PhD thesis, Monash University, Department of Physics, 2004.

[121] K. Okuda, K. Kurosawa, and S. Saito. High field magnetization process in FePS3. In *High field magnetism*. 1983.

[122] L. P. Regnault, J. Y. Henry, J. Rossat-Mignod, and A. De Combarieu. Magnetic properties of the layered nickel compounds BaNi2(PO4)2 and BaNi2(AsO4)2. *Journal of Magnetism and Magnetic Materials*, 15:1021–1022, 1980.

[123] S. K. Choi, R. Coldea, A. N. Kolmogorov, T. Lancaster, I. I. Mazin, S. J. Blundell, P. G. Radaelli, Yogesh Singh, P. Gegenwart, K. R. Choi, S.-W. Cheong, P. J. Baker, C. Stock, and J. Taylor. Spin waves and revised crystal structure of honeycomb iridate Na_2IrO_3. *Phys. Rev. Lett.*, 108:127204, Mar 2012.

[124] P. A. Joy and S. Vasudevan. Magnetism in the layered transition-metal thiophosphates MPS3 (M= Mn, Fe, and Ni). *Physical Review B*, 46(9):5425, 1992.

[125] N. Chandrasekharan and S. Vasudevan. Magnetism and exchange in the layered antiferromagnet NiPS3. *Journal of Physics: Condensed Matter*, 6(24):4569, 1994.

[126] S. S. Rosenblum and R. Merlin. Resonant two-magnon raman scattering at high pressures in the layered antiferromagnetic NiPS3. *Physical Review B*, 59(9):6317, 1999.

[127] H-J. Lee, S-Y. Jeong, C. R. Cho, and C. H. Park. Study of diluted magnetic semiconductor: Co-doped ZnO. *Applied Physics Letters*, 81(21):4020–4022, 2002.

[128] T. Dietl, H. Ohno, F. Matsukura, J. Cibert, and D. Ferrand. Zener model description of ferromagnetism in zinc-blende magnetic semiconductors. *Science*, 287(5455):1019–1022, 2000.

[129] P. Sharma, A. Gupta, K. V. Rao, F. J. Owens, R. Sharma, R. Ahuja, J. M. O. Guillen, B. Johansson, and G. A. Gehring. Ferromagnetism above room temperature in bulk and transparent thin films of Mn-doped ZnO. *Nature materials*, 2(10):673–677, 2003.

[130] J. M. D. Coey, M. Venkatesan, and C. B. Fitzgerald. Donor impurity band exchange in dilute ferromagnetic oxides. *Nature materials*, 4(2):173–179, 2005.

[131] Y. Q. Chang, D. B. Wang, X. H. Luo, X. Y. Xu, X. H. Chen, L. Li, C. P. Chen, R. M. Wang, J. Xu, and D. P. Yu. Synthesis, optical, and magnetic properties of diluted magnetic semiconductor Zn1-xMnxO nanowires via vapor phase growth. *Applied Physics Letters*, 83(19):4020–4022, 2003.

[132] G. Lawes, A. S. Risbud, A. P. Ramirez, and R. Seshadri. Absence of ferromagnetism in Co and Mn substituted polycrystalline ZnO. *Physical Review B*, 71(4):045201, 2005.

[133] S. J. Pearton, W. H. Heo, M. Ivill, D. P. Norton, and T. Steiner. Dilute magnetic semiconducting oxides. *Semiconductor Science and Technology*, 19(10):R59, 2004.

[134] K. R. Kittilstved, W. K. Liu, and D. R. Gamelin. Electronic structure origins of polarity-dependent high-Tc ferromagnetism in oxide-diluted magnetic semiconductors. *Nature materials*, 5(4):291–297, 2006.

[135] J. L. Costa-Krämer, F. Briones, J. F. Fernandez, A. C. Caballero, M. Villegas, M. Diaz, M. A. García, and A. Hernando. Nanostructure and magnetic properties of the MnZnO system, a room temperature magnetic semiconductor? *Nanotechnology*, 16(2):214, 2005.

[136] T. Dietl. A ten-year perspective on dilute magnetic semiconductors and oxides. *Nature materials*, 9(12):965–974, 2010.

[137] X. L. Wang, K. H. Lai, and A. Ruotolo. A comparative study on the ferromagnetic properties of undoped and Mn-doped ZnO. *Journal of Alloys and Compounds*, 542:147–150, 2012.

[138] Z. Micković, A. T. L. Duncan, A. Sienkiewicz, M. Mionić, L. Forró, and A. Magrez. Synthesis of nanosized Mn-Doped ZnO by low temperature decomposition of hydrozincite precursors. *Crystal Growth Design*, 10:4437–4441, 2010.

[139] N. S. Norberg, K. R. Kittilstved, J. E. Amonette, R. K. Kukkadapu, D. A Schwartz, and D. R. Gamelin. Synthesis of colloidal Mn^{2+}: ZnO quantum dots and high-Tc ferromagnetic nanocrystalline thin films. *Journal of the American Chemical Society*, 126(30):9387–9398, 2004.

[140] T. Chatterji, Y. Su, G. N. Iles, Y-C Lee, A. P. Khandhar, and K. M. Krishnan. Antiferromagnetic correlations in MnO nanoparticles. *Journal of Magnetism and Magnetic Materials*, 322:3333–3336, 2010.

[141] C-C. Lin, C-J. Chen, and R-K. Chiang. Facile synthesis of monodisperse MnO nanoparticles from bulk MnO. *Journal of Crystal Growth*, 338(1):152–156, 2012.

[142] H. Shaked, J. Faber Jr, and R. L. Hitterman. Low-temperature magnetic structure of MnO: a high-resolution neutron-diffraction study. *Physical Review B*, 38(16):11901, 1988.

[143] W. L. Roth. Magnetic structures of MnO, FeO, CoO, and NiO. *Phys. Rev.*, 110:1333–1341, 1958.

[144] J. Fu, X. Ren, S. Yan, Y. Gong, Y. Tan, K. Liang, R. Du, X. Xing, G. Mo, Z. Chen, et al. Synthesis and structural characterization of ZnO doped with Co. *Journal of Alloys and Compounds*, 558:212–221, 2013.

[145] J. H. Park, M. G. Kim, H. M. Jang, S. Ryu, and Y. M. Kim. Co-metal clustering as the origin of ferromagnetism in Co-doped ZnO thin films. *Applied Physics Letters*, 84(8):1338–1340, 2004.

[146] I. I. Mazin. Superconductivity gets an iron boost. *Nature*, 464(7286):183–186, 2010.

[147] M. D. Lumsden and A. D. Christianson. Magnetism in Fe-based superconductors. *Journal of Physics: Condensed Matter*, 22(20):203203, 2010.

[148] J. M. Tranquada, G. Xu, and I. A. Zaliznyak. Superconductivity, antiferromagnetism, and neutron scattering. *Journal of Magnetism and Magnetic Materials*, 350:148–160, 2014.

[149] W. Wu, J. Cheng, K. Matsubayashi, P. Kong, F. Lin, C. Jin, N. Wang, Y. Uwatoko, and J. Luo. Superconductivity in the vicinity of antiferromagnetic order in CrAs. *Nature communications*, 5, 2014.

[150] H. Kotegawa, S. Nakahara, H. Tou, and H. Sugawara. Superconductivity of 2.2 K under pressure in helimagnet CrAs. *Journal of the Physical Society of Japan*, 83(9):093702, 2014.

[151] Y. Kamihara, T. Watanabe, M. Hirano, and H. Hosono. Iron-based layered superconductor La[O1 − xFx] FeAs (x= 0.05-0.12) with Tc= 26 K. *Journal of the American Chemical Society*, 130(11):3296–3297, 2008.

[152] Z. A. Ren, J. Yang, W. Lu, et al. Superconductivity in the iron-based F-doped layered quaternary compound Nd[O1 − xFx]FeAs. *Europhys. Lett*, 82:57002, 2008.

[153] H. H. Wen and S. Li. Materials and novel superconductivity in iron pnictide superconductors. *Annu. Rev. Condens. Matter Phys.*, 2(1):121–140, 2011.

[154] A. D. Christianson, M. D. Lumsden, K. Marty, et al. Doping dependence of the spin excitations in the Fe-based superconductors Fe1 + xTe1 − ySey. *Phys. Rev. B*, 87:224410, Jun 2013.

[155] S. Liand, C. Zhang, M. Wang, et al. Normal-state hourglass dispersion of the spin excitations in FeSe$_x$Te$_{1-x}$. *Phys. Rev. Lett.*, 105:157002, Oct 2010.

[156] N. Tsyrulin, R. Viennois, E. Giannini, et al. Magnetic hourglass dispersion and its relation to high-temperature superconductivity in iron-tuned Fe1 + xTe0.7Se0.3. *New Journal of Physics*, 14(7):073025, 2012.

[157] R. Viennois, E. Giannini, D. van der Marel, et al. Effect of Fe excess on structural, magnetic and superconducting properties of single-crystalline Fe1+xTe1−ySey. *Journal of Solid State Chemistry*, 183(4):769 – 775, 2010.

[158] M. Bendele, A. Maisuradze, B. Roessli, et al. Pressure-induced ferromagnetism in antiferromagnetic $Fe_{1.03}Te$. *Phys. Rev. B*, 87:060409, Feb 2013.

[159] D. J. Scalapino and S. R. White. Superconducting condensation energy and an anti-ferromagnetic exchange-based pairing mechanism. *Physical Review B*, 58(13):8222, 1998.

[160] N. C. Gresty, Y. Takabayashi, A. Y. Ganin, et al. Structural phase transitions and super-conductivity in $Fe1+ \delta Se0.57Te0.43$ at ambient and elevated pressures. *Journal of the American Chemical Society*, 131(46):16944–16952, 2009.

[161] N. Katayama, K. Matsubayashi, Y. Nomura, et al. Conductivity and incommensurate antiferromagnetism of Fe1. 02Se0. 10Te0.90 under pressure. *EPL (Europhysics Letters)*, 98(3), MAY 2012.

[162] D. Lançon, N. Tsyrulin, M. Böhm, R. Viennois, S. Zabihzadeh, A. Kusmartseva, E. Gian-nini, and H. M. Rønnow. Pressure induced evolution of superconductivity and magnetic hourglass dispersion in Fe1.02Te0.7Se0.3. *New Journal of Physics*, 17(4):043020, 2015.

[163] T. J. Liu, J. Hu, B. Qian, D. Fobes, Z. Q. Mao, W. Bao, M. Reehuis, S. A. J. Kimber, K. Prokeš, S. Matas, et al. From $(\pi, 0)$ magnetic order to superconductivity with (π, π) magnetic resonance in $Fe1.02Te1 − xSex$. *Nature Materials*, 9(9):718–720, 2010.

[164] J.-G. Cheng, K. Matsubayashi, W. Wu, J. P. Sun, F. K. Lin, J. L. Luo, and Y. Uwatoko. Pressure induced superconductivity on the border of magnetic order in MnP. *Phys. Rev. Lett.*, 114:117001, Mar 2015.

[165] L. Keller, J. S. White, M. Frontzek, P. Babkevich, M. A. Susner, Z. C. Sims, A. S. Sefat, H. M. Rønnow, and Ch. Rüegg. Pressure dependence of the magnetic order in CrAs: A neutron diffraction investigation. *Physical Review B*, 91(2):020409, 2015.

[166] S. Yano, S. Itoh, T. Yokoo, S. Satoh, D. Kawana, Y. Kousaka, J. Akimitsu, and Y. Endoh. Mag-netic excitations in ferromagnetic phase of MnP. *Journal of Magnetism and Magnetic Materials*, 347:33–38, 2013.

[167] M. Matsuda, F. Ye, S. E. Dissanayake, J-G. Cheng, S. Chi, J. Ma, H. D. Zhou, J-Q. Yan, S. Kasamatsu, O. Sugino, et al. Pressure dependence of the magnetic ground states in MnP. *Physical Review B*, 93(10):100405, 2016.

Diane Lançon
Born March 13th 1988, Grenoble, France

Research Experience

10/2012 - 12/2016	**Laboratory for Quantum magnetism (LQM)** École Polytechnique Fédérale de Lausanne, Switzerland **PhD Student**, *Supervisor :* Henrik M. Rønnow
10/2012 - 12/2016	**TOF-HR, Institut Laue Langevin (ILL)** Grenoble, France **PhD Student**, *Supervisor :* Andrew R. Wildes **Neutron spectroscopy in the layered quantum magnet $SrCu_2(BO_3)_2$ and in transition metal phosphorus trisulfides (MPS_3)**
02/2012 - 09/2012	**Laboratory for Quantum magnetism (LQM)** École Polytechnique Fédérale de Lausanne, Switzerland **Master Thesis :** High energy magnetic excitations in layered cuprates

Education

2012 - 2016	PhD, Laboratory for Quantum magnetism (LQM) École Polytechnique Fédérale de Lausanne, Switzerland
2010-2012	M.Sc. Physics, École Polytechnique Fédérale de Lausanne, Switzerland
2007-2010	B.Sc. Physics, École Polytechnique Fédérale de Lausanne, Switzerland
2009-2010	3rd year Physics (ERASMUS), Royal Institute of Technology / KTH, Stockholm, Sweden
2006-2007	1rst year Bachelor in Linguistics, Université Stendhal, Grenoble, France
2006	Baccalauréat scientifique, Lycée International Europole, Grenoble, France

- **D. Lançon**, G. J. Nilsen, A. R. Wildes, K. Nemkovski, P. Huang, D. Fejes, H. M. Rønnow and A. Magrez *MnO nanoparticles as the cause of ferromagnetism in bulk dilute Mn-doped ZnO*, in Appl. Phys. Lett., vol 109, 2016;

- **D. Lançon**, H. C. Walker, E. Ressouche, B. Ouladdiaf, K. C. Rule, G. J. McIntyre, T. J. Hicks, H. M. Rønnow, and A. R. Wildes *The magnetic structure and magnon dynamics of the quasi-two dimensional antiferromagnet FePS$_3$*, in Phys. Rev. B, vol 94, 2016

- **D. Lançon**, N. Tsyrulin, M. Böhm, R. Viennois, S. Zabihzadeh, A. Kusmartseva, E. Giannini and H. M. Rønnow, *Pressure induced evolution of superconductivity and magnetic hourglass dispersion in Fe$_{1.02}$Te$_{0.7}$Se$_{0.3}$*, in New Journal of Physics, vol 17, 2015

- **D. Lançon**, R. A. Ewings, J. R. Stewart, M. Jimenez-Ruiz and H. M. Rønnow *The use of selected neutron absorption resonance filters to suppress spurious events on hot neutron spectrometers*, in Nuclear Instruments and Methods in Physics A, vol 780, 2015

- A. R. Wildes, V. Simonet, E. Ressouche, G. J. McIntyre, M. Avdeev, E. Suard, S. A.Kimber, **D. Lançon**, G. Pepe, B. Moubaraki , and T. J. Hicks *Magnetic structure of the quasi-two-dimensional antiferromagnet NiPS$_3$*, in Phys. Rev. B, vol 92, 2015

In preparation

- **D. Lançon**, M. Mena, Ch. Rüegg, P. Freeman, T. Guidi, R. I Bewley, and H. M. Rønnow, *Q-dependence of correlated damping for triplet excitations in SrCu$_2$(BO$_3$)$_2$*

- S. Yano, **D. Lançon**, H. M. Rønnow, T. Hansen , E. Ressouche, and J. S. Gardner, *A neutron diffraction investigation on MnP under pressure*

- P. Babkevich, N. E. Shaik, **D. Lançon**, A. Kikkawa, M. Enderle, R. A. Ewings, H. C. Walker, D. T. Adroja, P. Manuel, D. D. Khalyavin, T. Masuda, and H. M. Rønnow *Magnetic excitations from two-dimensional interpenetrating Cu framework in Ba$_2$Cu$_3$O$_4$Cl*